eman ta zabal zazu

Universidad del País Vasco

Euskal Herriko Unibertsitatea

Molecular Engineering of Semiconducting Polymers for Perovskite Solar Cells

PhD Thesis

Silvia Valero Moya

Supervised by

Dr. Juan Luis Delgado Cruz

Dr. Aurelio Mateo-Alonso

Donostia-San Sebastián

2019

POLYMAT

Basque Center for Macromolecular Design and Engineering

A mi Familia

CONTENTS

1. INTRODUCTION 1

1.1 Energy Supply and Climate Change 3

1.2 Photovoltaic Energy Conversion 6

1.2.1 Basics of Semiconductors 6

1.2.2 Principles of Solar Cells 10

1.2.3 Current-Voltage Characteristics of Solar Cells 12

1.3 Types of Solar Cells 13

1.3.1 Wafer-Based Solar Cells 14

1.3.2 Thin-Film Solar Cells 16

1.4 Dye-Sensitized Solar Cells 19

1.5 Perovskite Solar Cells 21

1.5.1 Historical Development of Perovskite Solar Cells 21

1.5.2 Hybrid Organic-Inorganic Perovskite Materials 22

1.5.3 Working Principle and Device Structures 25

1.6 Obstacles towards Large-Scale Application of PSCs 28

1.6.1 Long-Term Stability 28

1.6.2 Toxicity of Lead 31

1.6.3 Hysteresis 31

1.6.4 Scale up 32

2. DOPANT-FREE HOLE-TRANSPORTING POLYMERS FOR PEROVSKITE SOLAR CELLS 35

2.1 Introduction 37

2.1.1 Role and Properties of Hole-Transporting Materials in PSCs 37

2.1.2 Hole-Transporting Materials for PSCs..... 39

2.1.2.1 Spiro-Structured Hole-Transporting Materials 39

2.1.2.2 Hole-Transporting Polymers for PSCs.....41

2.1.3 Efficient Dopant-Free Hole-Transporting Polymers for PSCs 44

2.2 Objectives.....47

2.3 Results and Discussion.....48

2.3.1 Design and Synthesis of Polymers P1-P6 48

2.3.1.1 Synthesis of Functionalized Monomers 49

2.3.1.2 Synthesis of Polymers P1-P6.....52

2.3.2 Thermal, Optical and Electrochemical Properties 56

2.3.3 Perovskite Solar Cells Employing Polymers P1-P6..... 60

2.3.3.1 Perovskite-Based Device Fabrication.....61

2.3.3.2 Photovoltaic Device Testing.....62

2.3.3.3 Stability of Perovskite Solar Cells.....64

2.4 Conclusions 66

3. PERFLUORINATED ADDITIVES FOR PEROVSKITE SOLAR CELLS.....67

3.1 Introduction 69

3.1.1 Additive Engineering to Improve the Perovskite Layer 69

3.1.1.1 Semiconducting Chemical Additives 72

3.1.1.2 Fluorinated Additives for Perovskite Solar Cells.....74

3.2 Objectives.....78

3.3 Results and Discussion.....79

3.3.1 Design and Synthesis of Additives S1, P7 and P8 79

3.3.1.1 Synthesis of Intermediates 80
3.3.1.2 Synthesis of Additives S1, P7 and P8 81
3.3.2 Thermal, Optical and Electrochemical Properties 86
3.3.3 Perovskite Solar Cells Employing S1, P7 and P8 90
3.3.3.1 Perovskite-Based Device Fabrication 90
3.3.3.2 Photovoltaic Device Testing 91
3.3.3.3 Film Characterization 94
3.3.3.4 Stability Tests 99
3.4 Conclusions 101

4. ELECTRON-TRANSPORTING POLYMERS FOR PEROVSKITE SOLAR CELLS 103

4.1 Introduction 105
4.1.1 Role and Properties of Electron-Transporting Materials in PSCs 105
4.1.2 Organic Electron-Transporting Materials for PSCs 106
4.1.3 Naphthalene diimide-Based ETMs in PSCs 109
4.1.3.1 NDI-Based Small Molecules as ETMs in PSCs 109
4.1.3.2 NDI-Based Polymers as ETMs in PSCs 110
4.2 Objectives 113
4.3 Results and Discussion 114
4.3.1 Design of Novel NDI-Based Polymers 114
4.3.1.1 Synthesis of Model Compounds MC1-MC3 115
4.3.1.2 Optical, Electrochemical and Charge Transport Properties of Model Compounds MC1-MC3 116
4.3.2 Synthesis of NDI-Based Polymers P9-P11 120
4.3.2.1 Synthesis of Functionalized Monomers 120
4.3.2.2 Synthesis of Polymers P9-P11 121

4.3.3 Thermal, Optical and Electrochemical Properties 125

4.4 Conclusions 130

5. EXPERIMENTAL SECTION 131

5.1 General Methods and Materials 133

5.1.1 Nuclear Magnetic Resonance Spectroscopy 133

5.1.2 Mass Spectrometry 133

5.1.3 Size Exclusion Chromatography 134

5.1.4 Water Contact Angle Measurements 134

5.1.5 Thermal Analysis 134

5.1.6 Absorption and Fluorescence Spectroscopy 134

5.1.7 Cyclic Voltammetry 135

5.1.8 Time-Resolved Microwave Conductivity 135

5.1.9 Scanning Electron Microscopy 135

5.1.10 Atomic Force Microscopy 136

5.1.11 X-Ray Diffraction 136

5.2 Synthesis 136

5.2.1 Dopant-Free Hole-Transporting Polymers for PSCs 136

5.2.1.1 Synthesis of Precursors 1-8 136

5.2.1.2 Synthesis of Monomers M1-M5 142

5.2.1.3 Synthesis of Polymers P1-P6 146

5.2.2 Perfluorinated Additives for PSCs 153

5.2.2.1 Synthesis of Precursors 9 and 10 153

5.2.2.2 Synthesis of Monomers M6-M7 and Intermediate 11 155

5.2.2.3 Synthesis of Additives S1, P7 and P8 157

5.2.3 Electron-Transporting Polymers for PSCs 160

5.2.3.1 Synthesis of Model Compounds MC1-MC3 160
5.2.3.2 Synthesis of Precursors 12-14 163
5.2.3.3 Synthesis of Monomers M8-M10 165
5.2.3.4 Synthesis of Polymers P9-P11 168
5.3 Construction and Testing of Perovskite Solar Cells 171
5.3.1 Perovskite Solar Cells Employing P1-P6 as HTMs 171
5.3.1.1 Device Fabrication 171
5.3.1.2 Device Characterization 172
5.3.2 Perovskite Solar Cells Employing S1 and P7 as Additives 173
5.3.2.1 Device Fabrication 173
5.3.2.2 Device Characterization 174
6. SUMMARY/RESUMEN 177
6.1 Summary 179
6.2 Resumen 185
7. REFERENCES 191
ACKNOWLEDGEMENTS 211

Abbreviations and Symbols

In addition to the standard abbreviations, acronyms and symbols in organic chemistry, defined in the Journal of Organic Chemistry author guidelines, the following terms have been also used in this manuscript:

AcOH	Acetic acid
AcOEt	Ethyl acetate
AFM	Atomic force microscopy
a:Si-H	Hydrogenated amorphous silicon
a.u.	Arbitrary units
BDT	Benzo[1,2-b:4,5:b´]dithiophene
BHJ	Bulk heterojunction
BT	2,1,3-Benzothiadiazole
CB	Conduction band
CIGS	Copper indium gallium diselenide
c-TiO_2	Compact TiO_2
COD	1,5-Cyclooctadiene
CQD	Colloidal quantum dot
CZTS	Copper zinc tin sulfide
c-Si	Crystalline silicon
CV	Cyclic voltammetry
DBDMH	1,3-Dibromo-5,5-dimethylhydantoin
DCM	Dichloromethane
DMF	*N*,*N*-Dimethylformamide
Dba	Dibenzylideneacetone
DMSO	Dimethyl sulfoxide
dppf	1,1'-Bis(diphenylphosphino)ferrocene
dppp	1,3-Bis(diphenylphosphino)propane
dtbpy	4,4′-Di-*tert*-butyl-2,2′-bipyridine
DSSCs	Dye-sensitized solar cells
DSC	Differential scanning calorimetry
$\mathcal{E}$	Molar extinction coefficient
E_g	Energy gap
E_{HOMO}	HOMO energy
E_{LUMO}	LUMO energy
E_{onset}^{Ox1}	Onset potential of the first oxidation
$E_{1/2}^{Ox1}$	Half wave potential of the first oxidation

ESI	Electrospray ionization
ETL	Electron-transporting layer
ETM	Electron-transporting material
EtOH	Ethanol
e^-	Electron
FA	Formamidinium
Fc	Ferrocene
Fc^+	Ferrocinium
FF	Fill factor
FK102	Tris[2-(1H-pyrazol-1-yl)pyridine)]cobalt(III)tris(hexafluorophosphate)
FK209	Tris[2-(1H-pyrazol-1-yl)-4-tert-butylpyridine]-cobalt(III)-tris[bis(trifluoromethylsulfonyl)imide]
FTO	Fluorine-doped tin oxide
GBs	Grain boundaries
h^+	Hole
HI	Hysteresis index
HOMO	Highest occupied molecular orbital
HTL	Hole-transporting layer
HTM	Hole-transporting material
I	Current
ITO	Indium tin oxide
J	Current density
J_{SC}	Short-circuit current
Li-TFSI	Lithium bis[(trifluoromethyl)sulfonyl]amide
LUMO	Lowest unoccupied molecular orbital
MA	Methylammonium
MALDI	Matrix-assisted laser desorption/ionization
mc-Si	Multiple crystalline silicon
MeOH	Methanol
m-TiO_2	Mesoporous TiO_2
MJ	Multijunction
M_n	Number-average molecular weight
MPP	Maximum power point
M_w	Weight-average molecular weight
NBS	*N*-Bromosuccinimide
NDI	Naphthalene diimide
NDA	1,4,4,8-Naphthalenetetracarboxylic dianhydride

NMR	Nuclear magnetic resonance
OLEDs	Organic light-emitting diodes
OFETs	Organic field-effect transistors
OSCs	Organic solar cells
PCBM	[6,6]-Phenyl-C_{61}-butyric acid methyl ester
PCBTDPP	Poly[*N*-90-heptadecanyl-2,7carbazole-alt-3,6-bis(thiophen-5-yl)-2,5-dioctyl-2,5-dihydropyrrolo[3,4] pyrrole-1,4-dione]
PCPDTBT	Poly{2,6-[4,4-bis-(2-ethylhexyl)-4H-cyclopenta[2,1-b;3,4-b']dithiophene]-*alt*-4,7(2,1,3-benzothiadiazole)}
PCDTBT	Poly[*N*-9'-heptadecanyl-2,7-carbazole-*alt*-5,5-(4',7'-di-2-thienyl-2',1',3'-benzothiadiazole)]
PCE	Power conversion efficiency
PDI	Polydispersity
PEG	Poly-ethylene glycol
PDPPDBTE	Poly[2,5-bis(2-decyldodecyl) pyrrolo[3,4-c]pyrrole-1,4(2H,5H)-dione-(E)-1,2-di(2,2'-bithiophen-5-yl)ethene]
PDPP3T	Poly{2,2'-[(2,5-bis(2-hexyldecyl)-3,6-dioxo-2,3,5,6-tetrahydropyrrolo[3,4-c]pyrrole-1,4-diyl)dithiophene]-5,5'-diyl-*alt*-thiophen-2,5-diyl}
PE	Petroleum ether
PEDOT:PSS	Poly(3,4-ethylenedioxythiophene):polystyrene sulfonate
P3HT	Poly (3-hexylthiophene-2,5-diyl)
P_{in}	Power input
P_{max}	Power output
PSCs	Perovskite solar cells
PTAA	Poly[bis(4-phenyl)(2,4,6-trimethyl)amine]
rpm	Revolutions per minute
rps	Revolutions per second
R_s	Series resistance
sc-Si	Single crystalline silicon
SEC	Size exclusion chromatography
SEM	Scanning electron microscopy
spiro-OMeTAD	2,2',7,7'-tetrakis(N,N-di-p-methoxyphenylamine)-9-9' spirobifluorene
ss-DSSCs	Solid-state dye-sensitized solar cells
TBAHFP	Tetrabutylammonium hexafluorophospate
TRMC	Time-resolved microwave conductivity
*t*BP	4-*tert*-butylpyridine
TLC	Thin layer chromatography

T_d	Decomposition temperature
T_g	Glass transition temperature
T_m	Melting temperature
TGA	Thermogravimetric analysis
THF	Tetrahydrofuran
TOF	Time of flight
TPD	*N*,*N*′-diphenyl-N,N′-bis-(3-methylphenyl)-N,N′-bis(phenyl)benzidine
UV-vis	Ultraviolet-visible
VB	Valence band
V	Voltage
V_{OC}	Open-circuit voltage
X_n	Degree of polymerization
XRD	X-ray diffraction
λ	Wavelength
$\varphi\Sigma\mu$	Pseudo-photoconductivity
μ	Mobility
σ	Conductivity

1. INTRODUCTION

1 INTRODUCTION

1.1 Energy Supply and Climate Change

Since the discovery of fire by primitive humans, mankind has been searching ways to take advantage of different energy sources. Before the industrial revolution, wood was the primary energy source, which was used not only to fabricate buildings and homes at that time, but also for heating, cooking and other basic needs for survival. In addition, wind, water, tide etc. have been exploited as energy sources and are still used to power machines in many parts of the world.

However, since the industrial revolution and especially over the last decades, the consumption of energy has undergone an unprecedented change and nowadays, our current energy system is dominated by fossil fuels.[1]

Fossil fuels, including coal, oil and natural gas, are currently the world´s primary energy source (energy directly harvested from natural resources). They were formed millions of years ago when dead plants and animals were buried by sand and water and were subjected to intense heat and pressure. However, fossil fuels are considered non-renewable energy sources because they do not naturally replenish on a short enough timescale for humans to use.

In order to extract energy from fossil fuels they have to be burned. This process mainly releases carbon dioxide (CO_2) into the atmosphere together with other greenhouse gases. Those gases, trap heat prompting the raise in Earth´s temperature and are considered by scientists the main reason for the climate change.[2]

The role of energy is vital for the modern industrial economy and the consumption of energy is linked with the economic prosperity and social progress. However, over the last decades, population growth together with the raise of industrial production have resulted in a large increase in energy consumption. This has resulted in a drastic growth of the CO_2 concentration in the atmosphere caused by the extensive use of fossil fuels.[2] This concentration has changed from the stable value in recent

history, about 275 ppm, up to 413 ppm in 2019 in just 200 years, leading to serious environmental issues (Figure 1).[3]

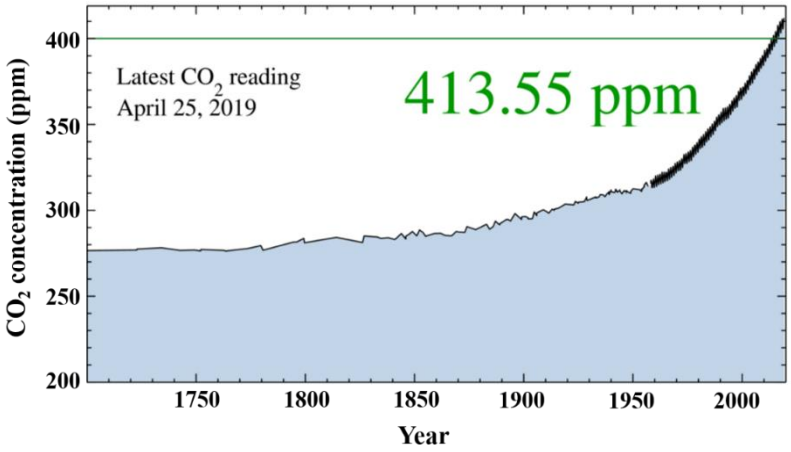

Figure 1. Atmospheric CO_2 concentration variation measured at Mauna Loa observatory (Hawaii).

There are strong indications suggesting that the climate is changing and as a result, observable phenomena are appearing. Global temperature rise, warming oceans, glaciers retreat, less snow cover, sea level rise, declining arctic sea ice (Figure 2), extreme events or ocean acidification are some of the phenomena related to the climate change caused by the fossil fuels consumption.[4–6]

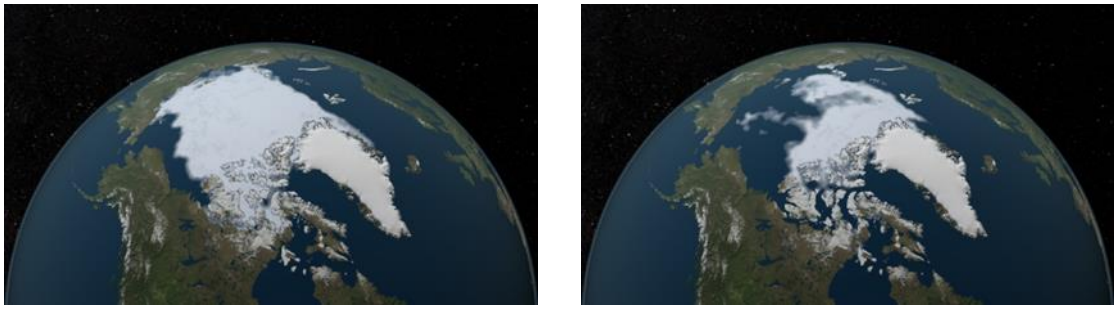

Figure 2. The area of the Arctic Ocean covered in ice increases during the winter and then shrinks during the summer. These images compare the 1984 minimum (left) with that of 2012 (right). A long-term downward trend of about 12 percent sea-ice loss per decade since the late 1970s has been observed.[7]

The situation expected for the near future is not promising. In fact, by 2040 is expected an increase in the world population from 7.4 billion to more than 9.2 billion people. This growth together with industrial energy needs will result in an increase in the energy demand (Figure 3).[8,9]

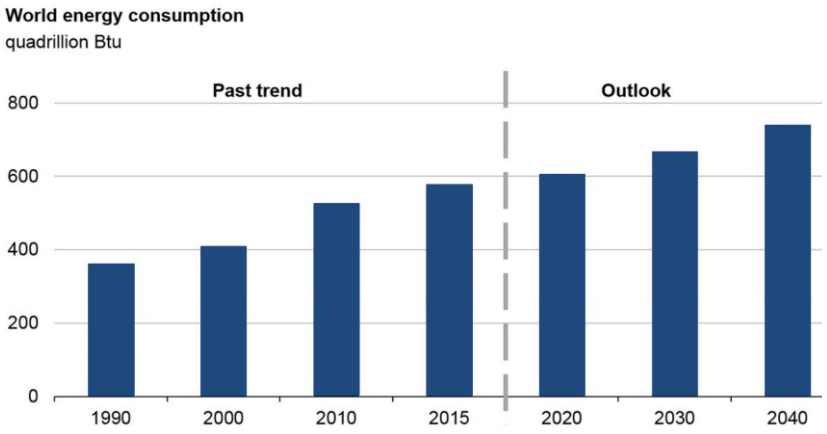

Figure 3. World energy consumption will rise 28% between 2015 and 2040.[9]

Nevertheless, what would happen if we burn the Earth's entire supply of fossil fuels or if we continue burning fossil fuels at that rate?

The environmental problem is threatening the Earth and humanity is becoming aware of this. In fact, 195 countries signed the Paris Agreement in 2015 to fight against the climate change. To this end, these countries committed themselves to take the necessary measures to keep the temperature rise during this century to no more than 2 ºC above the levels from the pre-industrial era (1850-1900).[10] For example, the European Union has set a greenhouse gases emissions reduction targets of 20, 30 and 80% by 2020, 2030 and 2080, respectively, relative to the levels existing in 1990.[11]

To achieve these targets, and considering the limited amount of non-renewable fossil fuels and the environmental impact of their use, a transition to a carbon-free world is compulsory. It will be strongly imperative a huge shift to lower-emission energy sources by developing new forms of clean, environmentally friendly and sustainable energy technologies.[12] That means a shift to renewables, which nowadays only constitute an 11% (Figure 4) of the total world energy consumption.[13]

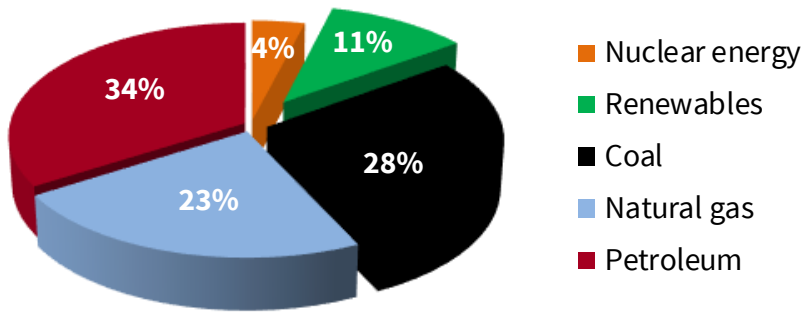

Figure 4. World energy consumption by energy source, 2017.

1.2 Photovoltaic Energy Conversion

"I would put my money on the sun and solar energy. What a source of power! I hope we do not have to wait until oil and coal run out before we tackle that"

Thomas Edison, 1931.[14]

As a matter of fact, solar energy is, together with wind energy, one of the best alternatives to fossil fuels.[15] Solar energy is the most abundant, clean and easily accessible renewable energy available, which could meet the energy needs of humankind. In fact, the sun energy that reaches earth surface every minute is enough to satisfy the world´s energy demand for a whole year if efficient conversion of solar energy to electricity is ensured. Therefore, designing systems that can effectively gather, transfer, or store solar energy has been a great and enduring challenge for researchers.[16]

1.2.1 Basics of Semiconductors

Although this thesis focuses on the synthesis of organic semiconductors for application in perovskite solar cells, this section will focus on some basic concepts related to classical inorganic semiconductors, which are essential to understand the principles of solar cells. To explain better the general characteristics and phenomena in semiconductors, in some cases we will use silicon semiconductors as an example.

Organic semiconductors show differences compared to conventional inorganic semiconductors but their physics is similar to that of classical inorganic semiconductors.[15]

Band structure, electrons and holes

Semiconductors exhibit conductivity, which is situated in the range between conductors and insulators. Furthermore, conductivity in semiconductors can vary depending on the environment. This ability makes semiconductors crucial in the fabrication of electronic devices.

Inorganic semiconductors are made up of individual atoms bonded together in a regular periodic structure to form a crystal lattice. In the case of silicon semiconductors, each atom is surrounded by 8 electrons, which are all taking part in covalent bonds (Figure 5).

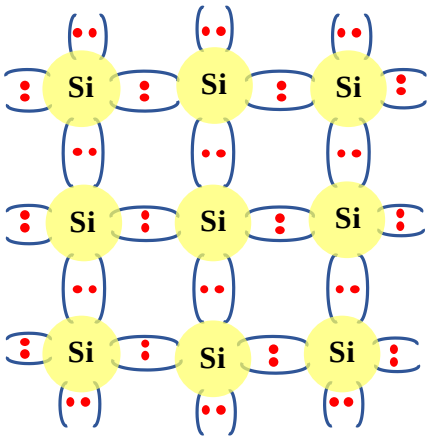

Figure 5. Schematic representation of Si-crystal.

Under certain conditions, the electrons could gain enough energy to escape from their bonds and they would be capable of moving in the whole crystal. In that situation, they behave as free electrons and as a result, they will be able to participate in conduction. The aforementioned free electrons are in a high-energy state, while electrons which cannot move, are in a low-energy state. Electrons cannot attain energy values in between these two energy states and consequently, they are at a low-energy position in the bond, or they have enough energy to move free. When the electron is excited to a high-energy state, it leaves also an empty "space" in the low-energy state. The space left behind by electrons allow a covalent bond to move from one electron to another, thus appearing to be a positive charge moving through the crystal lattice. This empty space is commonly called a hole (h^+), and it is similar to an electron (e^-), but with a positive charge.[17] Electrons and holes are the charge carriers in semiconductors.

The aforementioned energy that is required for an electron to break free is called band gap (E_g). Generally, E_g is defined as the energy difference between the highest occupied energy level called "valence band" (VB) and the lowest unoccupied energy level called "conduction band" (CB). Depending on the energy gap, materials in electronics can be classified into conductors, insulators and semiconductors (Figure 6).

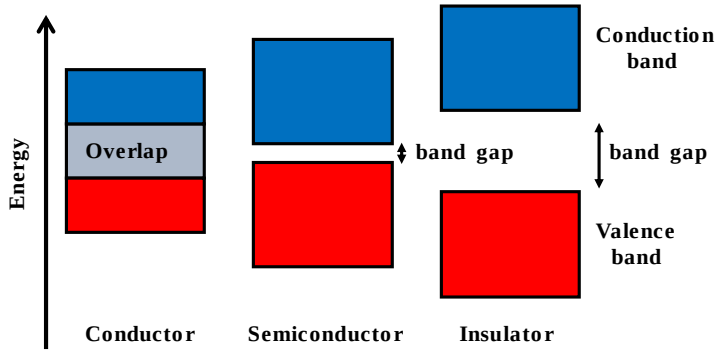

Figure 6. Conduction and valence bands in conductors, semiconductors and insulators.

Insulators have a large energy gap (> 5 eV) between their valence and conduction bands. In insulators, even at high temperatures, electrons do not normally gain enough energy to leave the VB and go to the CB. Therefore, with no electrons in the CB, conduction is not possible.

In conductors, there is no band gap between their valence and conduction bands, since they overlap. Consequently, electrons can move freely and participate in conduction.

Semiconductors have a small energy gap usually up to 4 eV. Like insulators, in a semiconductor at 0 K the VB is completely full and the CB is completely empty. However, since the band gap is so small, as temperature rises some electrons gain enough energy to jump from the VB to the CB leaving behind holes in the VB.

Organic semiconductors are mainly π-conjugated molecular systems in which the energy levels are organized in molecular orbitals. The most representative orbitals are the highest occupied molecular orbital (HOMO), which is analogous to the VB in inorganic semiconductors, and the lowest unoccupied molecular orbital (LUMO), which is similar to the CB in inorganic semiconductors. The difference between HOMO and LUMO determines the band gap of the organic semiconductor.[18]

Doping in semiconductors

To improve the conductivity of a semiconductor, the introduction of defects is necessary leading to an increase of the number of free electrons and holes in the material. This phenomenon is called doping and the defects are introduced using

dopants. A semiconductor that is not doped is called intrinsic semiconductor and it has a high degree of purity but low conductivity.

When an intrinsic Si semiconductor is doped with impurity atoms that have one electron more than Si in the outer electronic shell, e.g. phosphorous (P), this results in more electrons than holes in the crystal lattice. These extra electrons can move freely in the semiconductor. Because electrons are negatively charged, such doped semiconductor is called *n*-type (Figure 7 left). Similarly, when an intrinsic Si semiconductor is doped with impurity atoms that have one electron less than Si in the outer electronic shell, e.g. boron (B), there will be more holes than electrons in the crystal. Since holes are positively charged, such semiconductor is then called *p*-type (Figure 7 right).[17] Doped semiconductors are called extrinsic semiconductors.

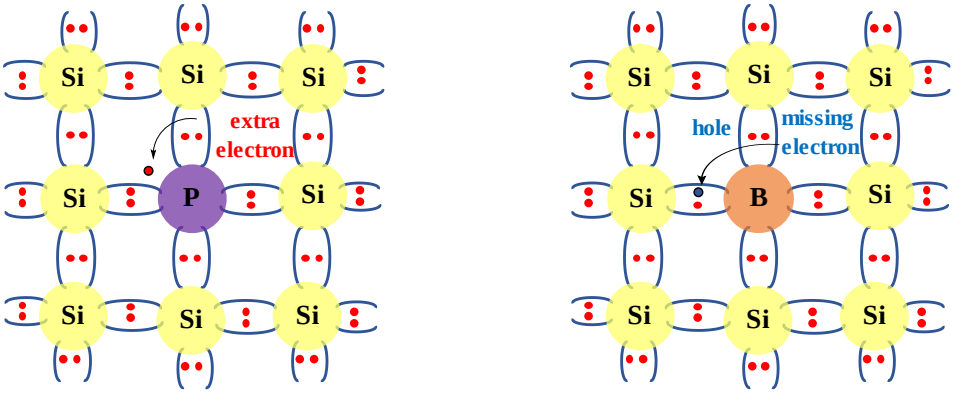

Figure 7. Schematic representation of Si-crystal doped with P to produce *n*-type semiconductors (left) and Si-crystal doped with B to produce *p*-type semiconductors (right).

Light absorption in semiconductors

Semiconductors are responsible for absorbing light in a solar cell. However, these materials are only able to absorb light of the solar spectrum with energy equal to or higher than their band gap. If the incident light has energy higher than the band gap of the semiconductor, part of the light is absorbed but the excess of energy will be lost in the form of heat. If the light energy is lower than the band gap, the semiconductor will not absorb this light. Since the solar spectrum encompasses photons with different energies which cannot be absorbed by a single semiconductor, a huge part of the energy is lost.[19] These losses are closely related to the maximum obtainable efficiency of

solar cells, which is determined by the band gap of the semiconductor, as is shown in Figure 8.

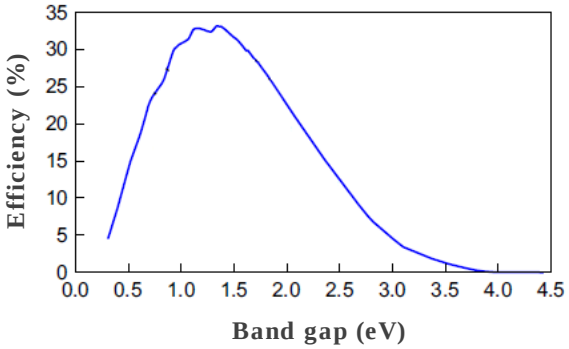

Figure 8. Maximum theoretical efficiency for a solar cell operated at 298.15 K and illuminated with the AM 1.5G spectral irradiance as a function of the band gap energy.[20]

In fact, solar cells with only one semiconductor have a maximum theoretical efficiency of 33.2%, which requires a semiconductor band gap of 1.34 eV.[20,21]

1.2.2 Principles of Solar Cells

When we talk about solar or photovoltaic cells we are referring to devices able to convert sunlight into electricity. These devices are usually integrated in larger structures called photovoltaic or solar modules. Each solar cell works taking the energy from the sun and converting it into electricity due to the photovoltaic effect.

The photovoltaic effect was discovered by Edmond Becquerel in 1839. He showed that when exposing certain materials (semiconductors) to sunlight they could generate electrical current. This effect is the basis not only of the majority of solar cells, but also many other electronic devices.[22]

A solar cell is created when *p*-type and *n*-type semiconductor materials come together forming a *p*-*n* junction. Figure 9 shows a schematic of the *p*-*n* junction.

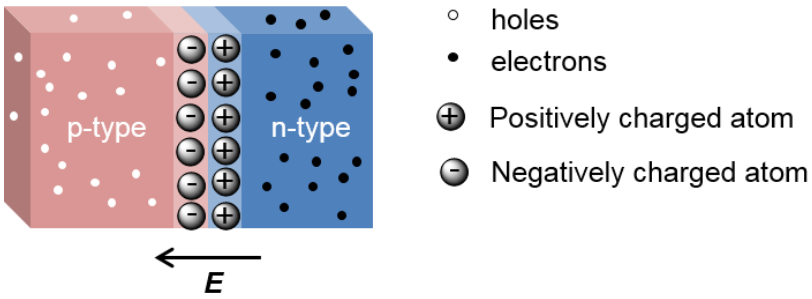

Figure 9. A schematic of the semiconductor *p*-*n* junction at equilibrium.

By joining these two types of semiconductors, extra electrons in the *n*-type semiconductor diffuse to the *p*-type semiconductor because the electron concentration in the *n*-type is higher than in the *p*-type semiconductor. Similarly, extra holes in the *p*-type semiconductor diffuse to the *n*-type semiconductor. When electrons and holes move across the junction, they leave behind charged particles. These charged particles are not able to move because they are taking part of the crystal lattice. In this way, positively charged particles stay at the *n*-side and negatively charged particles remain at the *p*-side of the junction. The process continues until eventually a state of equilibrium is achieved and an electric field (*E*) forms. This electric field acts as a "potential barrier" at the junction keeping away any free charge carrier from passing through the junction.[23]

If the *p*-*n* junction is connected to an external circuit and a positive voltage is applied to the *p*-type side and a negative voltage to the *n*-type side (forward bias), free charges will be able to overcome the potential barrier and move to the corresponding side of the junction. The charges driven round the circuit form an electric current and do useful work (Figure 10).[24]

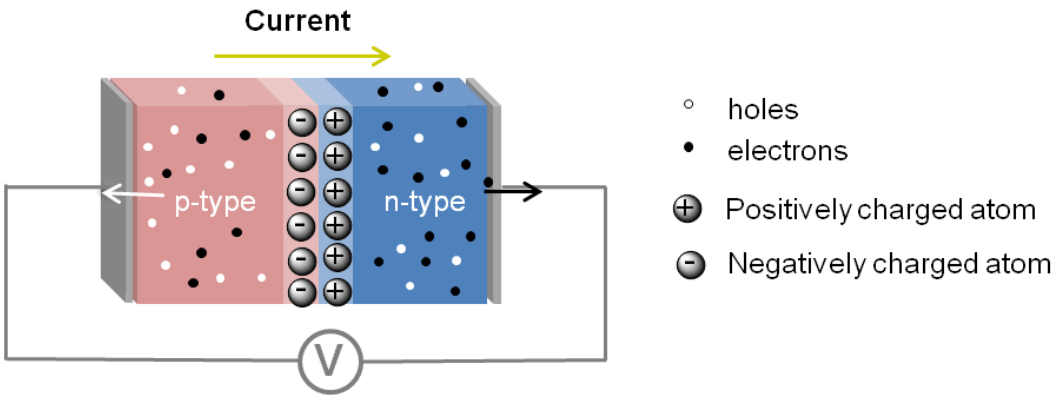

Figure 10. A schematic representation of the semiconductor *p*-*n* junction connected through an external circuit.

Solar cells are essentially illuminated *p*-*n* junctions. When light shines on them with an energy larger than the band gap of the semiconductor, an electron from the VB will be excited to the CB. Consequently, an electron in the CB and a hole in the VB, named as e^-/h^+ pair, will be generated. If these mobile charge carriers reach the vicinity of the junction, the electric field will push holes into the *p*-side and electrons into the *n*-side.

If both sides of the junction are connected through an external circuit, the accumulated electrons in the *n*-side will flow out of the *n*-side and will go to the *p*-side to recombine with the holes and current will be generated.

Essentially, three steps are necessary to transform sunlight into electricity in any photovoltaic device: 1) absorption of sunlight; 2) formation of free charges (electrons and holes), and 3) collection of charges at the respective electrodes.[25]

1.2.3 Current-Voltage Characteristics of Solar Cells

One of the most important characterization techniques for solar cells is the current density-voltage (*J*-*V*) measurements, from which the solar cell energy conversion can be determined (Figure 11). The *J*-*V* characteristics are monitored by changing the external voltage from zero (short-circuit conditions) to infinite voltage (open-circuit conditions), or by changing the external voltage in the opposite direction.[24]

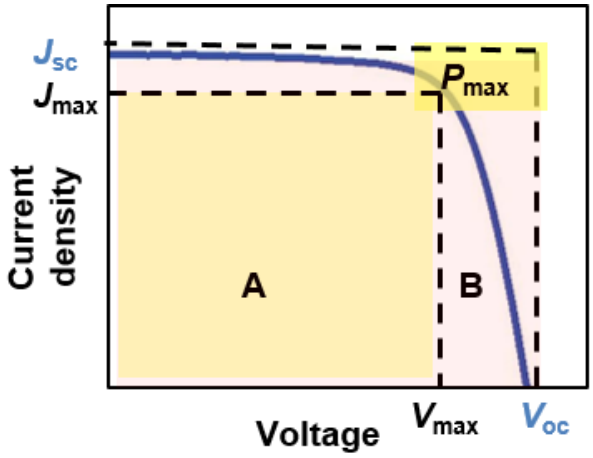

Figure 11. Current density-voltage curve of a solar cell under light illumination.

The power conversion efficiency (PCE) or **efficiency** (η) of any solar cell is defined as the ratio of energy output (P_{max}) from the solar cell to input (P_{in}) energy from the sun (Equation 1):

$$\eta = \frac{P_{max}}{P_{in}} = \frac{FF \cdot V_{OC} \cdot J_{SC}}{P_{in}} \qquad (1)$$

The key solar cell parameters are:

- **Short-circuit current (J_{SC})**. It is the maximum current from a solar cell that is recorded when the voltage across the cell is zero.
- **Open-circuit voltage (V_{OC})**. It is the maximum voltage available from a solar cell, and this occurs at zero current.
- **Fill factor (FF)**. It is defined as the ratio of the maximum power from the solar cell to the product of V_{OC} and J_{SC} (Equation 2):

$$FF = \frac{A}{B} = \frac{P_{max}}{V_{OC} \cdot J_{SC}} = \frac{V_{max} \cdot J_{max}}{V_{OC} \cdot J_{SC}} \qquad (2)$$

1.3 Types of Solar Cells

Depending on the device structure and architecture, photovoltaic technologies can be divided into two main groups (Figure 12):

- *Wafer-based solar cells*, which are produced from slices of semiconducting wafers. They are used directly without the necessity of using any substrate. However, wafers are typically covered with glass for mechanical stability and protection.
- *Thin-film solar cells*, which are produced by depositing thin layers of semiconductors onto a glass, metal or plastic foil substrate. These, in turn, are divided into *commercial* and *emerging thin-film solar cells.*[26]

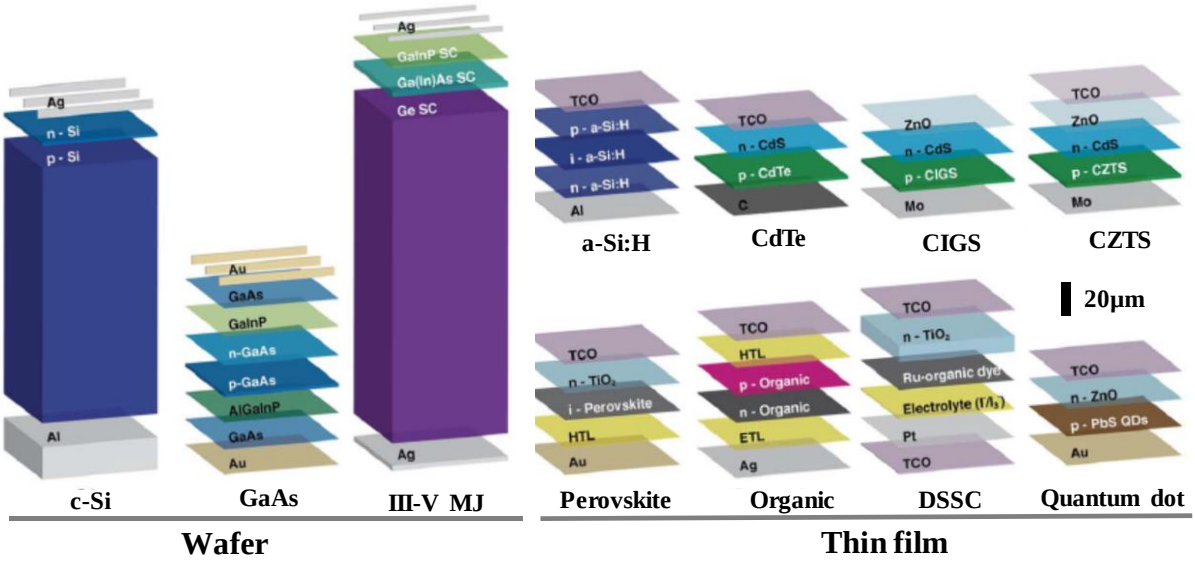

Figure 12. Classification of solar cells technologies based on device structure.[26]

1.3.1 Wafer-Based Solar Cells

Currently, wafer-based solar cells can be categorized into crystalline silicon (c-Si), gallium arsenide (GaAs) and multijunction (MJ) solar cells, which are all commercially available.

Crystalline silicon (c-Si) solar cells

About 90% of the world´s solar cells are made from wafers of crystalline silicon.[27] They can be made either of single crystal [single crystalline silicon (sc-Si) solar cells] or contain many small grains of silicon crystals [multiple crystalline silicon (mc-Si) solar cells] as shown in Figure 13.[28] Currently, the best efficiency for sc-Si solar cells and mc-Si solar cells are 26.7% and 22.3%, respectively. For large-area modules, records efficiencies are 24.4% and 19.9% for sc-Si and mc-Si, respectively.[29]

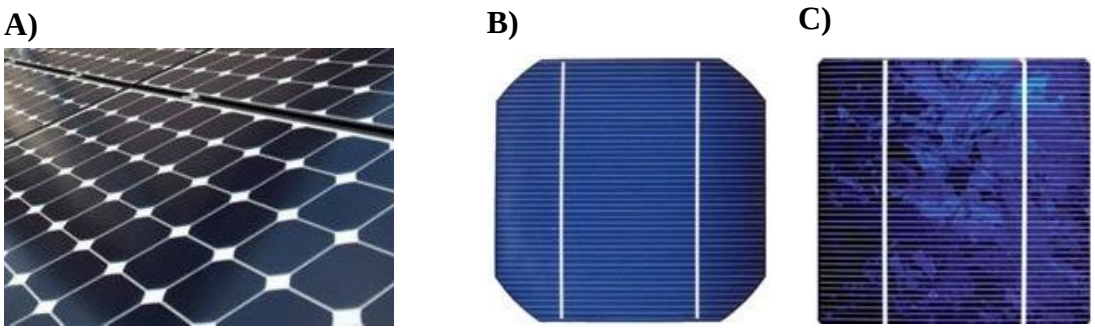

Figure 13. A) Single crystalline silicon-based solar panel, B) Single crystalline silicon solar cell and C) Multiple crystalline silicon solar cell.

A key disadvantage in c-Si solar cells is that crystalline silicon is a poor absorber, which requires the use of thick and rigid wafers. This leads to a limitation in terms of flexibility and modules design. In addition, the high level of material´s purity required, makes their manufacturing process slow and labour-intensive, which makes them very expensive.[30]

Despite these limitations, they are still the predominant photovoltaic technology because of their high photo-conversion efficiency, high stability, proven manufacturability, abundant materials, non-toxicity, long lifespan and reliable performance, among others.[28,30]

Gallium arsenide (GaAs) solar cells

Gallium arsenide (GaAs)-based photovoltaic cells are produced by depositing layers of gallium and arsenic onto a base of single crystal GaAs.[31]

GaAs is the highest efficiency solar material currently available in the world. GaAs single junction solar cells have achieved the highest power conversion efficiencies of any material system (29.1% for lab cells and 25.1% for modules).[29]

However, the high cost of GaAs solar cells has restricted their use in large-scale terrestrial applications and they are only used in applications in which high efficiencies are crucial, such as outer space exploration.

Both silicon and GaAs solar cells, discussed above, are known as single junction solar cells, since there is only one *p-n* junction in the device. To overcome the limitation of a single absorber, a multiple junction structure is proposed, in which several materials with different band gaps are used.

Multijunction (MJ) solar cells

The aim of multijunction or tandem solar cells is to use a combination of semiconductor materials, meaning several single *p-n* junctions, with different band gaps and stack them together. Each single junction would grew on top of each other and to ensure optimal absorption, top junctions should have higher band gaps than bottom junctions. In this way, the light passes first through a material which absorbs the high-energy photons and then lower-energy photons will be absorbed by the junctions at the bottom.[19]

A typical MJ solar cell uses two or more absorbing junctions, and the theoretical maximum efficiency increases with the number of junctions. They are semiconductor alloys that incorporate elements of the groups III and V of the periodic table such as gallium indium phosphate (GaInP), gallium indium arsenide (GaInAs) or gallium arsenide (GaAs).

This class of solar cells are produced in the same way as GaAs cells, i.e. depositing layers of material onto a single crystal base, which makes them very

expensive to produce, and only commercially viable for concentrated photovoltaic systems and space applications.[28] MJ solar cells are the most efficient solar cells ever developed with demonstrated efficiencies above 40% (38.8% for a solar cell with 5 junctions under 1 sun illumination and 46.0% for a triple junction solar cell under 508 suns).[29]

1.3.2 Thin-Film Solar Cells

Thin-film solar cells offer a wide variety of choices in terms of device design and fabrication, constituting about 10% of the global market.[26] They are cheaper to produce than wafer-based solar cells, not only because the amount of raw materials needed to produce the solar cell is smaller but also their fabrication requires less energy, since solar cells can grow themselves on top of a substrate. However, they are less efficient than wafer-based solar cells.

A) Commercial Thin-film Solar Cells

The three most widely commercialized thin-film solar cells include hydrogenated amorphous silicon (a:Si-H), cadmium telluride (CdTe) and copper indium gallium diselenide (CIGS) solar cells. Common among the three materials is their direct band gap, meaning that it is possible to make much thinner solar cells out of the materials, so they can be used through flexible layers for instance.[27,32]

Hydrogenated amorphous silicon (a:Si-H) solar cells

Hydrogenated amorphous silicon material has been used for the fabrication of solar cells because of their extensive variety of points of interest, such as high absorption coefficient (higher than crystalline silicon), non-toxic, low manufacturing cost, abundance of all raw materials, potential for large-scale manufacturing, easy integration of modules into facades, roofs and other substrates, among others.[22] However, the hydrogen passivation of the amorphous silicon is responsible for the light-induced degradation (degradation after illumination), that together with the low

efficiencies, is the major handicap for this class of devices limiting their market adoption.[26]

In a:Si-H solar cells intrinsic amorphous silicon is sandwiched between *p*-doped and *n*-doped materials that are responsible for creating the electric field at the junction.[33]

The highest efficiency reported so far for a:Si-H solar cells is 10.2%.[29] However, most of the commercial a-Si:H modules use multi junctions, which not only show higher performance but also exhibit less light-induced degradation. With the multi-junction concept it has been demonstrated a 13.6% certified cell record stabilized efficiency for a triple junction solar cell having a:Si-H/μc-Si/μc-Si subcells.[34]

Cadmium telluride (CdTe) solar cells

CdTe solar cells are the leading thin-film photovoltaic technology nowadays. Record efficiencies of 21.0% for cells and 18.6% for modules are among the highest for thin film solar cells.[29]

The *p*-*n* junction for making the device is composed of a *p*-type CdTe layer of about 2 μm thicker and a *n*-type layer of about 0.1 μm thicker, so the CdTe layer is the main absorber, which has a large absorption coefficient. However the toxicity of cadmium (Cd) together with the low abundance of tellurium (Te) is a limitation for large-scale applications.[24]

Copper indium gallium diselenide (CIGS) solar cells

Copper indium diselenide ($CuInSe_2$ or CIS) semiconductor has a band gap of 1.04 eV. In CIGS ($CuIn_xGa_{1-x}Se_2$) some indium (In) is replaced by gallium (Ga) in CIS semiconductor which modifies the band gap of the resulting material. Thus, the band gap can increased up to 1.7 eV in the case that all In is replaced by Ga.[30]

CIGS thin film solar cells have achieved 22.9% of efficiency for cells and 19.2% for modules, which are comparable to c-Si wafer-based solar cells.[29] However, the use of toxic elements like Cd and selenium (Se) and the very low abundance of In limits the possible large-scale application of CIGS solar cells.[24]

B) Emerging Thin-Film Solar Cells

Over the last years, several new thin-film photovoltaic technologies have emerged. They are the result of searching for new materials and devices in order to reduce costs and improve conversion efficiencies. These technologies are still at the research and development stage but they bear an enormous important potential for future commercialization. Emerging thin-film technologies include copper zin tin sulfide (CZTS) solar cells, colloidal quantum dot (CQD) solar cells, dye-sensitized solar cells (DSSCs), organic solar cells (OSCs) and perovskite solar cells (PSCs).[26]

Copper zinc tin sulfide (CZTS) solar cells

CZTS or Cu_2ZnSnS_4 solar cells are similar to CIGS solar cells, in which In is replaced by zinc (Zn) and Ga is replaced by tin (Sn). Therefore, all constituents of CZTS film are abundant in the crust of the earth and are non-toxic.[27] The record efficiency reached by a CZTS solar cell to date is 12.6%.[29]

Colloidal quantum dot (CQD) solar cells

This class of solar cells use colloidal quantum dots (CQDs) as light absorbing material. CQDs are nanocrystals produced from semiconductor materials, which are capped with surfactant molecules and dispersed in solution. The key point of quantum dots are that their optical and electrical properties can be tuned by adjusting the size and shape of the nanocrystals.[28,35]

CQD solar cells have reached record lab efficiencies of 16.6% and have the potential of easy fabrication and air-stable operation.[36]

Organic solar cells (OSCs)

This technology has attracted great attention owing to its attractive features and the possibility of low-cost upscaling. Some of these characteristics are simple fabrication, lightweight, affordable and tunable active layer materials with high absorption coefficients or possibility of deposition on a wide range of substrates.

Moreover, due to the possibility of using various absorbers to create coloured or transparent cells, OSCs are well suited for building-integrated application.[25,30,37–39]

OSCs use organic small molecules or polymers to harvest energy from light. They comprise electron donor and electron acceptor materials blended together rather than the classical semiconductor *p*-*n* junctions.[40]

The most successful OSC architecture to date is the bulk heterojunction (BHJ) design.[41] BHJ solar cells are formed by an electron donor (*p*-type) material mixed with and acceptor (*n*-type), sandwiched between two electrodes.[42] After light absorption, charge photogeneration takes place at the interface between the donor and the acceptor.[43] Currently, the best efficiency of a single junction OSC is 15.6%.[36]

1.4 Dye-Sensitized Solar Cells

To explain better the operation principles and main issues related to PSCs (section 1.5), we will first refer to DSSCs from which they derive.

After their discovery in 1991 by Grätzel and O´Regan,[44] DSSCs have been the subject of a great deal of research interest due to some of their properties: good performance, facile synthetic approach, low cost and low environmental impact. Moreover, DSSCs offer possibilities to design solar cells with flexibility in shape, colour, and transparency, which makes them very attractive for commercialization.[45,46]

However, although PCEs around 13% have been achieved with these devices, such cells suffer from stability problems associated with the corrosive and volatile nature of the liquid electrolyte, which is impractical for large-scale applications.[47,48] That problem was partially solved in 1998 by replacing the liquid electrolyte with a solid hole-transporting material (HTM), constituting the first example of solid-state dye sensitized solar cells (ss-DSSCs).[49]

A typical liquid state DSSC is composed of a conductive glass substrate, which serves as a working electrode. On top of it, a dye-sensitized wide band gap semiconductor (usually TiO_2) is deposited. This semiconductor oxide works as an electron-transporting material (ETM) which is finally topped with a platinum counter

electrode. Ultimately, the system is filled with an electrolyte (typically I^-/I_3^-), which serves as HTM (Figure 14).[47]

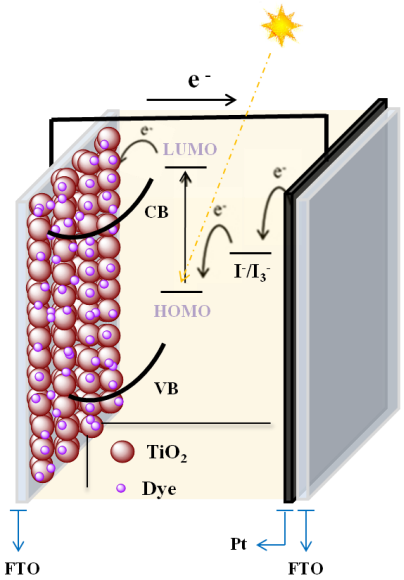

Figure 14. Schematic representation of a liquid state DSSC illustrating the basics underlying device operation.

Compared to all solar cells above-mentioned, in which the semiconductor assumes the task of light absorption and charge carrier transport, in DSSCs the two functions are separated.[50] When sunlight strikes in a DSSC, light is absorbed by the dye, exciting it from the ground state (Dye) to an excited state (Dye*), meaning that an electron from the dye is excited from HOMO to LUMO (Equation 3):

$$Dye + h\nu \rightarrow Dye^* \qquad (3)$$

The excited electrons are then injected into the CB of the TiO_2, resulting in the oxidation of the dye (Dye^+). Injected electrons travel between TiO_2 nanoparticles toward the working electrode (Equation 4):

$$Dye^* \rightarrow Dye^+ + e^- (TiO_2) \qquad (4)$$

The oxidized dye (Dye^+) is regenerated by the electrolyte, which prevents back transfer of the photogenerated electron or degradation of the dye (Equation 5):

$$2Dye^+ + 3I^- \rightarrow 2Dye + I_3^- \qquad (5)$$

Finally, the tri-iodide ions reduce back to iodide (regeneration), when they diffuse towards the counter electrode, by the electrons that return from the external load (Equation 6):[24]

$$I_3^- + 2e^- \xrightarrow{Pt} 3I^- \qquad (6)$$

1.5 Perovskite Solar Cells

1.5.1 Historical Development of Perovskite Solar Cells

In 2009, Miyasaka and co-workers used for the first time a perovskite as active light absorber instead of using the typical molecular dye in a DSSC. They showed a PCE of 3.1% when using the $CH_3NH_3PbBr_3$ perovskite and 3.8% when using the $CH_3NH_3PbI_3$ perovskite.[51] Then, in 2011, Park and co-workers reported the use of $CH_3NH_3PbI_3$ nanocrystals or quantum dots as sensitizer reaching a PCE of 6.5%. However, although the efficiency was improved these solar cells suffered from lack of long-term stability, because the perovskite gradually dissolved into the redox electrolyte, and the device showed a significant decrease in efficiency already in the first 10 minutes.[52]

The stability issues caused by the liquid electrolyte were overcome in 2012, when it was replaced by the solid HTM 2,2',7,7'-tetrakis(*N*,*N*-di-*p*-methoxyphenylamine)-9-9'-spirobifluorene (*spiro*-OMeTAD).[53] In this work, a solar cell was fabricated using $CH_3NH_3PbI_3$ perovskite nanocrystals as light harvesters deposited onto mesoscopic TiO_2 and using the HTM *spiro*-OMeTAD. Not only an efficiency of 9.7% was reached, but also devices remained stable after 500 hours.

Since this first report on a long-term durable solar cell, a great effort was devoted to the development of this new emerging photovoltaic technology, namely perovskite solar cells (PSCs). With further progress in device design and fabrication methods, efficiencies have progressively increased until reaching a PCE as high as 24.2%, which is already comparable to silicon-based technologies.[36]

Being a new technology, the progress of PSCs is unprecedented. Over 10 years of development PSCs got an efficiency of 24.2% (Figure 15), while for example GaAs solar cells have reached around 29% efficiency after more than 60 years, having started at 4% in 1956.[36,54] In fact, PSCs were recognized as one of the biggest scientific breakthroughs of 2013.[55]

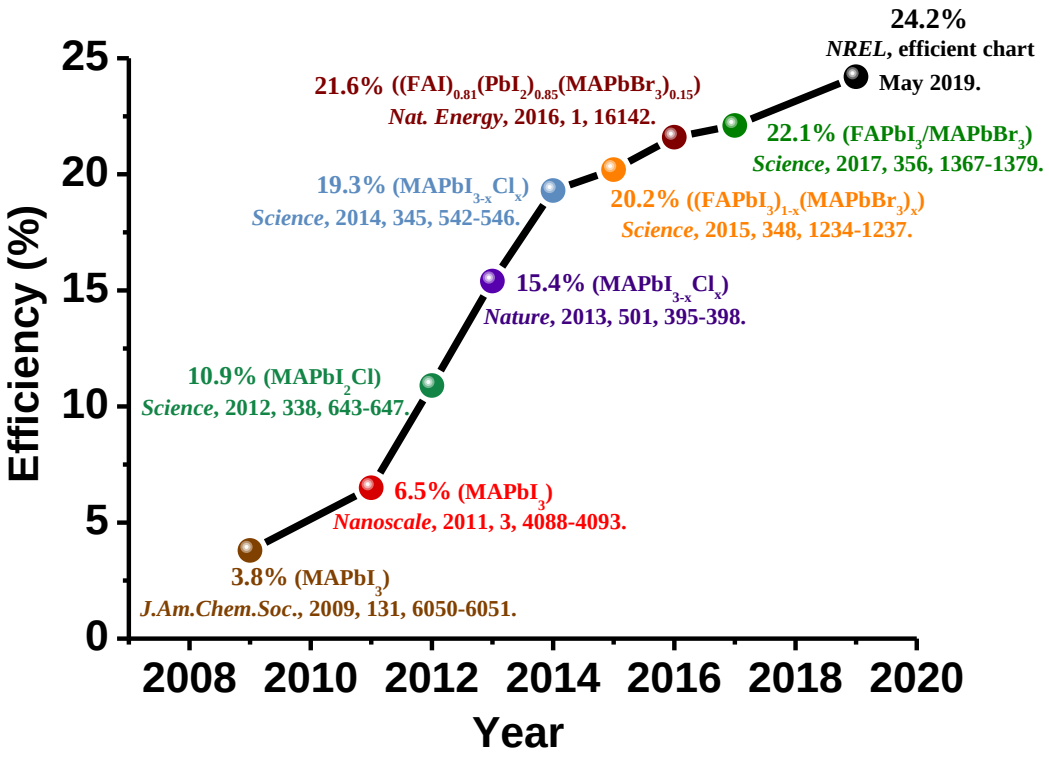

Figure 15. Efficiency evolution of perovskite solar cells.

These results illustrate the potential of PSCs and the possibility to achieve even higher efficiencies, and in that way to meet the energy needs of modern society by making a major impact in generating inexpensive and sustainable electricity.

1.5.2 Hybrid Organic-Inorganic Perovskite Materials

Structure

Perovskites are a class of crystalline materials with the general formula ABX_3 that exhibit a crystal structure similar to that of $CaTiO_3$. Specifically, they form a three-dimensional cubic structure based on corner sharing BX_6 octahedra, in which the X-anions are located at the corners, the smaller B cation is in the middle of the octahedra while the larger A cation occupies interstitial space created by eight adjacent octahedral

(Figure 16).[56] In the case of hybrid organic-inorganic perovskites (referred to as halide perovskites) A is a monovalent organic cation, B is a divalent metal and X is a monovalent halide anion.

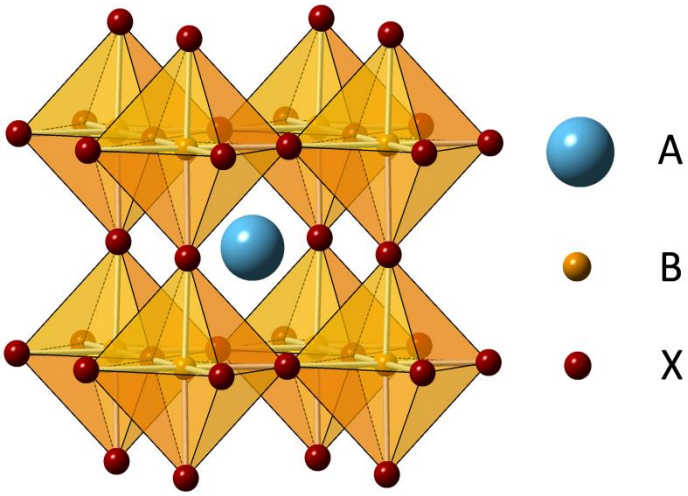

Figure 16. Cubic perovskite crystal structure (unit cell).

To predict the stability and distortion of the perovskite structure after the combination of the constituents A, B and X, the Goldschmidt tolerance factor (t) and the octahedral factor (μ) are used (Equations 7-8):

$$t = \frac{r_A + r_X}{\sqrt{2}\,(r_B + r_X)} \quad (7)$$

$$\mu = \frac{r_B}{r_X} \quad (8)$$

Where r_A, r_B and r_X are the ionic radii of A, B and X, respectively. Typical halide perovskites are stable when they have a tolerance factor in the range 0.81-1.11 and an octahedral factor in the range 0.44-0.90.[57] For instance, a [0.89-1.0] tolerance factor indicates a cubic structure of the perovskite, while a value lower than 0.89 indicates less symmetry, such as tetragonal or orthorhombic structure.[58,59]

The Goldschmidt tolerance factor dictates whether a stable perovskite crystal structure can form or not. In this respect, small cations on the A site, typically methylammonium (MA or $CH_3NH_3^+$), formamidinium (FA or $(NH_2)_2CH^+$), Cs^+ and/or, Rb^+ can form perovskites with halide X anions such as chlorine (Cl^-), bromine (Br^-),

and/or iodine (I^-). Finally, the structure is completed with the divalent metal cation (B) such as tin (Sn^{2+}), copper (Cu^{2+}) and/or lead (Pb^{2+}).[60–62]

Properties

Since the first use of perovskite materials in solar cells, they have attracted great attention because of their excellent semiconductor properties ideally suited to photovoltaics:[62]

- **Broad range of solar absorption** extending over visible or near-infrared region.

- **Strong optical absorption.** The absorption coefficient of perovskites is high across a wide wavelength range.[63] For instance, the absorption coefficient of the most common perovskite used in PSCs ($CH_3NH_3PbI_3$) is 1.5 x 10^4 cm^{-1} at 550 nm, which is one order of magnitude higher than that of the most typical dye used in DSSCs.[55,64,65] This large absorption coefficient guarantees efficient light-harvesting and generation of high density of photoexcited charges which enables the use of a small thickness perovskite layers.[66,67]

- **Tunable band gap.** By varying the A, B and X content of the precursor solution, the band gap of the perovskites can change from 1.1 to 2.3 eV.[65] In this way, it is possible to optimize light absorption tuning the composition in a controlled manner and as result, maximize the performance of the device.[57]

Figure 17 shows how the band gap changes by modifying the composition of the perovskite.[65]

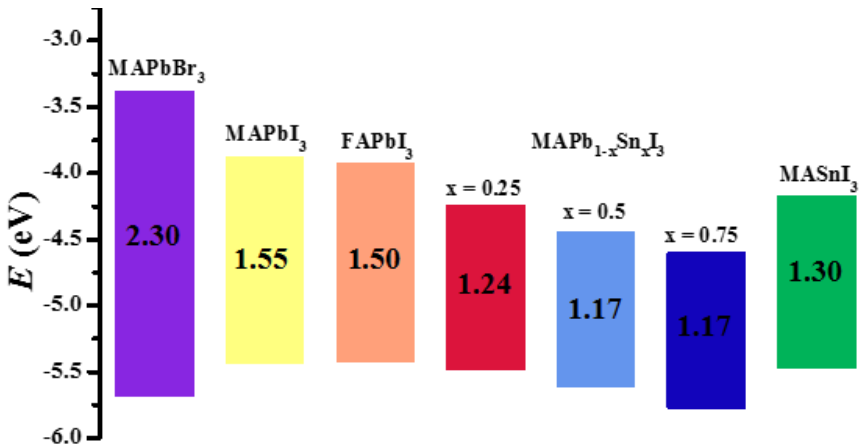

Figure 17. Band gaps of different perovskite materials.

- **Ambipolar charge-transport capabilities.** Perovskite materials not only act as light absorbers, but also as charge transporters of both electrons and holes, which can simplify the device structure.

- **Long electron and hole diffusion lengths** of 100 nm for $CH_3NH_3PbI_3$.[68] After electron-hole pair generation, the charges have to be able to reach their corresponding electrodes before recombining in order to generate current. The diffusion length is defined as the average distance that a charge carrier can do before recombining. Therefore, the higher diffusion length, the lower charge recombination and consequently, more charge carriers will get to the electrodes.

- **High charge carrier mobility**, which are in the range of 5-10 $cm^2\ V^{-1}\ s^{-1}$ for holes and 2-10 $cm^2\ V^{-1}\ s^{-1}$ for electrons.[69]

- **Low-binding energy.** It is still a matter of debate whether excitons or free charges are created after light absorption.[70] This is an important issue, which affect the operation of photovoltaic cells because the resulting exciton has an associate binding energy that needs to be overcome, for electrons and holes to contribute to the photocurrent. Recently, it has been demonstrated the formation of both excitons and free charges after photoexcitation of $CH_3NH_3PbI_3$.[71,72] But even if excitons are created, there are various studies indicating low lifetimes since the binding energy of those are in the range of a few electronvolts.[71–74]

All the aforementioned properties together with the fact that these inexpensive materials can be processed employing several techniques (including solution processing) makes them compatible with low-cost and large-scale roll-to-roll fabrication techniques.[75]

1.5.3 Working Principle and Device Structures

A typical PSC consists of a thin film light-harvesting perovskite layer sandwiched between an electron-transporting layer (ETL) and a hole-transporting layer (HTL) together with two electrodes. If sunlight enters through the ETL (*n*-side), electrons are collected at the bottom of the device and this structure is called *n-i-p* or *regular* structure. On the contrary, if the light goes through the HTL, so the holes are

collected at the bottom of de device, the structure is called *p-i-n* or *inverted*. The regular architecture can be classified into mesoscopic, in which a mesoporous oxide is used, or planar structure.[76,77]

Most of the PSC world record efficiencies were achieved with the regular mesoscopic architecture (Figure 18C), since devices with this architecture showed insignificant hysteresis (see section 1.6.3 for problems related to hysteresis).

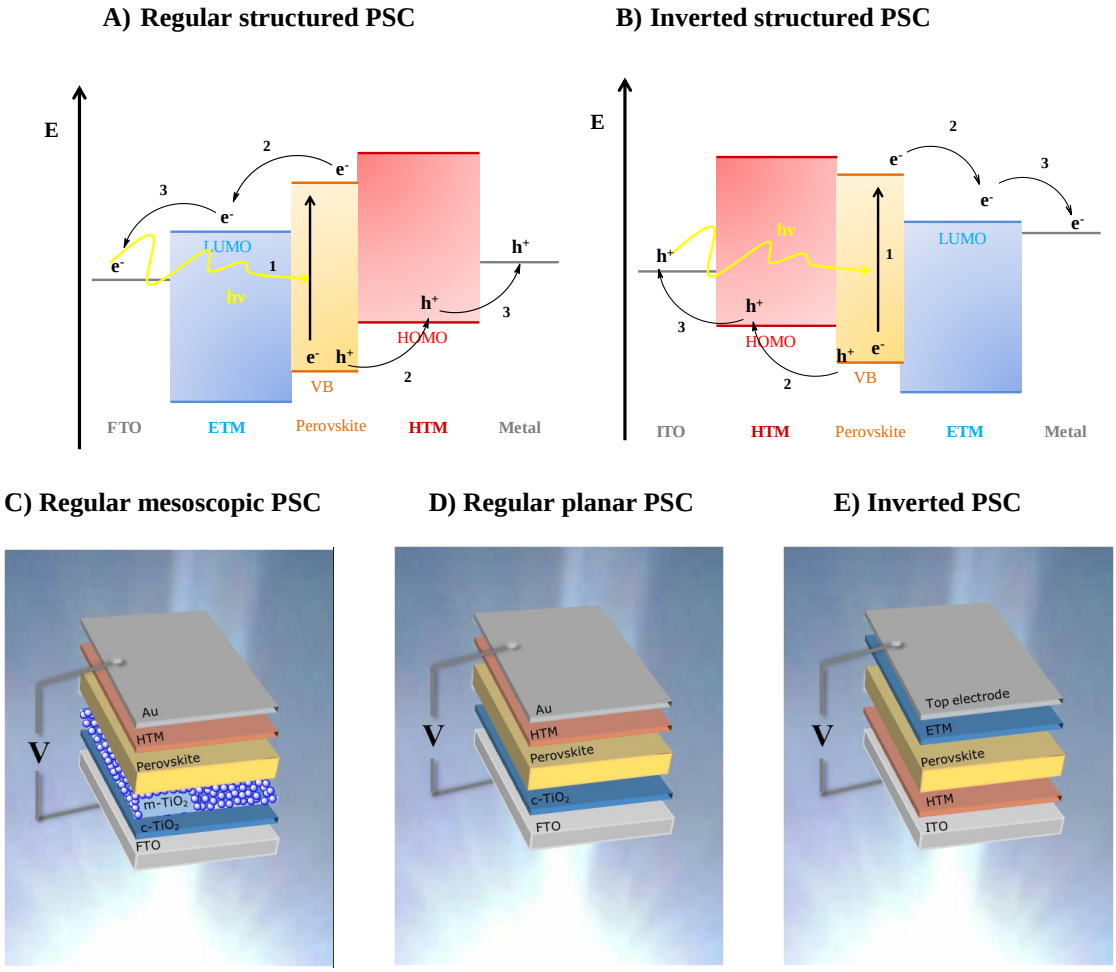

Figure 18. Energy level alignment of typical (A) regular and (B) inverted PSC and main processes: Absorption of photon and free charges generation (1), charge transport (2) and charge extraction (3). Examples of device structures of (C) regular mesoscopic, (D) regular planar and (E) inverted PSC.

In a mesoscospic structure a glass substrate coated with a fluorine-doped tin oxide (FTO) layer, which serves as an electrode, is covered by a compact hole blocking layer (normally TiO_2). The compact TiO_2 (c-TiO_2) plays an important role, suppressing charge recombination at the interface by preventing direct contact between the FTO and the ETM. On top of the compact layer, a mesoporous oxide is layered. If the metal

oxide is a semiconductor (TiO_2 typically, SnO_2, ZnO), this layer acts as an active scaffold, since it takes electrons from the perovskite layer and transport them to the electrode. When replacing the mesoporous semiconductor oxide by an insulator (Al_2O_3 typically, ZrO_2), the scaffold is passive, since it cannot transport charges and electron transport occurs inside the perovskite. After the mesoporous layer, the perovskite is deposited, penetrating through the pores of the oxide, and then covered with the HTM, usually *spiro*-OMeTAD or poly [bis(4-phenyl)(2,4,6-trimethyl)amine] (PTAA). Finally, the system is completed by the deposition of a metal electrode (usually gold) on top of the HTM.[76,78,79]

In the regular planar structure, the architecture is similar to the regular mesoscopic structure above described, but the mesoporous layer is skipped (Figure 18D).

The working principle of a PSC with a regular architecture is as follows (Figure 18A): Once illuminated by sunlight, the perovskite absorbs photons with energy equal to or greater than its band gap generating free electrons and holes. After excitation, electrons will be injected from the perovskite to the ETM at the ETL/perovskite interface, then transported through the ETM and finally collected by the FTO electrode. Correspondingly, holes will be extracted at the perovskite/HTL interface; transported across the HTM and collected to the back gold electrode.[25]

In the inverted or *p-i-n* structure, commonly indium tin oxide (ITO) is used as the hole-collecting bottom electrode, covered by the HTM [usually poly (3,4-ethylenedioxythiophene):polystyrene sulfonate (PEDOT:PSS) or NiO_x] and followed by the deposition of the perovskite absorber. Subsequently, an ETM, typically [6,6]-phenyl-C_{61}-butyric acid methyl ester (PCBM), is deposited and finally an aluminium or silver top electrode is used as the electron-collecting unit completing the device (Figure 18E). With this configuration the working principle is similar to the above described for the regular one, but for the places where the electrons and holes are collected (Figure 18B).[76,77]

1.6 Obstacles towards Large-Scale Application of PSCs

Despite the high efficiency and relatively low cost of the materials used in PSCs, there are several issues which have to be resolved in order to promote PSCs a feasible photovoltaic technology. These include long-term stability, toxicity, hysteresis and scale up of the cell area.[80]

1.6.1 Long-Term Stability

Long-term stability remains a major challenge toward large-scale application of PSCs since they suffer from high sensitivity to environmental factors like moisture, oxygen, ultraviolet (UV) light or high temperatures, among others.[81–86] As a matter of fact, to commercialize PSCs it is necessary that the devices can operate continuously for about 25 years in outdoor conditions.[87]

Oxygen and UV light

The instability of PSCs against UV radiation is primarily due to the widely employed mesoporous TiO_2 (m-TiO_2). PSCs show a decrease in efficiency after UV light exposure mainly because of the presence of surface defects in the TiO_2 structure. Moreover, the reaction between TiO_2 and the perovskite layer can lead to further drops in the efficiency.

TiO_2 contains many surface defects, most of them oxygen vacancies, which can be understood as unpaired electrons. These extra electrons can react with oxygen from the ambient air and lead to the formation of an anion radical (O_2^-). Upon UV excitation, an e^-/h^+ pair is created in the bulk of the TiO_2 structure and the h^+ migrates to the surface of the TiO_2. In that place, the h^+ recombines with the anion radical previously formed converting it into O_2, which gets desorbed from the TiO_2 surface, leaving a space (trap). If a PSC is illuminated, the perovskite will absorb photons and will create an e^-/h^+ pair. The electron could stay in one of these trap states and recombines with holes instead of travelling to the electrode and producing current, which would end up in a loss of efficiency.[88]

In addition, instability caused by UV in PSCs can partly arise from an interaction at the TiO_2/perovskite interface. The degradation mechanism of the perovskite layer could be understood taking into account the possible reactions at the TiO_2 surface (Equations 9-11):[89]

$$2I^- \leftrightarrow I_2 + 2e^- \quad (9)$$

$$3CH_3NH_3^+ \leftrightarrow 3CH_3NH_2\uparrow + 3H^+ \quad (10)$$

$$I^- + I_2 + 3H^+ + 2e^- \leftrightarrow 3HI\uparrow \quad (11)$$

First, TiO_2 extracts an electron from I^- in the $CH_3NH_3PbI_3$ crystal structure forming I_2 at the $TiO_2/CH_3NH_3PbI_3$ interface (Equation 9). That electron may return to the TiO_2 surface giving rise to the formation of HI (Equation 11). As H^+ is consumed (Equation 11), the equilibrium of equation 10 shifts to the right side, which results in the progressive degradation of the perovskite.

To overcome the UV-instability problem, pacifying electronic trap states, use of ultraviolet cut-off filters or replacing the mesoporous TiO_2 with other materials have been proposed.[90,91]

High temperature

Another factor that affects the PSC performance is temperature. This is an important issue to be addressed because an annealing process for crystallization after deposition of the perovskite is necessary, and depending on the temperature at which the process is carried out a difference morphology, composition and as a result, device performance will be achieved.[92] Moreover, solar modules will be exposed under standard operating conditions, so thermal stability is a key aspect that determines the efficiency of the device.

The thermal degradation of perovskite devices depends on several factors, such as the intrinsic temperature degradation of the perovskite, electrodes or charge transporting layers.[93] It has been demonstrated that $CH_3NH_3PbI_3$ suffers degradation when it is heated up to 100 ºC for a short period of time.[85,94]

Thus, perovskite not only undergoes rapid decomposition resulting in a decline in device performance, but one of the decomposition products, PbI_2, is water-soluble and it could lead to environmental problems due to its toxicity.

Moreover, perovskite materials suffer reversible phase transitions as a function of the temperature. For example, $CH_3NH_3PbI_3$ was shown to have three structural phases: a cubic phase above 330 K, a tetragonal phase from 160 to 330 K, and an orthorhombic phase below 160 K.[95] It has been shown a drop in photovoltaic performance at around 55 ºC corresponding to the transition between a tetragonal phase of $CH_3NH_3PbI_3$ to the cubic phase.[96,97]

One of the proposed strategies to improve the thermal stability of PSCs is the modification of the perovskite layer by adding additives. In this regard, Tress and co-workers employed carbon nanoparticles as additives to control the morphology of the perovskite film.[98] They demonstrated that perovskite films containing carbon nanoparticles as additives presented higher thermal stability than films without them.

Moisture

PSCs are also susceptible to moisture, which is one of the major factors of degradation. The perovskite hydrolyses in the presence of moisture producing the two precursors (Equation 12):

$$CH_3NH_3PbI_3\ (s) \leftrightarrow PbI_2\ (s) + CH_3NH_3I\ (aq) \quad (12)$$

Then, CH_3NH_3I decomposes to produce HI (Equation 13), which afterwards can react in the presence of oxygen (Equation 14), or after the exposition to UV light (Equation15).

$$CH_3NH_3I\ (aq) \leftrightarrow CH_3NH_2\ (aq) + HI\ (aq) \quad (13)$$

$$4HI\ (aq) + O_2\ (g) \leftrightarrow 2I_2(s) + 2H_2O\ (l) \quad (14)$$

$$2HI\ (aq) + h\nu \leftrightarrow H_2(g) + I_2\ (s) \quad (15)$$

Therefore, the preparation of PSCs should be conducted inside a glove box filled with an inert gas (normally nitrogen).[91]

1.6.2 Toxicity of Lead

An important issue of PSCs is the toxicity of lead, a component in the perovskite material, which is employed in most PSCs exhibiting good performance. This fact has opened up a new research field in order to solve this issue and to further explore non- or low-toxic perovskite materials.[99]

Actually, PSCs cannot be commercialized in the European Union because there is a strict directive. This regulation restricts to 0.1% in weight the maximum concentration of lead in each homogenous material contained in any electronic device. Unfortunately, all the halide perovskites that have been so far demonstrated as effective photovoltaic materials contain more than 10% lead in weight and indeed they are banned from the European energy market.[100]

In this context, recent research has focused on the replacement of Pb^{2+} with other suitable cations in perovskites.[101] As an example, germanium (II) (Ge^{2+}),[102] tin (II) (Sn^{2+})[103] or mixed Sn-Ge[104] were used as a substitute of Pb^{2+} in PSCs. However, the resulted perovskite materials exhibited low stabilities, because those cations tend to oxidize, from Sn^{2+} to Sn^{4+} or Ge^{2+} to Ge^{4+}, leading to vacancies that induced instability.[105]

1.6.3 Hysteresis

The hysteresis is a phenomenon occurring in PSCs whereby there are changes in the response of the device depending on the direction and rate of the applied voltage. In other words, a different *J-V* curve is obtained depending on whether a backward (from positive to negative voltage) or forward (from negative to positive voltage) scan is applied (Figure 19).[106]

Although the origin of hysteresis is still unclear, different mechanisms have been proposed that could rationalize the experimental findings. These include ferroelectric polarization, ion migration, charge trapping and capacitive effects.[107]

The hysteresis phenomenon hinders the proper characterization of PSCs because it prevents the accurate determination of the efficiency.

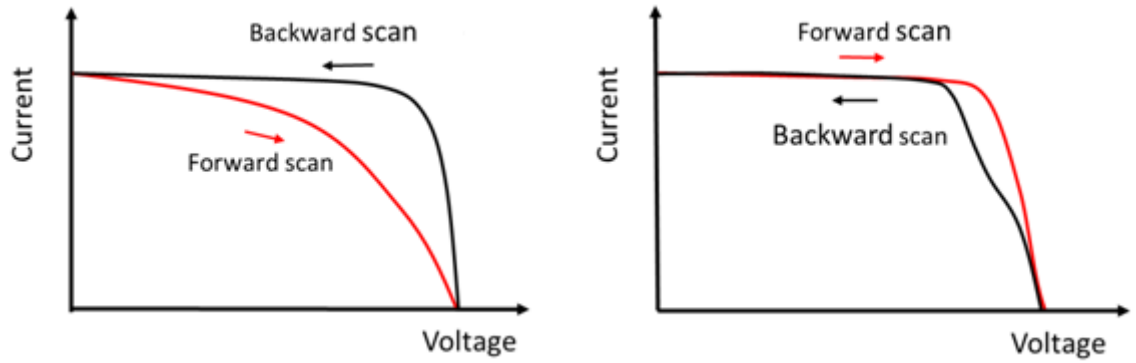

Figure 19. *J-V* hysteresis in regular (left) and inverted (right) PSCs. Discrepancy between the *J-V* curve when scanned from positive to negative voltage (black) and from negative to positive (red).[25]

1.6.4 Scale up

Transition from laboratory-scale fabrication to industrial manufacturing requires scaling up. However, there are some issues to address since the reported record efficiencies for PSCs generally come from devices with a very small active area and it is expected that efficiency drops when scaling up. In fact, it has been already demonstrated that increasing the cell dimension from 0.12 cm^2 to 1.10 cm^2 results in a PCE drop from 17.5% to 15.5%.[108]

There have been already reported photovoltaic panels based on PSCs. Fan and co-workers reported an efficiency of 10.6% for modules of 17.3 cm^2 of active area based on FTO/ZnO/active layer/carbon cells structure without degradation after 140 days of outdoor testing.[109] The same group has fabricated a perovskite module of 45 x 65 cm^2 using the same approach (Figure 20, left). Also, Han and co-workers demonstrated stable and 10.4% efficient 10 x 10 cm^2 perovskite modules, with an active area of 49 cm^2, using a 10 HTM free-based PSC with an FTO/c-TiO_2/m-TiO_2/m-ZrO_2/m-C/perovskite architecture.[110] 96 of those modules constituted a 1 m^2 panel, that together with 6 panels more, formed the photovoltaic panel that is shown in Figure 20 (right).

Apparently, for large-scale devices efficiency falls far behind the record values reported for small area lab devices. In addition, an important step towards the fabrication of large-area modules is the development of new deposition methods

suitable for industrial production that can provide high-layer uniformity with large crystals and fewer grain boundaries over the large area.

Figure 20. Left: Power plant composed of 32 modules with an area of 45 x 65 cm^2 connected in between.[109]. Right: 7 m^2 printable perovskite-based panels.[110]

The progress in PSCs has been tremendous so far, reaching up high efficiencies in a short period, and becoming a promising candidate in the photovoltaic field. However, as mentioned above, there are still several issues that should be addressed for further development of PSCs in order to be taken out of the lab for practical application. Optimizing the perovskite material, deposition techniques or device architectures as well as looking for different hole- and electron-transporting materials will be instrumental to overcome those issues.

2. DOPANT-FREE HOLE-TRANSPORTING POLYMERS FOR PEROVSKITE SOLAR CELLS

2 DOPANT-FREE HOLE-TRANSPORTING POLYMERS FOR PEROVSKITE SOLAR CELLS

2.1 Introduction

Over the past ten years, we have witnessed the rise of PSCs, one of the most impressive evolutions in the history of photovoltaics. PSCs have gained considerable research attention and have emerged as an extremely promising photovoltaic technology due to their remarkable photovoltaic performance and potentially low-production cost. However, this exceptional fast growth is not yet enough to guarantee a spot in the market of solar cells, which is still lead by silicon solar cells.

Among the serious challenges to be addressed, stability remains as one of the biggest issues to be resolved. Significant research efforts in different areas were devoted in attempts to fabricate not only efficient but also long-term stable PSCs. In this effort, among others, HTMs have been intensively studied with the objective of increasing the efficiency and improving the stability of the perovskite-based devices.

This chapter focuses on the role of different materials used as HTMs in influencing long-term stability, improving the photovoltaic parameters and thereby enhancing the efficiency of PSCs.

2.1.1 Role and Properties of Hole-Transporting Materials in PSCs

It has been shown in section 1.5.3 that the photovoltaic process in PSCs takes place in three steps, namely (1) absorption of sunlight and formation of free charges, (2) charge transport and (3) collection of charges at the electrodes (Figure 21). Toward the two latter processes, the HTM plays a crucial role in PSCs, ensuring an efficient hole extraction at the perovskite/HTM interface and improving hole transport from the perovskite to the electrode. Although perovskite materials can conduct holes, the use of HTMs remains indispensable in almost all the architectures utilized in PSCs.[111]

Unfortunately, during device operation, undesirable charge-transfer processes can take place in PSCs (dashed lines in Figure 21). In this context, apart from extracting

holes and transporting them to the electrode, the HTM helps to avoid these troublesome mechanisms, which affect prejudicially the solar cell performance.[112] For instance, if the HTM is correctly chosen, it can act as electron-blocking layer to prevent the recombination losses or back-transfer processes at the perovskite/HTM interface leading to improved device performance.[77] Moreover, the presence of the HTM avoids the direct contact of the metal electrode with the perovskite layer, which also minimizes charge recombination.[113] Furthermore, in many PSCs the HTM constitutes the first line of defence against external agents, so it plays an important role in the device performance as well as in the stability of PSCs.[114]

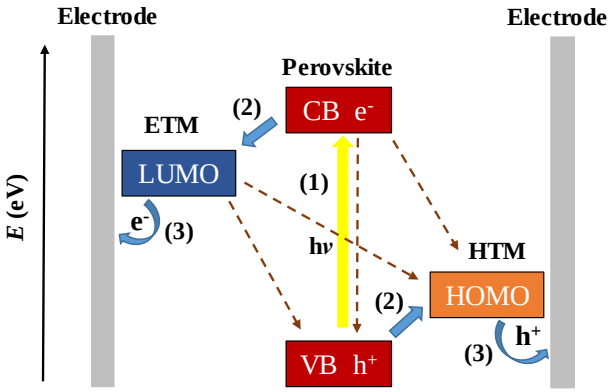

Figure 21. Schematic representation of electronic processes in PSCs. Adapted from reference [112].

For efficient PSCs an ideal HTM should fulfil several general requirements: (i) The HOMO energy level of the HTM should be higher than the VB energy of the perovskite in order to ensure an efficient extraction of the holes from the perovskite to the HTM, minimizing injection losses. Moreover, the HOMO level of the HTM influences the V_{OC}, which consequently affects the PCE of the device.[115] (ii) Furthermore, the HTM should have reasonable hole mobility and conductivity in order to allow rapid transport of the photogenerated holes to the back contact electrode (counter electrode) and prevent charge recombination.[114,116] Neverhteless, HTMs with low conductivity can be doped in order to enhance it, although the presence of dopant additives has been linked to long-term degradation. In an ideal situation, dopant-free HTMs will be paramount for the successful operation of PSCs. (iii) They must be thermal and photochemically stable and resistant to external degradation factors.[117] (iv) They should have enough solubility and good film-forming ability for processing

and device fabrication.[118,119] (v) Amorphous HTMs with appropriate glass transition temperature (T_g), usually above 100 ºC, are desirable.[120] Taking into account that devices operate at higher temperatures than room temperature, sustaining the amorphous state is important. (vi) They should be cheap and environmental-friendly. (vii) An ideal HTM should not absorb in the visible region for not competing with the perovskite in the absorption of light. A good strategy has proven to be using HTMs that absorb in regions where the perovskite has a weaker absorption. Since the most efficient perovskites have a band gap around 1.5 eV (onset at 820 nm), HTMs with lower band gaps would offer the possibility to absorb additional photons at longer wavelengths and consequently, the PCE of the solar cell would be improved.[117]

2.1.2 Hole-Transporting Materials for PSCs

2.1.2.1 Spiro-Structured Hole-Transporting Materials

Spiro-OMeTAD has been the most commonly used standard and is still the predominant HTM employed in the majority of PSCs (Figure 22, left).[116]

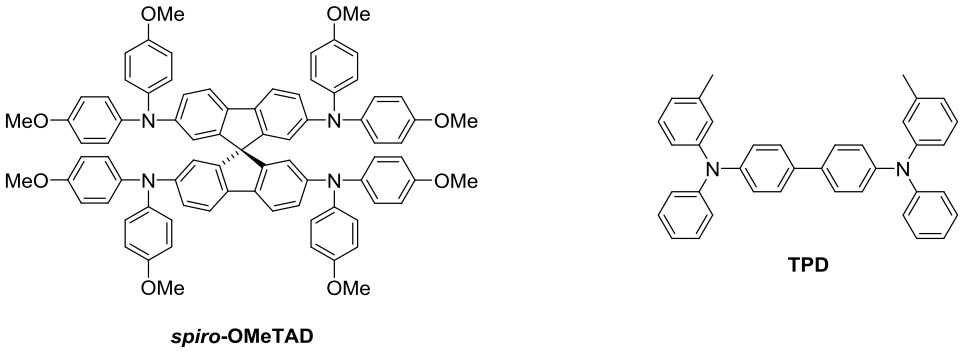

Figure 22. Molecular structures of *spiro*-OMeTAD (left) and TPD (right).

It could be intuited from its name that *spiro*-OMeTAD is based on the spiro structure, in which two extended π-systems are connected to a sp^3-hybridized atom. The perpendicular arrangement achieved with this configuration lends spiro-based molecules to a rigid structure, which give them high morphological stability, whereas the electronic properties of the electroactive moieties remain intact.[120]

Spiro-OMeTAD was first synthesized in 1997 by Salbeck and co-workers[121] as an alternative material to TPD [*N,N*′-diphenyl-*N,N*′-bis-(3-methylphenyl)-*N,N*′-

bis(phenyl)benzidine], which has been widely used as HTM in organic light-emitting diodes (OLEDs) (Figure 22, right). TPD suffers from low morphological stability of the amorphous state, due to its low T_g (62 ºC). In contrast, *spiro*-OMeTAD shows improved thermal stability (T_g = 124 ºC) compared to TPD without compromising its electronic properties.[122]

The incorporation of eight electron donating *p*-methoxy groups leads to an HOMO energy level of -5.22 eV, which is well-aligned with the VB of the most common perovskites used in PSCs. Moreover, *spiro*-OMeTAD is colorless (E_g = 2.95 eV) and consequently, it does not compete with the perovskite for light absorption.[123]

In addition to the good optoelectronic properties and appropriate glass-forming properties, it exhibits good solubility in common organic solvents, which is very important for good film formation and processing.[124] Nevertheless, *spiro*-OMeTAD is far from being the perfect HTM for different reasons. The drawbacks of *spiro*-OMeTAD are its synthetic complexity, high synthetic cost and the requirement of dopants to improve its hole-transport behavior and device performance. Furthermore, high temperatures are detrimental for this molecule, which crystallizes at 182 ºC losing its efficiency as HTM.[125,126]

Regarding the use of dopants, *spiro*-OMeTAD itself has low conductivity (~10^{-5} S cm^{-1}) and hole mobility (~10^{-6}-10^{-5} cm^2 V^{-1} s^{-1}) and to reach the best performances the use of additives is a prerequisite. For *spiro*-OMeTAD, the widely employed dopants are lithium bis[(trifluoromethyl)sulfonyl]amide (Li-TFSI), 4-*tert*-butylpyridine (*t*BP), and a series of organic cobalt salts such as tris[2-(1H-pyrazol-1-yl) pyridine)] cobalt (III) tris(hexafluorophosphate) (FK102) and tris[2-(1H-pyrazol-1-yl)-4-tert-butylpyridine]-cobalt(III)-tris[bis(tri-fluoromethylsulfonyl)imide] (FK209).

Those dopants act introducing additional holes, which leads to an increased charge carrier density in the doped molecule. This process results in a higher conductivity, according to equation 16, where σ is the conductivity, e the elementary charge and n_x y μ_x are the density and mobility of the positive (p) and negative (n) charge carriers, respectively.[127]

$$\sigma = \sigma_n + \sigma_p = (n_n e\mu_n) + (n_p e\mu_p) \quad (16)$$

However, the presence of dopants has been related to the reduction of the long-term stability, due to their migration throughout the perovskite layer.[128,129] To overcome these disadvantages, many research groups are working on replacing *spiro*-OMeTAD with alternative HTMs that yield PSC devices with high efficiency and stability. As a result, a number of organic small molecules, conducting polymers, organometallic complexes, and inorganic semiconductors have been reported as HTMs for high performing PSCs.[93,111,112,114,116,118,130] Among them, conjugated polymers have attracted great attention due to their thermal and mechanical stability, tunability via molecular design and synthesis, or the wide variety of choice.[131] Moreover, compared to small molecules, polymers own higher hole mobility and superior film-forming properties.[132]

If we have a look at the conjugated polymers that have been used as HTMs in PSCs, it is evident that most of them were previously used in OSCs as *p*-type materials. However, there are some polymers that have been specifically designed as HTMs for PSCs.

In the following section, we will comment some of the most representative examples of polymers that have been used as HTMs in PSCs in recent years.

2.1.2.2 Hole-Transporting Polymers for PSCs

In Figure 23 is displayed some of the most representative examples of hole-transporting polymers for PSCs.

PTAA (**HTM-1**) is a polymeric structure of triphenylamines, which was the first polymer tested in PSCs. PTAA exhibits high hole mobility (10^{-2}-10^{-3} cm^2 V^{-1} s^{-1}) compared with other polymers and a suitable HOMO, which determines its excellent hole-extraction and electron-blocking properties.[114] The group of Seok achieved an impressive 22.1% in efficiency using PTAA as HTM, which is the record efficiency in PSCs for a polymeric HTM.[133] In that work, they demonstrated that the introduction of additional iodide ions in the perovskite layer increased the V_{OC} and J_{SC}, by decreasing the concentration of deep-level defects.

An oligomer derivative from PTAA (S197, **HTM-2**) was obtained by Grätzel, Nazeeruddin, and co-workers. Its backbone consists of approximately 9 units that carry an additional *o,p*-dimethoxyphenylene substituent comparing to PTAA. It was found that devices using S197 as HTM in a mesoscopic regular architecture reached a 12.0% in efficiency, which was higher than those devices using PTAA as HTM under the same conditions.[134]

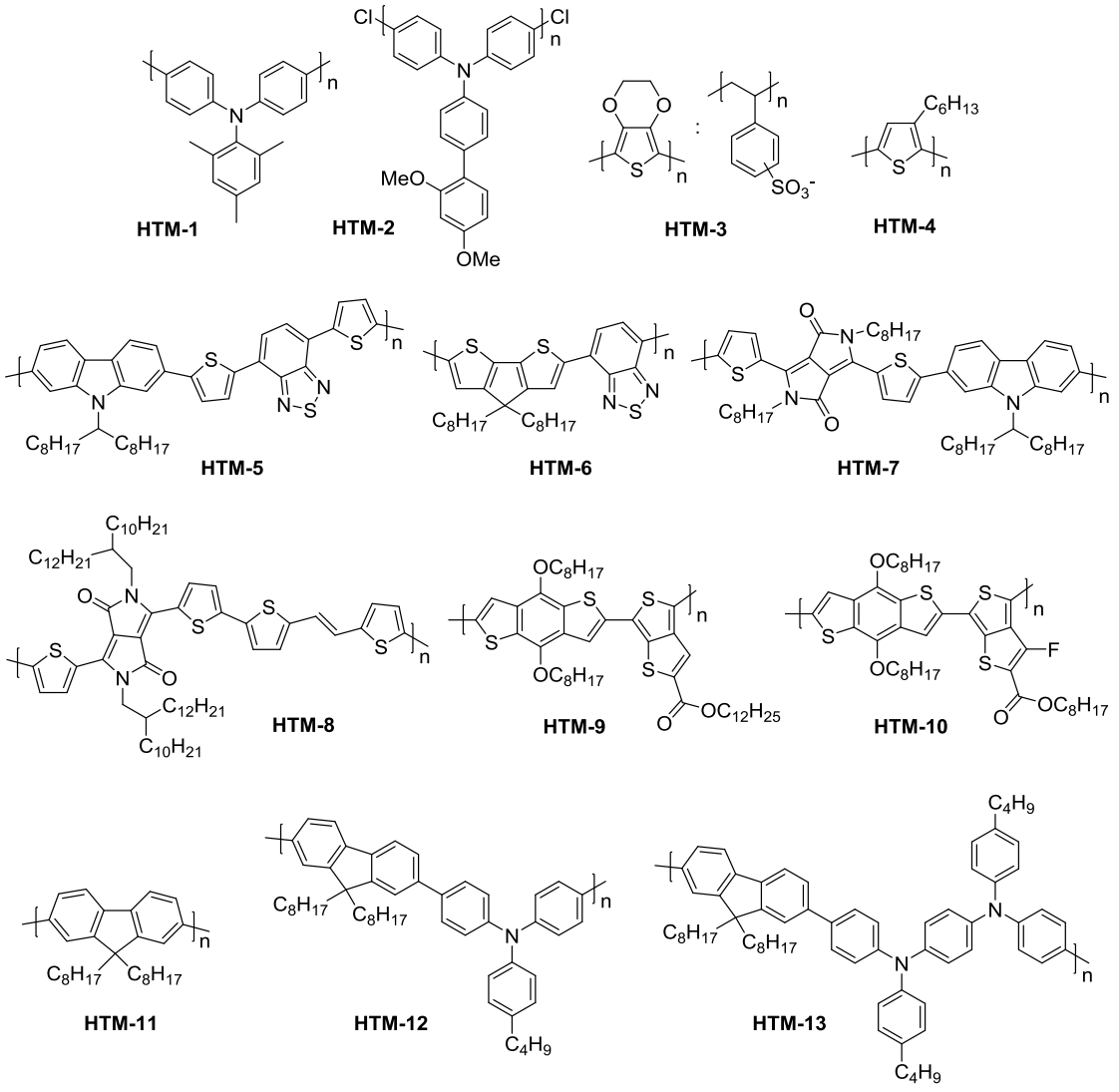

Figure 23. Structure of some polymeric HTMs used in PSCs.

PEDOT:PSS (**HTM-3**) is a polymer electrolyte consisting of positively charged conjugated PEDOT and negatively charged PSS. PEDOT is usually doped with PSS, which is a polymeric surfactant, which helps to disperse and stabilize PEDOT in solvents.[135] PEDOT:PSS is a commercial low-cost polymer that has been mostly employed as HTM in inverted PSCs. It exhibits an HOMO level compatible with the

VB of perovskites and also compatible with the work function of the ITO, which enables hole extraction and transport. Moreover, this polymer has excellent film properties and the low temperature necessary for the annealing process makes it compatible with flexible electronic devices.[93,112] The highest efficiency using PEDOT:PSS as HTM in PSCs was reported by Im and co-workers.[136] In that work, an efficiency of 18.1% was achieved with ITO/PEDOT:PSS/$CH_3NH_3PbI_3$/PCBM/Au inverted architecture using HI as additive to ensure a very high quality perovskite film. However, PEDOT:PSS is sensitive to humidity due to its hygroscopic nature, which affects the stability of PSCs.

In addition, the use of thiophene-based polymers, which have been used in the field of OSCs as electron donors, have been also investigated as HTMs in PSCs. Poly (3-hexylthiophene-2,5-diyl) (P3HT, **HTM-4**) has been one of the most widely used polymers among this family in PSCs.[137–139] It shows suitable optical and electrical properties, good thermal and chemical stability as well as high processability, but efficiencies remain lower than those using *spiro*-OMeTAD or PTAA. Lately, P3HT was used as HTM in a PSC using a regular mesoporous architecture and a 17.8% in efficiency was reached.[140]

Furthermore, donor-acceptor polymers with low-band gap have been also tested as HTMs in PSCs. Recently, Lidzey and co-workers[141] have reported the use of poly[*N*-9'-heptadecanyl-2,7-carbazole-*alt*-5,5-(4',7'-di-2-thienyl-2',1',3'-benzothiadiazole)] (PCDTBT, **HTM-5**) as HTM in a PSC reaching an efficiency of almost 16%, which was highly comparable with reference devices using *spiro*-OMeTAD. Also, in a work by Sun and co-workers [142] a PCE of 15.1% was achieved when poly{2,6-[4,4-bis-(2-ethylhexyl)-4H-cyclopenta[2,1-b;3,4-b']dithiophene]-*alt*-4,7(2,1,3-benzothiadiazole)} (PCPDTBT, **HTM-6**) was incorporated as HTM in PSCs. With further modifications, diketopyrrolopyrrole-based polymers, poly[*N*-90-heptadecanyl-2,7carbazole-*alt*-3,6-bis(thiophen-5-yl)-2,5-dioctyl-2,5-dihydropyrrolo[3,4] pyrrole-1,4-dione] (PCBTDPP, **HTM-7**)[143] and poly[2,5-bis(2-decyldodecyl) pyrrolo[3,4-c]pyrrole-1,4(2H,5H)-dione-(E)-1,2-di(2,2'-bithiophen-5-yl)ethene], (PDPPDBTE, **HTM-8**)[144] were also tested in PSCs, resulting in PCEs of 5.6% and 9.2%, respectively.

Other polymers based on benzodithiophene derivatives (i.e., **HTM-9**, **HTM-10**)[145] or polymers containing fluorene derivatives (i.e., **HTM-11**, **HTM-12**, or **HTM-13**)[146] have also been applied as HTMs in perovskite-based solar cells showing significant solar-cell performances.

The best performances obtained with many of the above-mentioned investigations (except from **HTM-9** and **HTM-10**), were achieved by doping the HTM solution with additives. As it was mentioned before, these dopants help to enhance the performances of the HTM with mechanisms that are not yet completely clear, even if it is supposed that they have effects on the conductivity of the layer. However, they are deliquescent and hygroscopic; they degrade the perovskite film as well as the organic HTL, diminishing the stability of the device and leading to important losses in performance.[122,147] For example, dopant LiTFSI is added to the HTM solution dissolved in CH_3CN, which is known to attack the perovskite and therefore, even if it is added in a very small amount, it could partially degrade the perovskite layer. Moreover, doping increases the overall cost and requires a strict optimization of the doping conditions.

For these reasons, the next generation of HTMs should have not only appropriate properties, but also they have to be able to work in the absence of dopants (so-called dopant-free HTMs). In that way, removing additives has become an important objective for long-term stability of PSCs.

2.1.3 Efficient Dopant-Free Hole-Transporting Polymers for PSCs

Working without dopants was already shown to be a feasible strategy for efficient and stable PSCs. Some small molecules have been tested recently as HTMs in PSCs in the absence of dopants and not only have they reached efficiencies comparable to that of devices using doped *spiro*-OMeTAD, but also they showed an improved stability.[148–155]

Polymers have been much less explored than small molecules even though they offer excellent properties. In Figure 24, some examples of dopant-free polymeric HTMs used in PSCs are shown.

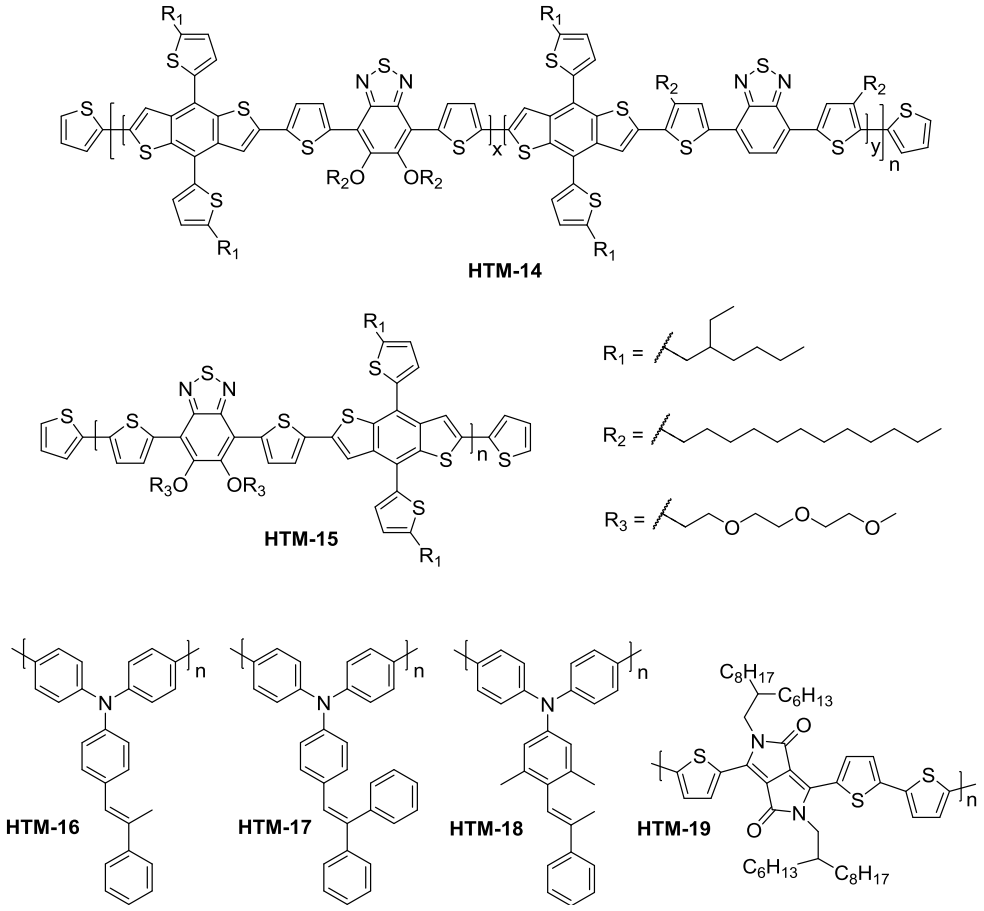

Figure 24. Molecular structures of dopant-free hole-transporting polymers.

Recently, Park and co-workers[147] reported a novel polymeric HTM based on benzo[1,2-*b*:4,5:*b*´]dithiophene (BDT) and 2,1,3-benzothiadiazole (BT) units (**HTM-14**), for using it in PSCs without any dopant. A PCE of 17.3% was achieved, maintaining its initial efficiency for more than 1400 hours. The same authors have reported the highest performance with a device fabricated with a dopant-free polymeric HTM. In their work the polymeric HTM, consisting in a BDT unit as a donor and a BT unit as acceptor connected with a π-bridge (**HTM-15**), was incorporated in PSCs reaching an impressive PCE of 19.8%.[156]

Also, in a work by Getautis, Saliba and co-workers[157] three new triarylamine-based polymers (**HTM-16**, **HTM-17** and **HTM-18**) were tested as HTMs in the absence of dopants leading to a PCE of 12.3% with the polymer poly[3,5-dimethyl-*N*,*N*-diphenyl-4-(2-phenylprop-1-en-1-yl)aniline-4',4''-diyl] (**HTM-18**), which was higher than that of PTAA (10.8%) measured under the same conditions. Moreover, devices prepared with this dopant-free polymer were stable for over 140 hours without

significant changes in the PCE, while devices with the doped polymer showed a significant decrease in efficiency already in the first few hours. Qiao and colleagues[158] reported the well-known polymer poly{2,2'-[(2,5-bis(2-hexyldecyl)-3,6-dioxo-2,3,5,6-tetrahydropyrrolo[3,4-c]pyrrole-1,4-diyl)dithiophene]-5,5'-diyl-alt-thiophen-2,5-diyl} (PDPP3T, **HTM-19**) as dopant-free HTM in PSCs reaching a PCE of 12.3%, which was comparable with devices prepared with doped *spiro*-OMeTAD (12.34%). In addition, PDPP3T-based PSC devices showed a better stability in ambient air than the doped *spiro*-OMeTAD.

All these results verify the possibility of using polymers as dopant-free HTMs for the development and commercialization of stable PSCs avoiding the use of any additive.

2.2 Objectives

Undoubtedly, the use of dopants to increase the conductivity of the HTM, although beneficial for the PCE, strongly deteriorates perovskite-device stability and decreases lifetime. Moreover, the strategy of using dopants involves more chemicals and more cost in terms of money and time. Therefore, developing dopant-free HTMs is essential for achieving the desired long-term stability of PSCs.

On the other hand, polymers seem to be very suitable for their incorporation as dopant-free HTMs because of their excellent solution processability, tunable energy levels, thin film uniformity or thermal stability.

In this sense, the **main objective** of this chapter is the design and synthesis of new dopant-free HTMs for developing stable and high-efficient PSCs. In order to achieve this purpose, the work has been divided into:

- Design and synthesis of new polymeric HTMs for application in PSCs. The aim is the preparation of a series of novel polymers derived from the combination of different well-known accepting units, such as thiophene, triarylamine and spirobifluorene. The characterization of the polymers will be carried out by nuclear magnetic resonance (NMR), mass spectrometry and size exclusion chromatography (SEC).

- Characterization of the newly polymers by thermal, optical and electrochemical techniques in order to evaluate their properties. In this regard, the newly polymers should have optimal HOMO energy levels in order to warrant hole transport while maintaining low visible absorption, as their function in the device is ensuring good electronic transport from the perovskite to the electrode and not absorbing light. Moreover, the objective polymers should have enough solubility for film formation as well as high thermal stability.

- The polymers will be incorporated as dopant-free HTMs in PSCs in order to evaluate their device performance. Furthermore, we identified thermal stability as a fundamental weak point of PSCs and the effect of the new dopant-free HTMs on stability against temperature will be tested.

2.3 Results and Discussion

2.3.1 Design and Synthesis of Polymers P1-P6

The chemical structures of the target polymers **P1-P6** are displayed in Figure 25. The design of the 6 new polymers was inspired by *spiro*-OMeTAD and PTAA, being the latter the only polymeric HTM that could work as efficiently as spiro-type small molecules.[159]

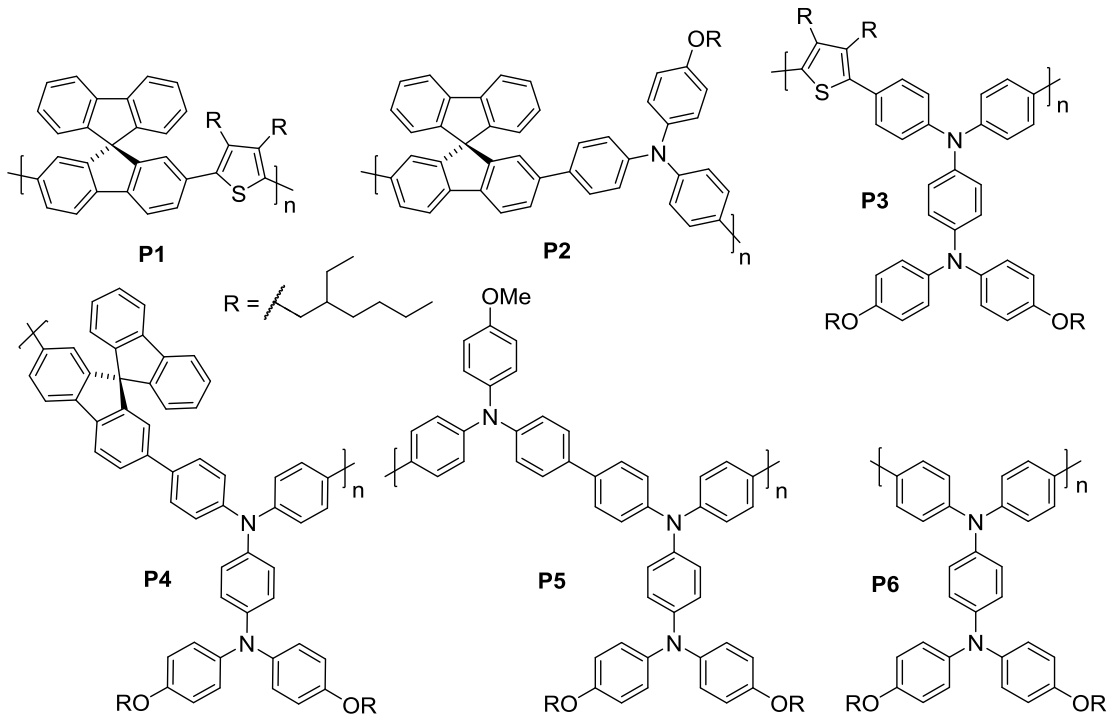

Figure 25. Chemical structures of the target polymers **P1**-**P6**.

Polymers **P1** and **P2** are composed of a spirobifluorene unit in combination with two different donor moieties, a thiophene and a triarylamine derivative, respectively, which are known to possess high hole-transporting and electron-blocking abilities. Thiophenes have been intensively used as building blocks for organic semiconductors due to their favourable optoelectronic properties. In particular, their high hole mobility presents an attractive feature for HTM design.[111] In case of triarylamine derivatives, because of their excellent charge-transporting properties and easy oxidizability they have been also widely used as donor materials in several optoelectronic materials as OLEDs, organic field-effect transistors (OFETs), DSSCs or PSCs. Especially, polymeric triaryalmine derivatives hold great potential due to advantages such as

possibility of extended π-conjugation and excellent film-forming properties.[160] Finally, the motivation to synthesize HTMs with a spiro-linked molecular fragment was to achieve materials with high T_g, morphological stability and easy processability while keeping good electronic properties.[122] Moreover, to ensure sufficiently high solubility for device fabrication and good film formation, branched alkyl chains (2-ethylhexyl) were introduced in key positions of those donor units.

In polymers **P3**-**P6**, the introduction of more donor groups in their backbone than in polymers **P1**-**P2** was explored in order to modulate their HOMO energy levels for an optimized hole transport from the perovskite to the HTM. Therefore, we designed polymers **P3**-**P6**, each one containing triphenylamine extended units in combination with different donor systems as thiophene (**P3**), spirobifluorene (**P4**), or triarylamine (**P5**) units. As in polymers **P1** and **P2**, polymers **P3**-**P6** will benefit from the enhanced solubility given by the alkyl groups.

2.3.1.1 Synthesis of Functionalized Monomers

In order to prepare the target polymers, difunctionalized monomers with bromine or boronic ester moieties were synthesized (Figure 26). Both moieties enable the use of Pd-catalyzed *Suzuki* cross coupling reaction for further polymerization. In addition, Ni-mediated *Yamamoto* polymerization reaction could be performed.

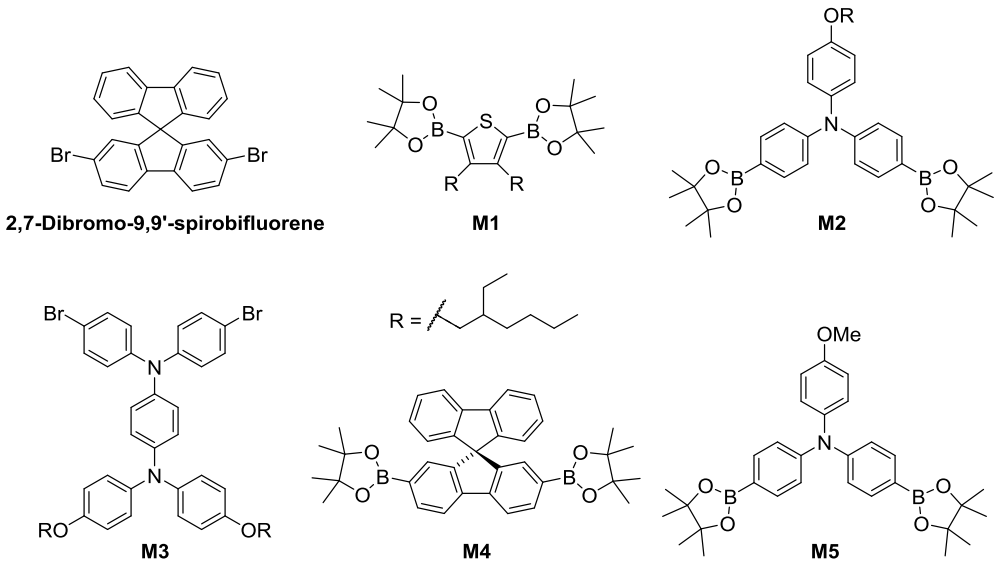

Figure 26. Chemical structures of monomers **M1**-**M5** and 2,7-dibromo-9,9'-spirobifluorene.

The procedure for the synthesis of monomer **M1** is shown in Scheme 1, while the complete experimental details can be found in the experimental section. First, the *Kumada* coupling of 3,4-dibromothiophene with 2-(ethylhexyl)magnesiumbromide (RMgBr) provided thiophene **1**, which after Ir-catalyzed borylation afforded monomer **M1**.

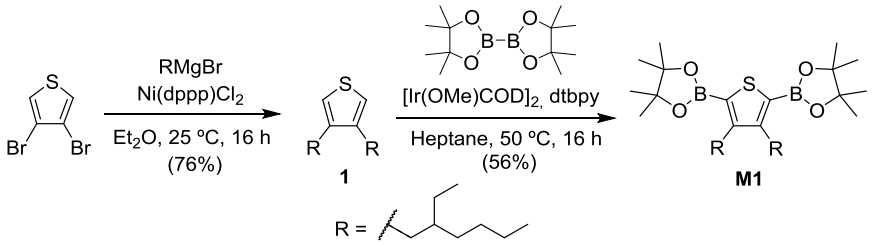

Scheme 1. Synthetic route to monomer **M1**.

Monomer **M2** was prepared according to the synthetic route outlined in Scheme 2, following literature procedures.[161–163] In this regard, the reaction between 4-iodophenol and 2-ethylhexilbromide (RBr) in *N*,*N*-dimethylformamide (DMF) using K_2CO_3 as base gave 1-(2-ethylhexyloxy)-4-iodobenzene (**2**) in high yield. Next, *Buchwald-Hartwig* reaction of compound **2** with diphenylamine resulted in the formation of 4-(2-ethylhexyloxy)-*N*,*N*-diphenylaniline (**3**), which was subjected to react with an excess of *N*-bromosuccinimide (NBS), yielding triarylamine **4**. Finally, *Miyaura* borylation of compound **4** led monomer **M2** in moderate yield.

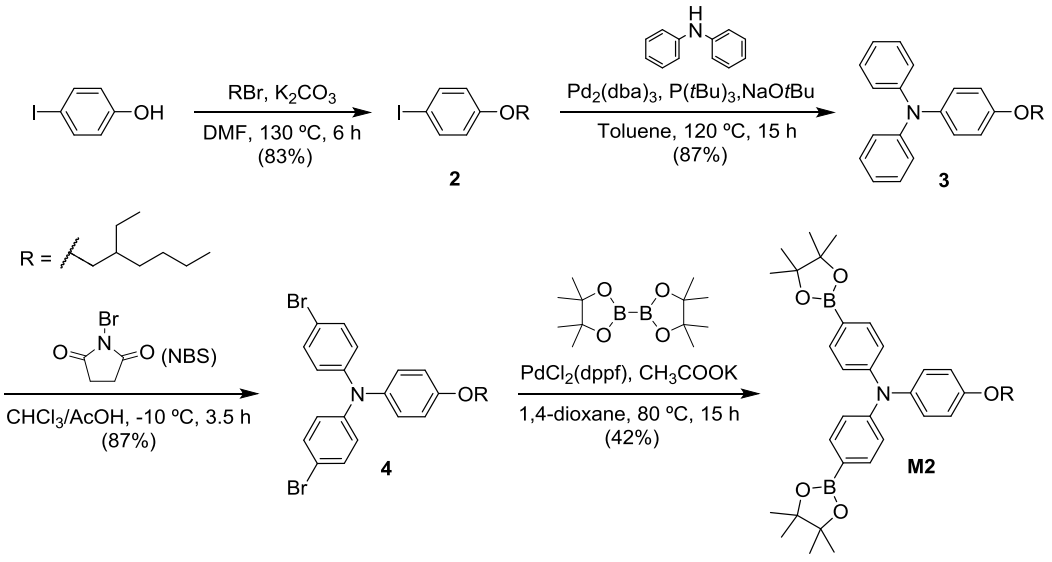

Scheme 2. Synthetic pathway for the preparation of monomer **M2**.

The synthesis of monomer **M3** started with the reaction between 1-(2-ethylhexyloxy)-4-iodobenzene (**2**) and 4-bromophenylamine to give triarylamine **5**. After that, *Buchwald-Hartwig* reaction of compound **5** with diphenylamine gave triarylamine **6,** which finally reacted with an excess of NBS yielding monomer **M3** (Scheme 3).

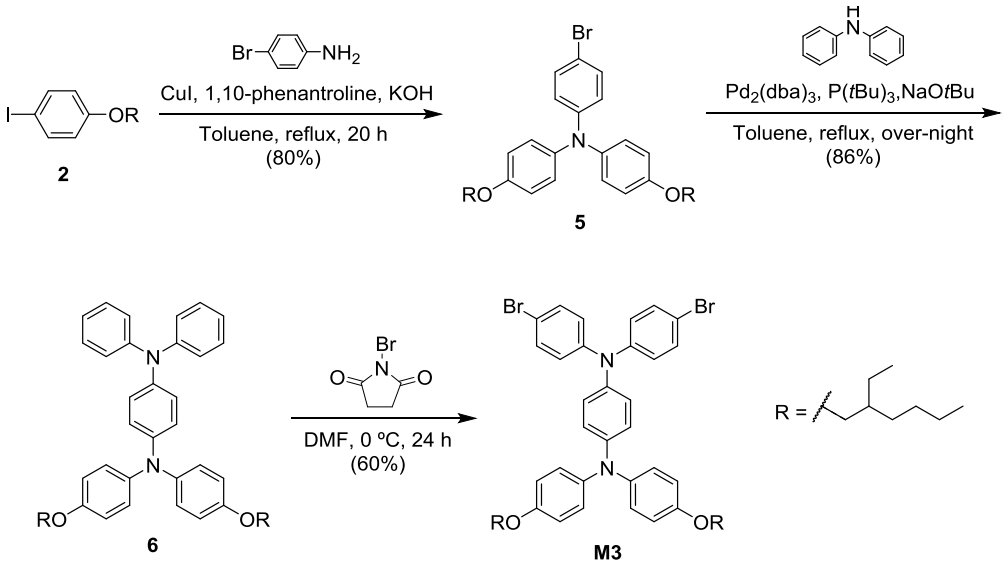

Scheme 3. Synthesis of di-bromine functionalized monomer **M3**.

The synthesis of monomer **M4** was synthesized through *Miyaura* borylation of the commercially available 2,7-dibromo-9,9'-spirobifluorene according to published procedures (Scheme 4).[164]

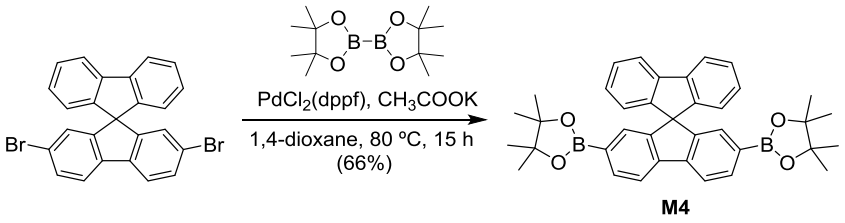

Scheme 4. Synthesis of monomer **M4**.

Finally, the synthesis of monomer **M5** was prepared following a three-step synthetic procedure (Scheme 5). Firstly bis(4-bromophenyl)amine (**7**) was obtained by treating diphenylamine with an excess of NBS following reported procedures.[165] Triarylamine **8** was also synthesized by reported procedures by Cu-catalyzed *Ullmann* coupling of compound **7** and 1-iodo-4-methoxybenzene.[166] Finally, monomer **M5** was

obtained by *Miyaura* borylation of the previous synthesized triarylamine **8** in 44% yield.

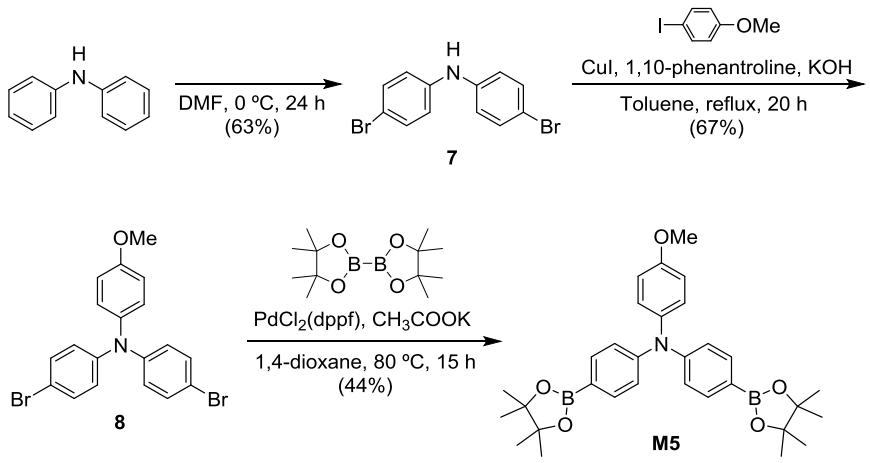

Scheme 5. Synthetic route to monomer **M5**.

2.3.1.2 Synthesis of Polymers P1-P6

The six new polymers **P1**-**P6** were then synthesized recurring to either *Suzuki* (**P1**-**P5**) or *Yamamoto* (**P6**) coupling polymerization.

We started with the synthesis of copolymers **P1** and **P2** bearing a spirobifluorene unit in combination with two different donor moieties. The procedure for the synthesis of both polymers is shown in Scheme 6.

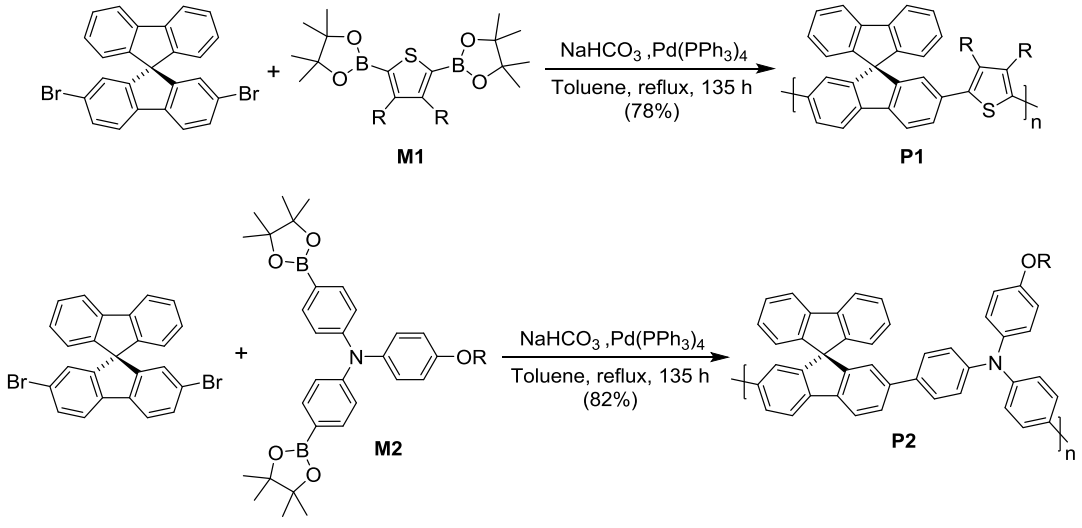

Scheme 6. Synthesis of polymers **P1** and **P2**.

P1 and **P2** were synthesized by Pd-catalyzed *Suzuki* coupling copolymerization of the corresponding diboronic ester monomers **M1** and **M2**, respectively, and 2,7-

dibromo-9,9'-spirobifluorene in toluene using $NaHCO_3$ as base. After extraction and precipitation processes, the resulting polymers were purified from the residual catalyst and low molecular weight impurities by subsequent *Soxhlet* extraction with different solvents, yielding polymers **P1** and **P2** in good yields. Both polymers showed good solubility in common organic solvents, such as dichloromethane (DCM), chloroform, tetrahydrofuran (THF) or toluene. The composition and chemical structure of both polymers were confirmed by ^{1}H NMR and mass spectrometry (MALDI-TOF).

^{1}H NMR spectra of polymers **P1** and **P2** revealed the representative spectroscopic features corresponding to the formation of both polymers. It is interesting to observe the change in shape of the NMR signals from monomers to polymers, being the signals of the latter broader. As representative example, ^{1}H NMR spectrum of **P2** in CD_2Cl_2 is shown in Figure 27, where all the signals were assigned to the structure.

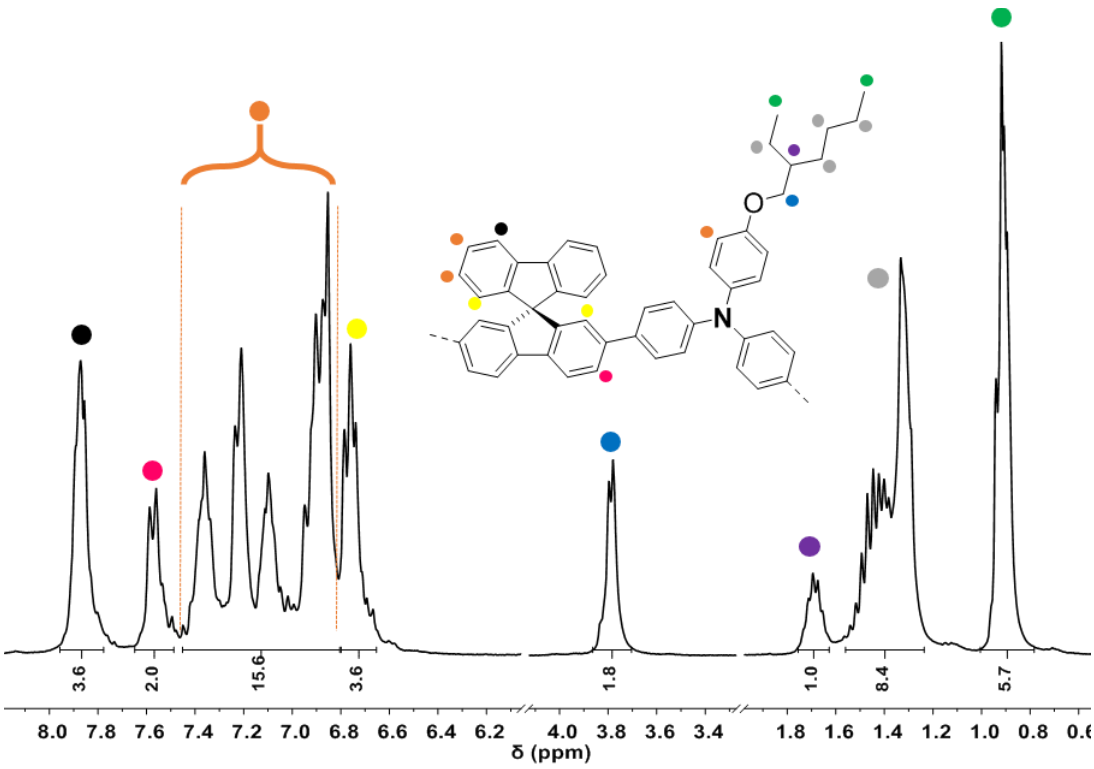

Figure 27. ^{1}H NMR (300 MHz, CD_2Cl_2, 298K) spectrum of polymer **P2**.

In case of MALDI-TOF, peaks which differ from each other by a value which corresponds to the building blocks of both polymers were clearly visible. As an example, MALDI-TOF spectrum of polymer **P2** is shown in Figure 28, where

differences between some peaks corresponding to the building block ($C_{51}H_{43}NO$ $[M]^+$: 685.338) of **P2** were found.

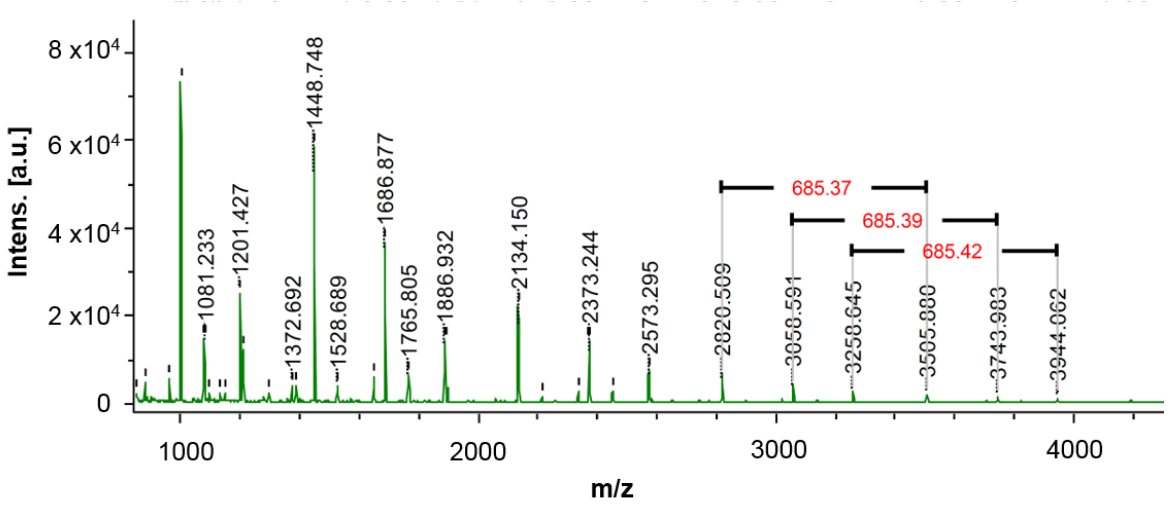

Figure 28. MALDI-TOF spectrum of polymer **P2**.

The size of the polymers was estimated by size exclusion chromatography (SEC) in THF with polystyrene standards for calibration and the data are found in Table 1. The number-average molecular weights M_n of **P1** and **P2** were 9651 and 5551 g mol^{-1}, leading to degrees of polymerization (X_n) of 16 and 8, respectively. The corresponding weight-average molecular weights (M_w) were 21635 g mol^{-1} (**P1**) and 11390 g mol^{-1} (**P2**), and both polymers showed relatively small polydispersities (PDI = M_w/M_n) of 2.2 and 2.0 for **P1** and **P2**, respectively.

The synthetic route for preparing polymers containing triphenylamine extended units (**P3**-**P6**) was conducted as it follows in Scheme 7.

Polymers **P3**, **P4** and **P5** were synthesized by *Suzuki* coupling copolymerization reaction of the corresponding monomers **M1**, **M4** and **M5** with monomer **M3**, respectively, using the same procedure described for polymers **P1** and **P2**. Homopolymer **P6** in contrast, was synthesized through Ni-mediated *Yamamoto* polymerization of **M3** in the presence of 1,5-cyclooctadiene (COD) and 2,2'-bipyridine in a solvent mixture of DMF and toluene (1:1).

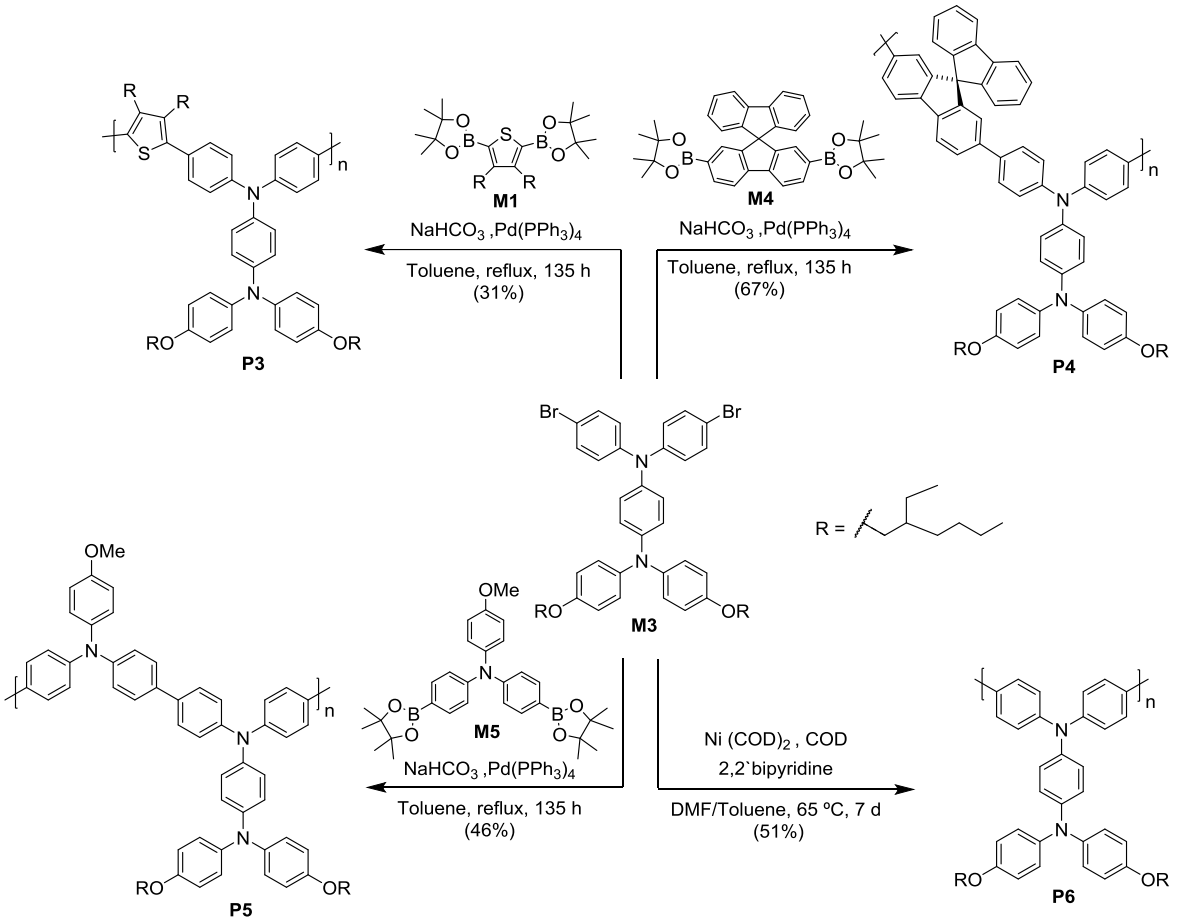

Scheme 7. Synthesis of the target polymers **P3**-**P6**.

After extraction of the organic phase and precipitation in MeOH (**P3**-**P5**) or MeOH:HCl (**P6**), the resulting polymers were purified by subsequent *Soxhlet* extraction with different solvents. This process gave polymers in good (**P4**-**P6**) or moderate (**P3**) yields. All polymers showed good solubility in common organic solvents, such as DCM, chloroform, THF or toluene.

The structures of the polymers **P3**-**P6** were confirmed by ^{1}H NMR and MALDI-TOF (see experimental section for more details) while the molecular weights were estimated by SEC analysis in THF compared to a polystyrene standard. Molecular weights of polymers **P3**-**P6** are shown in Table 1. Polymers **P3**, **P4**, **P5** and **P6** showed comparable M_n values of 3209, 4403, 4681 and 5812 g mol^{-1}, respectively, with a PDI in the range of 1.48-2.39.

Polymer	M_n (g mol^{-1})	M_w (g mol^{-1})	X_n	PDI
P1	9651	21635	15.5	2.24
P2	5551	11390	8.08	2.05
P3	3209	4746	3.30	1.48
P4	4403	10528	4.48	2.39
P5	4681	8663	4.98	1.85
P6	5812	12443	8.71	2.14

Table 1. Molecular weights of polymers **P1-P6**.

2.3.2 Thermal, Optical and Electrochemical Properties

a) Thermal properties

Thermogravimetric analysis (TGA) carried out at a heating rate of 10 °C min^{-1} under nitrogen atmosphere indicated the high thermal stability of copolymers **P1-P5** and homopolymer **P6** (Figure 29A), showing decomposition temperatures (T_d) (2% weight loss) ranging from 303 °C to 392 °C (Table 2), which was well above operational conditions of PSCs. All polymers exhibited weight loss before decomposition, which may be attributed to the loss of solvent traces.

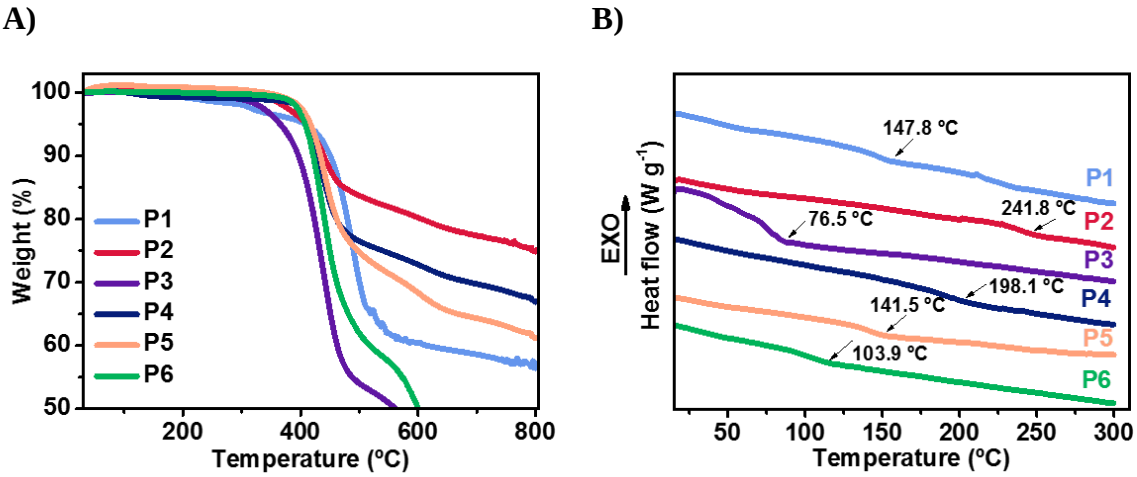

Figure 29. A) Thermogravimetric heating curves of polymers **P1-P6** (heating rate 10 °C min^{-1}). B) Differential scanning calorimetry curves for the second heating of polymers **P1-P6** (heating rate 20 °C min^{-1}).

Differential scanning calorimetry (DSC) measurements of the investigated polymers **P1**-**P6** revealed their amorphous nature (Figure 29B, Table 2). DSC measurements showed that the T_g of polymers **P1**, **P2**, **P4** and **P5** were at 147.8, 241.8, 198.08, 141.53 °C, respectively, which were higher than that of *spiro*-OMeTAD (125ºC)[167] indicating a more stable amorphous state. The T_g of polymer **P6** was determined to be 103.85 ºC, whereas the additional thiophene unit in polymer **P3** significantly influence the T_g, lowering it to 76.5 ºC.

Polymer	T_d (°C)[a]	T_g (°C) [b]
P1	302.57	147.8
P2	371.74	241.8
P3	327.14	76.5
P4	392.03	198.1
P5	390.62	141.5
P6	390.66	103.9

Table 2. Thermal properties of polymers **P1**-**P6**. [a] Decomposition temperature determined from TGA (2 % weight loss). [b] Glass transition temperature determined from DSC (second heating curve).

b) Optical properties

The UV-vis absorption spectra of polymers **P1-P6** in DCM are depicted in Figure 30A. Absorption peaks of all polymers were located in the UV region and there was no significant absorption in the visible region, which is necessary for not competing with the perovskite in the absorption of light.[77] Polymer **P2** presented a maximum absorption wavelength ($\lambda_{max,abs}$) at 394 nm, which was redshifted compared to **P1** (358 nm). This is because of the larger π-conjugated system, mostly due to the presence of three additional phenyl rings in **P2**. This is also the reason why copolymer **P2** presented a higher molar extinction coefficient ($\mathcal{E}$) than polymer **P1** at the maximum wavelength.

As for polymers **P3-P6**, which bear the triphenylamine extended unit, they showed $\lambda_{max,abs}$ values in between 350-380 nm. As the amount of delocalization in the polymer increases, the energy gap between π and π* orbitals becomes smaller. Therefore, polymers **P3** and **P6** presented $\lambda_{max,abs}$ values at 348 and 349 nm, respectively, while polymers **P4** and **P5**, with more phenyl rings in their backbone, that

imply more delocalization, presented $\lambda_{max,\ abs}$ values at 383 and 365 nm, respectively. With larger conjugated systems in polymers **P4** and **P5**, the $\mathcal{E}_{max}$ values of them were higher (40399 and 45329 $M^{-1}\ cm^{-1}$, respectively) than those of polymers **P3** and **P6** (33982 and 26586 $M^{-1}\ cm^{-1}$, respectively).

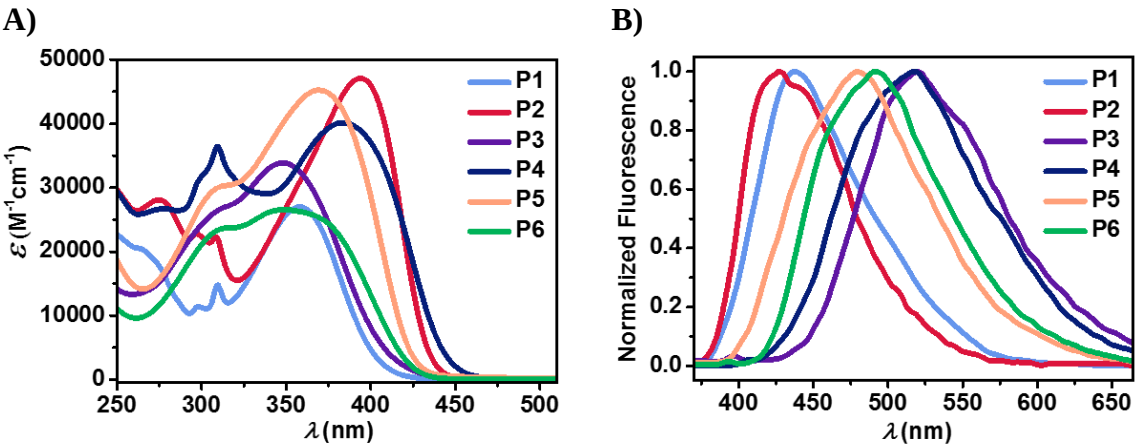

Figure 30. A) Absorption spectra of **P1**-**P6** in DCM. B) Normalized Fluorescence spectra of polymers **P1**-**P6** in DCM.

From the onset of the absorption (λ_{onset}) edge in the longer wavelength region, the optical band gap (E_g) was estimated, and the values are ranging from 2.87 eV to 3.08 eV (Table 3). In addition, the photoluminescence spectra (Figure 30B) showed maximum emission wavelength ($\lambda_{max,fl}$) at 437, 427, 519, 518, 479 and 491 nm, in order, for polymers **P1**-**P6**.

Polymer	$\lambda_{max,fl}$ (nm)	$\lambda_{max,abs}$ (nm)	$\mathcal{E}_{max}$ ($M^{-1}\ cm^{-1}$)	λ_{onset} (nm)	E_g (eV)
P1	437	358	27055	403	3.08
P2	427	394	46168	432	2.87
P3	519	348	33982	408	3.04
P4	518	383	40399	443	2.80
P5	479	369	45329	423	2.93
P6	491	349	26586	423	2.93

Table 3. Optical properties of polymers **P1**-**P6**.

c) Electrochemical properties

The electrochemical properties of the polymers were investigated by cyclic voltammetry (CV), measured in a 0.1 M solution of tetrabutylammonium hexafluorophospate (TBAHFP) in anhydrous DCM. Their HOMO energy levels

(E_{HOMO}, Table 4) were obtained from the onset potential of the first oxidation (E^{Ox1}_{onset}) during CV measurements using the ferrocene/ferrocinium (Fc/Fc^+) redox couple as the internal standard. Therefore, the E_{HOMO} was calculated according to equation 17:

$$E_{HOMO}\ (eV) = -4.8 - E^{Ox1}_{onset} \qquad (17)$$

Polymer **P1** showed a poorly reversible oxidation wave at E^{Ox1}_{onset} value of 0.61 V vs Fc/Fc^+, while polymer **P2** exhibited one reversible oxidation process at $E^{Ox1}_{1/2}$ value of 0.31 V vs Fc/Fc^+ indicating its electrochemical stability (Figure 31A).

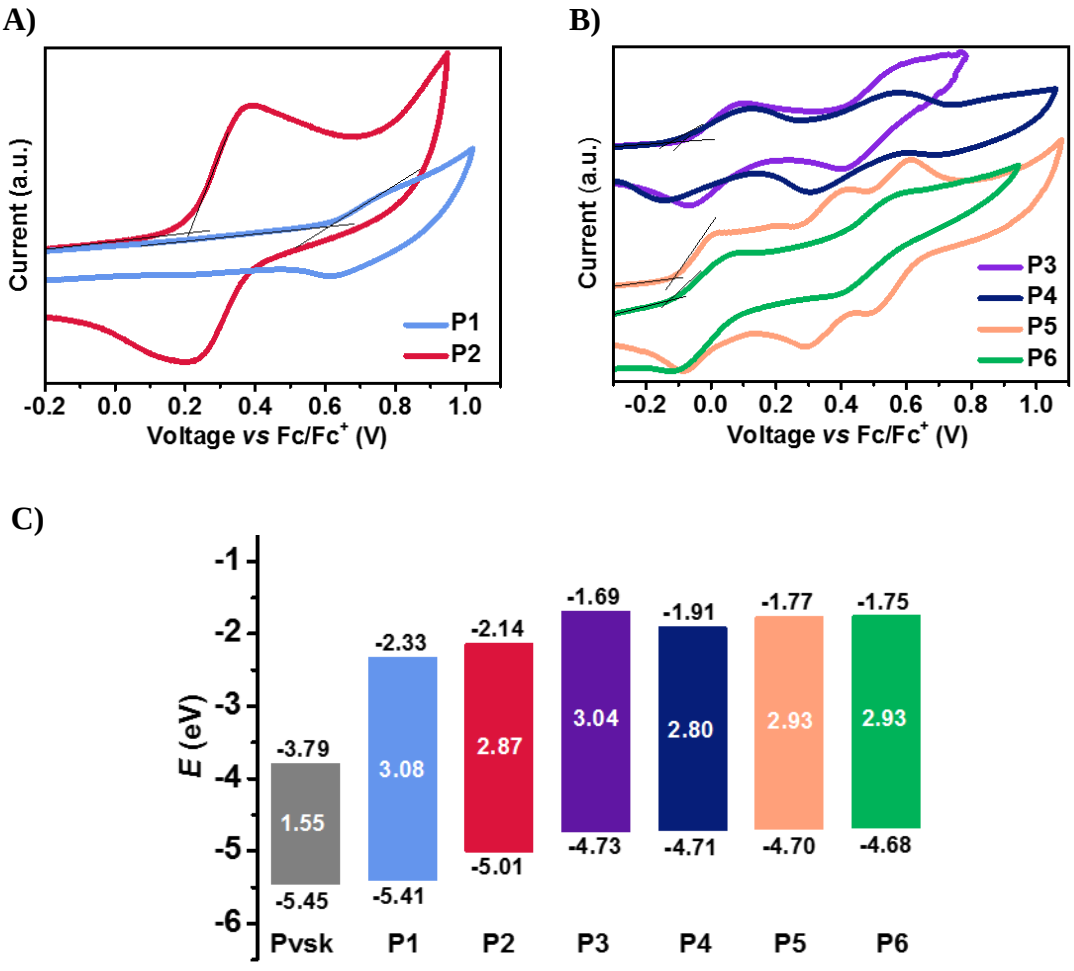

Figure 31. Cyclic voltammograms of A) polymers **P1**-**P2** and B) polymers **P3**-**P6** in DCM /TBAHFP (0.1 M) at a scan rate of 250 mV s^{-1}. C) Energetic levels of polymers **P1**-**P6** and perovskite light absorber used in this study.

Comparing the electrochemical data, we could find that **P2** was more easily oxidized than **P1**. The E_{HOMO} values of polymers **P1** and **P2** calculated from CV are -5.41 and -5.01 eV, respectively. The reported E_{HOMO} for the triple cation perovskite,

used in this work, is -5.45 eV,[168] revealing the favourable energetics for efficient hole transfer from the perovskite to the HTMs (Figure 31C). Moreover, the LUMO energy levels (E_{LUMO}) were estimated from the difference between E_{HOMO} and E_g of the polymers as -2.33 and -2.14 eV for **P1** and **P2**, respectively.

As in polymers **P1**-**P2**, the voltammograms of polymers **P3**-**P6** showed only oxidation processes, while no reduction processes were observed in the operation window of the solvent-electrolyte (Figure 31B). Polymers **P3**, **P4** and **P6** showed two reversible oxidations waves, while polymer **P5** showed three reversible oxidations. The strong electron-donor properties of the additional diaryalmine substituents in polymers **P3**-**P6** compared to polymer **P1**-**P2** are reflected at the remarkably low 1st oxidation potentials at $E_{1/2}^{Ox1}$ values of 0.01, -0.01, -0.03 and -0.02 V vs Fc/Fc^+, for **P3**, **P4**, **P5** and **P6**, respectively. According to the similar redox potentials, the E_{HOMO} of polymers **P3**-**P6** were also nearly identical, with values around -4.7 eV. With this values, polymers **P3**-**P6** could be suitable for efficient hole transfer from the perovskite to the HTM, similarly to polymers **P1** and **P2**. The E_{LUMO} of polymers **P3**-**P6** lied between -1.69 eV and -1.91 eV, as shown in Table 4.

Polymer	$E_{1/2}^{Ox1}$ (V)	E_{onset}^{Ox1} (V)	E_{HOMO} (eV)	E_{LUMO} (eV)
P1	-	0.61	-5.41	-2.33
P2	0.31	0.21	-5.01	-2.14
P3	0.01	-0.07	-4.73	-1.69
P4	-0.01	-0.09	-4.71	-1.91
P5	-0.03	-0.10	-4.70	-1.77
P6	-0.02	-0.12	-4.68	-1.75

Table 4. Electrochemical properties and energy levels of polymers **P1**-**P6**.

2.3.3 Perovskite Solar Cells Employing Polymers P1-P6

To demonstrate the function of the novel polymers as dopant-free HTMs, polymers **P1**-**P6** were incorporated as HTMs in PSCs. Moreover, the stability of some devices against temperature was studied in order to determine if these polymers could enhance the stability of PSCs. This study was carried out in collaboration with Silvia

Collavini (PhD student of Hybrid Materials for Photovoltaics Group) at Ecole Polytechnique Fédérale de Lausanne (EPFL, Switzerland) in M. Grätzel´s group.

2.3.3.1 Perovskite-Based Device Fabrication

The device architecture used for this study was the mesoporous regular structure: FTO/c-TiO_2/m-TiO_2/ $Cs_5(MA_{0.17}FA_{0.83})_{95}Pb(I_{0.83}Br_{0.17})_3$/HTM/Au (Figure 32A). The perovskite contains three different organic cations namely Cs^+, MA^+ and FA^+.[168]

A)

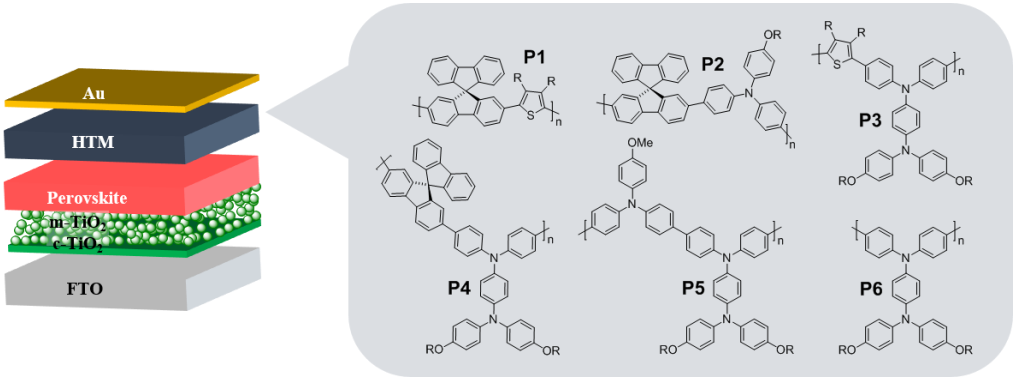

B)

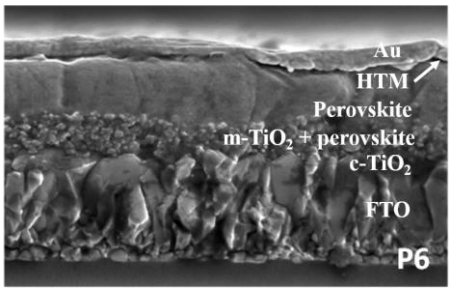

Figure 32. A) Simplified model of the perovskite-based solar cell used for testing polymers **P1**-**P6**. B) Cross sectional SEM micrographs of a device with **P6** as HTM.

Briefly, in a transparent and conductive FTO, serving as the electron collector, a compact TiO_2 was deposited by spray pyrolisis. The latter serves as selective electron-transport layer and efficient hole-blocking layer. Subsequently, a mesoporous TiO_2 layer was employed by spin-coating, into which the perovskite penetrates (also deposited by spin-coating). The perovskite was covered with a thin layer of the synthesized polymeric HTMs at a concentration of 7 mg mL^{-1}. The compounds were spin-coated from chlorobenzene solution and were used without any doping additives. Finally, the cell stack were topped with a gold counter electrode deposited by thermal

evaporation. The detailed fabrication procedure can be found in the experimental part. The cell architecture of the fabricated device using polymer **P6** as HTM can be appreciated from the scanning electron microscopy (SEM) cross-sectional micrograph displayed in Figure 32B. The HTM layer can be barely distinguished, since it is very thin (~20 nm).

2.3.3.2 Photovoltaic Device Testing

Figure 33 shows the current density-voltage (*J-V*) curves for the best perovskite solar cell devices measured under the standard AM 1.5G illumination at 1 sun (100 W cm^{-2}) using the novel polymers as HTMs.

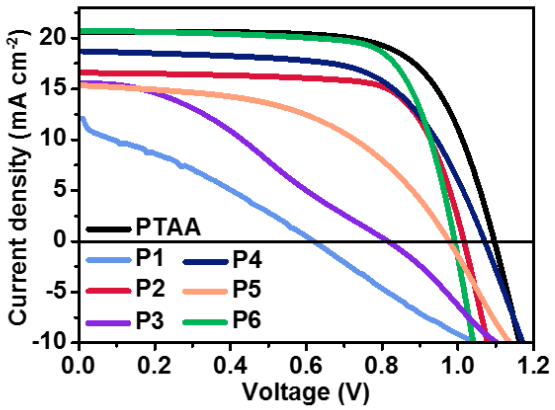

Figure 33. Best *J-V* curves of PSCs using polymers **P1**-**P6** and PTAA as HTMs.

To get a better idea about the reproducibility of the devices, statistical data based on several batches of PSCs are shown in Figure 34. The photovoltaic parameters extracted from *J-V* curves are summarized in Table 5.

HTM	V_{OC} (V)	J_{SC} (mA cm^{-2})	FF (%)	PCE (%)
PTAA	1.05 (1.09)	19.4 (21.1)	59 (68)	12.0 (15.8)
P1	0.51 (0.69)	11.8 (12.0)	50 (26)	1.77 (2.19)
P2	1.03 (1.04)	14.9 (15.9)	55 (60)	8.32 (9.80)
P3	0.76 (0.82)	15.2 (15.6)	31 (34)	3.55 (4.34)
P4	1.06 (1.09)	17.6 (18.5)	59 (63)	11.0 (12.8)
P5	0.78 (0.97)	14.0 (15.3)	44 (50)	5.00 (7.51)
P6	0.98 (1.03)	16.0 (20.7)	67 (72)	10.5 (12.4)

Table 5. Average photovoltaic parameters determined form *J-V* measurements using polymers **P1**-**P6** and PTAA as HTMs. The photovoltaic parameters of the best working cells are shown in brackets.

The highest efficiency corresponded to reference devices, with an average PCE of 12.0%, which was closely followed by devices using polymers **P4** and **P6**, with an average in efficiency of 11.0 and 10.5%, respectively. PSCs using polymers **P2** and **P5** as HTMs showed moderate efficiencies with average PCE values of 8.32% and 5.00%, respectively, while devices containing polymers **P1** and **P3** led to the lowest efficiencies (average: 1.77 and 3.55%, respectively).

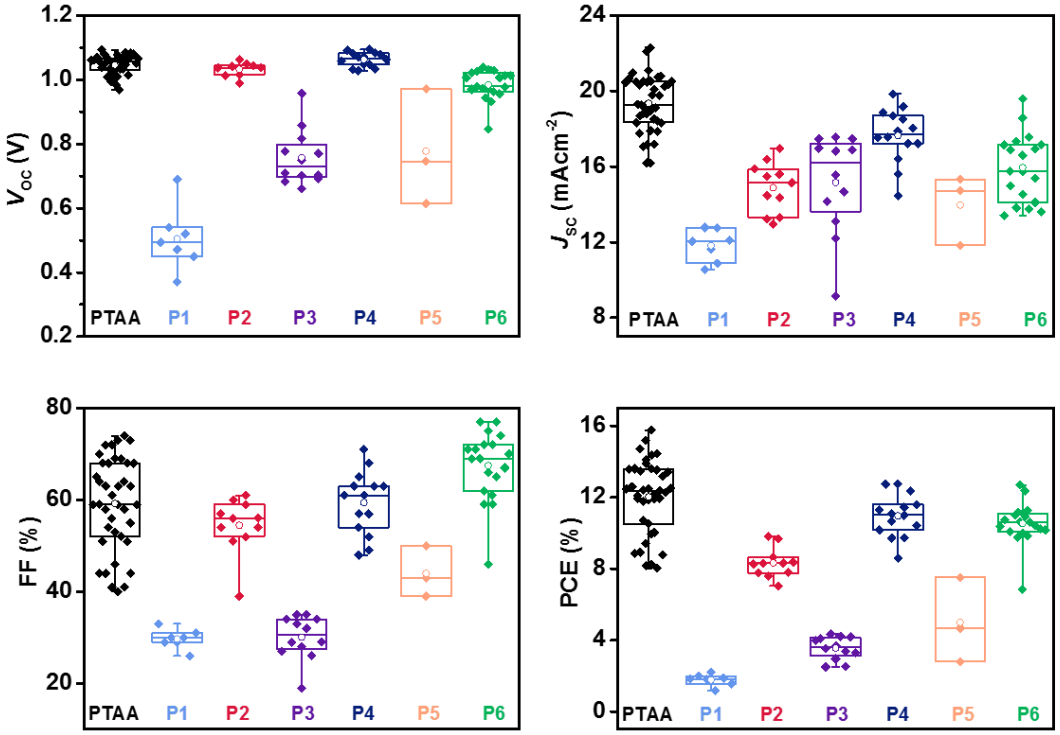

Figure 34. Statistical deviation of the photovoltaic parameters for PSCs using polymers **P1-P6** and PTAA as HTMs. Whiskers show minimum and maximum values, box represents the values between 25% and 75%, circles represent mean values.

Unexpectedly, thiophene-containing polymers **P1** and **P3** gave very low efficiencies despite possessing a very similar structure compared to the rest of the polymers. The most affected parameters were V_{OC} and FF, the latter being an indicator of a bad conductivity of the material. *J*–*V* curves of these polymers showed an S-shape (Figure 33) which was symptom of bad charge extraction and also led to low V_{OC}. This is usually attributed to a high energy barrier between the VB of the perovskite and the HOMO of the HTM, but since this was not the case, a low conductivity could explain this behaviour. To confirm this hypothesis we studied the series resistance (R_S) of the devices.

The R_S is extracted from the inverse of the slope of the current (I)-voltage (V) curves at the V_{OC} point, as is shown in Figure 35A. Thus, the R_S value is linked to the FF value. It is clearly visible in Figure 35B that the polymers which gave the lowest efficiency (because of the low FF) presented the highest series resistance.

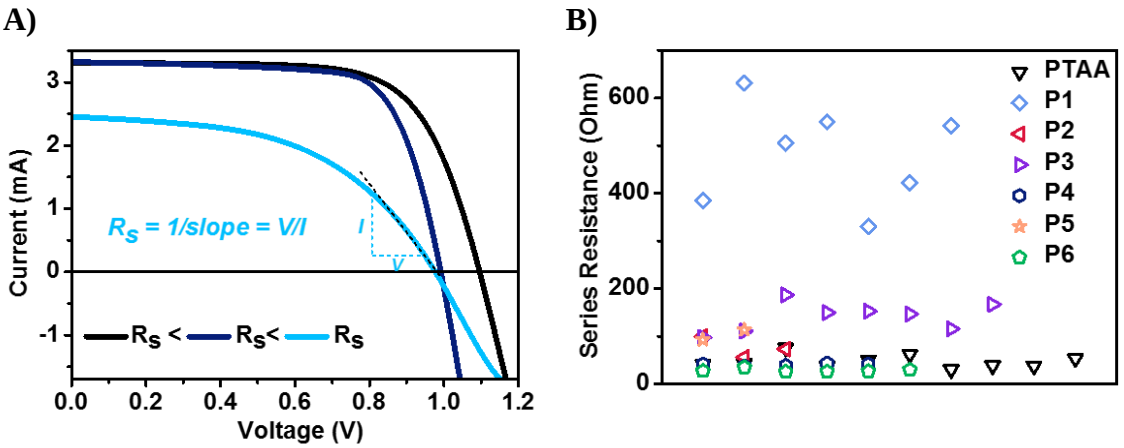

Figure 35. A) Effect of the series resistance on the *I*-*V* curves. B) Series resistance of polymers **P1**-**P6** compared with PTAA.

On the contrary, the rest of the polymers showed good efficiencies, which in the case of **P4** and **P6** were highly comparable to those obtained using PTAA. Even considered that devices were not fully optimized, promising PCEs of 12.8% and 12.4% for polymers **P4** and **P6**, respectively, were achieved. Regarding **P4**, the V_{OC} of the devices containing this polymer exceeded that of PTAA-based PSCs. The slightly lower FF of polymer **P4**, which is correlated to a lower conductivity, might be the cause of the lower PCE compared to PTAA. Polymer **P6**, on the contrary, presented the highest FF in the series, but both J_{SC} and V_{OC} were slightly lower than reference devices. This might be due to lower charge collection ability because the conductivity of **P6** seems to be higher than that of PTAA, according to the *R*s values (Figure 35B). Finally, polymers **P2** and **P5** gave efficiencies a bit lower than the previous structures, due to a low J_{SC}.

2.3.3.3 Stability of Perovskite Solar Cells

It was mentioned in the general introduction of this thesis that one of the factors which causes rapid degradation of PSCs is high temperature, which is one of the drawbacks of the most used HTMs. However, the operation temperature of a solar cell

can reach up to 85 ºC. For his reason, thermal stability of PSCs is of paramount importance for the commercial viability of those devices. Employing HTMs with enhanced thermal stability, as the newly prepared polymers **P1**-**P6**, is a prerequisite for improving the overall device resistance to temperature stress.[169]

To investigate the effect of the novel HTMs on the stability of PSCs, the best devices, using polymers **P4** and **P6,** underwent a high-temperature stability test, to evaluate their resistance to this kind of stress in comparison with PTAA-based devices. High-performing devices were heated for 12 hours at 65 ºC in nitrogen atmosphere. The PCE of the devices was recorded before and after the temperature stress and the drop of the efficiency due to thermal degradation is illustrated in Figure 36. Apparently, PSCs employing polymers **P4** or **P6** as HTMs showed improved stability in comparison with the device employing PTAA (Figure 36). The **P4**- and **P6**- containing devices maintained 93 and 95%, respectively, of their initial efficiency after 12 hours of thermal stress, while the reference device showed more pronounced degradation and its PCE dropped to 90% after the same time. These results clearly indicate that the novel compounds enhance the thermal stability of perovskite-based devices. Moreover, the new HTMs were employed without any need of dopants, which can further contribute to the overall stability of devices.

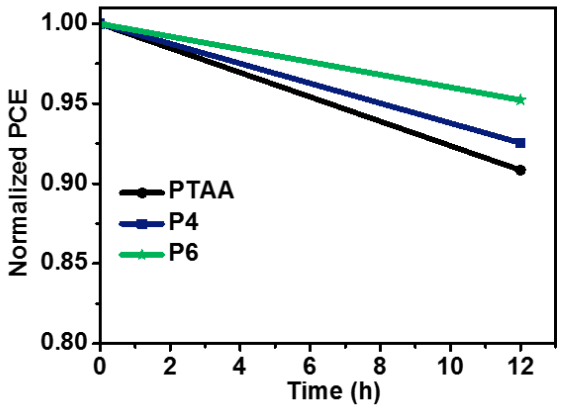

Figure 36. Normalized PCE for champion devices prepared with PTAA, **P4** and **P6** as HTMs.

2.4 Conclusions

In conclusion, several polymeric materials (**P1-P6**) based on thiophene, triarylamine or spirobifluorene units have been successfully synthesized, characterized and incorporated into PSCs as HTMs. The novel HTMs exhibited excellent thermal and optoelectronic properties and they presented suitable HOMO levels, which were perfectly aligned with that of the perovskite material. PSCs based on dopant-free **P4** and **P6** as the HTM afforded PCE values of 12.8% and 12.4%, respectively, which were comparable to that obtained employing the well-known PTAA. In addition, we demonstrated that devices based on polymers **P4** and **P6** showed higher thermal stability than devices based on PTAA, most likely because both polymers presented high thermal stability. Further investigation is required to dig deeper into the possible advantages that these polymers could give, since devices were not optimized and more in-depth investigations regarding stability are required. However, this study clearly demonstrates that investigation of new possible structures as charge carriers is fundamental in order to achieve stable and efficient PSCs. The possibility of working without doping additives is undoubtedly an important step towards this goal and in that way, to open up a space for PSCs in the market.

3. PERFLUORINATED ADDITIVES FOR PEROVSKITE SOLAR CELLS

3 PERFLUORINATED ADDITIVES FOR PEROVSKITE SOLAR CELLS

3.1 Introduction

At present, the most challenging issue in PSCs is the long-term stability, which must be resolved before their future commercialization. More specifically, this type of devices suffer a number of degradation processes mostly associated with the degradation of the perovskite active layer.[170] However, stability issues related to interfacial degradation under operation or chemical instability of the charge transporting layers and electrodes have also been reported.[25]

Among the tremendous efforts to enhance the long-term stability of PSCs, some approaches to improve the perovskite layer, including compositional engineering,[171–175] or controlling the quality of that layer,[176–179] have achieved considerable results. However, in order to obtain highly durable perovskite devices, there are still many critical issues and related research questions that must be addressed in this emerging photovoltaic technology.

In this regard, this chapter provides a summary of the additives used for improving the quality of the perovskite layer and presents a novel approach for enhancing the long-term stability of PSCs without damaging their PCE.

3.1.1 Additive Engineering to Improve the Perovskite Layer

The quality of the perovskite layer, including crystallinity, morphology and coverage, has been recognized as one of the most crucial parameters for achieving not only highly efficient but also long-term stable PSCs.[176] In this sense, for the construction of devices with superior performance is compulsory a great surface coverage of the substrate with the perovskite compound. The incomplete surface coverage of perovskite not only reduces light harvesting, but also brings a great number of pinholes, which are points of charge recombination. Ideally, a dense-uniform and smooth layer of large crystals should constitute the perovskite layer, which can be achieved by regulating the perovskite crystallization process.[176]

An easy-to-implement approach for optimizing the morphology of the perovskite layer is the use of additives, which in small quantities fine-tune the materials properties and increases the stability of the devices.[180] Additives or dopants can be incorporated into the perovskite material or simply blended within the perovskite layer in order to improve the perovskite morphology and covering through controlling crystallization.

Rational design of these additives can introduce different functionalities and target specific interactions between the additive and perovskite, or specific properties such as hydrophobicity, surface passivation, high-quality crystal growth and many others.[180,181] Moreover, additives containing electron-donating S, N and O atoms can effectively passivate surface defects in grain boundaries (GBs) through coordination with non-coordinated Pb^{2+}, thanks to the electron lone pair in the heteroatoms.[182] In fact, these Pb cations are responsible for crystal defects, which lead to recombination, ion migration and moisture/oxygen permeation, decreasing the device performance and stability.[183] Furthermore, these heteroatoms can form hydrogen bonds with the organic fragments in the perovskite which facilitates the formation of compact protecting barriers on top of the perovskite crystals.[184,185]

Figure 37 displays examples of additives, which have been incorporated into the perovskite layer. For instance, Din and co-workers demonstrated that adding NH_4Cl (**A-1**) to the perovskite precursor solution led to a smoother and better coverage perovskite film compared to that without additive.[186] Although the mechanism by which NH_4Cl improved the perovskite layer is not clear, the authors suggested that NH_4Cl could slow down the crystallization process to make perfect perovskite crystals. **A-1**-based PSCs showed a remarkable enhancement of efficiency compared to reference devices. Furthermore, organic molecules as *N*-cyclohexyl-2-pyrrolidone (**A-2**)[187] or 1,8-dioodoctane (**A-3**)[188] have proven to be very effective additives for improving the quality of the perovskite film and as a consequence, the overall performance of PSCs. For instance, when additive **A-3** was incorporated into the perovskite layer the resulting film was smoother with more ordered crystals and better coverage of the underlying substrate compared to the undoped one. This led to a 30% enhancement in efficiency of devices containing **A-3**, compared to those without it.

The authors explained this result by the fact that **A-3** (Lewis base) could temporally coordinate with Pb^{2+} (Lewis acid) during crystal growth.[188] Similarly, formamidine acetate organic salt (**A-4**)[189] or 2-pyridylthiourea (**A-5**)[190] have been incorporated as additives into the perovskite precursor solution. In both cases, not only an improved PCE for additive-containing devices was obtained, but also the stability was improved compared to control devices. As in case of additive **A-3**, the better morphology and crystallinity of the perovskite film were explained through interactions between the additive and the perovskite precursor. Fullerenes derivatives have also been used as additives in PSCs. In this regard, Delgado, Grätzel and co-workers synthesized a series of poly-ethylene glycol (PEG)-functionalized C_{60} fullerenes (**A-6**, **A-7** and **A-8**), which were incorporated into the perovskite layer when device preparation. PSCs fabricated with those fullerene additives reached around 16% of efficiency and they showed improved stability against moisture and reduced hysteresis compared to reference devices.[191] This improved stability against moisture was justified by the coordination between PEG and water molecules, which prevented the degradation of the perovskite structure.

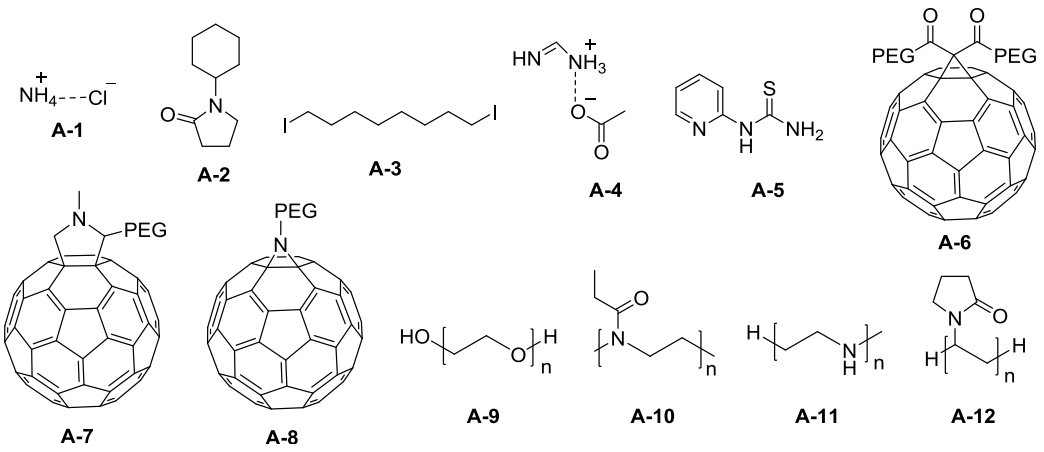

Figure 37. Chemical structures of some additives used for improving the quality of the perovskite layer.

The interest of implementing larger size molecules is well supported in literature, as polymers bearing different functional fragments in their structure have been proven as stabilizing additives. Their main advantage as additives is linked to their long polymeric chains, which are able to network crystalline domains and form more compact films.[184,192]

In this regard, Su and co-workers reported the first polymer used as additive for enhancing the morphology of the perovskite film.[192] They added PEG (**A-9**) into the perovskite precursor solution improving the coverage of the perovskite film, which led to 25% higher PCE of **A-9**-based PSCs compared to those fabricated without **A-9**. In addition, other polymers as poly-(2-ethyl-2-oxazoline) (**A-10**),[193] polyethylenimine (**A-11**)[194] or poly-vinylpyrrolidine (**A-12**)[195] have been tested as additives in PSCs leading in all cases to an improvement in the quality of the perovskite layer. In case of additive **A-12**, it was incorporated into a $CsPbI_3$-based perovskite, reaching the highest efficiency of $CsPbI_3$-based PSCs. In addition, PSCs based on this additive showed excellent thermal and moisture stability.[195]

3.1.1.1 Semiconducting Chemical Additives

Although additives yield high-quality films, the inherent insulating properties of most of them can prevent from an efficient transport and extraction of charge carriers. In this sense, semiconductor additives were also found to improve not only the stability, but also the device performance of PSCs.[182,196–198]

Figure 38 shows some examples of semiconducting additives used for stabilizing the perovskite active layer. In this regard, the well-known semiconducting polymer PCDTBT (**HTM-5** in chapter 2) was used as additive and, as a result, perovskite layers with bigger crystal grains and higher density than control films were achieved. Moreover, the PCE of additive-containing devices were 16% enhanced compared to those without additives, with and also improved stability.[182] Similarly, Ma and co-workers showed that employing conjugated polymers (**A-13** and **A-15**) was beneficial for achieving improved charge transport along multiple-directions in the perovskite crystals, resulting in an enhanced efficiency. Besides, the authors showed that fluorine-containing conjugated polymers (**A-14** and **A-16**) led to further improvement of the air-stability and photostability of the perovskite due to the enhanced hydrophobicity of the polymers.[196] The quality of the perovskite layer was also improved by adding polymers **A-17**, **A-18**, **A-19** and **A-20.**[198] PSC efficiencies using those polymers as additives were improved compared to unmodified devices, reaching values as high as 19% as well as an improved stability.

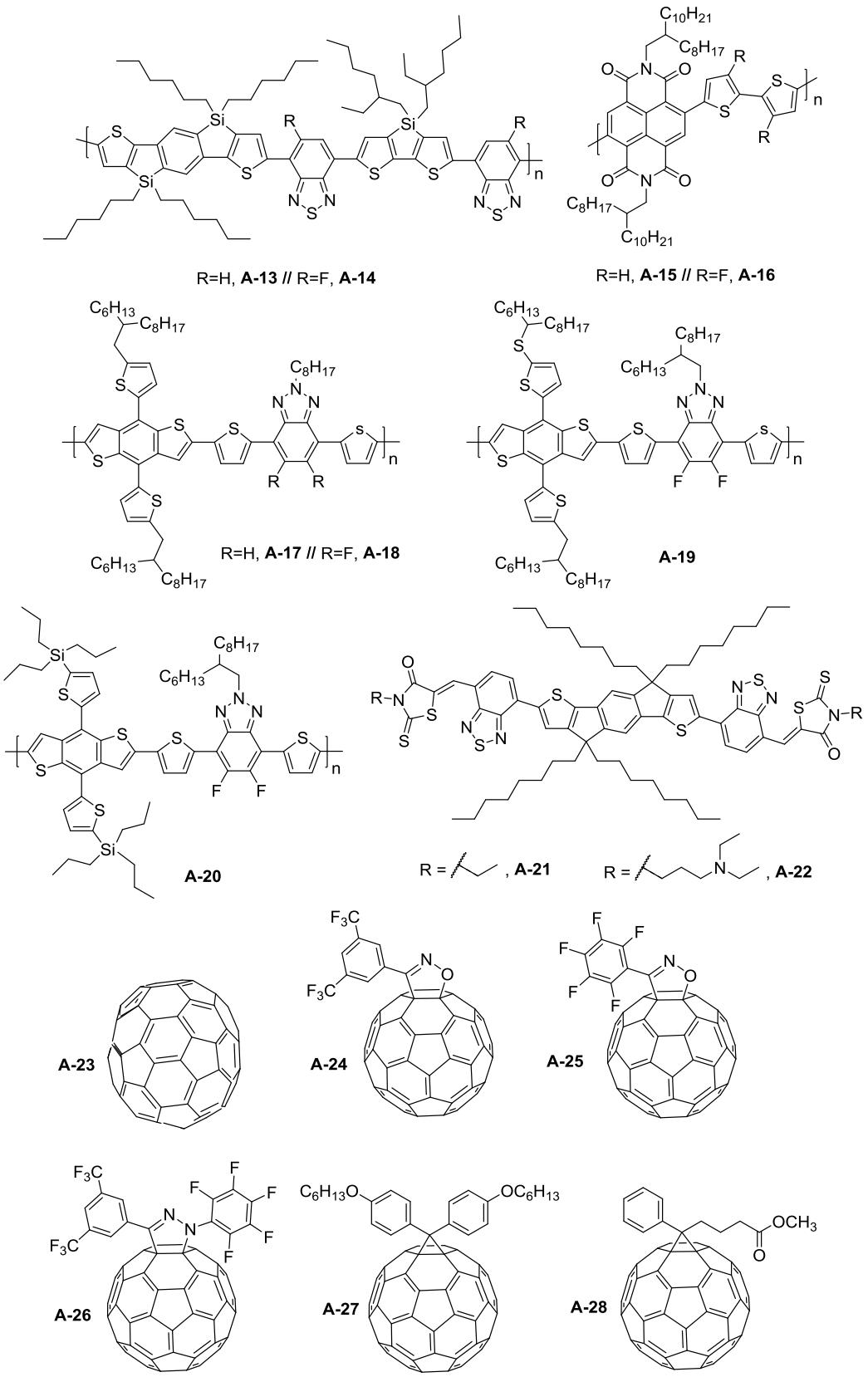

Figure 38. Chemical structures of semiconductive additives used for improving the quality of the perovskite layer.

Regarding non-polymeric semiconducting additives, very recently, Song, Kwon and co-workers used additives **A-21** and **A-22** to the perovskite layer.[197] **A-21**- and **A-22**- based devices reached 18.7 and 20.3% in efficiency, respectively, which were higher values compared to those of reference devices (16.7%). The higher stability of **A-22**- compared to **A-21**-based PSCs could be explained by the successful passivation of the non-coordinated Pb cations of the perovskite crystals by **A-22**, which led to much more stables devices compared to control ones. For instance, after 170 hours of illumination, reference cells maintained only 10% of their initial PCE, while **A-22**-based devices kept 84% of their initial PCE. The authors explained the good performance of additive-based devices by the synergic effect of increasing the quality of the film and the semiconductor properties of them.

Furthermore, C_{70} fullerene (**A-23**) has also found application as additive in PSCs. Taking advantage of the electron-transporting properties of C_{70}, it was incorporated into the perovskite precursor solution to fabricate efficient (13.6%) ETL-free PSCs. C_{70} doped-perovskite films showed no pinholes (which is the main issue for ETL-free PSCs) and their integration into PSCs led to more stable devices compared with the conventional PSCs with TiO_2 as ETM.[199] Following this work, a variety of chemically modified C_{60} fullerenes (**A-24**-**A-28**) showing different electron-accepting capabilities were used as additives to the perovskite layer to prepare ETL-free PSCs. Not only have they reached higher efficiencies than those of devices without additives in the perovskite layer, also they showed an improved stability.[200]

3.1.1.2 Fluorinated Additives for Perovskite Solar Cells

Taking into account that humidity and thermal instability have a huge impact on the performance of PSCs, there is a need for materials that can protect them from those external factors. In this regard, fluorinated compounds generally have excellent moisture and thermal-resistant properties. In fact, as it has already been proven in literature, the incorporation of highly fluorinated alkyl chains to materials effectively enhances the stability to air and temperature, due to the formation of kinetic barriers against the diffusion of O_2 and/or H_2O.[201]

In this sense, the hydrophobic nature of fluorine-containing organic additives has demonstrated to protect the perovskite from moisture degradation. Moreover, the possibility of fluorine atoms of forming hydrogen bonds with the organic cations (A^+) of the perovskite (ABX_3), helps to immobilize A cations into the perovskite structure leading to an improved thermal stability.[202]

Figure 39 shows examples of fluorinated-based additives that have been already used in PSCs.

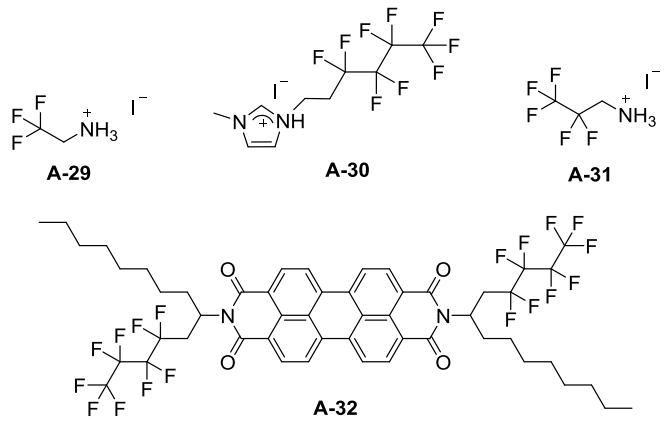

Figure 39. Structure of fluorinated-based additives used in PSCs.

For instance, Nazeeruddin, Gao and co-workers showed that a fluorinated amphiphilic organic salt (**A-29**) could tune the morphology and enhance the environmental stability of the perovskite layer which resulted in retarded degradation of the devices in ambient air.[203] In this regard, **A-29** was added into the perovskite precursor solution and a smoother and more continuous surface than that of pristine perovskite was achieved. As a result, PSCs based on this new additive showed improved efficiency (17.9%) as well as enhanced long-term stability compared to PSCs fabricated without additives. Moreover, the decomposition rate of the $MAPbI_3$ perovskite against moisture was checked by recording X-ray diffraction (XRD) patterns of perovskite films with and without **A-29**. It was found that the new phase of PbI_2, which is a decomposition product of $MAPbI_3$, could be seen in both samples after 40 days in 30% relative humidity ambient air. However, the intensity of which the PbI_2 phase increased with time was much faster for the undoped perovskite films.

In another work by Ahmad and colleagues, the effect of incorporating an imidazolium salt additive (**A-30**), containing a perfluorinated fragment with 9 fluorine atoms, into the perovskite layer was investigated. **A-30**-based devices reached 15.4% in efficiency and a negligible loss in photovoltaic performance after 52 days in ambient conditions (57-60% relative humidity).[204,205] In the same line, Mathews and co-workers demonstrated that when the perovskite surface is passivated with pentafluoropropyl ammonium iodide (**A-31**), superior moisture stability and improved device performance was achieved.[206] In this regard, **A-31**-based PSCs exhibited enhancement of the PCE from 14.8 (control) to 16.6%, which was attributed to the larger perovskite crystals and lower surface roughness compared with the standard perovskite. Moreover, the PCE of the standard device dropped by about 40% from its initial value, whereas the additive-treated device retained about 94% of its initial value after 169 days under ambient conditions (55% relative humidity).

Recently, a perylenediimide with two perfluorinated side chains in its structure (**A-32**) has been reported as additive for PSCs.[207] The authors investigated the effect of incorporating additive **A-32** into the perovskite layer and not only they achieved an impressive PCE of 19.3%, but also they demonstrated that adding **A-32** led to more stables PSCs compared to unmodified devices. In fact, **A-32**-based devices were subjected to a long-term stability test, in which the cells were kept either in air (50% relative humidity) or under nitrogen. After 40 days of storage in air, **A-32**-based devices maintained over 80% of their initial efficiency while reference devices kept less than 20% of their initial efficiency. The same tendency was found when devices were measured after 90 days kept under a nitrogen atmosphere. Moreover, devices containing **A-32** showed better thermal stability than those without it. The hydrophobic character of additive **A-32** would explain the enhancement of the humidity stability, while F^--MA^+ interactions, which contribute to immobilize MA cations into the perovskite structure, would explain the improvement on thermal stability. The improved efficiency and stability of **A-32**-incorporated devices could be explained by an improvement on the quality of the perovskite layer. First, the fluorine anions in **A-32** can interact with MA cations creating hydrogen bonds between them, which retards crystallization and as a result, larger grain size and less grain boundaries as well as

reduced pinholes were obtained. Second, **A-32** can effectively passivate trap states because the carbonyl groups in its structure can chelate with non-coordinated Pb^{2+}.

It can be concluded that by treating the perovskite layer with fluorinated additives, the access of moisture into the perovskite layer can be significantly suppressed. Moreover, it is worth mentioning that in all the examples, fluorine-containing devices showed negligible hysteresis which could be explained by the reduction of ion migration due to the fluorine-organic cation (perovskite) interactions, previously mentioned.

3.2 Objectives

All the aforementioned examples soundly demonstrate that carefully-designed additives are able to significantly affect the crystallization kinetics of perovskites, suppress trap formation, tailor and improve optoelectronic properties. All this eventually leads to enhanced lifetime of the devices and often improves the photovoltaic performance of PSCs. In addition, the advantage of compatibility of the additive with the perovskite material has been demonstrated, so additives with semiconductive properties are highly desired in order to favour charge transport. On the other hand, the lack of examples of additives with large perfluorinated units in the literature, together with our interest to know if these compounds could improve the overall performance of PSCs, motivated the beginning of this research work.

With all this in mind, we have proposed as **main objective** of this chapter the design, synthesis and application of three perfluorinated semiconducting organic materials as novel dopants or additives for PSCs. In order to achieve the main objective, other tasks more specific were defined:

- Design and synthesis of a small molecule and two polymeric materials which contain highly perfluorinated chains in their structure (26 fluorine atoms per unit). The structure of the compounds will be confirmed by NMR and mass spectrometry while the molecular mass distribution of the two polymers will be determined by SEC.

- Characterization of the newly compounds by thermal, optical and electrochemical techniques in order to evaluate their properties. In this regard, the newly materials should have optimal HOMO levels in order to not hinder the hole transport, and in that way, favouring the hole transport from the perovskite to the electrode. In addition, they should have minimal absorption in the visible region.

- The novel additives will be incorporated into the perovskite precursor solution and their effect on the film formation, stability and performance of PSCs will be investigated.

3.3 Results and Discussion

3.3.1 Design and Synthesis of Additives S1, P7 and P8

Figure 40 displays the chemical structures of the proposed compounds. We have designed a novel small molecule (**S1**) and two polymeric compounds (**P7** and **P8**) which contain 26 fluorine atoms per unit.

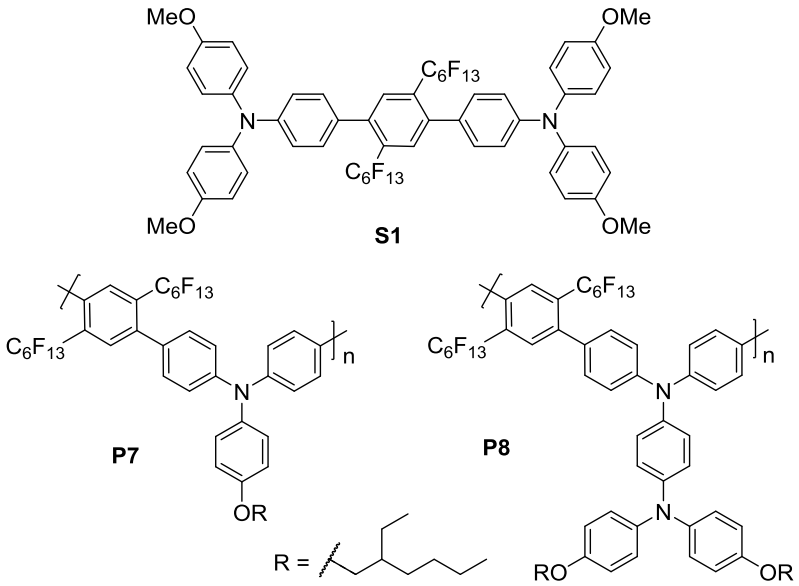

Figure 40. Chemical structures of the target compounds **S1**, **P7** and **P8**.

The addition of an additive into the perovskite layer could affect the energy levels or the interface between the HTM and the perovskite and increases the transport resistance, which would reduce the efficiency of the resulting PSC.[179] For this reason, to facilitate charge transport and extraction in the perovskite layer and to guarantee optimal photovoltaic performance, all compounds derive from the family of triarylamines, which are one of the most used *p*-type organic semiconductors. Molecule **S1** contains two triarylamine units, attached to a central benzyl ring, which bears two perfluorinated chains, each one containing 13 fluorine substituents. Polymers **P7** and **P8** are composed of a perfluorinated benzyl unit in combination with two different donor moieties, a triaryalmine and a triarylamine extended unit, respectively. Both polymers benefit from the enhanced solubility given by the introduction of alkyl groups in their structures, making them easier to process. To the best of our knowledge, the

three novel materials contain the largest amount of fluorine atoms reported for additives in PSCs.

The electron rich methoxy groups in **S1** and oxygen-containing fragments in **P7** and **P8** are expected to enhance the supramolecular interaction between the perovskite and the additive via hydrogen bonding and passivate non-coordinated Pb^{2+}.[184,185]

3.3.1.1 Synthesis of Intermediates

For the synthesis of the various additives **S1**, **P7** and **P8**, it was necessary to synthesize different functionalized monomers (**M2**, **M6** and **M7**) or intermediates (**11**) containing bromine or boronic ester groups (Figure 41). These functionalized molecules will allow us in a further step use Pd-catalyzed *Suzuki* cross coupling reaction for obtaining the target compounds.

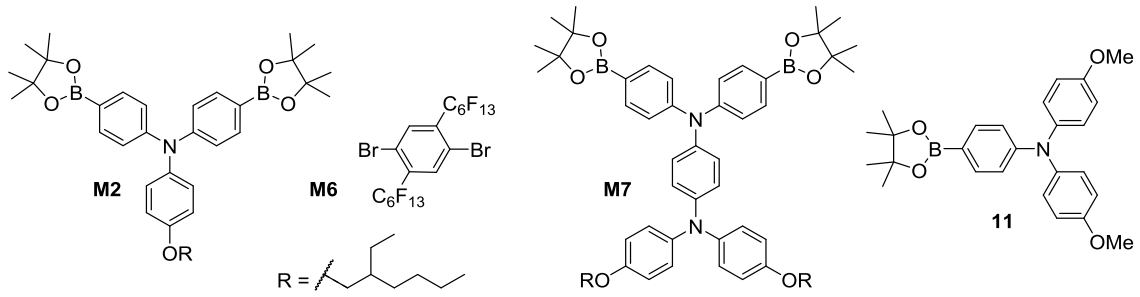

Figure 41. Chemical structures of monomers (**M2**, **M6** and **M7**) and intermediate **11**.

The synthesis of monomer **M6**, which bears the perfluorinated chains, was carried out by following reported procedures (Scheme 8).[208] First, the reaction of 1,4-diiodobenzene with an excess of perfluorohexyl iodide in dimethyl sulfoxide (DMSO) gave 1,4-bis(perfluorohexyl)benzene (**9**) in high yield. Then, the treatment of compound **9** with NBS in acidic media led to the desired monomer **M6**.

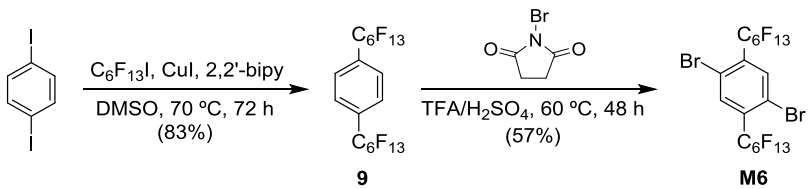

Scheme 8. Synthesis of monomer **M6** functionalized with bromine groups and bearing the perfluorinated chains.

Monomer **M7** was synthesized by *Miyaura* coupling of the dibrominated monomer **M3**, previously synthesized, and bis(pinacolato)diboron using $PdCl_2$(dppf) as catalyst (Scheme 9).

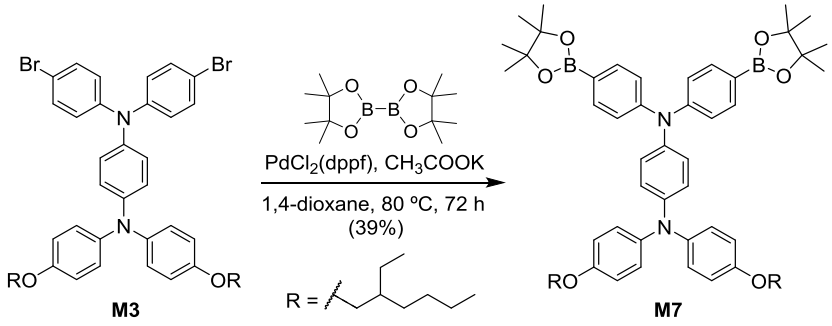

Scheme 9. Synthesis of monomer **M7**.

Finally, the synthesis of intermediate **11** was carried out following a two-step synthetic procedure, as shown in Scheme 10. First, the *Ullmann* reaction of 4-bromoaniline and 4-iodoanisole gave triaryalmine **10** following a reported procedure.[209] Then, intermediate **11** was obtained by *Miyaura* borylation of compound **10** in moderate yield.

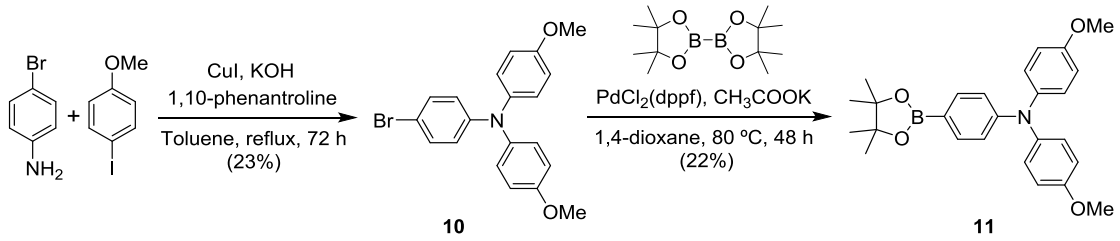

Scheme 10. Synthesis of intermediate **11**.

The synthesis of monomer **M2** was already described in page 50.

3.3.1.2 Synthesis of Additives S1, P7 and P8

The novel compounds **S1**, **P7** and **P8** were then synthesized by *Suzuki* coupling reaction. Perfluorinated monomer **M6** was coupled with two molecules of borylated triarylamine **11** through *Suzuki* cross coupling, using $Pd(PPh_3)_4$ as catalyst in anhydrous toluene to obtain **S1** (Scheme 11).

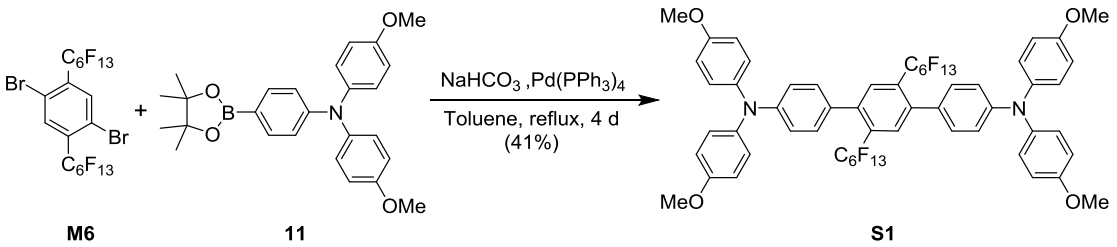

Scheme 11. Synthesis of small molecule **S1**.

The composition and chemical structure of the synthesized compound **S1** was confirmed by ^{1}H NMR, ^{13}C NMR, ^{19}F NMR and mass spectrometry (ESI). Further evidences of the presence of compound **S1** were found by tracking the changes in the ^{19}F NMR spectrum originating from perfluorinated chains, which occur after the coupling of compound **M6** with triarylamine **11**. Figure 42 shows the ^{19}F NMR spectrum of monomer **M6**.

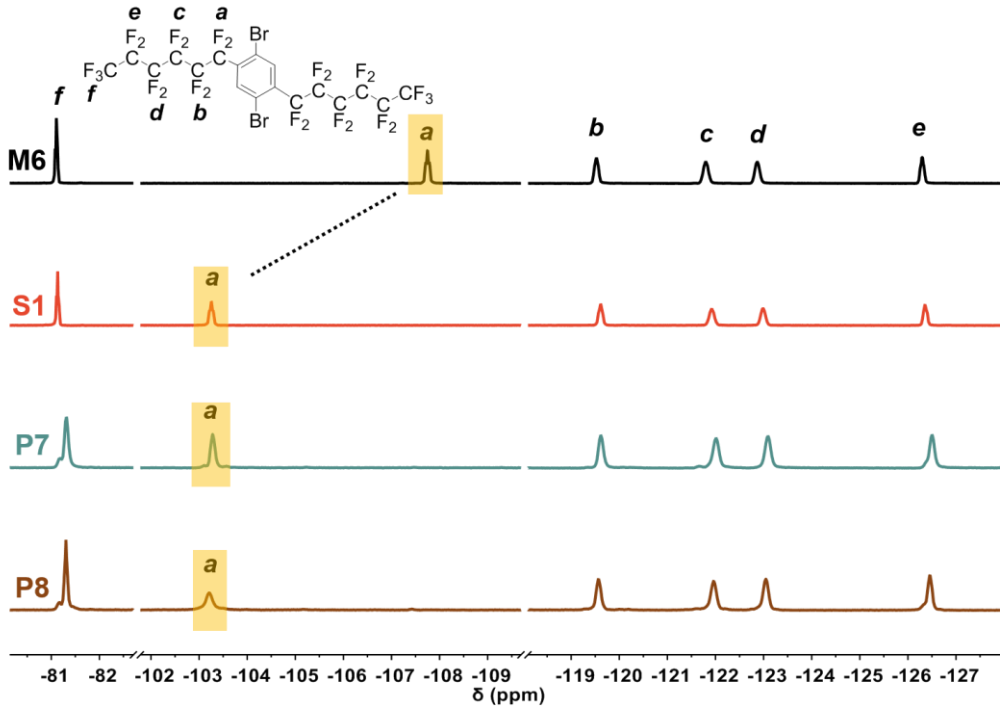

Figure 42. ^{19}F NMR spectra (376 MHz, CD_2Cl_2, 298 K) of **M6**, **S1**, **P7** and **P8**.

At room temperature, the spectrum exhibits the usual pattern of an aromatic-bonded C_6F_{13} group, with the appropriate number of ^{19}F resonance signals.[210] The signal at -107.75 ppm is attributed to the fluorine atoms closer to the aromatic ring, denoted as ***a***. The rest of fluorine atoms of **M6**, which are denoted as ***b*-*e***, are all assigned to the structure as can be seen in Figure 42. After the coupling between

compound **M6** and triarylamine **11**, the resonance signal ***a***, shifts to approximately -103.25 ppm in molecule **S1**, as a consequence of the deshielding effect of the new substituent. (Figure 42).

The mass analysis revealed that for **S1** a molecular peak for $[M + H]^+$:1321.249 was detected (Figure 43).

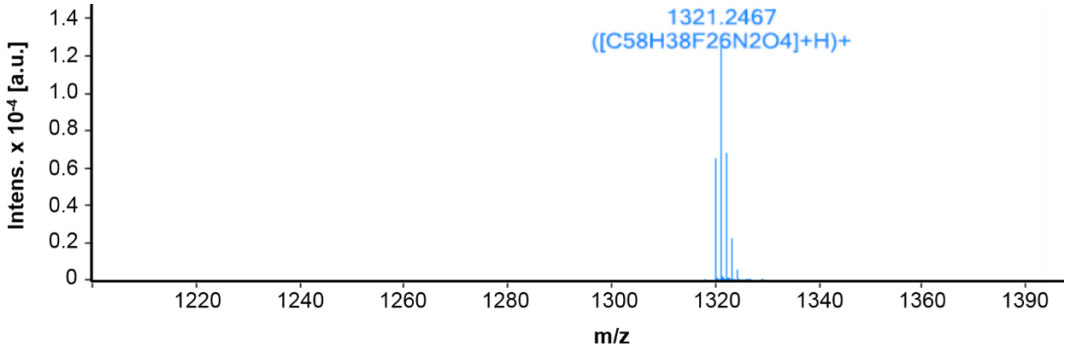

Figure 43. ESI-TOF of molecule **S1**.

Similarly, polymers **P7** and **P8** were synthesized by *Suzuki* coupling polymerization of the corresponding diboronic ester monomers **M2** and **M7**, respectively, with monomer **M6** in the presence of $Pd(PPh_3)_4$ in toluene using $NaHCO_3$ as base (Scheme 12).

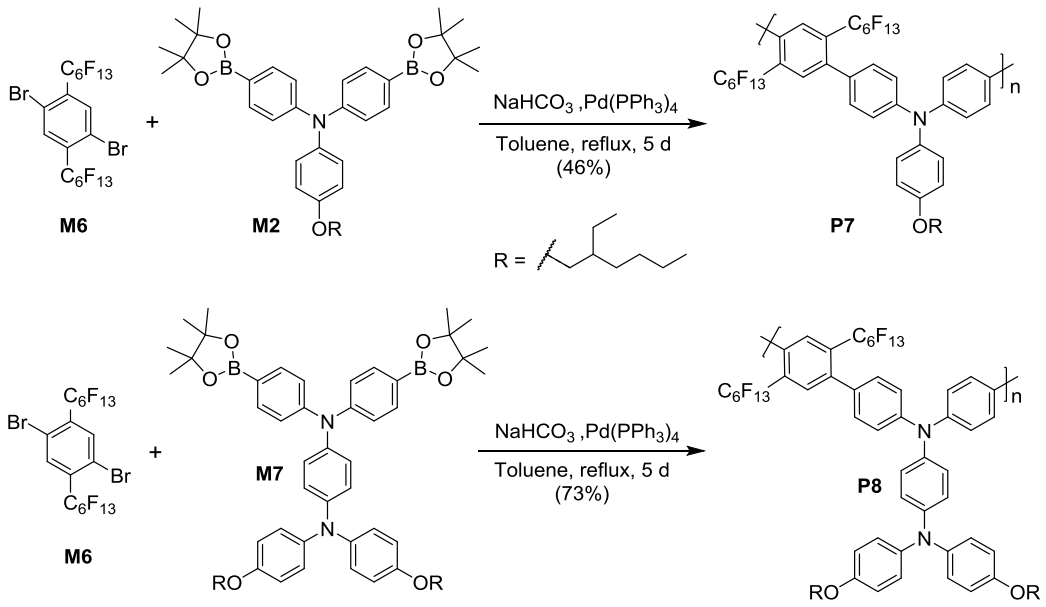

Scheme 12. Synthesis of the target polymers **P7** and **P8**.

After extraction and precipitation processes, the resulting polymers (**P7** and **P8**) were purified from the residual catalyst and low molecular weight impurities by subsequent *Soxhlet* extraction with different solvents. The composition and chemical structure of the synthesized compounds were confirmed by ^{1}H NMR, ^{19}F NMR and mass spectrometry (MALDI-TOF).

As it was mentioned before for molecule **S1**, the signal at -107.75 ppm in the ^{19}F NMR spectrum of monomer **M6** are shifted at -103.28 and -103.21 ppm in polymers **P7** and **P8**, respectively, as a consequence of the incorporation of the triarylmine groups (Figure 42).

In case of MALDI-TOF, peaks which differ from each other by a value which corresponds to the building blocks of both polymers were clearly visible. As an example, MALDI-TOF spectrum of polymer **P7** is displayed in Figure 44, where differences between some peaks corresponding to the building block ($C_{44}H_{31}F_{26}NO$ $[M]^{+}$: 1083.198) of **P7** were found.

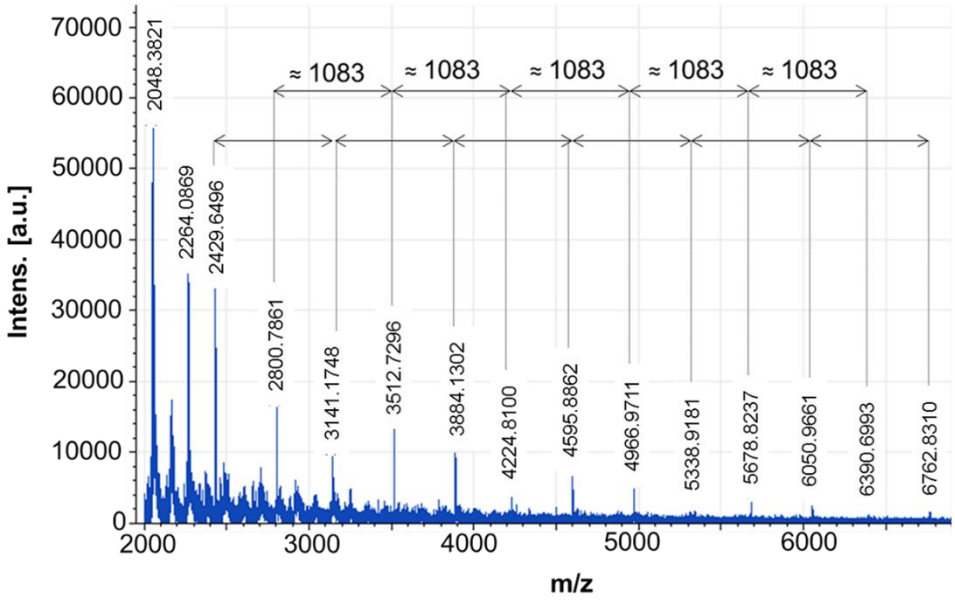

Figure 44. MALDI-TOF spectrum of polymer **P7**. Detection of the building block with molecular weight of 1083 is demonstrated.

Molecular weights distributions of polymers **P7** and **P8** were determined by SEC with THF as eluent and using polystyrene as a standard (Table 6). The M_n of **P7** was 10231 g mol^{-1}, leading to a X_n value of 9. The M_w was 16144 g mol^{-1} with a relatively small PDI value of 1.58. For **P8**, M_n and M_w were 10750 g mol^{-1} and 17600

g mol^{-1}, respectively, with a PDI of 1.64 and X_n of 8. It is worth mentioning that during the optimization of the synthetic procedures, we have been able to obtain fractions with higher molecular weights as M_n of 18563 $gmol^{-1}$ corresponding to X_n of 17 for **P7** or M_n of 25764 $gmol^{-1}$ (X_n = 19) in case of polymer **P8**. However, for the current study, fractions characterized by $X_n = 9$ and $X_n = 8$ for **P7** and **P8**, respectively, were employed.

Polymer	M_n (g mol^{-1})	M_w (g mol^{-1})	X_n	PDI
P7	10231	16144	9	1.58
P8	10750	17600	8	1.64

Table 6. Molecular weights of polymers **P7** and **P8**.

As expected, the perfluorinated chains modify the solubility of the compounds due to the hydrophobic nature of the substituents. The compounds are insoluble in EtOH and MeOH, show low solubility in DMF, DMSO and acetone and moderate solubility in chlorobenzene and chloroform (5 mg mL^{-1}).

To characterize the hydrophobicity of **S1**, **P7** and **P8**, water contact angle measurements of spin-coated films of the compounds were carried out. Hydrophobicity is commonly characterized by the water contact angle which is higher than 90° for hydrophobic surfaces and higher than 150° for superhydrophobic surfaces.[211] The contact angles of the water droplet were 107°, 106° and 102º for **S1**, **P7** and **P8**, respectively, demonstrating the outstanding hydrophobic nature of the compounds (Figure 45).

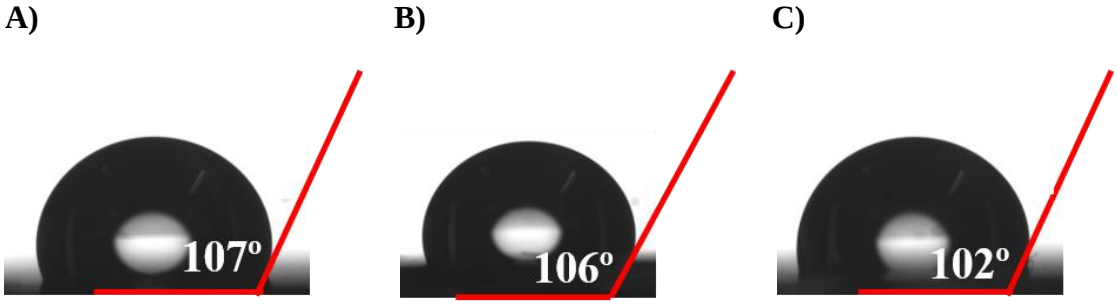

Figure 45. Water contact angles of A) molecule **S1**, B) polymer **P7** and C) polymer **P8**.

3.3.2 Thermal, Optical and Electrochemical Properties

a) Thermal properties

TGA analysis carried out at a heating rate of 10 °C min^{-1} under nitrogen atmosphere indicated the high thermal stability of molecule **S1** and polymers **P7** and **P8** (Figure 46A). Additives **S1**, **P7** and **P8**, showed T_d at 249, 284 and 274 ºC, respectively (Table 7), which were well above operational conditions of PSCs. All compounds exhibited a weight loss before decomposition, which was attributed to the loss of solvent traces.

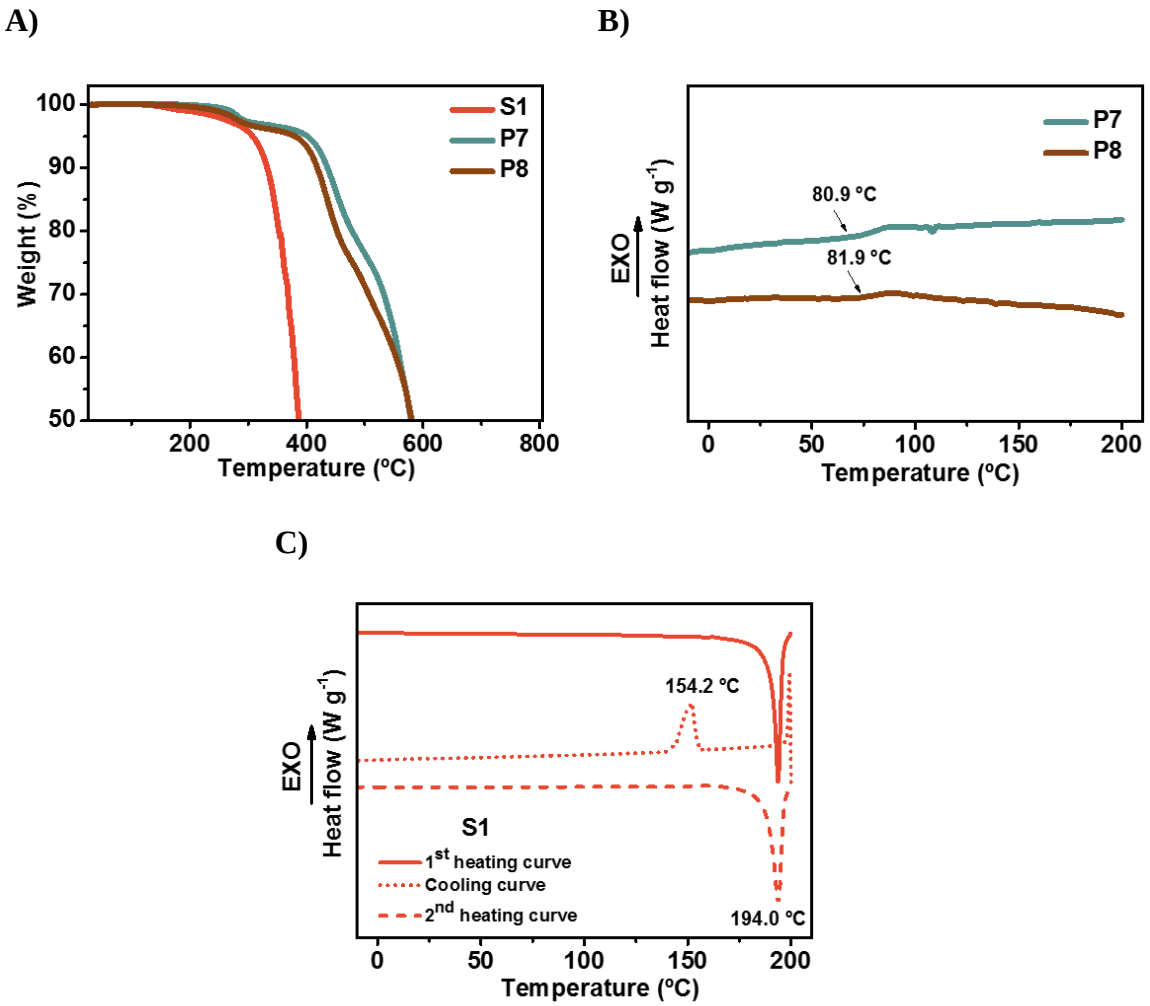

Figure 46. A) Thermogravimetric heating curves of compounds **S1**, **P7** and **P8** (heating rate 10 °C min^{-1}). B) Differential scanning calorimetry of the second heating curves for polymers **P7** and **P8** (heating rate 20 °C min^{-1}).C) Differential scanning calorimetry curves for molecule **S1** at a scan rate of 20 °C min^{-1}.

DSC measurements revealed that polymers **P7** and **P8** were fully amorphous showing T_g values at 81 and 82 ºC, respectively (Figure 46B). In contrast, molecule **S1** showed only a peak corresponding to the melting of the material at 194 °C during the first heating, and no glass transition was detected upon heating. During the cooling, an exothermic process of crystallization was observed at 153 °C indicating that below that temperature the material was crystalline. In the second heating process, the melting of the material was observed again, but no crystallization process, because the material was already crystalline (Figure 46C).

Sample	T_d (°C) [a]	T_g (°C) [b]	T_m (°C) [c]	T_c (°C) [d]
S1	248.89	-	193.97	153.26
P7	284.04	80.92	-	-
P8	274.10	81.85	-	-

Table 7. Thermal properties of molecule **S1** and polymers **P7** and **P8**. [a] Decomposition temperature determined from TGA (2 % weight loss). [b] Glass transition temperature determined from DSC (second heating curve). [c] Melting temperature determined from DSC (first or second heating curve). [d] Crystallization temperature determined from DSC (cooling curve).

b) Optical properties

The UV-vis absorption spectra of **S1**, **P7** and **P8** are shown in Figure 47A and the absorption spectrum of polymer **P6** are depicted for comparison with that of polymer **P8** (Figure 47B). As expected, all compounds did not display significant absorption in the visible region. On the other hand, these materials presented strong absorption in the UV region, with $\lambda_{max,abs}$ around 300-330 nm. The $\mathcal{E}$ value at the absorption maximum of **S1** was around 40000 M^{-1} cm^{-1} while for polymers **P7** and **P8** were around 20000 and 30000 M^{-1} cm^{-1}, respectively (Table 8).

Introducing more electron-withdrawing groups on the structure of a molecule makes λ_{onset} and $\lambda_{max,abs}$ values of the molecule blue-shifted. For example, the λ_{onset} and $\lambda_{max,abs}$ values of polymer **P8** are 12 nm and 20 nm blue-shifted from those of polymer **P6** (synthesized in chapter 2), respectively. This leads to a widening in the energy band gap, as is shown in Table 8. This behaviour was already reported.[212] In case of polymer **P7**, with less phenyl rings in its backbone than polymer **P8**, a shorter $\lambda_{max,abs}$ value

compared to **P8** was found (Table 8). Finally, molecule **S1**, with less conjugated systems than the polymers, has the shortest $\lambda_{max,abs}$ value among the 3 new compounds, which is centred at 302 nm.

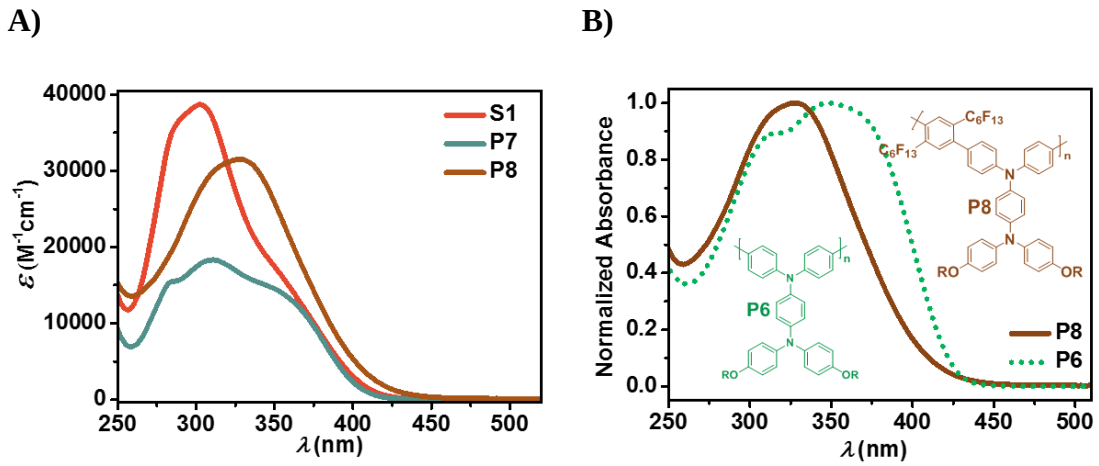

Figure 47. A) Absorption spectra of **S1**, **P7** and **P8** in DCM. B) Comparison of normalized UV-vis spectra of polymers **P6** and **P8** in DCM.

The E_g values, estimated from the absorption spectra, of **S1**, **P7** and **P8** were practically equal with values of 3.07 eV for **S1** and **P7** and 3.02 eV for **P8** (Table 8).

Sample	$\lambda_{max,abs}$ (nm)	ε ($M^{-1}cm^{-1}$)	λ_{onset} (nm)	E_g (eV)
S1	302	39458	404	3.07
P7	311	18375	404	3.07
P8	329	31305	411	3.02
P6	349	26586	423	2.93

Table 8. Optical properties of compounds **S1**, **P7** and **P8**.

c) Electrochemical properties

The electrochemical properties of molecule **S1** and polymers **P7** and **P8** were studied by CV, measured in a 0.1 M solution of TBAHFP in anhydrous DCM (Figure 48A). Their E_{HOMO} values were obtained from E_{onset}^{Ox1} during CV measurements using the Fc/Fc^+ redox couple as the internal standard. Therefore, E_{HOMO} is calculated according to the equation 17 and the data is listed in Table 9.

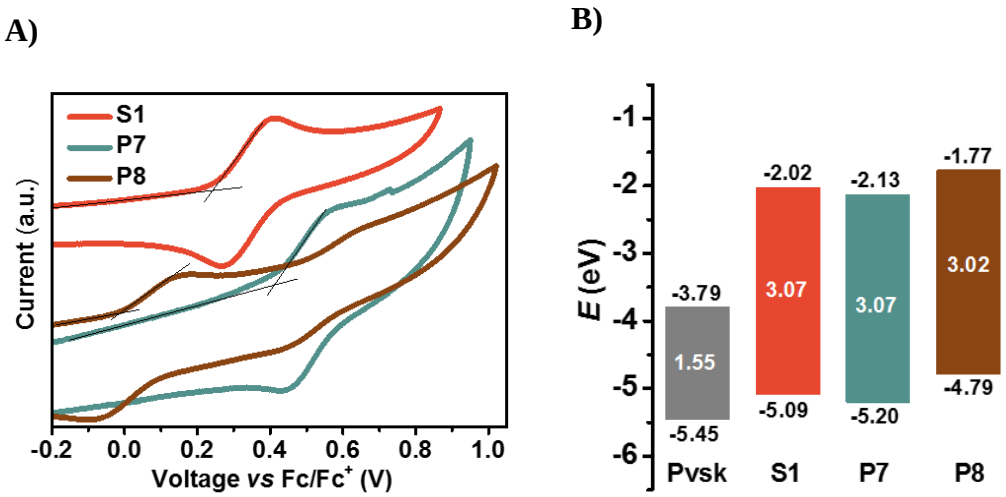

Figure 48. A) Cyclic voltammograms of **S1**, **P7** and **P8** in DCM/TBAHFP (0.1 M) at a scan rate of 250 mV s^{-1}. B) Energetic levels of polymers **S1**, **P7, P8** and perovskite light absorber layer used in this study.

S1 and **P7** exhibited one reversible oxidation wave at $E_{1/2}^{Ox1}$ values of 0.34 and 0.51 V vs Fc/Fc^+, respectively, indicating their electrochemical stability. The E_{onset}^{Ox1} values at 0.29 and 0.40 V values for **S1** and **P7**, respectively, led to E_{HOMO} levels of -5.09 and -5.20 eV, respectively. As the E_{HOMO} for the triple cation perovskite, used in this work, is -5.45 eV,[168] a possible hole transfer from the perovskite to the donor is possible which implies that both additives would not impede the charge transport within the perovskite material (Figure 48B). Thus, with the above absorption onset at 3.07 eV for both compounds **S1** and **P7**, the E_{LUMO} values were estimated to be -2.02 and -2.13 eV, respectively.

For polymer **P8** two different oxidation waves were observed, being the second one no reversible. The strong electron-donor properties of polymer **P8** compared to polymer **P7** was reflected in the decreasing of its first oxidation potential by 0.41 V compared to **P7**. With an E_{onset}^{Ox1} value of -0.01 V an E_{HOMO} of -4.79 eV was obtained, that in combination with the above calculated E_g led to an E_{LUMO} value of -1.77 eV. As in compounds **S1** and **P7**, polymer **P8** exhibited good band alignment with the VB of the perovskite (Figure 48B), not hindering the transport of charges.

Sample	$E_{1/2}^{Ox1}$(V)	E_{onset}^{Ox1}(V)	E_{HOMO} (eV)	E_{LUMO} (eV)
S1	0.34	0.29	-5.09	-2.02
P7	0.51	0.40	-5.20	-2.13
P8	0.05	-0.01	-4.79	-1.77

Table 9. Electrochemical properties and energy levels of **S1**, **P7** and **P8**.

3.3.3 Perovskite Solar Cells Employing S1, P7 and P8

To investigate the role of compounds **S1**, **P7** and **P8** in the perovskite film, these materials were incorporated into the perovskite layer as additives in regular planar devices. This study was carried out in collaboration with Dra. Nevena Marinova from the Hybrid Materials for Photovoltaics Group (Polymat, San Sebastián, Spain).

3.3.3.1 Perovskite-Based Device Fabrication

The solar cell architecture, depicted in Figure 49, was composed of FTO/SnO_2/Perovskite+additive (**S1**, **P7** or **P8**)/*spiro*-OMeTAD/Au, where the SnO_2 and *spiro*-OMeTAD acted as electron- and hole-transport layers, respectively.

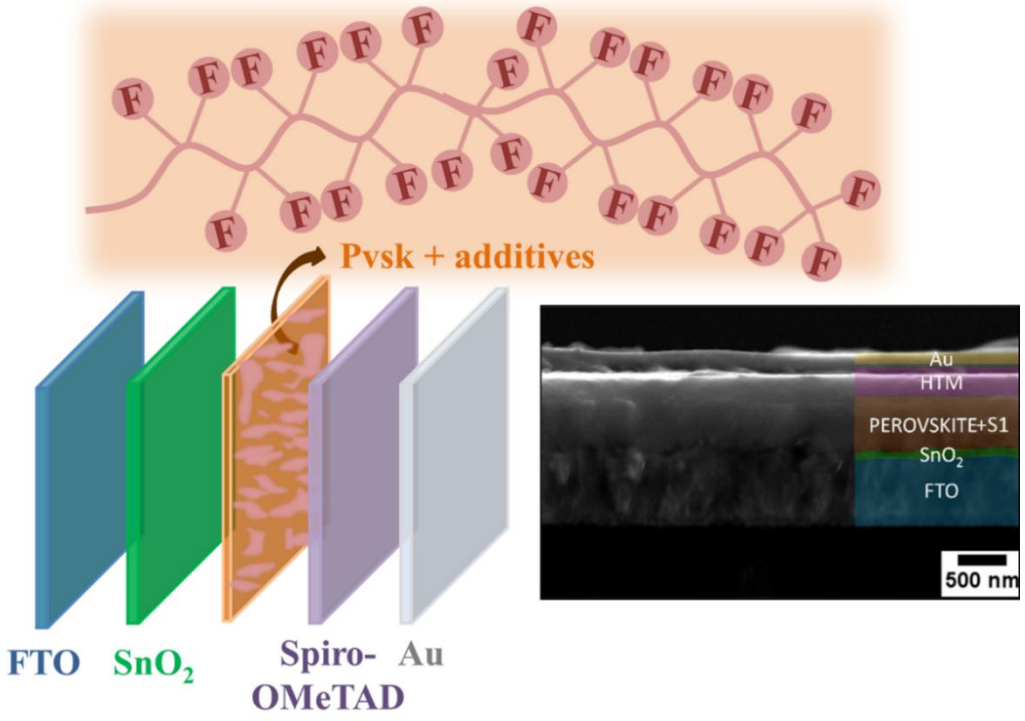

Figure 49. Simplified model of the perovskite-based solar cell used for testing additives **S1**, **P7** and **P8** and cross sectional SEM image of a device with **S1** as additive.

The additives were simply added with the weight concentration of 2 mg mL^{-1} to a precursor solution of the perovskite with the composition FAI (1 M), CsI (0.05 M), PbI_2 (1.1 M), MABr (0.2 M) and $PbBr_2$ (0.22 M) in DMF:DMSO (4:1) solvent mixture. The perovskite used in this study was the triple cation perovskite of the generic form "$Cs_{0.05}(MA_{0.17}FA_{0.83})_{0.95}Pb(I_{0.83}Br_{0.17})_3$".

The cell architecture of the fabricated device using molecule **S1** as additive can be appreciated from the SEM cross-sectional image displayed in Figure 49.

3.3.3.2 Photovoltaic Device Testing

PSCs using compounds **S1**, **P7** and **P8** as additives within the perovskite were fabricated and tested under simulated AM 1.5G illumination at 100 W cm^{-2} with masking aperture of 0.16 cm^2. Figure 50 shows the *J-V* curves of the highest performance PSCs.

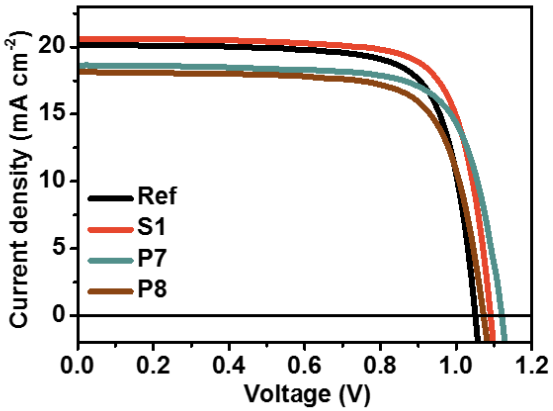

Figure 50. *J-V* curves for the best performing PSCs using compound **S1**, **P7** and **P8** as additives.

The statistics for the device parameters are shown in Figure 51 and Table 10 summarizes the photovoltaic characteristics of the resulting devices.

The reference devices showed average PCE of 14% with maximum value of 15.9%. Doping the perovskite material with **S1** slightly decreased the average PCE, mainly due to reduced *V*oc and FF. However, some of the **S1**-devices deviated from this trend, showed high current and record efficiency, reaching 17% (Table 10). The **P7**-doped PSCs showed *V*oc comparable with reference devices and PCEs slightly lower. Finally **P8**-doped perovskite devices had a FF and *J*sc similar to reference

devices, while the *V*oc was slightly lower than in reference devices, as in case as polymer **P7**. In general, doping the perovskite with additives **S1**, **P7** and **P8** slightly affected the device performance, which implies that the semiconductor properties of the perovskite, such as charge transport, were unaffected.

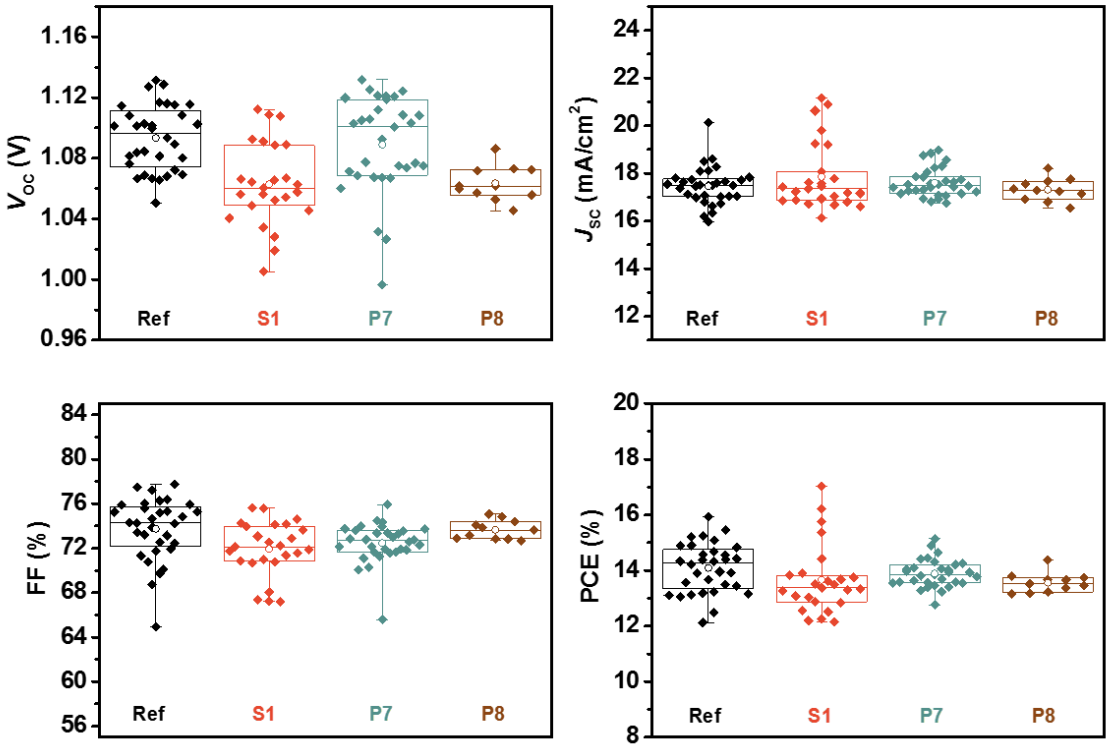

Figure 51. Comparison of the devices parameters for reference and perovskite solar cells with **S1**, **P7** and **P8**. Whiskers show minimum and maximum values, box represents the values between 25% and 75% and circles show mean values.

Sample	V_{OC} (V)	J_{SC} (mA cm^{-2})	FF (%)	PCE (%)
Ref	1.09 (1.05)	17.5 (20.1)	74 (75)	14.1 (15.9)
S1	1.06 (1.09)	17.9 (20.6)	72 (76)	13.7 (17.0)
P7	1.09 (1.12)	17.6 (18.3)	72 (74)	13.9 (15.1)
P8	1.06 (1.07)	17.3 (18.2)	74 (74)	13.6 (14.4)

Table 10. Average photovoltaic parameters devices determined form *J-V* measurements using **S1**, **P7** and **P8** as additives in PSCs. The photovoltaic parameters of the best working cells are shown in brackets.

One of the main limitations to the advancements of PSCs is the presence of hysteresis in the *J-V* curves depending if the measurement is carried out with forward or reverse scan. The hysteric behaviour of the devices tends to vary from batch to batch

independent of the devices type. In case of devices prepared in this study, frequently, all the devices from certain batch showed no hysteresis (Table 11). In order to quantify the hysteresis magnitude the hysteresis index (HI) is used, as reported in literature.[213] The HI for the cases when PCE (reverse) > PCE (forward) is calculated using equation 18, while for cases when PCE (reverse) < PCE (forward), equation 19 is used:

$$HI = [P_{max,r}/P_{max,f}]\text{-}1 \qquad (18)$$

$$HI = [P_{max,f}/P_{max,r}]\text{-}1 \qquad (19)$$

Where $P_{max,f}$ and $P_{max,r}$ are the maximum power points on the forward and the reserve scan, respectively.

Sample	Device	Scan direction	V_{OC} (V)	J_{SC} (mA cm^{-2})	FF (%)	PCE (%)	P (mW)	HI
Ref	A	F	1.08	16.93	72.55	13.20	2.11	**0.03**
		R	1.07	16.79	72.26	13.55	2.17	
	B	F	1.07	16.81	73.71	13.28	2.13	**0.01**
		R	1.07	16.74	73.42	13.11	2.10	
	C	F	1.07	17.64	72.68	13.75	2.20	**0.04**
		R	1.07	17.55	76.37	14.33	2.29	
S1	A	F	1.05	16.85	72.87	12.84	2.05	**0.00**
		R	1.04	16.74	74.04	12.83	2.05	
	B	F	1.03	17.64	72.21	13.17	2.11	**0.04**
		R	1.03	17.61	75.57	13.68	2.19	
	C	F	1.03	16.62	71.97	12.30	1.97	**0.02**
		R	1.02	16.61	74.18	12.56	2.01	
P7	A	F	1.08	17.22	72.31	13.41	2.15	**0.01**
		R	1.06	17.14	74.30	13.54	2.17	
	B	F	1.06	17.75	72.14	13.58	2.17	**0.02**
		R	1.05	17.74	71.70	13.35	2.14	
	C	F	1.08	17.42	74.33	13.92	2.23	**0.03**
		R	1.05	17.24	74.86	13.56	2.17	
P8	A	F	1.07	16.61	73.41	13.08	2.09	**0.01**
		R	1.06	16.54	75.08	13.16	2.11	
	B	F	1.06	17.75	72.91	13.74	2.20	**0.02**
		R	1.05	17.69	72.57	13.42	2.15	
	C	F	1.07	28.21	73.64	14.38	2.30	**0.02**
		R	1.06	18.07	73.61	14.07	2.25	

Table 11. Examples of hysteresis index from one batch. F= forward scan; R= reverse scan.

As is shown in Table 11, for this batch, no significance hysteresis could be observed, being even cero for a **S1**-doped device.

However, there are some batches, in which all the devices showed hysteresis in the *J-V* curves. We attributed this alteration to variation in the quality of the SnO_2 electron-transport layer for every batch, due to low reproducibility of the layer formation.

3.3.3.3 Film Characterization

a) X-ray diffraction analysis

In order to confirm the structure of the perovskite films, XRD measurements were performed. Figure 52 shows the diffractograms of pristine perovskite and doped perovskite films with **S1**, **P7** and **P8** deposited onto a FTO glass substrate. All films displayed the typical pattern for perovskite, with the most pronounced peaks at 2θ = 14.16º and 28.5º corresponding to the (110) and (220) planes of the perovskite, respectively.[214] The same diffraction peaks for all perovskite films indicated that additives were not embedded in the perovskite crystal lattice and could only exist at GBs or surface of perovskite films.[207]

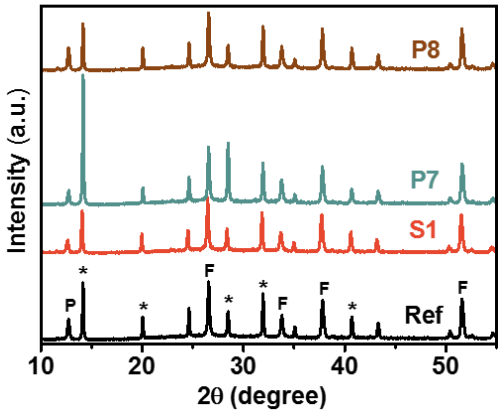

Figure 52. X-ray diffractograms of pristine perovskite (**Ref**) and doped perovskite with **S1**, **P7** or **P8** deposited on FTO covered glass. Peaks marked with P corresponds to PbI_2, F to FTO and * to perovskite.

The increased peak intensity at 2θ = 14.16º for **P7**-doped layer suggests improved crystallinity of the perovskite.[215] Due to the slight excess of PbI_2, all samples

displayed a small peak at 12.7º.[173] This peak, however, decreased slightly in intensity with the addition of additives **S1** and **P7** suggesting an improved conversion.

b) Optical properties

The UV-vis absorption spectra of pristine perovskite and **S1**, **P7** or **P8**-doped perovskite deposited onto FTO/SnO_2 substrates are shown in Figure 53. All films displayed the typical for triple cation perovskite absorption and are practically identical, so the deposition of the hydrophobic compounds (**S1**, **P7** or **P8**) did not compromise the absorption of the perovskite. Moreover, the intrinsic characteristics of the perovskite were not influenced by a small amount of these novel perfluorinated materials.

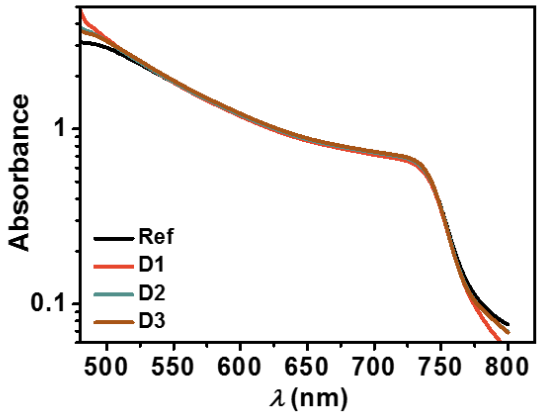

Figure 53. UV-vis absorption spectra of FTO/SnO_2/perovskite film (Ref) and FTO/SnO_2/perovskite+**S1**, **P7** or **P8** films.

c) Water contact angle measurements

To assess the effect of the dopants on the hydrophobicity of the perovskite we performed water contact angle measurements of pristine perovskite and perovskite doped with **S1**, **P7** and **P8** deposited onto FTO/SnO_2 substrates. We recorded contact angles of 56° for the pristine perovskite versus measured angles of 68°, 62° and 60º for **S1**-, **P7**- and **P8**-doped perovskite, respectively (Figure 54). This result showed that the surface of the perovskite layer was modified by the hydrophobic compound and that the compounds were embedded in the perovskite film and/or on its surface.

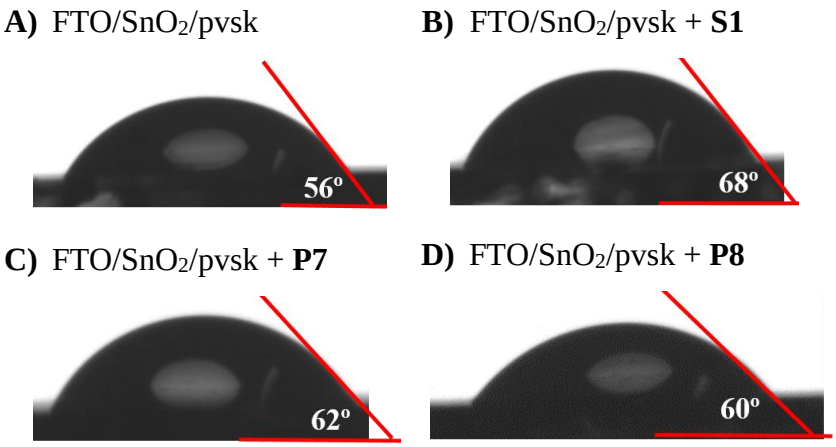

Figure 54. Water contact angle measurements after dropping water onto A) FTO/SnO_2/perovskite film, B) FTO/SnO_2/perovskite+**S1** film, C) FTO/SnO_2/perovskite+**P7** film and D) FTO/SnO_2/perovskite+**P8** film

d) Scanning electron microscopy measurements

Figure 55 shows top-view SEM micrographs of the prepared pristine perovskite film and those of films doped with **S1**, **P7** or **P8**. As can be seen, films were composed of perovskite grains, which in the pristine perovskite appear to be clearly faceted with sharp edges and GBs. The doped perovskite layers were composed of grains with slightly bigger size and reduced grain boundaries. This trend is especially pronounced for the case of polymer **P7**-doped perovskite.

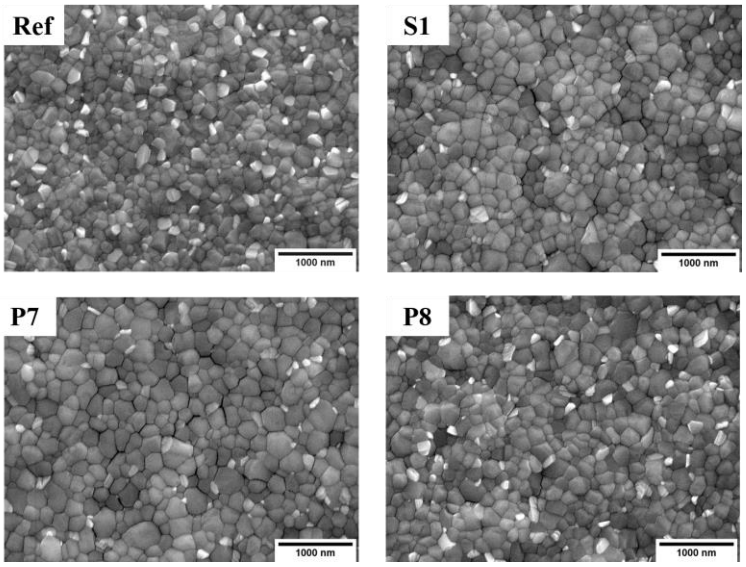

Figure 55. Top-view SEM micrographs of the pristine perovskite film and the doped-perovskite film with **S1**, **P7** or **P8**. The perovskite film were deposited onto SnO_2/FTO substrate.

To quantify the effect of the additives on the film morphology and grain size we analyzed the SEM micrographs with an image-process software. Table 12 contains the grain size parameters obtained from the micrographs. The mean grain diameter of the reference perovskite is 160 nm, which was consistent with previously reported data for this type of perovskite.[98] The addition of **S1**, **P7** or **P8** into the perovskite layer led to an increase in mean grain size to 195 nm for **S1**-doped-perovskite, above 200 nm for **P7**-doped perovskite and to 173 nm for **P8**-doped perovskite. The increment of the grain size and improved perovskite quality is frequently observed when suitable additives are employed. The reason for this is that in the presence of small quantities of additives, the formation of disordered gel-sol precursor phase is promoted during the process of crystallization and grain growth, more specifically during the early stage of the spin-coating. This disordered precursor phase slows down the crystallization process, which results in larger grains.[198,216]

Sample	Mean Area (nm^2)	Mean Diameter (nm)[a]	Particle counts[b]
Ref	22286	159	682
S1	33699	195	431
P7	38331	207	379
P8	26535	173	575

Table 12. Grain parameters of the reference perovskite film and perovskite films doped with **S1**, **P7** and **P8**. [a] The diameter is expressed as the diameter of a circle having an area equal to the area enclosed by the shape's contour. [b] The analyzed area is the same for all the images. The reduced particle number reflects the increased particle size.

It is worth to say that we cannot affirm that the less increment in grain size when the perovskite film is doped with polymer **P8** comparing with the other two additives (**S1** and **P7**), is due to the material itself. Polymer **P8** turned to be very insoluble in the DMSO:DMF perovskite precursor solution, so it is highly likely that the concentration of this compound in the perovskite layer is much less than that achieved with the other two additives. For this reason, at this point, we decided to continue the study without polymer **P8**.

e) Atomic force microscopy measurements

To further investigate the effects of doping in the perovskite layer, morphology of pristine perovskite and doped perovskite (with **S1** or **P7**) films were also study by atomic force microscopy (AFM). The difference in shape was also evident from the topography and phase images derive from those measurements (Figure 56). As can be seen, the undoped perovskite was composed of smaller, cuboid-like grains with pronounced edges, which affected the surface of the film. **S1**- and **P7**-doped perovskite films, in contrast, showed smoother edged and round-shaped flat grains with reduced grain boundaries. From AFM topography images, we obtained the root mean square roughness, which were 12.8, 11.9 and 11.8 nm for pristine perovskite, **S1**-doped perovskite and **P7**-doped perovskite, respectively. The lower roughness value for doped-perovskite layers indicates a smoother and more uniform layers than that of pristine perovskite.

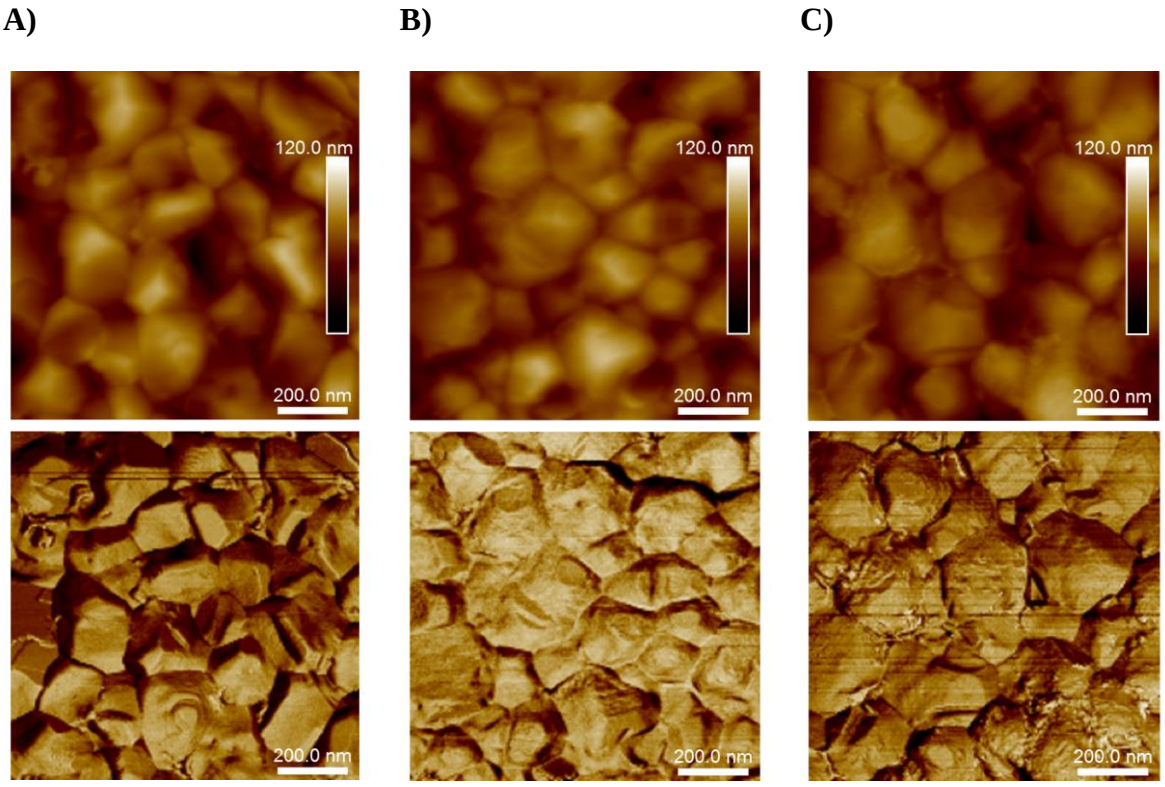

Figure 56. Top: Topography AFM micrographs of A) pristine perovskite film, B) **S1**-doped perovskite film and C) **P7**-doped perovskite film deposited onto FTO/SnO_2 substrates. Bottom: AFM phase images of the surface of A) pristine perovskite film, B) **S1**-doped perovskite film and C) **P7**-doped perovskite film deposited onto FTO/SnO_2 substrates.

3.3.3.4 Stability Tests

To better clarify the effect of the incorporation of the additives on the stability of the devices, we performed stability tests of PSCs using molecule **S1** and polymer **P7** as additives to the perovskite layer.

We carried out two types of stability measurements in air without encapsulation. In the first experiment, the power output was measured for 80 minutes using pristine perovskite and doped-perovskite layers (with **S1** or **P7**) in corresponding devices. During the measurement, we measured their stabilized power output keeping the solar cells at bias close to their maximum power point (MPP)[1]. The measurement was carried out in air in the solar simulator. As shown in Figure 57A, the reference device started degrading gradually since the beginning of the measurement and after 40 minutes severe degradation issues were observed. This led to the complete breakdown of the device after 80 minutes of operation under these conditions. In contrast, **S1**-doped devices showed very stable power output practically without any decay for about 40 minutes. Then, the power started to decline slowly and after 80 minutes of aging in air the device maintained 94% of the initial power. **P7**-doped devices showed gradual decrease of output power, which was delayed compared to reference devices and reached 85% of its initial power after 80 minutes.

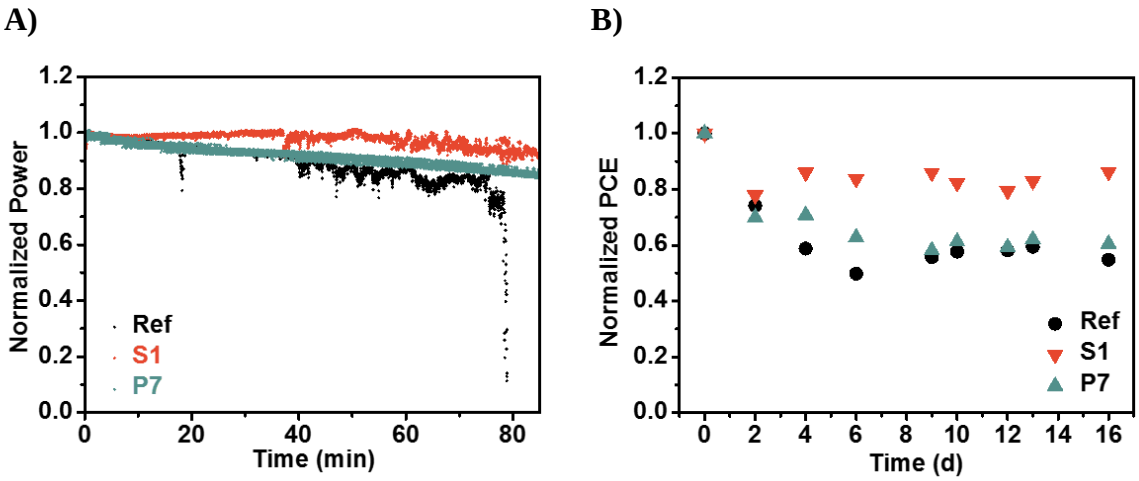

Figure 57. A) Normalized power measured as a function of time for reference and stabilized cells kept at MPP in air. B) Normalized PCE measured for reference and stabilized devices storage in air.

[1] When a solar cell receives solar radiation, it produces power, which is the product of current and voltage. The highest power output for a solar cell is called maximum power point (MPP)

In the second experiment, stability assays of pristine perovskite and **S1**- or **P7**-doped perovskite devices upon storage in air (50-70% relative humidity) were also performed. The normalized PCE as a function of storage time is shown in Figure 57B. As can be seen, substantial differences in stability were noted for doped devices compared to the reference device. The PCE of the reference device dropped to 54% of their initial value after 16 days of storage. **S1**- and **P7**-doped devices kept 86% and 60% of their initial PCE, respectively. This result further demonstrated the stabilizing effect of the novel perfluorinated dopants. The weaker stabilization effect of **P7** compared to **S1** could be explained by the T_g value of the polymer. In this sense, after perovskite deposition, an annealing process at 100 °C was carried out, which could lead to phase transition of the polymer, which could alter the morphology of the perovskite film.

It was already mentioned that perovskite devices are very sensitive when operating in ambient air and they degrade quickly due to a number of degradation processes related to the effect of oxygen, humidity, temperature among others, in the solar cell stack.[170,217–220] Doping the perovskite with the perfluorinated additives modifies the surface, thus increasing the hydrophobicity of the perovskite and providing a protective barrier for the oxygen, which retards the degradation when devices are operating in air. Furthermore, prolonged operation causes heating of the device. In this study, we have measured the temperature of the cavity in the solar simulator where devices were measured in prolonged experiment, and we observed that in less than 10 minutes the temperature of the air in the measuring cavity set to 46°C and remained constant (Figure 81, experimental part). This inevitably caused heating of the devices, without taking into account the intrinsic heating of a solar cell due to resistive effects, etc. Therefore, we can hypothesize that the perfluorinated dopants retard the degradation of the devices when operating in air under elevated temperature (higher than the standard measuring conditions) also due to improved thermal stability. This is consistent with previous studies, which report that perfluorinated compounds enhance the thermal stability of the materials.[221]

3.4 Conclusions

In summary, three novel perfluorinated additives (**S1**, **P7** and **P8**) for PSCs have been developed. The compounds were successfully synthesized and their chemical, thermal and optoelectronic properties studied. The novel additives contain 26 fluorine atoms per unit, which is the largest amount of fluorine atoms reported for additives in PSCs. The presence of those perfluorinated chains increases the hydrophobicity of the perovskite when adding to the material in very small quantity. Additives were incorporated into the perovskite layer and the overall effect of the compounds in PSCs was studied. Fluorine-containing organic additives are known to provide thermal stability to the materials as well as protection against humidity and oxygen due to their hydrophobicity, while at the same time improve the morphology of the perovskite layer. In this regard, the doped-perovskite films showed larger crystals and reduced GBs compared to the undoped one. Moreover, the stability of devices based on additives **S1** and **P7** were studied and as a result, **S1**- or **P7**-based devices showed increased stability, maintaining 86% and 60% of their initial performance, respectively, after 16 days of exposure to ambient atmosphere (50-70% relative humidity). The stabilizing effect is most likely due to combined protective action against humidity and oxygen, because of the formation of a protective barrier by the perfluorinated compound. Nevertheless, the stabilization upon heating under operation could also be considered as a possible mechanism of action. Importantly, the semiconducting nature of the novel additives might be favouring charge transport, leading to efficiencies comparable to reference devices, and allowing **S1**-containing device to achieve an improved PCE value (17.0%) compared to the reference device. However, the novel compounds showed low solubility in the perovskite precursor solution, which limited their application in higher concentration. Therefore, improved molecular design and synthesis of perfluorinated compounds with increased compatibility with the precursor solution and increased T_g would be required to further explore the full potential of perfluorinated compounds in PSCs. Overall, these new perfluorinated compounds are presented as excellent additive candidates towards stable and efficient PSCs.

4. ELECTRON-TRANSPORTING POLYMERS FOR PEROVSKITE SOLAR CELLS

4 ELECTRON-TRANSPORTING POLYMERS FOR PEROVSKITE SOLAR CELLS

4.1 Introduction

In contrast to widely investigated HTMs, a fewer types of ETMs have been developed. However, ETMs play also a crucial role in both regular and inverted PSC architectures, so the exploration of novel ETMs is also necessary.

In this chapter a discussion on ETM requirements together with an overview of the developed materials used as ETMs for PSCs are highlighted, which in a further step will help us to design new ETMs for perovskite-based devices.

4.1.1 Role and Properties of Electron-Transporting Materials in PSCs

The main function of an ETM is the extraction of the photogenerated electrons from the perovskite and transporting them to the electrode, although it has many other important contributions. For instance, as mentioned previously, in the course of a PSC operation, undesirable processes can occur, such as recombination of the charge carriers at the interfaces, that in case of taking place would lead to a reduction in the device performance.[222] In this regard, the ETM could help to avoid these processes by serving as hole-blocking layer, suppressing charge recombination at the perovskite/ETM interface.[223] Moreover, the ETM can act as a barrier against external factors, such as oxygen or moisture, and in that way protecting the perovskite from them. In regular-type PSCs the ETM is a vital component since it will determine the final quality of the perovskite layer, because is the substrate in which the perovskite is deposited.[224] Although there have been already reported ETL-free devices, the incorporation of ETMs in PSCs is still necessary in order to achieve efficient and stable PSCs.[225,226]

In order to obtain high-performance PSCs, an ETM should satisfy some general requirements: (i) The energy levels of the ETM should be well-aligned with those of the active perovskite layer and with the work function of the electrode. In this regard,

the LUMO level of the ETM should be lower than the CB of the perovskite in order to facilitate electron extraction and transport. On the other hand, the HOMO of the ETM should be lower than the VB of the perovskite to fulfil the hole-blocking function, avoiding recombination losses, as above-mentioned.[227] (ii) Moreover, a relatively high electron mobility/conductivity is also needed for an efficient charge transport.[228] (iii) ETMs should show good chemical stability as well as good photo and thermal stability.[227,229] (iv) They should have enough solubility in the appropriate solvent and good-film forming ability for processing and device fabrication. In this sense, a high-quality pinhole-free dense ETL layer with few defects and seamless interface with other layers is desirable for high-performance PSCs.[227,228,230] (v) An ideal ETM should not suffer any phase transition during device fabrication/operation. (vi) They should be cheap and environmental friendly. (vii) The E_g of the ETM should be wide enough to ensure transparency and allow light to pass through, while not competing with the perovskite in light absorption.[231]

4.1.2 Organic Electron-Transporting Materials for PSCs

Taking into account that PSCs were first developed based on DSSCs, in which TiO_2 acts as an ETM, it is not surprising that TiO_2 was used in the first perovskite-based device.[51] Since then, TiO_2 has been widely used and is still the dominant ETM in PSCs. However, TiO_2 has a major disadvantage: it usually requires a high-processing temperature (~ 500 ºC) for highly efficient perovskite devices, which translates not only in higher costs but also impedes the development of flexible devices.[232] Moreover, as it was already mentioned, TiO_2 suffers UV instability, leading to trap states, which can affect both efficiency and stability of PSCs. To overcome these limitations a variety of ETMs, including inorganic, organic or polymers, has been tested in last years.[229]

Organic semiconductors are easy to prepare and manipulate and their properties can be finely tuned through chemical synthesis.[77] Fullerenes and their derivatives are the most used organic ETMs in PSCs. This is due to their excellent properties, such as efficient electron-transporting properties, suitable energy alignment with that of

perovskites or acceptable electron mobility. Moreover, they are well-known for reducing the undesirable phenomenon of hysteresis because of their capability of passivating trap states, and they can be processed at low temperatures.[233]

The first time in which fullerenes were used as ETMs in PSCs was in 2013. In particular, fullerene C_{60} (**ETM-1**) and its derivatives phenyl-C_{60}-butyric acid methyl ester ($PC_{61}BM$, **ETM-2**), and tetrahydro-di[1.4] methanonaphthaleno[5,6]fullerene-C_{60} indene bisadduct (ICBA, **ETM-3**) were introduced into PSCs by Guo, Chen and co-workers, reaching PCEs of 3.0, 3.9 and 3.4%, respectively, using an inverted PSC configuration (Figure 58).[234] Since then, many other fullerenes have been developed and used as ETMs in PSCs.[154,235] Figure 58 displays selected examples of fullerenes, which recently led to highly efficient, stable and hysteresis-free PSCs.

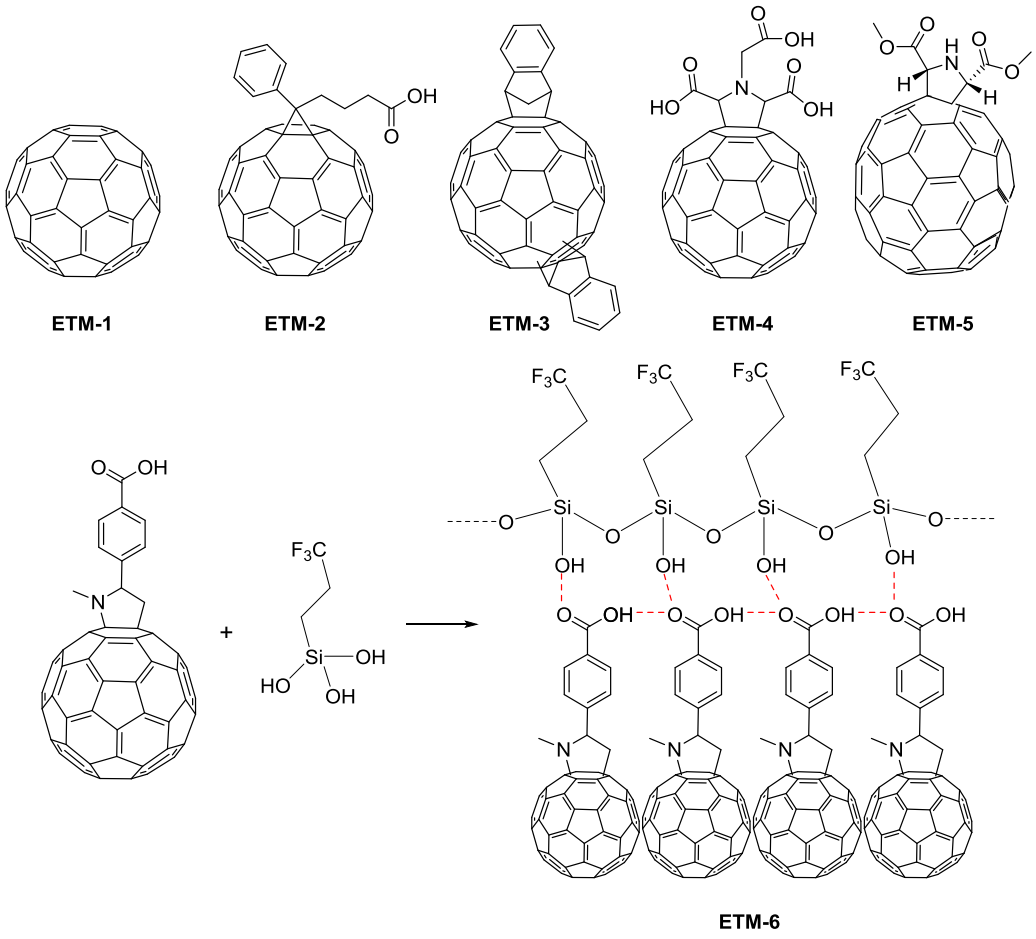

Figure 58. Structure of some fullerene derivatives used as ETMs in PSCs.

For example, the PCE of perovskite-based devices with $PC_{61}BM$ (**ETM-2**) as ETM has been improved to 20.9%.[236] In that work, the authors fabricated an inverted

PSC with an ITO/PTAA/perovskite/$PC_{61}BM$/C_{60}/bathocuproine (BCP)/Cu architecture achieving an impressive improvement of the device stability. Moreover, a work done by Fang and co-workers has shown the usefulness of fullerene derivatives as ETMs in regular planar PSCs. The C_{60} fullerene derivative **ETM-4** was deposited directly onto ITO, leading to an uniform and robust layer due to the esterification of the carboxylic groups of **ETM-4** with the ITO substrate. The resulted long term-stable PSC reached an efficiency of 18.4% with an ITO/**ETM-4**/$MAPbI_3$/*spiro*-OMeTAD/Au architecture. Moreover, a PCE up to 17% was demonstrated when the device was constructed onto flexible devices, showing the applicability of **ETM-4** in flexible PSCs.[237] In another work by Echegoyen and co-workers, a C_{70} fullerene derivative endowed with hydrogen bonding moieties (**ETM-5**) was used as ETM in inverted PSCs with an ITO/PEDOT:PSS/perovskite/**ETM-5**/Al architecture, reaching 18.6% in efficiency.[238]

To enhance the electron-transporting properties, together with the water and moisture resistance, Huang and co-workers used **ETM-6** to prepare inverted PSCs. The authors synthesized the ETM by bonding a crosslinkable silane coupling agent, which had hydrophobic functional groups, onto a C_{60}-substituted benzoic acid self-assembled monolayer (SAM). Perovskite-based devices (ITO/PTAA/$MAPbI_3$/**ETM**/Cu) using **ETM-6** not only showed 19.5% in efficiency but also devices maintained 90% of their initial PCE after 30 days in ambient atmosphere. The authors explained this high performance due to the fact that the crosslinking process improved the transport properties of the ETL, while the hydrophobic groups present in the silane fragment enhanced the moisture resistance.[239]

Apart from fullerenes derivatives, other organic small molecules and polymers have been tested as ETMs in PSCs.[77,228,240] However, since this chapter will be dedicated to naphthalene diimides (NDIs)-based molecules, in the following sections we will focus on NDI derivatives, both small molecules and polymers, that have been used in PSCs.

4.1.3 Naphthalene diimide-Based ETMs in PSCs

Naphthalene diimides are the smallest component of the family of rylene diimides (Figure 59), which consist of a naphthalene core with imide substituents at the 1,4,5,8 positions. NDIs are among the most versatile class of aromatic molecules and functionalization through core-substitution produce NDI analogues, whose properties are variable, while the imide position could be used to tune the solubility or for tethering a specific functional fragment.[241]

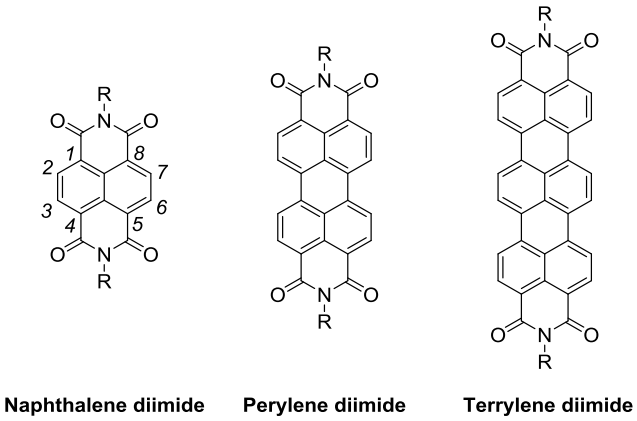

Figure 59. General structure of some common diimide derivatives of the rylene family.

This class of molecules are electron-deficient aromatic compounds, due to the two strong electron-withdrawing diimide groups. They are neutral planar molecules with the ability to stack in an arrangement with itself or other aromatic molecules, leading to potential conducting pathways. Moreover, they also have good electron mobility, and excellent thermal and oxidative stability as well as good solution processability. All these properties together with their easy and low-cost synthesis make them promising candidates for photovoltaic devices, although they have been already used for a variety of applications, ranging from biomedicine to electronics.[241,242]

4.1.3.1 NDI-Based Small Molecules as ETMs in PSCs

Figure 60 displays some of the most recently examples in which NDI-based small molecules were used as ETMs in PSCs.

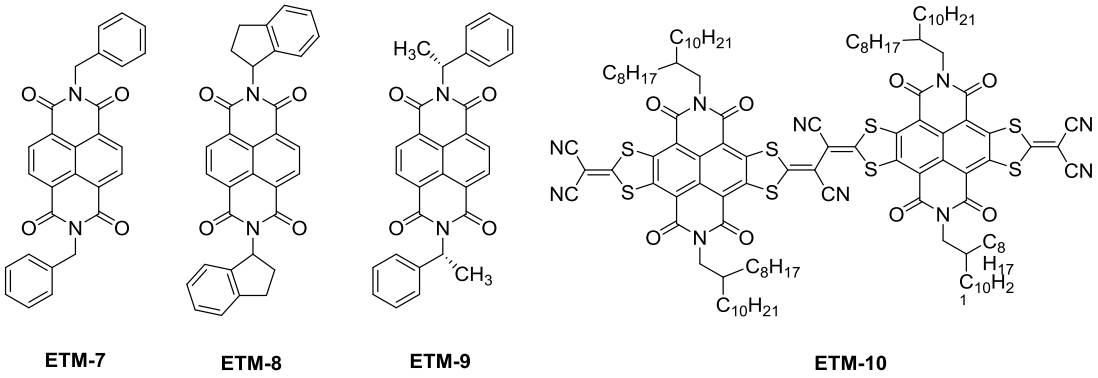

Figure 60. Chemical structure of small molecules based on naphthalene diimides.

Kwon, Im and co-workers introduced **ETM-7** into inverted PSCs showing a PCE (19.6%) close to that of the conventional $PC_{61}BM$ (**ETM-2**)-based reference device (20.0%). Furthermore, **ETM-7**-based PSCs exhibited better thermal stability than reference devices due to better molecular packing and additionally higher thermal stability of **ETM-7** compared to $PC_{61}BM$.[242] In another work, **ETM-8** with *N*-substituted indane group exhibited a PCE of 20.2%, which was better than that of the $PC_{61}BM$-based device. Moreover, **ETM-8**-based devices retained 90% of their initial efficiency after 500 hours at 100 ºC in ambient atmosphere.[243] Very recently, **ETM-9** has been used by Kim, Im, Kwon and co-workers to prepare PSCs.[244] The **ETM-9**-based inverted PSC achieved a PCE of 20.5%, better than that of the $PC_{61}BM$-based reference device. Furthermore, **ETM-9** exhibited good film-forming properties, due to the high solubility given by the asymmetry of the NDI-based molecule, which could be one explanation for the good PSC performance.

A NDI dimer with twisted molecular backbone (**ETM-10**) was also employed as ETM for inverted PSCs. Due to the isotropic charge transport paths caused by the twisted backbone, high electron mobility, well-aligned LUMO energy level with the CB of the perovskite, and good film-forming property, **ETM-10**-based device yielded a PCE of 12.9%.[245]

4.1.3.2 NDI-Based Polymers as ETMs in PSCs

Polymer semiconductors have excellent features that make them attractive candidates for using them as ETMs in PSCs. In addition, the film-forming properties of polymers is generally better than those of small molecules, which provide better

processing window for eventually deposition of high-quality films, based on scalable coating methods. Figure 61 shows some of the most representative examples of NDI-based polymers used as ETMs in PSCs reported recently in the literature.

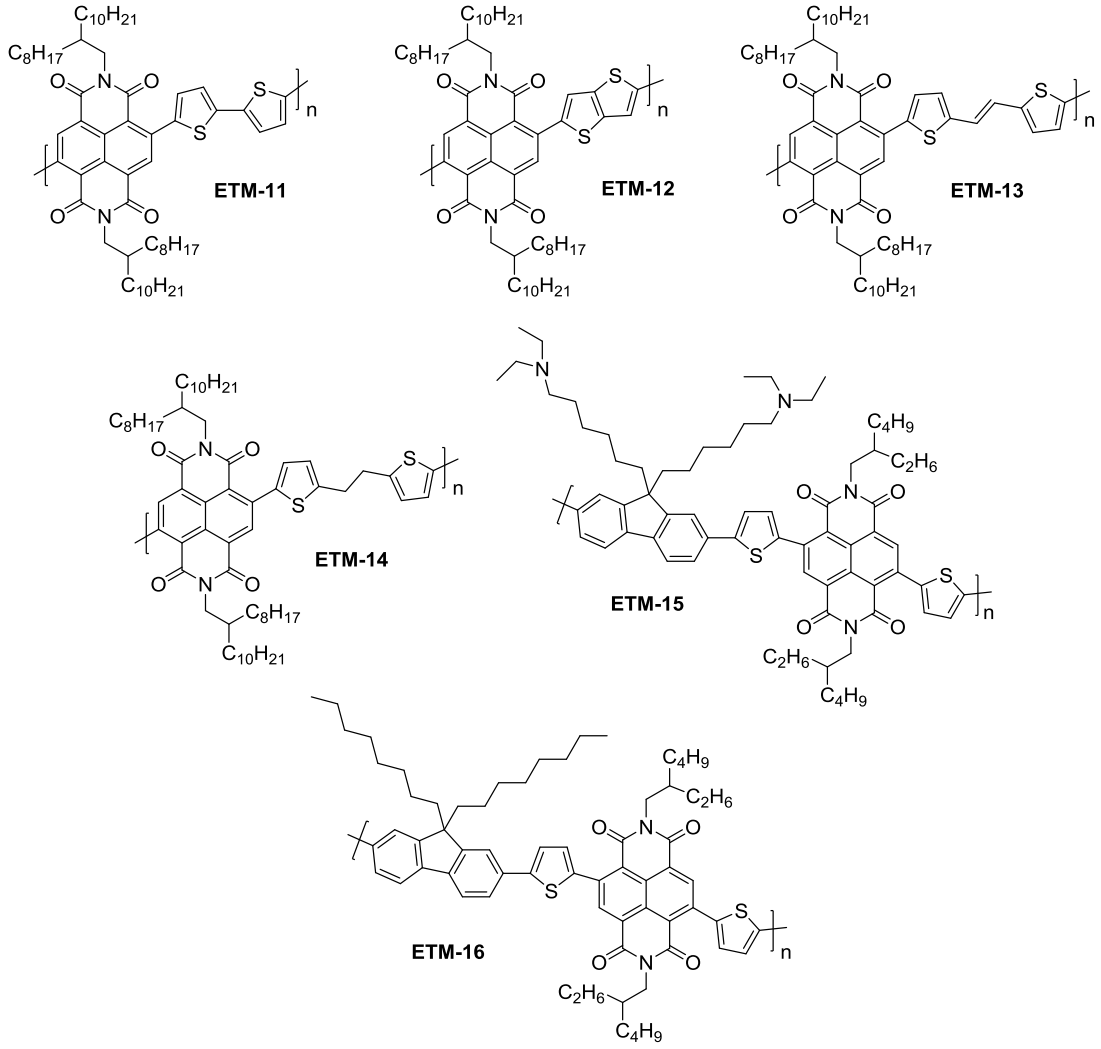

Figure 61. Chemical structure of polymers containing naphthalene diimides in their backbone.

In 2015, Wang, Ma and co-workers introduced for the first time *n*-type polymers as ETMs in PSCs. They investigated the performance of three different NDI-based polymers (**ETM-11**, **ETM-12** and **ETM-13**) by using the same inverted architecture (ITO/PEDOT:PSS/$CH_3NH_3PbI_3$-xCl_x/Polymer/ZnO/Al).[246] With **ETM-11**, which is known as N2200, an efficiency of 8.2% was obtained, which was comparable (at that time) with reference devices fabricated with $PC_{61}BM$. The other two polymers **ETM-12** (known as PNDI2OD-TT) and **ETM-13** (known as PNVT-8) achieved an efficiency of 6.1 and 7.1%, respectively. Although both polymers (**ETM-12** and **ETM-13**)

displayed LUMO levels more aligned with that of the perovskite, which led to higher V_{OC}, the low FFs of the devices generated lower PCEs compared to that of polymer **ETM-11**. One year later, Loi and co-workers compared **ETM-11** with **ETM-14**, revealing the effects of co-units in NDI polymers.[247] At that time, **ETM-11** achieved an efficiency of 10.8% when using as ETM in an ITO/PEDOT:PSS/$CH_3NH_3PbI_{3-x}Cl_x$/**ETM-11**/Al architecture, while when **ETM-14** was evaluated under the same conditions 0.18% in efficiency was obtained. The ethylene unit in the backbone of **ETM-14** reduces the conjugation length and consequently, the electron mobility of **ETM-14** is three order of magnitude lower than that of polymer **ETM-11**. Therefore, electrons are accumulated and trapped at the perovskite/**ETM-14** interface, leading to high rate of recombination, which would explain the low PCE value of **ETM-14**-based device. Around the same time, Wang, Huang and co-workers used **ETM-15** to fabricate inverted PSCs and a PCE of 16.7% in ITO/PEDOT:PSS/$CH_3NH_3PbI_{3-x}Cl_x$/**ETM-15**/Ag-based devices was achieved. [248] The backbone of polymer **ETM-15** was composed of a NDI-based acceptor moiety, a fluorene-based donor molecule with amine functional groups to its side chain, and a thiophene spacer. Within this report, other polymer (**ETM-16**) analogues to **ETM-15** was employed by using the above-mentioned device architecture. **ETM-16**-based device showed nearly no photovoltaic performance (PCE: 0.1%). Taking into account that the only difference between **ETM-15** and **ETM-16** is the presence of amine groups in the fluorene unit of **ETM-15**, it was demonstrated that in this case, the amino functionalization is critical. In fact, it was proven that the lone pair at the nitrogen atom helps to passivate trap states at the surface and GBs of the perovskite crystals, facilitating the electron-extraction properties and reducing recombination, leading to a higher PCE as well as devices with negligible hysteresis.

4.2 Objectives

Polymers appear to be very good candidates for their incorporation as ETMs in PSCs. These materials display very good film-forming ability and their properties can be tuned through suitable molecular engineering. Thus, their LUMO or hydrophobicity can be improved in order to obtain efficient and stable PSCs

In this regard, the **main objective** of the current chapter is the development of new organic semiconductors that meet the requirements to be used as ETMs in PSCs. In order to achieve this target, other more specific points have been established:

- Design and synthesis of new polymeric ETMs for application in PSCs. The aim is the preparation of a series of novel polymers based on the NDI core. The structures of these polymers have been studied using NMR and mass spectrometry while molecular mass distributions have been studied by SEC.
- Characterization of the new polymers by thermal, optical and electrochemical techniques in order to evaluate their properties. In this regard, the new polymers should have optimal LUMO energy levels in order to warrant electron transport, while maintaining low visible absorption, as their function in the device is ensuring good electronic transport from the perovskite to the electrode and not absorbing light. Moreover, polymers should have enough solubility for film formation as well as high thermal stability.
- A series of NDI-based small molecules bearing identical fragments to those of polymers has also been prepared for comparison purposes. The charge transporting properties of these molecules have been investigated by means of time-resolved microwave conductivity. Moreover, the thermal and optoelectronic properties of the three small molecules have also been studied.

4.3 Results and Discussion

4.3.1 Design of Novel NDI-Based Polymers

The chemical structures of the synthesized polymers **P9**-**P11** are displayed in Figure 62.

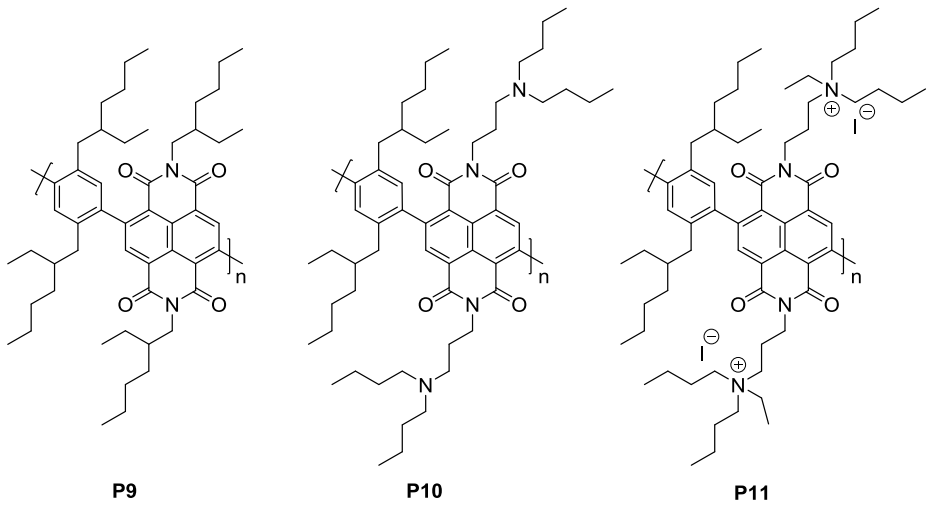

Figure 62. Chemical structures of polymers **P9**, **P10** and **P11.**

The backbone of polymers **P9**-**P11** composes a benzene unit in combination with different NDI-based moieties, which, as above-mentioned, are attractive candidates for using them as ETMs in PSCs.[249] On the other hand, the benzene unit connected to the 2,6-positions of the NDI core should allow for a more extended conjugation than bonding via the sterically congested NDI positions. Furthermore, to ensure sufficiently high solubility for device fabrication and good film formation, branched alkyl chains (2-ethylhexyl) were introduced in that benzene unit.

Polymers **P9**, **P10** and **P11** hold an alkyl, amino or ammonium-functionalized side chains at the imide position of the key NDI core, respectively. It has been proven that both amino or quaternary ammonium halides can effectively passivate trap states in perovskites, which reduce charge recombination and improve charge extraction at the perovskite/ETM interface.[248,250] Moreover, a report showed that both tertiary and quaternary ammonium groups improve the conductivity of polymeric *n*-type organic semiconductors.[251] Therefore, it is expected an increase on the conductivity of polymers **P10** and **P11** compared to that of polymer **P9**. To confirm this hypothesis we

synthesized three NDI-based model compounds bearing the same fragments than those of the NDIs present in polymers **P9**-**P11** to study the variation on the conductivity. We envisaged that polymers **P9**-**P11** would follow the same variation on the conductivity than these model compounds or even better as they contain multiple amino or ammonium fragments.

4.3.1.1 Synthesis of Model Compounds MC1-MC3

In order to study the effect of the tertiary amino (in polymer **P10**) and ammonium (in polymer **P11**) groups on the conductivity and mobility of the polymers, we designed and synthesized three NDI-based model compounds (**MC1**-**MC3**) (Figure 63).

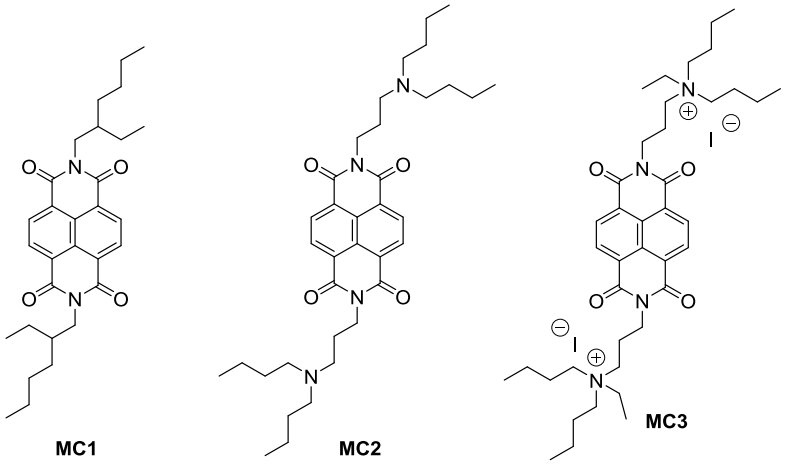

Figure 63. Chemical structures of model compounds **MC1**-**MC3**.

The synthetic route to NDI derivatives **MC1**-**MC3** is shown in Scheme 13, and all the experimental details can be found in the experimental section of this thesis. When the commercially-available 1,4,4,8-naphthalenetetracarboxylic dianhydride (NDA) was treated with 2-ehtylhexlamine or 3-(dibutylamino)propylamine in DMF at 140 ºC using microwave irradiation, **MC1** and **MC2**, were obtained, respectively. Both compounds were soluble in common solvents as chloroform, DCM, MeOH or hexane. However, the solubility of compound **MC1** in DMF was limited and was insoluble in DMSO, while compound **MC2** was soluble in both DMF and DMSO.

Molecule **MC3** was synthesized by treating **MC2** with iodoethane in CH_3CN at room temperature in the absence of light for 5 days. This compound had limited

solubility in DCM, chloroform and MEOH and it was insoluble in hexane. On the other hand, it was soluble in DMSO and DMF and it presented some solubility in water.

All compound **MC1**-**MC3** were characterized by ^{1}H NMR, ^{13}C NMR and mass spectrometry.

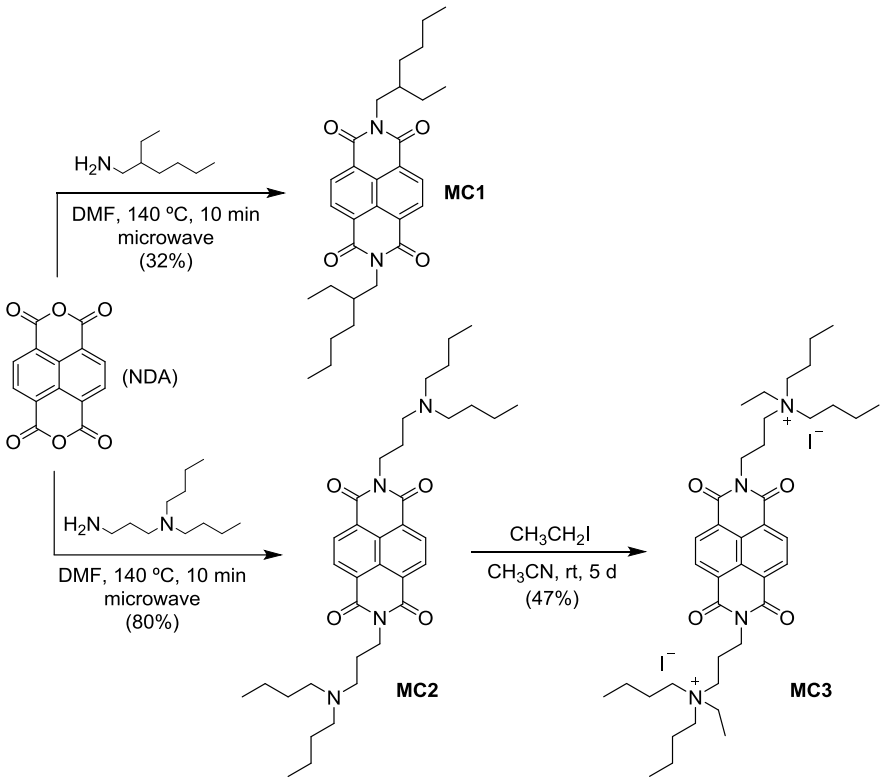

Scheme 13. Synthetic routes of the model compounds **MC1**-**MC3**.

4.3.1.2 Optical, Electrochemical and Charge Transport Properties of Model Compounds MC1-MC3

a) Optical properties

The optical properties of the model compounds were inspected by means of UV-vis absorption. Figure 64A shows the absorption spectra of the NDI derivatives **MC1**, **MC2** and **MC3** recorded in DCM. As can be seen, all the spectra feature similar patterns showing that the imide substituents of the NDI derivatives had little effect on their absorption properties. In this regard, each compound showed two intense absorption bands below 400 nm attributed to the π-π* transitions (Table 13).[252] Moreover, the E_g values of NDI-derivatives were estimated from the absorption onset of the longest absorption wavelength with values of 3.19 eV for **MC1** and **MC2** and 3.14 eV for **MC3**.

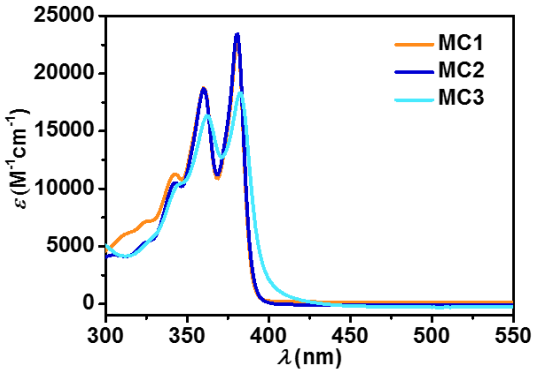

Figure 64. Absorption spectra of **MC1-MC3** in DCM.

Compound	λ_{abs} (nm)	$\mathcal{E}$ ($M^{-1}cm^{-1}$)	λ_{onset} (nm)	E_g (eV)
MC1	360	19072	389	3.19
	381	23656		
MC2	360	18802	389	3.19
	381	23480		
MC3	362	15425	394	3.14
	382	17424		

Table 13. Optical properties of compounds **MC1-MC3**.

b) Electrochemical properties

The electrochemical properties of the model compounds were investigated by CV, measured in a 0.1 M solution of TBAHFP in anhydrous DCM (Figure 65). Their E_{LUMO} values (Table 14) were obtained from the onset potential of the first reduction (E_{onset}^{Red1}) during CV measurements using the Fc/Fc^+ redox couple as the internal standard. Therefore, the E_{LUMO} is calculated according to the equation 20:

$$E_{LUMO}\ (eV) = -4.8 - E_{onset}^{Red1}. \qquad (20)$$

All three compounds **MC1-MC3** undergone two reversible reduction processes, which are typical for the NDI derivatives (Figure 65). These two characteristic NDI reduction waves indicate initial radical anion and subsequent dianion formation.[253] The E_{LUMO} values for **MC1**, **MC2** and **MC3** were estimated to be -3.91, -3.87 and -4.12 eV, respectively, according to their E_{onset}^{Red1} values at -0.89, -0.93 and -0.68 V vs Fc/Fc^+, respectively. The low E_{LUMO} value for molecule **MC3** could be explained due to anion π-interactions between the electron deficient aromatic NDI core and the I anions.[254,255] In Figure 65 is shown that **MC3** with a pendant ammonium group

suffered two oxidation processes, which were non-reversible, while **MC2** with a pendant amino group did not exhibit any oxidation. This effect could be explained by the lone pair electrons on the nitrogen atom being prone to transfer onto the electron-deficient NDIs and leading to the formation of charge transfer complexes, which was also observed in previous reports.[251,256]

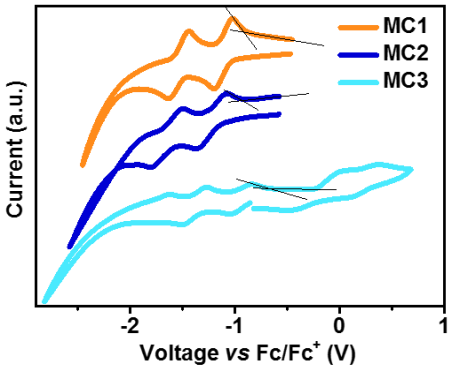

Figure 65. Cyclic voltammograms of model compounds **MC1-MC3** in DCM /TBAHFP (0.1 M) at a scan rate of 100 mV s^{-1}.

Moreover, the E_{HOMO} values of the model compounds (estimated from the difference between their E_{LUMO} and E_g values) were -7.10, -7.06 and -7.26 eV for **MC1**, **MC2** and **MC3**, respectively.

Compound	$E_{1/2}^{Red1}$(V)	$E_{1/2}^{Red2}$(V)	E_{onset}^{Red1} (V)	E_{HOMO} (eV)	E_{LUMO} (eV)
MC1	-1.11	-1.54	-0.89	-7.10	-3.91
MC2	-1.22	-1.64	-0.93	-7.06	-3.87
MC3	-0.94	-1.39	-0.68	-7.26	-4.12

Table 14. Electrochemical properties and energy levels of compounds **MC1-MC3**.

c) Charge transport properties

The intrinsic charge-transport properties of molecules **MC1-MC3** were explored by flash-photolysis time-resolved microwave conductivity (FP-TRMC) by which is possible to estimate the pseudo-photoconductivity ($\varphi\Sigma\mu$), where φ is the quantum yield and $\Sigma\mu$ is the sum of the hole and electron mobilities (Figure 66).[257] The measurements were carried out in collaboration with Prof. Seki at Kyoto University (Japan).

This technique is based on the measurement of the change of the microwave power (due to charge carriers generated by a laser pulse) reflected by a sample. The temporal decay of the conductivity (i.e. microwave absorbance) reflects the lifetime of the photogenerated carriers and the relative change of the reflected microwave power can be related to a variation of the sample conductivity.[258] In order to carry out the measurements, two methods were used for the deposition of the NDI derivatives (**MC1**-**MC3**): dropcasting and vapour deposition. In both cases, it was demonstrated an increase on the pseudo-photoconductivity when alkyl chains (**MC1**) were substituted by tertiary (**MC2**) or ammonium (**MC3**) chains (Figure 66).

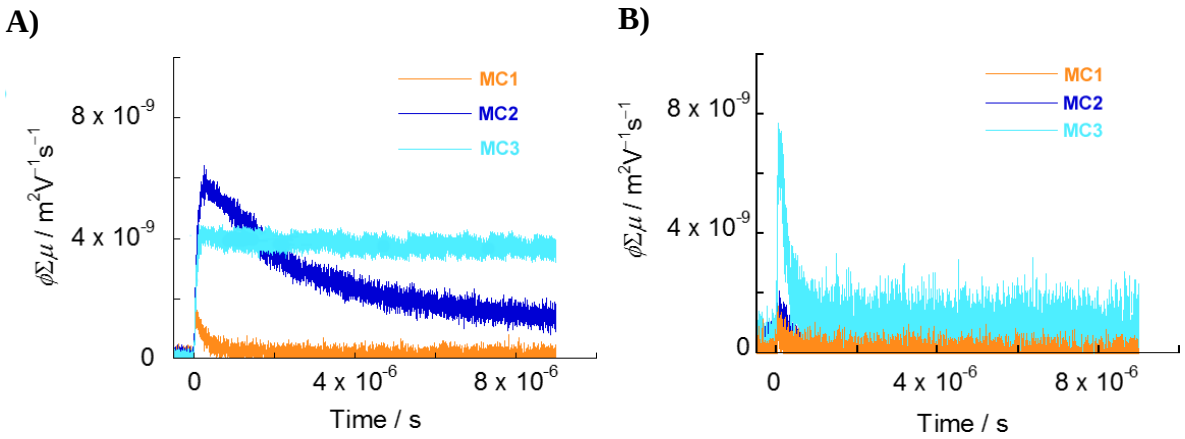

Figure 66. Kinetic traces of conductivity transients observed for **MC1**-**MC3** drop casted (A) or vapor deposited films (B) upon exposure to 355 nm.

The results depicted in Table 15 showed a maximum $\varphi\Sigma\mu$ ($\varphi\Sigma\mu_{max}$) value of 5.80 x 10^{-9} m^2 V^{-1} s^{-1} from the **MC2**-sample, while the $\varphi\Sigma\mu_{max}$ value in case of **MC1** was lower (1.06 x 10^{-9} m^2 V^{-1} s^{-1}) and slightly lower for model compound **MC3** (4.16 x 10^{-9} m^2 V^{-1} s^{-1}). In case of vapor deposited films, the highest $\varphi\Sigma\mu_{max}$ value came from the ammonium-functionalized molecule **MC3** (6. 70 x 10^{-9} m^2 V^{-1} s^{-1}), followed by **MC2** (1.20 x 10^{-9} m^2 V^{-1} s^{-1}) and **MC1** (0.93 x 10^{-9} m^2 V^{-1} s^{-1}).

Compound	$\phi\Sigma\mu_{max}$ (10^{-9} m^2 V^{-1} s^{-1}) dropcasting	$\phi\Sigma\mu_{max}$ (10^{-9} m^2 V^{-1} s^{-1}) vapor deposition
MC1	1.06	0.93
MC2	5.80	1.20
MC3	4.16	6.70

Table 15. Observed pseudo-photoconductivity ($\varphi\Sigma\mu$) values for the series of compounds **MC1**-**MC3** under 355 nm excitation.

These results illustrate an increase in the charge transporting properties of **MC2** and **MC3** compared with **MC1**, due to the presence of the tertiary and quaternary ammonium groups, which improve the conductivity of *n*-type organic semiconductors.[251]

4.3.2 Synthesis of NDI-Based Polymers P9-P11

4.3.2.1 Synthesis of Functionalized Monomers

In order to prepare polymers **P9**-**P11**, it was necessary to prepare functionalized monomers **M8**-**M10** in a previous stage (Figure 67). These monomers enable the use of Pd-catalyzed *Suzuki* cross coupling reaction to achieve a suitable polymerization.

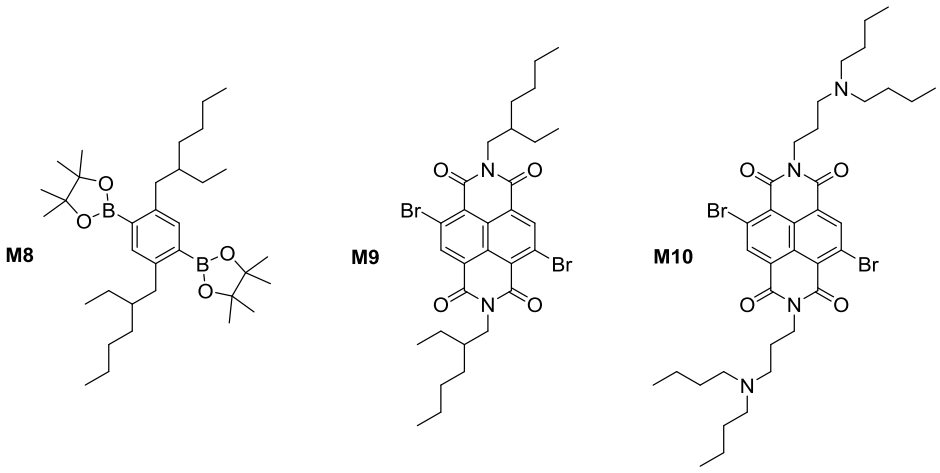

Figure 67. Chemical structures of monomers **M8**-**M10**.

The synthetic strategy to prepare monomer **M8** is shown in Scheme 14. First, the *Kumada* coupling of 3,4-dibromobenzene with 2-(ethylhexyl)magnesiumbromide (RMgBr) provided 1,4-bis(2-ethylhexyl)benzene (**12**). The resulting compound **12** was brominated leading to compound **13**, which after a *Miyaura* borylation gave monomer **M8** in high yield.

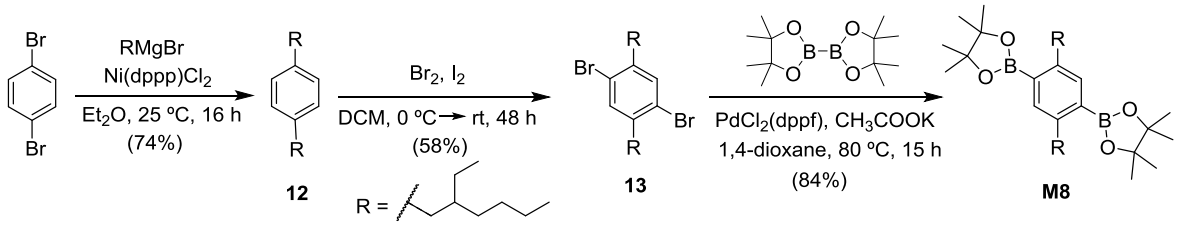

Scheme 14. Synthetic route to monomer **M8**.

In case of monomers **M9** and **M10**, the preparation of intermediate **14** was necessary, as shown in Scheme 15. The synthesis of **14** was carried out following a reported procedure.[259] The reaction between NDA and 1,3-dibromo-5,5-dimethylhydantoin (DBDMH) in H_2SO_4 gave intermediate **14** in 89% yield (Scheme 15). Then, the imidation of compound **14** with 2-ethylhexylamine or 3-(dibutylamino)propylamine in acetic acid (AcOH) led to monomers **M9** and **M10**, respectively (Scheme 15).

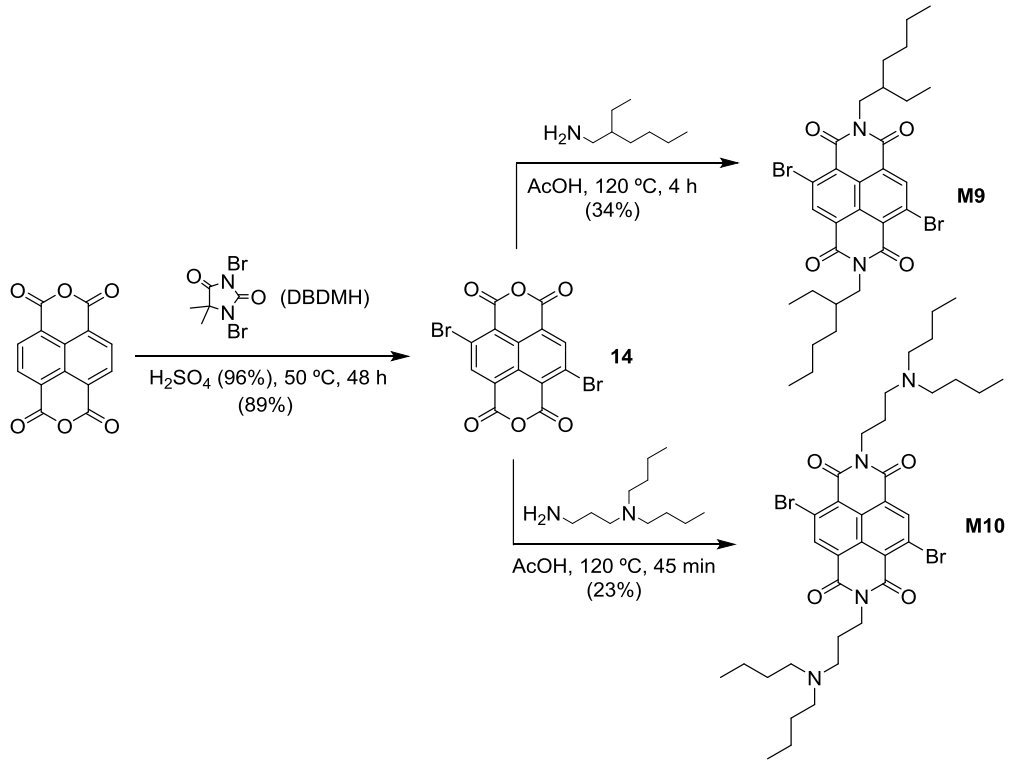

Scheme 15. Synthetic pathway for the preparation of monomers **M9** and **M10**.

4.3.2.2 Synthesis of Polymers P9-P11

The synthesis of polymer **P9** was performed by Pd-catalyzed *Suzuki* coupling copolymerization of the corresponding diboronic ester monomer **M8** with the NDI-based monomer **M9** in THF using $NaHCO_3$ as base (Scheme 16).

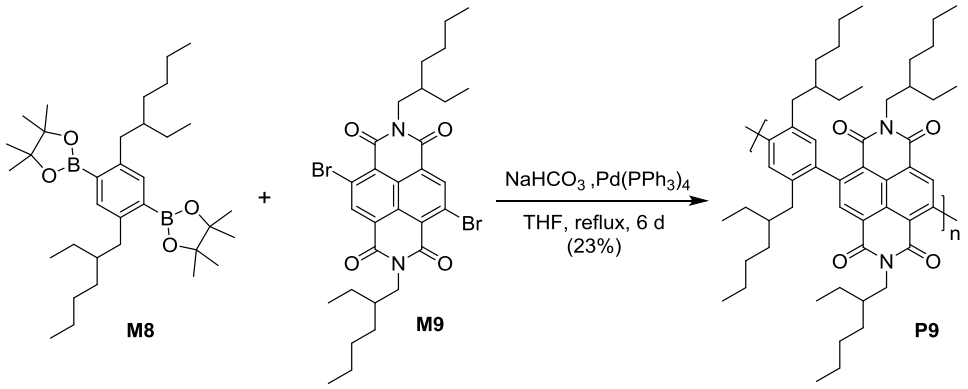

Scheme 16. Synthesis of polymer **P9**.

The resulting polymer was purified by *Soxhlet* extraction in MeOH, CH_3CN and acetone giving **P9** in moderate yield. The composition and chemical structure of **P9** was confirmed by ^{1}H NMR and MALDI-TOF spectrometry. The ^{1}H NMR spectrum revealed the presence of the polymer, exhibiting signals at 8.9 and 7.1 ppm for the protons of the NDI core (pink circle) and the benzene ring (purple circle), respectively (Figure 68). It can also be observed, the characteristic signal of the CH_2 protons present at the side chains of the NDI unit at 4.1 ppm (blue circle) and in between 2.7 and 2.2 ppm for that of the benzene unit (green circle). Moreover, a set of aliphatic signals belonging to the alkyl side fragments can be appreciated between 2.0 and 0.5 ppm.

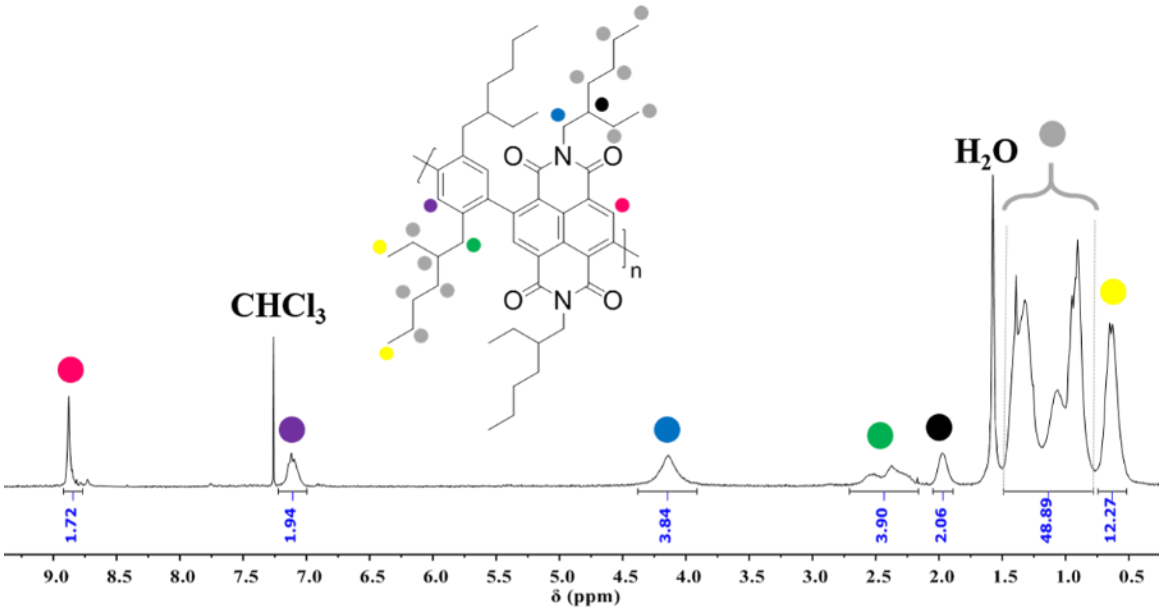

Figure 68. ^{1}H NMR (300 MHz, $CDCl_3$, 298 K) spectrum of polymer **P9**.

MALDI-TOF spectrum of polymer **P9** showed a series of peaks in which the peaks differ from each other by a value which corresponds to the building block

($C_{52}H_{72}N_2O_4$ $[M]^+$: 788.548) of **P9** (Figure 69). This observation, in addition to the above mentioned findings observed in the NMR, further confirm the structural identity of **P9**.

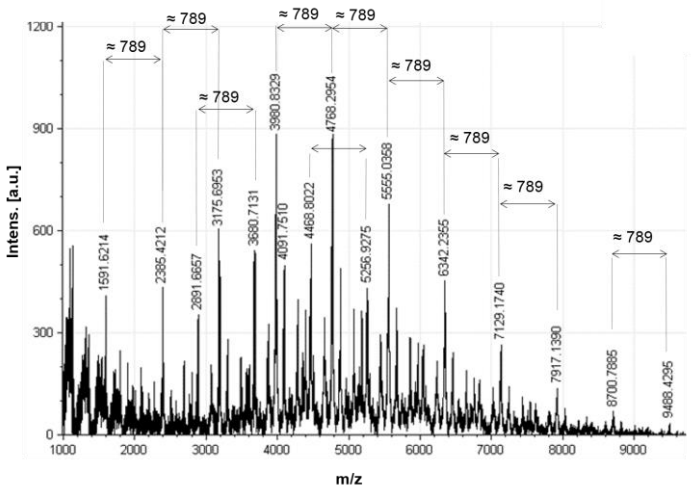

Figure 69. MALDI-TOF of polymer **P9**.

Polymer **P10** was synthesized by *Suzuki* copolymerization of monomer **M8** with monomer **M10** using the same procedure described for polymer **P9** (Scheme 17).

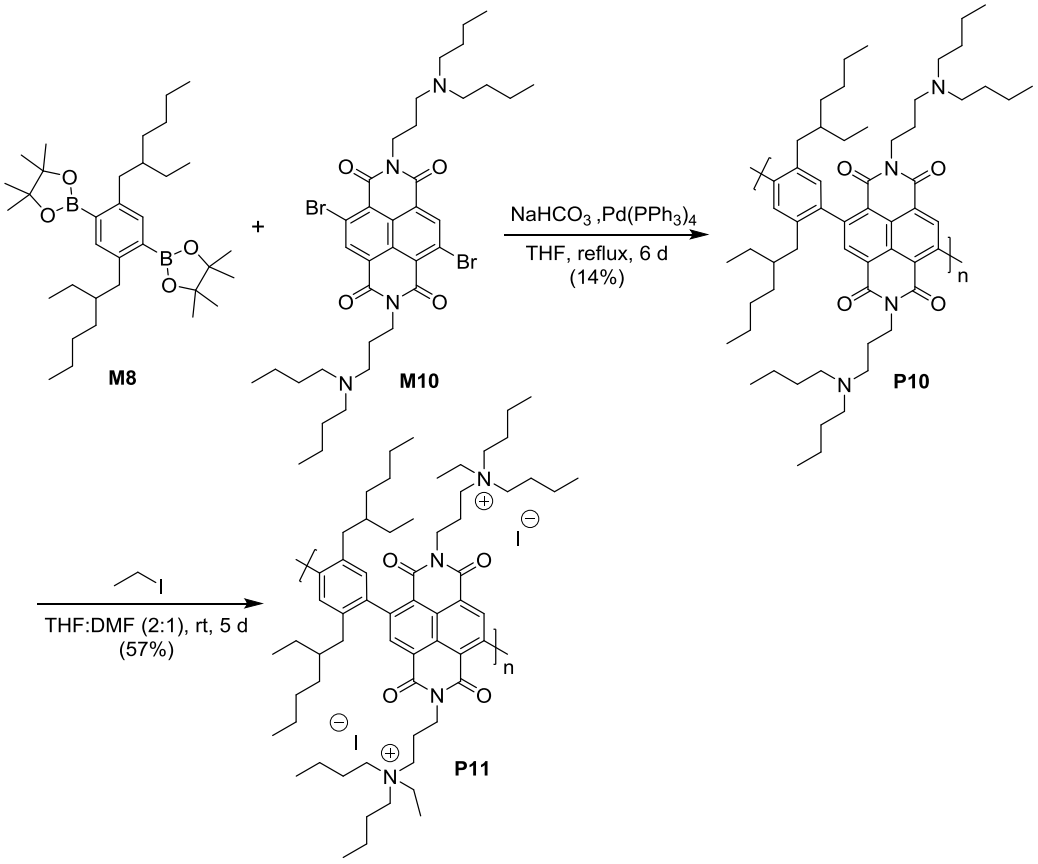

Scheme 17. Synthesis of polymers **P10** and **P11**.

In the case of polymer **P11**, it was obtained by quaternizing the precursor polymer **P10** with an excess of iodoethane in a mixture of DMF:THF solution at room temperature in darkness for 5 days (Scheme 17).

As in polymer **P9**, the chemical structure of both polymers **P10** and **P11** were confirmed by ^{1}H NMR spectroscopy, where all the signals related with the presence of both polymers can be seen (see experimental part for more details). In MALDI-TOF spectrum, it was possible to find peaks which differ from each other by a value that corresponds to the building block ($C_{58}H_{86}N_4O_4$ $[M]^+$: 902.664) of **P10** (see Figure 80, experimental part). Polymer **P11** could not be analyzed by MALDI-TOF, most likely due to the difficulty of polycationic polymers to be ionized.[260]

Figure 70 displays the ^{1}H NMR spectra of polymers **P10** and **P11**. It can be observed how the signal between 2.20-2.70 ppm (highlighted in blue) attributed to the hydrogen atoms closer to the amine in polymer **P10**, are shifted between 2.80-3.74 ppm in polymer **P11**, due to the deshielding effect produced by the protonated amine. Moreover, in that region it appeared other signal, which is assigned to the proton close to the quaternized amine (-NC<u>H</u>$_2$CH$_3$) in polymer **P11**. These are evidences of the conversion of polymer **P10** into polymer **P11**.

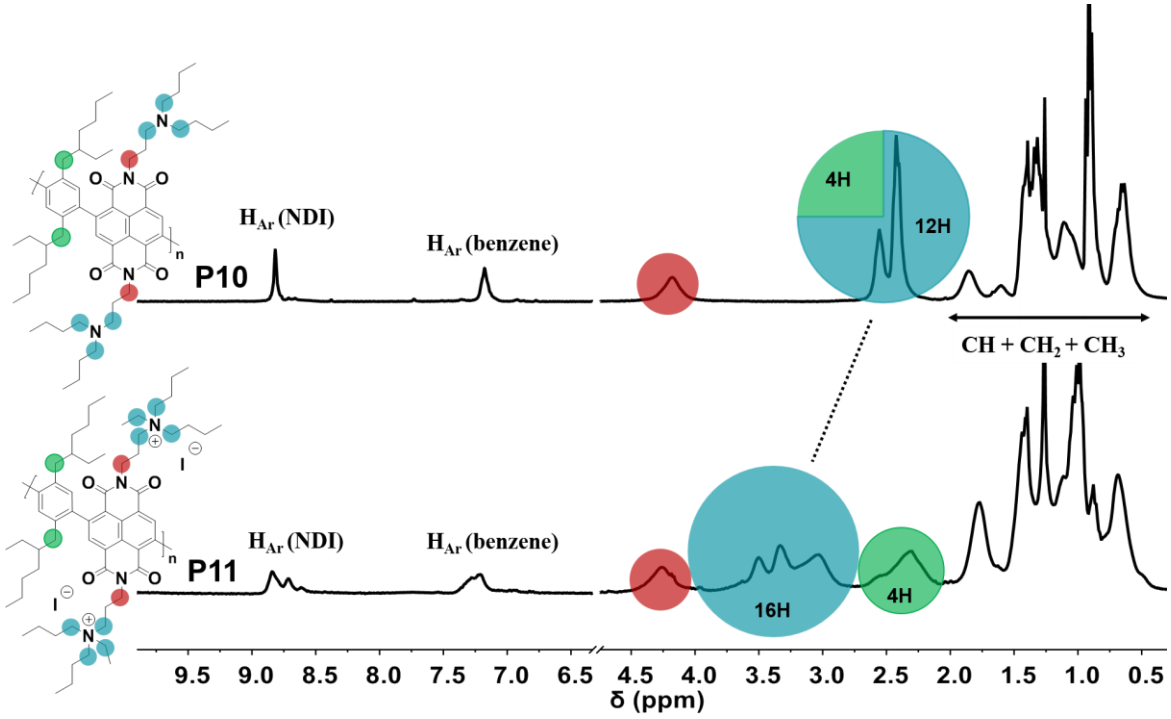

Figure 70. ^{1}H NMR spectra (300 MHz, CD_2Cl_2, 298 K) of polymers **P10** (top) and **P11** (bottom).

The molecular weights of polymers **P9** and **P10** were estimated by SEC analysis in THF compared to a polystyrene standard (Table 16). Both copolymers showed M_n values of 6405 and 4350 g mol^{-1}, leading to X_n values of 8 and 5 for **P9** and **P10**, respectively. These values were comparable to those obtained for other NDI-based polymers described in literature.[253,261–264] In case of the quaternized polymer **P11**, it was not possible to measure its molecular weight by SEC since it is not soluble in THF. However, it is safe to assume that polymer **P11** would have a molecular weight of the same order as that of its neutral precursor **P10**. This assumption is based on the process used to obtain **P11**, which only implies the use of iodoethane without resorting to further polymerization processes.

Polymer	M_n (g mol^{-1})	M_w (g mol^{-1})	X_n	PDI
P9	6405	10694	8	1.67
P10	4350	6953	5	1.60

Table 16. Molecular weights of polymers **P9** and **P10**.

4.3.3 Thermal, Optical and Electrochemical Properties

a) Thermal properties

The thermal behaviour of copolymers **P9-P11** was evaluated by TGA and DSC analysis. Figure 71A shows the thermograms of these copolymers at a heating rate of 10 °C min^{-1} under nitrogen atmosphere. As depicted in Table 17, polymer **P9** showed a T_d at 410 ºC while polymers **P10** and **P11** exhibited T_d values at 240 and 188 ºC, respectively. The main decomposition of copolymer **P9** occurred when the alkyl chains began to cleave, whereas for copolymer **P10**, the main decomposition process could be related to the loss of the amino groups in the polymer. In case of polymer **P11**, the first mass loss was attributed to the loss of the ethyl iodide groups, followed by the loss of the amino groups in the polymer. Thereafter, both **P10** and **P11** underwent the second major degradation process owing to the split of the alkyl chains as in polymer **P9**. This trend in the thermal properties was also observed in other conjugated polymers with terminal amino or ammonium side groups.[251,265,266] All polymers exhibited weight loss before decomposition, which may be attributed to the loss of solvent traces.

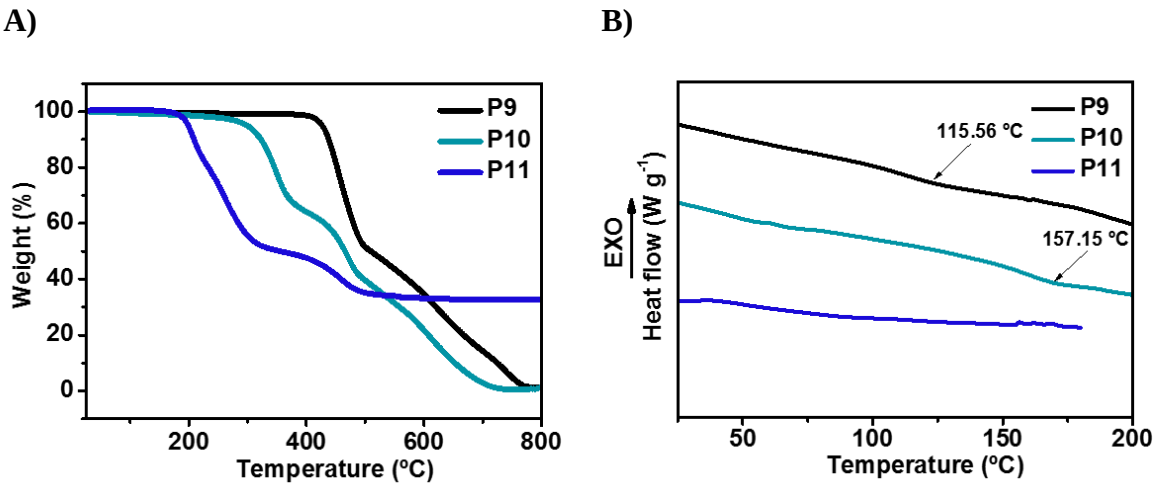

Figure 71. A) Thermogravimetric heating curves of polymers **P9**-**P11** (heating rate 10 °C min^{-1}). B) Differential scanning calorimetry second heating curves for polymers **P9**-**P11** (heating rate 20 °C min^{-1}).

DSC measurements of the investigated polymers **P9** and **P10** revealed their amorphous nature, showing T_g values at 115.26 and 157.15 ºC, respectively. On the contrary, polymer **P11** did not show any thermal feature in the second heating cycle over the temperature range of 25-180 ºC (Figure 71B, Table 17).

Polymer	T_d (°C)[a]	T_g (°C) [b]
P9	410.30	115.26
P10	240.20	157.15
P11	188.34	-

Table 17. Thermal properties of polymers **P9**-**P11**. [a] Decomposition temperature determined from TGA (2 % weight loss). [b] Glass transition temperature determined from DSC (second heating curve).

b) Optical properties

The absorption spectra of polymers **P9-P11** in DCM are depicted in Figure 72, with the relevant data summarized in Table 18. Here, it was confirmed that these polymers displayed very low absorption in the visible range (400-700 nm) which was favourable for their application in perovskite-based devices.

All three copolymers exhibited a similar absorption behaviour with four distinct absorption bands consisting of three sharp ones at the high-energy region (249-380 nm) and a broader one at the low-energy region (400-520 nm). The former bands can be

assigned to π-π* transitions of the backbones while the latter are related to a charge transfer process.

The absorption band centred in between 249 and 253 nm could be assigned to π- π* transitions of the benzene unit. This band was the most intense with $\mathcal{E}$ values at 42996, 52204 and 48462 M^{-1} cm^{-1}, for polymers **P9**, **P10** and **P11**, respectively. The other two absorption bands at the high-energy region with a maximum at 359 and 379 nm (378 nm for **P10**) are characteristics of π- π* transitions of the NDI core, similar to those presented in model compounds **MC1**-**MC3**. Finally, the polymers exhibited a long-wavelength absorption band with maximum values at 438, 444 and 447 nm, for **P9**, **P10** and **P11**, respectively. This band, which was relatively less intense than the other three could be attributed to an intramolecular charge transfer (ICT) between the electron donor (benzene) and the NDI electron-deficient unit, which was in accordance with previously reported NDI-donor copolymers.[267–270] The ICT absorption peak of the ammonium-functionalized copolymer **P11** was slightly red-shifted compared with that of polymer **P9** and **P10**, which could be due to the electrostatic perturbation by ions in close proximity to the optically segment, solvatochromic effects arising from the polar solvent, or multichain aggregation.[251]

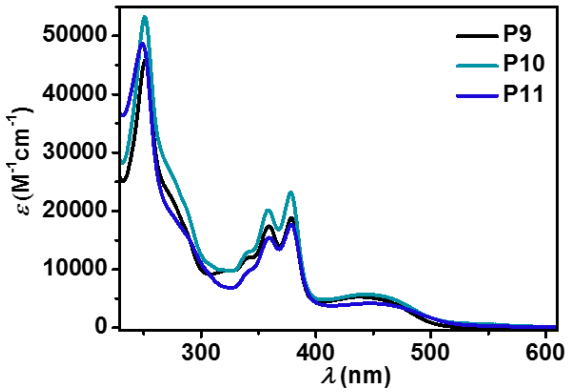

Figure 72.Absorption spectra of polymers **P9**-**P11** in DCM.

The E_g values of polymers **P9**, **P10** and **P11** were estimated to be 2.44, 2.41 and 2.35 eV, respectively, according to their λ_{onset} values at 508, 514 and 528 nm (Table 18).

Polymer	λ_{abs} (nm)	$\mathcal{E}$ ($M^{-1}cm^{-1}$)	λ_{onset} (nm)	E_g (eV)
P9	253	42996	508	2.44
	359	16860		
	379	18336		
	438	5238		
P10	251	52204	514	2.41
	359	19580		
	378	22413		
	444	5640		
P11	249	48462	528	2.35
	359	15260		
	379	17478		
	447	4229		

Table 18. Optical properties of polymers **P9**-**P11**.

c) Electrochemical properties

The electrochemical characterization of NDI-based polymers **P9**-**P11** was carried out by CV measured in a 0.1 M solution of TBAHFP in anhydrous DCM. The voltammograms illustrate that all compounds are highly electron-deficient, consistent with the presence of the NDI moiety (Figure 73).

Their E_{LUMO} values (Table 19) were calculated according to equation 20, as it was explained for model compounds **MC1**-**MC3**.

As for model compounds **MC1**-**MC3**, polymers **P9**-**P11** showed two reversible reduction processes, due to the NDI core (Figure 73). The E_{LUMO} values for **P9**, **P10** and **P11** were estimated to be -3.88, -3.80 and -4.03 eV, respectively, according to their E_{onset}^{Red1} values at - 0.92, -1.0 and -0.77 V vs Fc/Fc^+, respectively. The E_{LUMO} value of polymer **P11** was lower than those of polymers **P9** and **P10**, which could be explained due to anion π-interactions between the NDI and the iodine anions, as it occurred in **MC3**. Moreover, polymer **P11** suffered two non-reversible oxidation processes, while polymer **P10** did not exhibit any oxidation (Figure 73B). This effect may be explained due to the existence of an electron transfer process from the nitrogen to the NDI core on polymer **P10**, as it was above mentioned.

With these E_{LUMO} values, these novel NDI-based polymers are perfect candidates to act as suitable ETMs in PSCs using triple cation perovskite (Figure 73C).

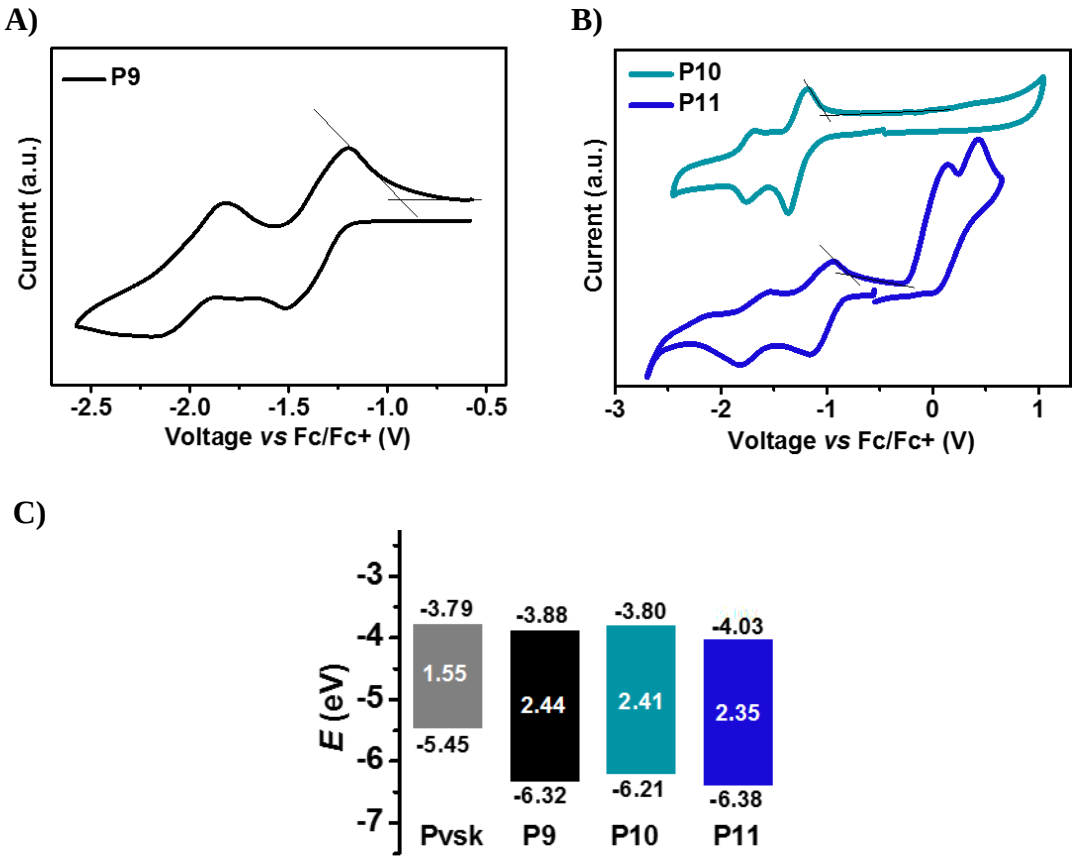

Figure 73. Cyclic voltammograms of A) polymer **P9** and B) polymers **P10-P11** in DCM /TBAHFP (0.1 M) at a scan rate of 100 mV s^{-1}. C) Energetic levels of polymers **P9-P11** and triple cation perovskite light absorber used in photovoltaic studies performed in chapters 2 and 3.

Moreover, the E_{HOMO} levels were estimated from the difference between E_{LUMO} and E_g of the polymers as -6.32, -6.21 and -6.38 eV for **P9**, **P10** and **P11**, respectively (Table 19). These low-lying E_{HOMO} levels indicate that the three polymers possess hole-blocking properties. Thus, these materials can behave as suitable filters towards electrons, while efficiently blocking holes, which is of primary importance in order to design innovative ETMs for PSCs.

Polymer	$E_{1/2}^{Red1}$(V)	$E_{1/2}^{Red2}$(V)	E_{onset}^{Red1} (V)	E_{HOMO} (eV)	E_{LUMO} (eV)
P9	-1.36	-1.68	-0.92	-6.32	-3.88
P10	-1.27	-1.72	-1.00	-6.21	-3.80
P11	-1.05	-1.67	-0.77	-6.38	-4.03

Table 19. Electrochemical properties and energy levels of polymers **P9-P11**.

4.4 Conclusions

In summary, three novel *n*-type NDI-based polymers (**P9**-**P11**) were designed, synthesized and fully characterized. The novel polymers meet the requirements to be used as ETMs in PSCs. In particular, the polymers showed suitable energy levels with low-lying LUMO levels of about -4 eV and HOMO levels around -6 eV, which would ensure electron extraction from the perovskite and hole-blocking functionality, respectively. Moreover, thermal analysis indicated that polymers were thermally stable with no phase transition under operation temperature of PSCs. All of them possessed good solubility providing a facile way to process ETLs.

Furthermore, three NDI-based small molecules (**MC1**-**MC3**), with similar structure to the NDI unit of the backbone of polymers **P9**-**P11**, were synthesized and fully characterized. The charge transporting properties of those small molecules were studied by FP-TRMC to estimate their pseudo-photoconductivity. Both the amino and iodine-quaternized ammonium groups in molecules **MC2** and **MC3** exhibited higher pseudo-conductivity compared to molecule **MC1**.

Polymers **P9**-**P11** display the same structural amino or ammonium fragments than model compounds **MC1**-**MC3**. Thus, in principle we could expect good charge transporting properties for these innovative polymers in addition to their excellent ETM characteristics. To confirm this trend, we are currently collaborating with Prof. Seki at Kyoto University (Japan) as well as working on the optimization of OFETs of **MC1-MC3** and **P9-P11.**

The next logical step would be the incorporation of these innovative NDI-based polymers as ETMs in PSCs. However, taking into account the amount of polymer necessary to carry out a complete photovoltaic study, the study on their charge transporting properties is of primary importance to guarantee a successful incorporation of these compounds in devices based on triple cation perovskites.

5. EXPERIMENTAL SECTION

5 EXPERIMENTAL SECTION

5.1 General Methods and Materials

All commercially available reagents and solvents were used as received without further purification. Anhydrous solvent was dried using a SPS purification system. Column chromatography was carried out using silica gel (40 to 60 µm, 60 Å) as stationary phase. Thin layer chromatography (TLC) was performed on precoated silica gel and observed under UV light.

5.1.1 Nuclear Magnetic Resonance Spectroscopy

The ^{1}H NMR, ^{13}C NMR and ^{19}F NMR spectra were taken on Bruker NMR spectrometers (300 MHz, 400 MHz and 500 MHz for ^{1}H NMR, 75 MHz, 100 MHz and 125 Hz for ^{13}C NMR and 376 MHz for ^{19}F NMR) at room temperature.

Coupling constants (J) are denoted in Hz and chemical shifts (δ) in ppm. Abbreviations of coupling patterns are as follows: s = singlet, d = doublet, t = triplet, m = multiplet, dd = doublet of doublets, td = triplet of doublets. The abbreviation used for indicating a quaternary C-atom is q.

5.1.2 Mass Spectrometry

MALDI-TOF: Matrix Assisted Laser Desorption Ionization (MALDI) experiments, coupled to a Time-of-flight (TOF) analyzer, were recorded on Bruker REFLEX spectrometer.

ESI-TOF: Electrospray ionization (ESI) measurements were carried out on HPLC Agilent 1200 Series system coupled to a hybrid quadrupole-time of flight (LC-QTOF) mass spectrometer Agilent 6520 from Agilent Technologies (Santa Clara, CA, USA).

5.1.3 Size Exclusion Chromatography

The molecular weight distribution of the polymers was determined by size exclusion chromatography (SEC, Waters). The setting consisted of a pump, a differential refractometer (Waters 2410) and three columns in series (Styragel HR2, HR4 and HR6; with a pore size from 10^2 to 10^6 Å). The analysis were performed at 35 ºC and THF was used as solvent at a flow rate of 1 mL min^{-1}. Calibration was relative to polystyrene standards. A series of polystyrene standards in the range of 580-3,848,000 g mol^{-1} were used to prepare a universal calibration curve.

5.1.4 Water Contact Angle Measurements

Water contact angles were measured in an OCA 20 instrument (Dataphysics). For contact angle measurements, distilled water droplets of 10 μL were placed on the surface of the films. The values given are an average of five measurements per film.

5.1.5 Thermal Analysis

The thermogravimetric analysis (TGA) were performed on a TA Q500 using a 10 °C min^{-1} heating rate under a nitrogen flow.

Differential scanning calorimetry (DSC) was performed on a DSC3$^+$ Mettler Toledo at a scan rate of 20 °C min^{-1} in the nitrogen atmosphere.

5.1.6 Absorption and Fluorescence Spectroscopy

Absorption measurements were recorded on a Perkin-Elmer Lambda 950 spectrometer. All the compounds were measured at various concentrations (10^{-5}-10^{-7} mol L^{-1}) to affirm linear behaviour. The measurements of films of compounds in chapter 3 were performed on samples that were spin-coated from the respective solvent onto a FTO/SnO_2 substrates. The optical band gap (E_g) was estimated from the onset of the absorption edge (λ_{onset}) in the longer wavelength region.

Emission measurements were recorded on a LS55 Perkin-Elmer Fluorescence spectrometer.

5.1.7 Cyclic Voltammetry

Cyclic voltammograms were carried out on a Princeton Applied Research Parstat 2273 in a 3-electrode single compartment cell with platinum disc working electrode, a platinum wire counter electrode and a silver wire pseudoreference electrode. For electrochemical measurements of polymers **P9**-**P11** a glassy carbon disc working electrode was used instead of using the platinum disc working electrode. All the potential values were reported versus the redox potential of the ferrocene/ferrocenium redox couple.

E_{HOMO} and E_{LUMO} values were obtained from the onset potentials of cyclic voltammetry measurements. The potential of Fc/Fc^+ is 0.2 V vs. the normal hydrogen electrode (NHE), which has an absolute potential of -4.6 eV vs. vacuum.[271] Therefore, the energy levels are $E_{HOMO/LUMO}$ (eV) = -4.8 – $E_{onset}^{Ox1/Red1}$ (as it was shown in equations 17 and 20) and the optical band gap $E_g = E_{LUMO} - E_{HOMO}$.

5.1.8 Time-Resolved Microwave Conductivity

Time resolved microwave conductivity (TRMC) experiments were conducted for the sample on a quartz plate using a third harmonic generator (THG; 355 nm) of a Nd:YAG laser (Continuum, Inc., Surelite II, 5-8 ns pulse duration, 10 Hz) as the excitation source (9.1×10^{15} photons cm^{-2} $pulse^{-1}$). The photoconductivity transient $\Delta\sigma$ was converted to the product of the quantum yield (φ) and the sum of the charge carrier mobilities, $\Sigma\mu$ ($\mu^+ + \mu^-$) by $\varphi\Sigma\mu = \Delta\sigma\ (eI_0F_{light})^{-1}$, where e and F_{light} are the unit charge of a single electron and the correction (or filling) factor, respectively.

5.1.9 Scanning Electron Microscopy

Scanning electron microscopy (SEM) was performed on a ZEISS Merlin HR-SEM. Scanning Probe Image Processor (SPIP) software was used for processing and

analysing the micrographs in order to obtain the mean area and mean diameter showed in chapter 3.

5.1.10 Atomic Force Microscopy

Atomic force microscopy (AFM) measurements were recorded on a Bruker Dimension ICON on a tapping mode.

5.1.11 X-Ray Diffraction

X-ray diffraction (XRD) patterns were obtained on a Bruker D8 Advance X-Ray diffractometer with Cu Kα (λ = 1.5418 Å) radiation.

5.2 Synthesis

5.2.1 Dopant-Free Hole-Transporting Polymers for PSCs

5.2.1.1 Synthesis of Precursors 1-8

Synthesis of 3,4-bis(2-ethylhexyl)-thiophene (1)[272]

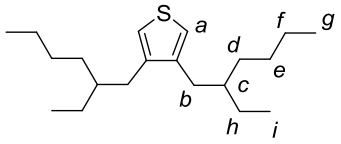

A procedure reported in the literature was adapted with some modifications. 2-Ethylhexyl bromide (2.95 mL, 16.5 mmol) dissolved in 5 mL of anhydrous diethyl ether (Et_2O) was added to a solution of magnesium turnings (602 mg, 24.8 mmol) in 5 mL of anhydrous Et_2O, containing one crystal of iodine, over a period of 30 min. After complete addition, the mixture was ultrasonicated at 40 °C under a nitrogen atmosphere for a further hour. The obtained (Grignard) solution was slowly added to a mixture of 3,4-dibromothiophene (1.00 g, 4.13 mmol), Ni(dppp)Cl_2 (65.0 mg, 120 μmol) in 10 mL of anhydrous Et_2O at 0 °C, together with 10 mL of Et_2O (to transfer the Grignard reagent completely). The reaction mixture was stirred for 16 h at room temperature under nitrogen atmosphere. Afterwards, an aqueous solution of HCl (1 M, 50.0 mL)

was added to the solution, which was previously chilled to 0 °C. The phases were separated and the aqueous phase was extracted with Et_2O (3 x 50 mL) .The combined organic phases were washed with water (2 x 100 mL) and finally with brine (1 x 100 mL). The organic phase was dried over Na_2SO_4, concentrated under reduced pressure and the resulting yellowish oil was purified by flash column chromatography using hexane as eluent to give compound **1** as colourless oil (959 mg, 76%). It was used directly in the next step without further purification.

^{1}H NMR (300 MHz, $CDCl_3$), δ (ppm): 6.85 (s, 2H, H_a), 2.44 (d, J = 7.1 Hz, 4H, H_b), 1.61-1.51 (2H, H_c), 1.41-1.17 (16H, $H_{d\text{-}f}$ + H_h), 0.94-0.80 (12H, H_g + H_i).

Synthesis of 1-(2-ethylhexyloxy)-4-iodobenzene (2)[161]

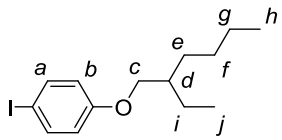

K_2CO_3 (3.86 g, 27.9 mmol) was added to a solution of 4-iodophenol (4.00 g, 18.2 mmol) and 2-ethylhexyl bromide (3.90 mL, 21.8 mmol) in 20 mL of DMF. The reaction mixture was stirred for 6 h at 130 °C. After cooling down, the suspension was filtered and the solvent removed under vacuum. The resulting residue was diluted with DCM (40 mL) and washed with water (3x 40 mL) and brine (1 x 40 mL). The organic phase was dried over anhydrous Na_2SO_4, concentrated under reduced pressure and purified by flash column chromatography using hexane as eluent yielding the target product as a colourless oil (5.00 g, 83%).

^{1}H NMR (300 MHz, CD_2Cl_2), δ (ppm): 7.58-7.51 (m, 2H, H_a), 6.72-6.68 (m, 2H, H_b), 3.81 (d, J = 5.7 Hz, 2H, H_c), 1.76-1.64 (m, 1H, H_d), 1.56-1.26 (8H, $H_{e\text{-}g}$ + H_i), 0.95-0.84 (6H, H_h + H_j).

Synthesis of 4-(2-ethylhexyloxy)-*N*,*N*-diphenylaniline (3)[162]

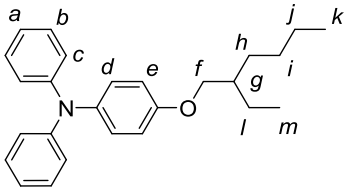

A procedure reported in the literature was adapted with some modifications.[162] 1-(2-Ethylhexyloxy)-4-iodobenzene (**2**, 1.50 g, 4.52 mmol) was introduced into a Schlenk flask, and three cycles of nitrogen-vacuum were then applied. Next, sodium *tert*-butoxide (1.18 g, 12.3 mmol), $Pd_2(dba)_3$ (37.5 mg, 0.04 mmol), tri-*tert*-butyl phosphine (1M in toluene, 410 µL, 410 µmol) and anhydrous toluene (25 mL) were added. After purged with nitrogen for 30 min, diphenylamine (696 mg, 4.11 mmol) was added and the mixture was stirred at 120 °C for 15 h. Afterwards, the reaction was allowed to cool down and 40 mL of water and 40 mL of chloroform were added. The aqueous phase was extracted with chloroform (2 x 40 mL) and the combined organic phases were washed with water (2 x 150 mL) and brine (1 x 150 mL). The organic phase was dried over anhydrous Na_2SO_4, concentrated under reduced pressure and purified by flash column chromatography using hexane:toluene (5:1) as eluent to afford **3** as a white solid (1.33 g, 87%).

^{1}H NMR (300 MHz, CD_2Cl_2), δ (ppm): 7.28-7.21 (4H, H_b), 7.11-7.04 (6H, H_c + H_d), 7.00-6.95 (2H, H_a), 6.92-6.87 (2H, H_e), 3.89 (d, J = 5.7 Hz, 2H, H_f), 1.84-1.72 (1H, H_g), 1.65-1.36 (8H, $H_{h\text{-}j}$ + H_l), 1.02-0.91 (6H, H_k + H_m).

Synthesis of triarylamine 4[163]

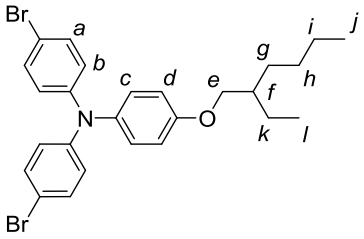

4-(2-Ethylhexyloxy)-*N*,*N*-diphenylaniline (**3**, 0.53 g, 1.42 mmol) was dissolved in 12 mL of a mixture of chloroform/AcOH (5:1) and degassed for 30 min with a nitrogen stream. After cooling the solution to -10 °C, NBS (250 mg, 2.98 mmol) was added in small portions under exclusion of light. The reaction mixture was stirred for 3.5 h at -10 °C and quenched with NaOH (1 M, 50 mL). The aqueous phase was extracted with DCM (2 x 50 mL) and the organic phase was washed with water (2 x 100 mL) and brine (1 x 100 mL), dried over anhydrous Na_2SO_4 and concentrated under reduced pressure. The resulting residue was purified through flash column

chromatography using petroleum ether (PE):DCM (10:1) as eluent to afford triarylamine **4** as a dark orange oil (660 mg, 87%).

^{1}H NMR (300 MHz, CD_2Cl_2), δ (ppm): 7.35-7.29 (m, 4H, H_a), 7.05-6.99 (m, 2H, H_c), 6.92-6.83 (m, 6H, H_b + H_d), 3.84 (d, J = 5.7 Hz, 2H, H_e), 178-1.66 (m, 1H, H_f), 1.56-1.30 (8H, $H_{g\text{-}i}$ + H_k), 0.96-0.85 (6H, H_j + H_l).

Synthesis of triarylamine 5[273]

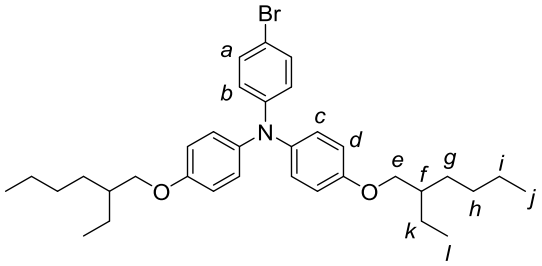

A procedure reported in the literature was adapted with some modifications.[273] 1-(2-Ethylhexyloxy)-4-iodobenzene (**2**, 1.00 g, 3.01 mmol) was introduced into a Schlenk flask and three cycles of argon-vacuum were applied. Next, 4-bromoaniline (172 mg, 1.00 mmol), KOH (651mg, 11.6 mmol) and anhydrous toluene (10 mL) were added and the flask was purged with argon for 30 min. Upon addition of copper (I) iodide (12.5 mg, 0.07 mmol) and 1,10-phenantroline (11.9 mg, 66.0 μmol) the mixture was refluxed for 20 h. Afterwards, the reaction was allowed to cool and the crude product was dissolved in 20 mL of DCM and washed with 20 mL of HCl (1 M). The aqueous phase was extracted with DCM (2 x 20 mL) and the combined organic phases were washed with brine (1 x 40 mL). The organic phase was dried over anhydrous Na_2SO_4, concentrated under reduced pressure and purified by flash column chromatography using PE:DCM (20:1→10:1) as eluent to afford **5** as an orangish solid (0.46 g, 80%).

^{1}H NMR (300 MHz, CD_2Cl_2), δ (ppm): 7.26-7.19 (m, 2H, H_a), 7.01 (d, J = 8.7 Hz, 4H, H_d), 6.87-6.80 (m, 4H, H_c), 6.75 (d, J = 8.7 Hz, 2H, H_b), 3.82 (d, J = 5.7 Hz, 4H, H_e), 1.77-1.64 (m, 2H, H_f) , 1.55-1.27 (16H, $H_{g\text{-}i}$ + H_k), 1.00-0.81 (12H, H_j + H_l).

Synthesis of triarylamine 6

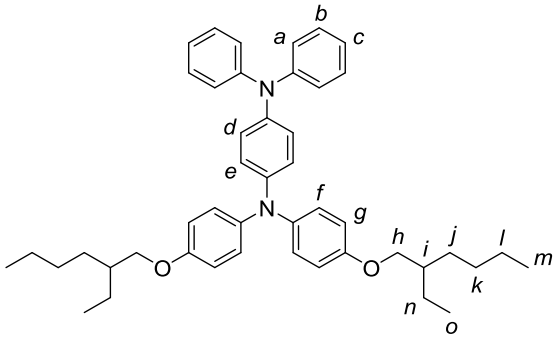

Compound **5** (2.20 g, 3.79 mmol) was added to a Schlenk flask and three cycles of argon-vacuum were then applied. Next tri-*tert*-butyl phosphine (1 M in toluene, 400 µL, 400 µmol) and sodium *tert*-butoxide (1.09 g, 11.4 mmol) were dissolved in dry toluene (18 mL) degassed with argon for 30 min. Upon addition of $Pd_2(dba)_3$ (36.9 g, 40.3 µmol), diphenylamine (614 mg, 3.79 mmol) was added and the mixture was refluxed over-night. Afterwards, the reaction was allowed to cool down and 20 mL of water and 20 mL of DCM were added to the crude product. The aqueous phase was extracted with DCM (2 x 20 mL) and the combined organic phases were washed with brine (1 x 40 mL). The organic phase was dried over anhydrous Na_2SO_4, concentrated under reduced pressure and purified by flash column chromatography using PE:DCM (10:1) as eluent to afford **6** as an orange-yellowish solid (2.17 g, 86%).

^{1}H NMR [300 MHz, $(CD_3)_2CO$)], δ (ppm): 7.29-7.21 (4H, H_b), 7.08-6.83 (18H, H_a + H_c + H_{d-g}), 3.89 (d, J = 5.6 Hz, 4H, H_h), 1.80-1.68 (m, 2H, H_i), 1.61-1.32 (16H, H_{j-l} + H_n), 1.02-0.88 (12H, H_m + H_o).

^{13}C NMR [(75 MHz, $(CD_3)_2CO$)], δ (ppm): 156.54 (q), 148.99 (q), 145.90 (q), 141.82 (q), 141.47 (q), 130.03 (CH), 127.10 (CH), 127.02 (CH), 123.86 (CH), 122.92 (CH), 122.66 (CH), 116.18 (CH), 71.25 (CH_2), 40.34 (CH), 31.32 (CH_2), 29.82 (CH_2, overlapping with the solvent signal), 24.60 (CH_2), 23.73 (CH_2), 14.37 (CH_3), 11.46 (CH_3).

MS (MALDI-TOF): calculated for $C_{46}H_{56}N_2O_2$ $[M]^+$: 668.434, found: 668.403.

Synthesis of bis(4-bromophenyl)amine (7)[165]

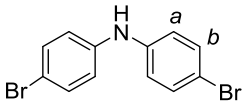

A solution of NBS (4.20 g, 23.6 mmol) in 20 mL of DMF was added dropwise to an ice-cooled solution of diphenylamine (2.00 g, 11.8 mmol) in 20 mL of DMF. Next, the mixture was stirred for 24 h at room temperature. Afterwards, 40 mL of water were added, and the precipitate was filtered and dried under vacuum affording the target product as a white solid (2.45 g, 63%).

^{1}H NMR (300 MHz, $CDCl_3$), δ (ppm): 7.40-7.32 (m, 4H, H_b), 6.96-6.89 (m, 4H, H_a), 6.04-5.34 (1H, N<u>H</u>).

Synthesis of triarylamine 8[166]

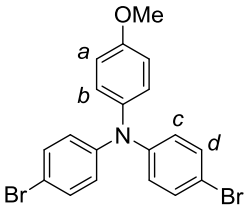

4-Iodoanisole (690 mg, 2.95 mmol) was added to a Schlenk flask and three cycles of argon-vacuum were then applied. Next, KOH (1.61 g, 28.7 mmol) and dry toluene (15 mL) were added. Afterwards, the reaction mixture was degassed with a stream of argon for 10 min before and after 1,10-phenanthroline (28.8 mg, 160 μmol) and copper (I) iodide (30.5 mg, 160 μmol) were added. Then, bis(4-bromophenyl)amine (**7**, 800 mg, 2.46 mmol) was added and the mixture was refluxed for 20 h. Afterwards, 20 mL of DCM and 20 mL of HCl (1 M) were added and the phases were separated. The aqueous phase was extracted with DCM (2 x 20 mL) and the combined organic phases were washed with water (2 x 40 mL) and brine (1 x 40 mL). The organic phase was dried over anhydrous Na_2SO_4, concentrated under reduced pressure and purified by flash column chromatography using PE:DCM (4:1→1:3) as eluent to give the product as a white solid (710 mg, 67%).

^{1}H NMR [(300 MHz, $(CD_3)_2CO$)], δ (ppm): 7.45-7.33 (m, 4H, H_d), 7.12-7.05 (m, 2H, H_a), 7.00-6.87 (6H, H_b + H_c), 3.81 (s, 3H, O-C<u>H</u>$_3$).

5.2.1.2 Synthesis of Monomers M1-M5

Synthesis of monomer M1

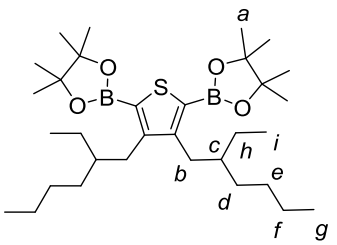

4,4′-di-tert-butyl-2,2′-bipyridine (48.3 mg, 180 μmol) and bis (pinacolato)diboron (1.88 g, 7.39 mmol) were added, subsequently, to a 100 mL two-neck flask containing 3,4-bis(2-ethylhexyl)-thiophene (**1**, 1.90 g, 6.16 mmol), under nitrogen atmosphere. After three cycles of nitrogen-vacuum, 25 mL of degassed heptane were injected into the flask together with. $[Ir(OMe)(COD)]_2$ (58.8 mg, 88.7 μmol). The reaction mixture was stirred at 50 °C for 16 h under nitrogen atmosphere. After cooling down to room temperature, the mixture was filtered and washed with hot hexane. The filtrated was concentrated, and the crude product was purified by flash column chromatography, eluting with ethyl acetate (AcOEt):hexane (5:95) to give a colourless oil (1.92 g, 56%).

^{1}H NMR (300 MHz, $CDCl_3$), δ (ppm): 2.74 (d, J = 7.3 Hz, 4H, H_b), 1.52-1.43 (2H, H_c), 1.35-1.15 (40H, H_a + $H_{d\text{-}f}$ + H_h), 0.91-0.79 (12H, H_g + H_i).

^{13}C NMR (75 MHz, $CDCl_3$), δ (ppm): 153.48 (q), 83.65 (q), 41.58 (CH), 33.33 (CH_2), 32.72 (CH_2), 29.28 (CH_2), 25.75 (CH_2), 24.93 (CH_3), 23.36 (CH_2), 14.33 (CH_3), 11.21 (CH_3).

MS (MALDI-TOF, LDI): calculated for $C_{32}H_{58}B_2NaO_4S$ $[M+Na]^+$: 583.414, found: 583.398.

Synthesis of monomer M2[274]

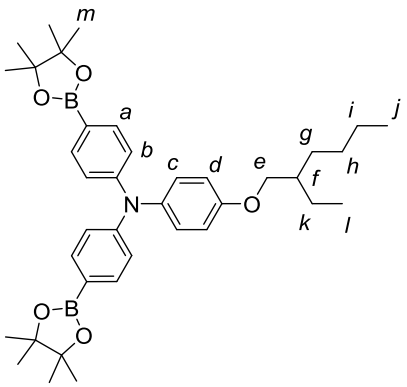

Compound **4** (250 mg, 471 µmol), bis (pinacolato)diboron (350 mg, 1.39 mmol) and potassium acetate (360 mg, 3.70 mmol) were dissolved in 5 mL of anhydrous 1,4-dioxane. The resulting suspension was degassed with a nitrogen stream before and after the addition of $PdCl_2$(dppf) (10.1 mg, 13.9 µmol). This mixture was stirred at 80 °C for 15 h under nitrogen atmosphere. After cooling down to room temperature, 40 mL of water was added, and the aqueous phase was extracted with DCM (2 x 40 mL). The combined organic phases were washed with water (2 x 150 mL), brine (1 x 150 mL) and then dried over anhydrous Na_2SO_4, concentrated under reduced pressure and purified by flash column chromatography using PE:AcOEt (20:1) as eluent. The residue was further purified by crystallization in MeOH to afford **M2** as a white solid (0.12 g, 42%).

^{1}H NMR (300 MHz, CD_2Cl_2), δ (ppm): 7.65-7.51 (4H, H_a), 7.10-6.95 (6H, H_b + H_c), 6.91-6.83 (2H, H_d), 3.84 (d, J = 5.7 Hz, 2H, H_e), 1.79-1.64 (m, 1H, H_f), 1.55-1.27 (32H, $H_{g\text{-}i}$ + H_k + H_m), 0.98-0.83 (6H, H_j + H_l).

^{13}C NMR (75 MHz, CD_2Cl_2), δ (ppm): 157.48 (q), 150.91 (q), 140.03 (q), 136.27 (CH), 128.78 (CH), 122.16 (CH), 116.05 (CH), 84.13 (q) 71.36 (CH_2), 40.05 (CH), 31.13 (CH_2), 29.70 (CH_2), 25.26 (CH_3), 24.48 (CH_2), 23.67 (CH_2), 14.47 (CH_3), 11.52 (CH_3).

MS (MALDI-TOF): calculated for $C_{38}H_{53}B_2NO_5$ $[M]^+$: 625.411, found: 625.440.

Synthesis of monomer M3

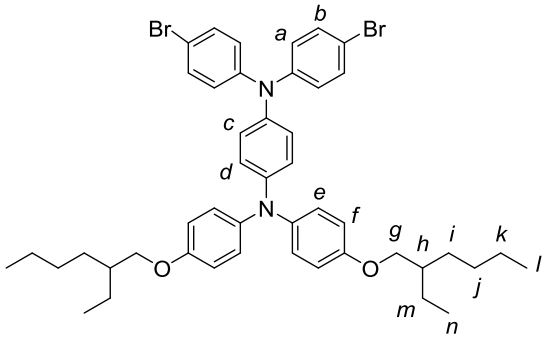

Compound **6** (730 mg, 1.08 mmol) was dissolved in 15 mL of DMF and the solution was degassed for 30 min with an argon stream. After cooling down the solution to 0 °C, NBS (410 mg, 2.27 mmol) was added in small portions under exclusion of light. Next, the reaction mixture was allowed to stir for 24 h at room temperature. Afterwards, the solvent was removed under reduced pressure and 20 mL of DCM and 20 mL of water were added. The phases were separated and the aqueous phase was extracted with DCM (2 x 20 mL). The combined organic phases were washed with water (2 x 50 mL) and brine (1 x 50 mL), dried over Na_2SO_4, filtered and the solvent removed under reduced pressure. The residue was purified by flash column chromatography using PE:DCM (30:1→10:2) as eluent to afford **M3** as an oil (0.54, 60%).

^{1}H NMR [(300 MHz, $(CD_3)_2CO$)], δ (ppm): 7.43-7.33 (m, 4H, H_b), 7.08-6.81 (16H, H_a + H_{c-f}), 3.87 (d, J = 5.6 Hz, 4H, H_g), 1.17-1.65 (2H, H_h), 1.59-1.27 (16H, H_{i-k} + H_m), 0.98-0.85 (12H, H_l + H_n).

^{13}C NMR [(75 MHz, $(CD_3)_2CO$)], δ (ppm): 157.23 (q), 148.27 (q), 147.33 (q), 141.90 (q), 140.28 (q), 133.47 (CH), 128.10 (CH), 127.84 (CH), 125.76 (CH), 122.50 (CH), 116.67 (CH), 115.40 (q), 71.46 (CH_2), 40.53 (CH), 31.52 (CH_2), 30.05 (CH_2, overlapping with the solvent signal), 24.81 (CH_2), 23.94 (CH_2), 14.58 (CH_3), 11.68 (CH_3).

MS (MALDI-TOF): calculated for $C_{46}H_{54}Br_2N_2O_2$ $[M]^+$: 824.255, found: 824.399.

Synthesis of monomer M4[164]

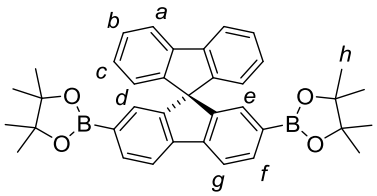

2,7-Dibromo-9,9'-spirobifluorene (200 mg, 422 μmol), bis (pinacolato)diboron (320 mg, 1.27 mmol) and potassium acetate (330 mg, 3.38 mmol) were dissolved in 8 mL of anhydrous 1,4-dioxane. The resulting suspension was degassed with an argon stream before and after $PdCl_2$(dppf) (9.50 mg, 12.9 μmol) was added and the mixture was stirred at 80 °C for 15 h under argon atmosphere. After cooling down to room temperature, the residue was dissolved in 40 mL of water and 40 mL of DCM and the phases were separated. The aqueous phase was extracted with DCM (2 x 40 mL) and the combined organic phases were washed with water (2 x 80 mL) and brine (1 x 80 mL). Finally, the resulting organic phase was dried over anhydrous Na_2SO_4, concentrated under reduced pressure and purified by flash column chromatography using hexane:AcOEt (9:1) as eluent to afford **M4** as a white solid (0.16 g, 66%).

^{1}H NMR (300 MHz, CD_2Cl_2), δ (ppm): 7.92 (d, J = 7.6 Hz, 4H, H_a + H_g), 7.82 (dd, J = 0.9 Hz, 7.6 Hz, 2H, H_f), 7.42 (td, J = 1.0 Hz, 7.5 Hz, 2H, H_b), 7.14 (td, J = 1.0 Hz, 7.6 Hz, 2H, H_c), 7.04 (s, 2 H, H_e), 6.67 (d, J = 7.6 Hz, 2H, H_d), 1.23 (s, 24H, H_h).

Synthesis of monomer M5[166]

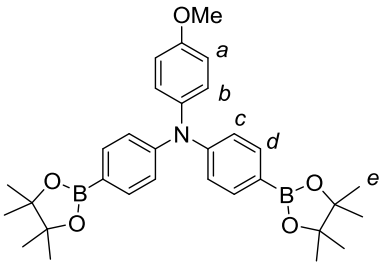

Compound **8** (1.07 g, 2.47 mmol), bis (pinacolato)diboron (1.88 g, 7.41 mmol) and potassium acetate (1.94 g, 19.8 mmol) were dissolved in 20 mL of anhydrous 1,4-dioxane. The resulting suspension was degassed with a nitrogen stream before and after $PdCl_2$(dppf) (51.1 mg, 69.9 μmol) was added, and the mixture was stirred at 80 °C for 15 h under nitrogen atmosphere. After cooling down to room temperature, water (20

mL) was added and the aqueous phase was extracted with DCM (3 x 30 mL). The combined organic phases were washed with water (2 x 60 mL), brine (1 x 60 mL) and dried over anhydrous Na_2SO_4, concentrated under reduced pressure and purified by flash column chromatography using hexane:AcOEt (9:1) as eluent. The residue was further purified by crystallization in EtOH to give monomer **M5** as a white solid (680 mg, 44%).

^{1}H NMR [(300 MHz, $(CD_3)_2CO$)], δ (ppm): 7.66-7.59 (m, 4H, H_d), 7.12-7.04 (m, 2H, H_a), 7.02-6.93 (6H, H_b + H_c), 3.82 (s, 3H, O-C$\underline{H}_3$), 1.32 (s, 24H, H_e).

5.2.1.3 Synthesis of Polymers P1-P6

Synthesis of polymer P1

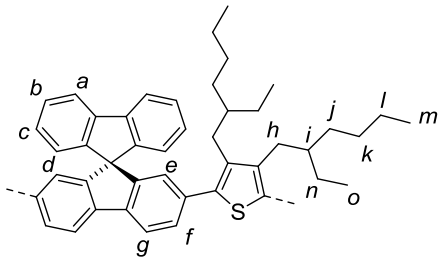

Monomer **M1** (368 mg, 657 µmol) was added to a Schlenk flask under nitrogen. Next, anhydrous toluene (16 mL) and aq. $NaHCO_3$ (0.2 M. 5.98 mL, 1.20 mmol) were injected together with 2,7-dibromo-9,9'-spirobifluorene (312 mg, 657 µmol) and Aliquat 336 (56.8 mg) under nitrogen atmosphere. The reaction mixture was degassed by bubbling nitrogen for 30 min before and after $Pd(PPh_3)_4$ (11.4 mg, 9.86 µmol) was added, and the mixture was stirred vigorously and refluxed for 135 h. Afterwards, 30 mL of chloroform and 30 mL of water were added and upon separation of the phases, the organic phase was washed with 50 mL of brine. Next, the solvent was removed under reduced pressure and the resulting residue was dissolved in 4 mL of chloroform and dripped into 150 mL of cold MeOH. The green precipitate was filtered off and washed consecutively with MeOH (3 d), hexane (7 d) and acetone (1 d) using a *Soxhlet* extractor to afford polymer **P1** (319 mg, 78%). SEC: M_n = 9651, M_w = 21635, PDI = 2.2.

^{1}H NMR (300 MHz, $CDCl_3$), δ (ppm): 7.87-7.70 (4H, H_a + H_g), 7.40-7.24 (4H, H_f + H_b), 7.12-6.99 (2H, H_c), 6.77-6.65 (4H, H_e + H_d), 2.42-2.14 (4H, H_h), 1.22-1.10 (2H, H_i), 1.10-0.78 (16H, CH_2), 0.76-0.65 (6H, CH_3), 0.51-0.36 (6H, CH_3).

MS (MALDI-TOF): The detection of the building block ($C_{45}H_{48}S$ $[M]^+$: 620.347) of **P1** was demonstrated:

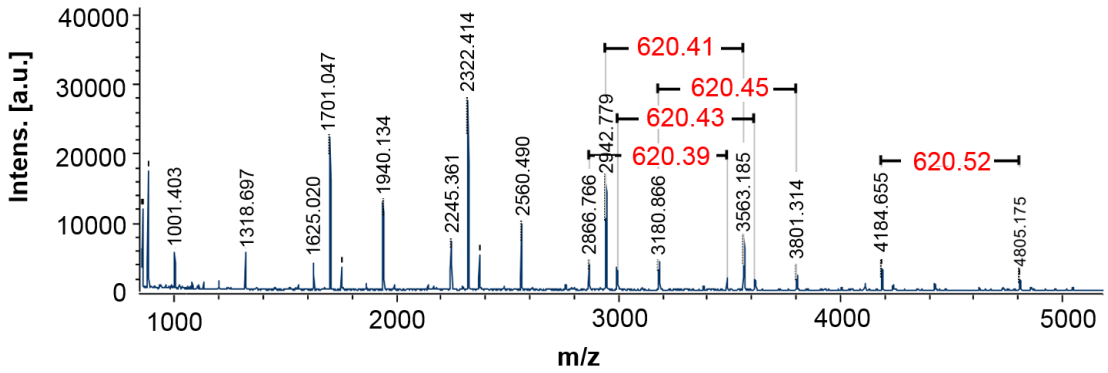

Figure 74. MALDI-TOF spectrum of polymer **P1**.

Synthesis of polymer P2

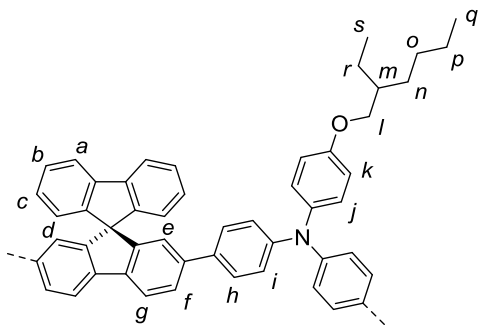

Monomer **M2** (358 mg, 571 µmol) was added to a Schlenk flask under nitrogen. Next, anhydrous toluene (14 mL) and aq. $NaHCO_3$ (0.2 M. 5.20 mL, 1.04 mmol) were injected together with 2,7-dibromo-9,9'-spirobifluorene (271 mg, 571 µmol) and Aliquat 336 (60.9 mg) under nitrogen atmosphere. The reaction mixture was purged with nitrogen for 30 min before and after $Pd(PPh_3)_4$ (9.90 mg, 8.57 µmol) was added. The mixture was stirred vigorously and refluxed for 135 h and 30 mL of chloroform and 30 mL of water were added afterwards. After separation of the phases, the aqueous phase was extracted with chloroform (1 x 30 mL) and the combined organic phases were washed with 50 mL of brine, dried over anhydrous Na_2SO_4 and concentrated

under reduced pressure. The residue was dissolved in 4 mL of chloroform and dripped into 150 mL of cold MeOH. The green precipitate was filtered off and washed consecutively with MeOH (3 d), hexane (4 d) and acetone (2 d) using a *Soxhlet* extractor to afford polymer **P2** (322 mg, 82%). SEC: M_n = 5551, M_w = 11390, PDI = 2.1.

^{1}H NMR (300 MHz, CD_2Cl_2), δ (ppm): 7.99-7.76 (4H, H_a + H_g), 7.66-7.48 (2H, H_f), 7.45-6.81 (16H, $H_{b,c}$ + H_{h-k}), 6.81-6.67 (4H, H_e + H_d), 3.86-3.71 (2H, H_l), 1.77-1.62 (1H, H_m), 1.56-1.22 (8H, H_{n-p} + H_r), 1.01-0.80 (6H, H_q + H_s).

MS (MALDI-TOF): The detection of the building block ($C_{51}H_{43}NO$ $[M]^+$: 685.322) of **P2** was demonstrated (Figure 28).

Synthesis of polymer P3

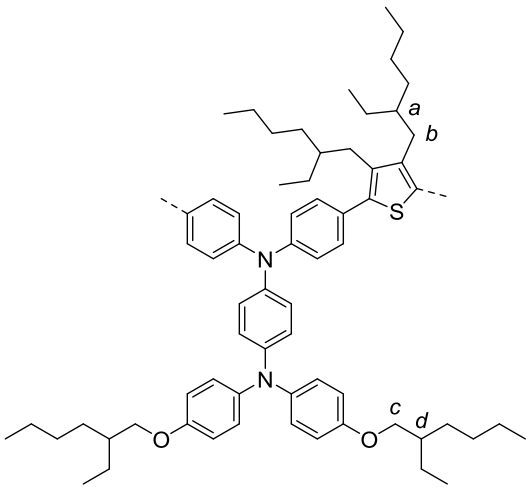

The dibrominated monomer **M3** (446 mg, 539 µmol) was added to a Schlenk flask under nitrogen. Next, anhydrous toluene (13 mL) and aq. $NaHCO_3$ (0.2 M, 4.90 mL, 981 µmol) were injected together with monomer **M1** (301 mg, 539 µmol) and Aliquat 336 (45.0 mg) under nitrogen atmosphere. The reaction mixture was purged with nitrogen for 30 min before and after $Pd(PPh_3)_4$ (9.34 mg, 8.09 µmol) was added. The mixture was stirred vigorously and refluxed for 135 h and 30 mL of DCM and 30 mL of water were added afterwards. The aqueous phase was extracted with DCM (1 x 30 mL) and the combined organic phases were washed with 50 mL of brine, dried over anhydrous Na_2SO_4 and concentrated under reduced pressure. The residue was dissolved in 4 mL of DCM and dripped into 150 mL of cold MeOH. The green

precipitate was filtered off and washed consecutively with MeOH (4 d), CH_3CN (2 d) and acetone (7 d) using a *Soxhlet* extractor to afford polymer **P3** (160 mg, 31%). SEC: M_n = 3209, M_w = 4746, PDI = 1.5.

^{1}H NMR (300 MHz, CD_2Cl_2), δ (ppm): 7.52-6.78 (20H, H_{Ar}), 3.86-3.77 (4H, H_c), 2.69-2.56 (4H, H_b), 179-1.64 (2H, H_d), 1.57-1.03 (34H, CH_2 + H_a), 0.99-0.64 (24H, CH_3).

MS (MALDI-TOF): The detection of the building block ($C_{66}H_{88}N_2O_2S$ $[M]^+$: 972.656) of **P3** was demonstrated:

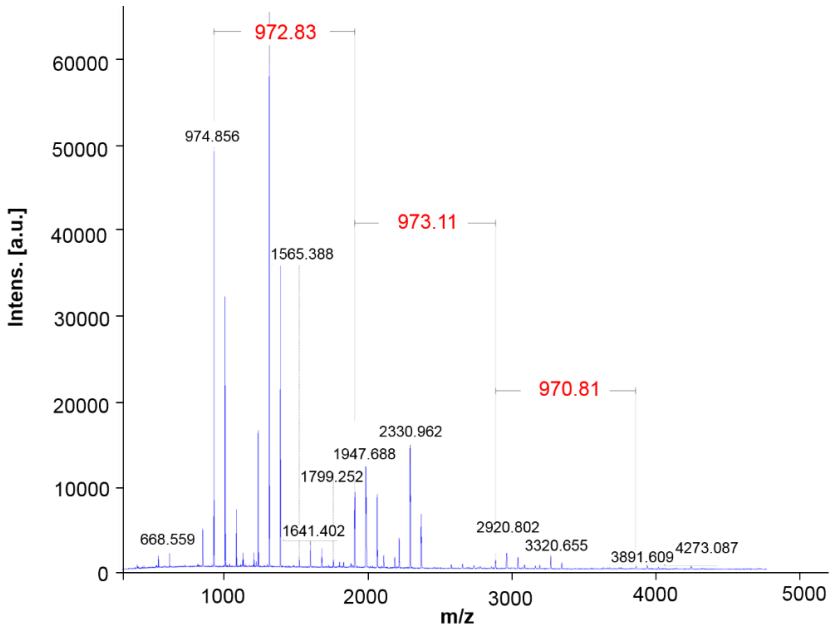

Figure 75. MALDI-TOF spectrum of polymer **P3**.

Synthesis of polymer P4

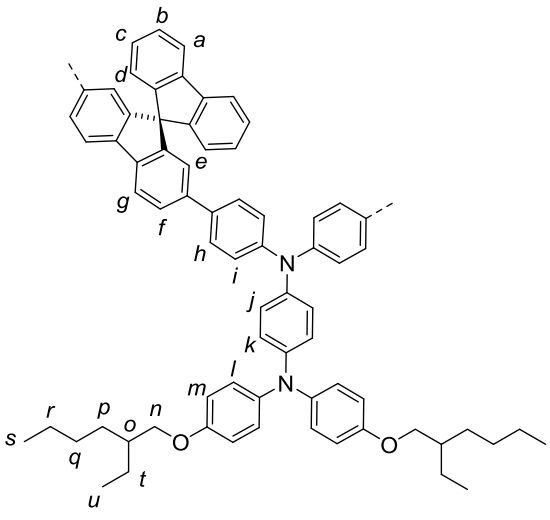

The dibrominated monomer **M3** (345 g, 417 µmol) was added to a Schlenk flask under nitrogen. Next, anhydrous toluene (10 mL) and aq. $NaHCO_3$ (0.2 M, 3.79 mL, 758 µmol) were injected together with monomer **M4** (237 mg, 417 µmol) and Aliquat 336 (35.0 mg) under nitrogen atmosphere. The reaction mixture was purged with nitrogen for 30 min before and after $Pd(PPh_3)_4$ (7.72 mg, 6.25 µmol) was added. The mixture was stirred vigorously and refluxed for 135 h. Afterwards, 30 mL of DCM and 30 mL of water were added and the phases were separated. The aqueous phase was extracted with DCM (1 x 30 mL) and the combined organic phases were washed with 50 mL of brine, dried over anhydrous Na_2SO_4 and concentrated under reduced pressure. The residue was dissolved in 4 mL of DCM and dripped into 150 mL of cold MeOH. The green precipitate was filtered off and washed consecutively with MeOH (5 d), hexane (2 d) and acetone (4 d) using a *Soxhlet* extractor to afford polymer **P4** (276 mg, 67%). SEC: M_n = 4403, M_w = 10528, PDI = 2.4.

^{1}H NMR (300 MHz, CD_2Cl_2), δ (ppm): 8.04-6.68 (34H, H_{Ar}), 3.87-3.74 (4H, H_n), 178-1.65 (2H, H_o), 1.55-1.25 (16H, CH_2), 1.01-0.81 (12H, CH_3).

MS (MALDI-TOF, DCTB): The detection of the building block ($C_{71}H_{69}N_2O_2$ $[M+H]^+$: 981.535) of **P4** was demonstrated:

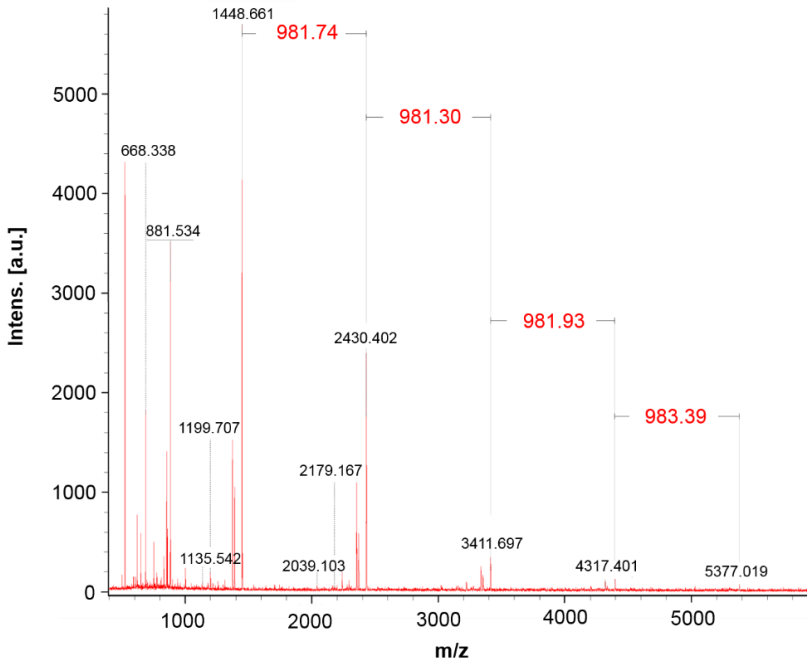

Figure 76. MALDI-TOF spectrum of polymer **P4**.

Synthesis of polymer P5

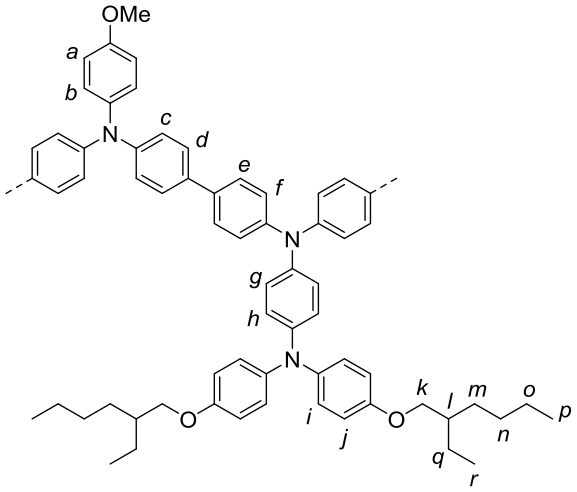

The dibrominated monomer **M3** (306 mg, 370 µmol) was added to a Schlenk flask under nitrogen. Next, anhydrous toluene (9 mL) and aq. $NaHCO_3$ (0.2 M, 3.37 mL, 673 µmol) were injected together with monomer **M5** (231 mg, 370 µmol) and Aliquat 336 (47.8 mg) under nitrogen atmosphere. The reaction mixture was purged with argon for 30 min before and after $Pd(PPh_3)_4$ (6.42 mg, 5.55 µmol) was added. The mixture was stirred vigorously and refluxed for 4 d and 30 mL of DCM and 30 mL of water were added afterwards. The aqueous phase was extracted with 30 mL of DCM and the combined organic phases were washed with 50 mL of brine, dried over anhydrous Na_2SO_4 and concentrated under reduced pressure. The residue was dissolved in 4 mL of DCM and dripped into 150 mL of cold MeOH. The brown precipitate was collected by filtration and washed consecutively with MeOH (3 d), acetone (2 d), hexane (2 d) and MeOH (3 d) using a *Soxhlet* extractor to afford **P5** (176 mg, 46%). SEC: M_n = 4681, M_w = 8663, PDI = 1.9.

^{1}H NMR (300 MHz, CD_2Cl_2), δ (ppm): 7.66-6.64 (32H, $H_{a\text{-}j}$), 3.89-3.66 (7H, $OC\underline{H}_3$ + H_k), 179-1.61 (2H, H_l), 1.58-1.21 (16H, $H_{m\text{-}o}$ + H_q), 1.01-0.77 (12H, H_p + H_r).

MS (MALDI-TOF): The detection of the building block ($C_{65}H_{69}N_3O_3$ $[M]^+$: 939.533) of **P5** was demonstrated:

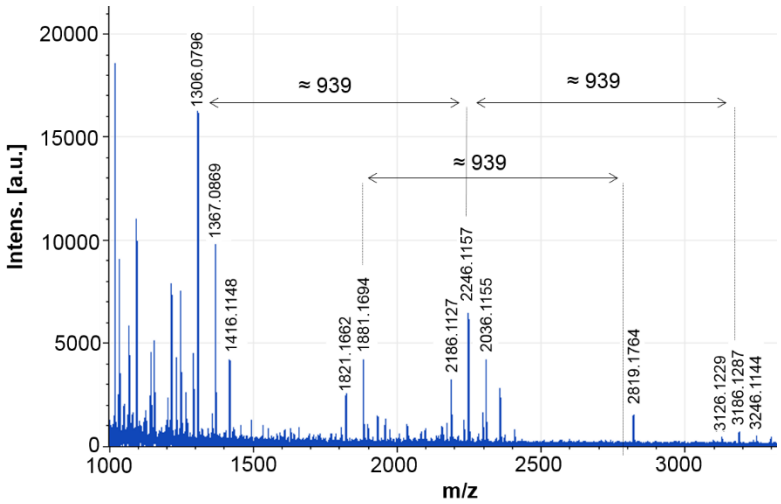

Figure 77. MALDI-TOF spectrum of polymer **P5**.

Synthesis of polymer P6

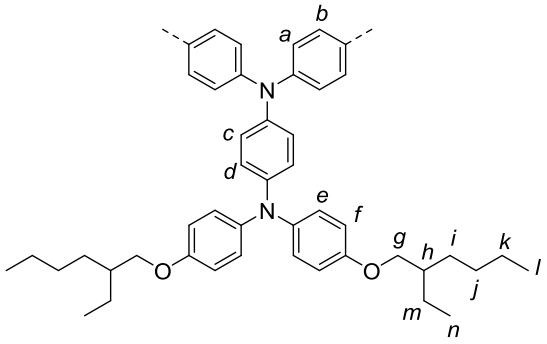

A mixture of $Ni(COD)_2$ (375 mg, 1.36 mmol), 2,2'-bipyridine (213 mg, 1.36 mmol), 1,5-cyclooctadiene (167 µL, 1.36 mmol), degassed anhydrous toluene (3 mL), and degassed anhydrous DMF (3 mL) was stirred at room temperature under nitrogen atmosphere for 30 min. A solution of monomer **M3** (470 mg, 568 µmol) in degassed anhydrous toluene (9.5 ml) and degassed anhydrous DMF (9.5 ml) was added, and the mixture was stirred at 65 °C for 7 d. The reaction mixture was poured into MeOH:HCl (20%) (4:1, 500 ml) and stirred for 30 min. The green precipitate was filtered off and washed consecutively with MeOH (6 d), acetone (2 d) and CH_3CN (3 d) using a *Soxhlet* extractor to afford polymer **P6** (194 mg, 51%). SEC: M_n = 5812, M_w = 12443, PDI = 2.1.

^{1}H NMR (300 MHz, CD_2Cl_2), δ (ppm): 7.54-7.30 (4H, H_b), 7.18-6.70 (16H, H_a + H_{c-f}), 3.93-3.73 (4H, H_g), 178-1.62 (2H, H_h), 1.57-1.21 (16H, H_{i-k} + H_m), 1.01-0.81 (12H, H_n + H_o).

MS (MALDI-TOF): The detection of the building block ($C_{46}H_{54}N_2O_2$ $[M]^+$: 666.417) of **P6** was demonstrated:

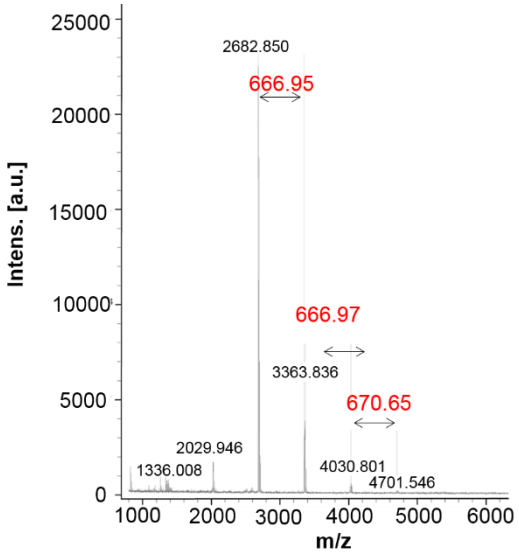

Figure 78. MALDI-TOF spectrum of polymer **P6**.

5.2.2 Perfluorinated Additives for PSCs

5.2.2.1 Synthesis of Precursors 9 and 10

Synthesis of 1,4-bis(perfluorohexyl)benzene (9)[208]

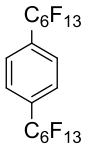

To a stirred solution of 1,4-diiodobenzene (3.30 g, 10.0 mmol), Cu powder (5.08 g, 80.0 mmol) and 2,2´bipyridine (156 mg, 1.00 mmol) in 30 mL of anhydrous DMSO, perfluorohexyl iodide (6.50 mL, 30.1 mmol) was added under argon atmosphere. The resulting mixture was stirred for 72 h at 70 ºC and the reaction was then poured into 200 mL of water:Et_2O (1:1) and stirred vigorously for 30 min. After removing the

solids by filtration, the organic layer was washed with dilute NH_4OH solution (2 x 100 mL), water (2 x 100 mL) and dried over anhydrous Na_2SO_4. The solvent was removed under vacuum and the resulting residue was sublimated to give compound **9** as a white solid (5.92 g, 83%).

^{1}H NMR (400 MHz, CD_2Cl_2), δ: (ppm) 7.79 (s, 4H).

^{19}F NMR (376 MHz, CD_2Cl_2), δ: (ppm) -126.4 (4F), -123.0 (4F), -122.0 (4F), 121.6 (4F), -111.4 (4F), -81.14 (6F).

Synthesis of 4-bromo-*N*,*N*-bis(4-methoxyphenyl)aniline (10)[209]

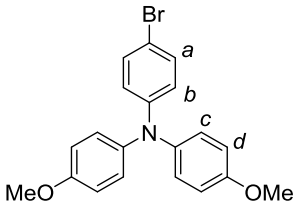

4-Iodoanisol (16.5 g, 70.5 mmol), copper (I) iodide (255 mg, 1.34 mmol), 1,10-phenantroline (241 mg, 1.34 mmol) and KOH (14.7 g, 261 mmol) were dissolved in previously degassed anhydrous toluene (80 mL). Then, 4-bromoaniline (5.77 g, 33.6 mmol) was added and after degassing for 5 min the reaction mixture was stirred at 80 ºC for 3 d. After cooling down to room temperature, 100 mL of water and 80 mL of DCM was added and the phases separated. The aqueous phase was extracted with DCM (2 x 100 mL) and the combined organic phases were washed with water (1 x 200 mL). The organic phase was dried over anhydrous Na_2SO_4, concentrated under reduced pressure and purified by flash column chromatography on silica gel using PE:DCM (1:1) as eluent to give triarylamine **10** as a white solid (2.98 g, 23%).

^{1}H NMR [300 MHz, $(CD_3)_2CO$)], δ (ppm): 7.36-7.30 (m, 2H, H_a), 7.13-7.06 (m, 4H, H_c), 6.99-6.92 (m, 4H, H_d), 6.81-6.75 (m, 2H, H_b), 3.83 (s, 6H, CH_3).

5.2.2.2 Synthesis of Monomers M6-M7 and Intermediate 11

Synthesis of 1,4-dibromo-2,5-bis(perfluorohexyl)benzene (M6)[208]

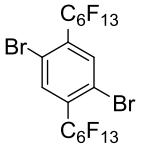

To a solution of 4-bis(perfluorohexyl)benzene (**9**, 2.70 g, 3.78 mmol) in 27 mL of trifluoroacetic acid and 8 mL of H_2SO_4 (c), NBS (2.01 g, 11.3 mmol) was added. The latter was added in small portions (335 mg h^{-1}) under stirring over a period of 5 h, followed by stirring at 60 °C for 48 h. After that time, the reaction mixture was poured into iced water and the obtained yellow precipitate was collected by filtration and recrystallized in EtOH to give monomer **M6** as a white solid (1.87 g, 57%).

^{1}H NMR (400 MHz, CD_2Cl_2), δ (ppm): 7.99 (s, 2H).

^{19}F NMR (376 MHz, CD_2Cl_2), δ (ppm): -126.3 (4F), -122.9 (4F), -121.8 (4F), 119.5 (4F), -107.7 (4F), -81.1 (6F).

Synthesis of monomer M7

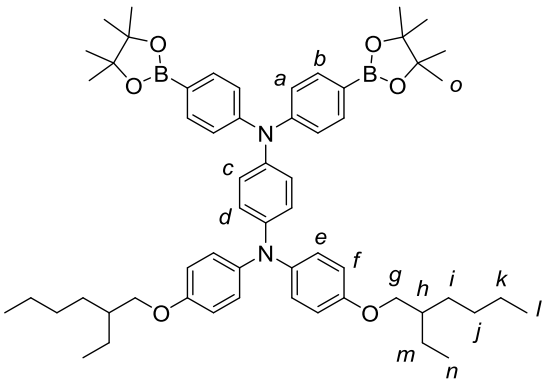

Compound **M3** (0.67 g, 0.81 mmol), bis(pinacolato)diboron (617 mg, 2.43 mmol) and potassium acetate (635 mg, 6.47 mmol) were dissolved in 15 mL of anhydrous 1,4-dioxane. The solution was degassed for 15 min with an argon stream and $PdCl_2$(ddpf) (14.5 mg, 19.8 μmol) was added. The reaction mixture was allowed to stir for 3 d at 80 ºC. After cooling to room temperature, 40 mL of water and 40 mL of DCM were added and the phases were separated. The aqueous phase was extracted

with DCM (3 x 40 mL) and the combined organic layers were washed with water (2 x 100 mL), brine (1 x 100 mL), dried over anhydrous Na_2SO_4 and concentrated under reduced pressure. The crude product was purified by flash column chromatography on silica gel using hexane:AcOEt (15:1) with 0.5% NEt_3 as eluent to give monomer **M7** as a white solid (200 mg, 39%).

^{1}H NMR [500 MHz, $(CD_3)_2CO$)], δ (ppm): 7.63 (d, J = 8.3 Hz, 4H, H_a), 7.08-6.84 (16H, $H_{b\text{-}f}$), 3.87 (d, J = 5.6 Hz, 4H, H_g), 1.76-1.65 (m, 2H, H_h), 1.57-1.23 (40H, $H_{i\text{-}k}$ + H_m + H_o), 0.97-0.86 (12H, H_l + H_n).

^{13}C NMR [125 MHz, $(CD_3)_2CO$)], δ (ppm): 156.96 (q), 151.33 (q). 147.08 (q), 141.71 (q), 140.23 (q), 136.87 (CH), 128.31 (CH), 127.60 (CH), 122.73 (CH), 122.16 (CH), 116.41 (CH), 84.43 (q), 71.40 (CH_2), 40.50 (CH), 31.48 (CH_2), 29.98 (CH_2, overlapping with the solvent signal), 25.38 (CH_3), 24.76 (CH_2), 23.90 (CH_2), 14.54 (CH_3), 11.63 (CH_3).

MS (MALDI-TOF): calculated for $C_{58}H_{78}B_2N_2O_6$ $[M]^+$: 920.600, found 920.595.

Synthesis of intermediate 11[275]

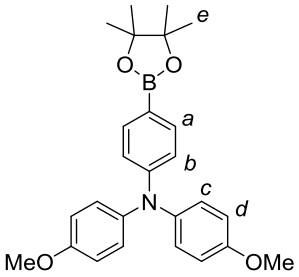

4-Bromo-*N*,*N*-bis(4-methoxyphenyl)aniline (**10**, 1.00 g, 2.60 mmol), bis(pinacolato)diboron (990 mg, 3.90 mmol) and potassium acetate (2.04 g, 20.8 mmol) were dissolved in 20 mL of anhydrous 1,4-dioxane. The resulting suspension was degassed with an argon stream before and after $PdCl_2$(dppf) (51.1 mg, 69.8 μmol) was added and the mixture was stirred at 80 ºC for 48 h under argon atmosphere. After cooling to room temperature, 40 mL of water and 20 mL of DCM were added and the phases were separated. The aqueous phase was extracted with DCM (3 x 40 mL) and the combined organic phases were washed with water (1 x 200 mL) and brine (1 x 200

mL). The organic phase was dried over anhydrous Na_2SO_4, concentrated under reduced pressure and purified by flash column chromatography on silica gel using PE:DCM (1:2) as eluent to give the product as a white solid (0.25 g, 22%).

^{1}H NMR [400 MHz, $(CD_3)_2CO$)], δ (ppm): 7.56-7.50 (m, 2H, H_a), 7.12-7.04 (m, 4H, H_c), 6.97-6.88 (m, 4H, H_d), 6.81-6.74 (m, 2H, H_b), 3.80 (s, 6H, CH_3), 1.30 (12H, s, H_e).

5.2.2.3 Synthesis of Additives S1, P7 and P8

Synthesis of additive S1

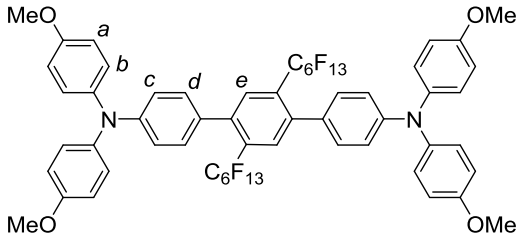

Compound **11** (223 mg, 517 µmol), 1,4-dibromo-2,5-bis(perfluorohexyl) benzene (**M6**, 205 mg, 235 mmol), aq. $NaHCO_3$ (0.2 M, 4.70 mL, 0.94 mmol) were dissolved in 3 mL of anhydrous toluene. The resulting suspension was degassed with an argon stream before and after $Pd(PPh_3)_4$ (37.0 mg, 32.3 µmol) was added and the mixture was stirred and refluxed for 4 d under argon atmosphere. After cooling to room temperature, 20 mL of water and 20 mL of DCM were added and the phases separated. The aqueous phase was extracted with DCM (3 x 20 mL) and the combined organic phases were washed with water (1 x 80 mL) and brine (1 x 80 mL). The organic phase was dried over anhydrous Na_2SO_4, concentrated under reduced pressure and purified by flash column chromatography on silica gel using toluene (0.5% NEt_3) as eluent to give additive **S1** as a yellowish solid (128 mg, 41%).

^{1}H NMR (400 MHz, $CDCl_3$), δ (ppm): 7.58 (s, 2H, H_e), 7.14-7.03 (12H, H_b + H_d), 6.94-6.89 (m, 4H, H_c), 6.89-6.82 (m, 8H, H_a), 3.81 (s, 12H, CH_3).

^{19}F NMR (376 MHz, CD_2Cl_2), δ (ppm): -126.33 (4F), -122.99 (4F), -121.92 (4F), -119.61 (4F), -103.25 (4F), -81.13 (6F).

^{13}C NMR (100 MHz, CD_2Cl_2) δ (ppm): 156.81 (q), 149.17 (q), 142.56 (q), 141.16 (q), 133.78 (CH), 130.66 (q), 130.38 (CH), 130.17-129.42 (C-F) 127.44 (CH), 119.13 (CH), 115.24 (CH), 55.98 (CH_3).

MS (ESI-TOF): calculated for $C_{58}H_{39}F_{26}N_2O_4$ $[M+H]^+$: 1321.249, found 1320.247 (Figure 43).

Synthesis of additive P7

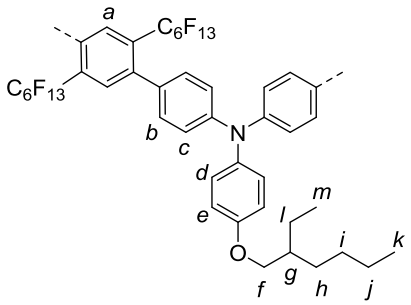

Monomer **M2** (100 mg, 160 µmol) was added to a Schlenk flask under argon atmosphere. Next, anhydrous toluene (4 mL), water (1 mL) and $NaHCO_3$ (540 mg, 6.40 mmol) were injected together with 1,4-dibromo-2,5-bis(perfluorohexyl) benzene (**M6**, 140 mg, 160 µmol) under argon atmosphere. The reaction mixture was purged with argon for 30 min before and after $Pd(PPh_3)_4$ (11.0 mg, 9.60 µmol) was added. The mixture was stirred vigorously and refluxed for 5 d and after cooling, 20 mL of DCM and 20 mL of water were added. The phases were separated and the aqueous phase was extracted with DCM (1 x 20 mL). The combined organic phases were washed with 50 mL of brine, dried over anhydrous Na_2SO_4 and concentrated under reduced pressure. The residue was dissolved in DCM and dripped into 150 mL of cold MeOH. The obtained precipitate was collected by filtration and washed consecutively with MeOH (3 d) and CH_3CN (3 d) using a *Soxhlet* extractor to afford polymer **P7** (80 mg, 46%). SEC: M_n = 10231, M_w = 16144, PDI = 1.6.

^{1}H NMR (400 MHz, CD_2Cl_2), δ (ppm): 7.65 (s, 2H, H_a), 7.20-6.85 (12H, H_{b-e}), 3.89-3.80 (2H, H_f), 1.79-1.67 (1H, H_g), 1.59-1.29 (8H, H_{h-j} + H_l), 1.01-0.85 (6H, H_k + H_m).

^{19}F NMR (376 MHz, CD_2Cl_2), δ (ppm): -126.5 (4F), -123.1 (4F), -122.0 (4F), -119.6 (4F), -103.3 (4F), -81.31 (6F).

MS (MALDI-TOF): The detection of the building block ($C_{44}H_{31}F_{26}NO$ $[M]^+$: 1083.198) of **P7** was demonstrated (Figure 44).

Synthesis of additive P8

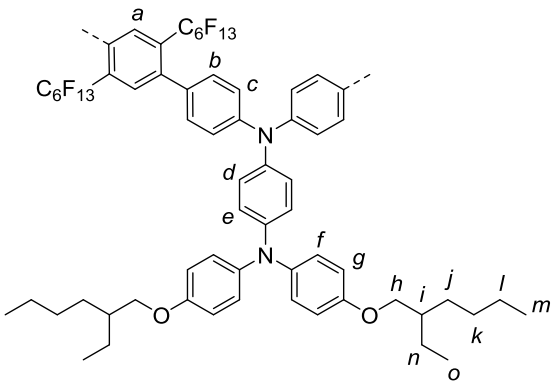

Monomer **M7** (143 mg, 155 µmol) was added to a Schlenk flask under argon. Next, anhydrous toluene (3.8 mL) and aq. $NaHCO_3$ (0.2 M, 1.41 mL, 282 µmol) were injected together with 1,4-dibromo-2,5-bis(perfluorohexyl) benzene (**M6**, 135 mg, 155 µmol) under argon atmosphere. The reaction mixture was purged with argon for 30 min before and after $Pd(PPh_3)_4$ (11.0 mg, 9.30 µmol) was added. The mixture was stirred vigorously and refluxed for 5 d and after cooling, 20 mL of DCM and 20 mL of water were added. The phases were separated and the aqueous phase was extracted with DCM (1 x 20 mL). The combined organic phases were washed with 50 mL of brine, dried over anhydrous Na_2SO_4 and concentrated under reduced pressure. The residue was dissolved in DCM and dripped into 150 mL of cold MeOH. The obtained precipitate was collected by filtration and washed consecutively with MeOH (3 d) and CH_3CN (3 d) using a *Soxhlet* extractor to afford polymer **P8** (156 mg, 73%). SEC: M_n = 10750, M_w = 17600, PDI = 1.6.

^{1}H NMR (300 MHz, $CDCl_3$), δ (ppm): 7.63 (s, 2H, H_a), 7.21-6.77 (20H, H_{b-g}), 3.81 (d, J = 5.4 Hz, 4H, H_h), 1.74-1.66 (2H, H_i), 1.50-1.27 (16H, H_{j-l} + H_n), 0.96-0.84 (12H, H_m + H_o).

^{19}F NMR (376 MHz, CD_2Cl_2), δ (ppm): -126.46 (4F), -123.1 (4F), -122.0 (4F), -119.6 (4F), -103.2 (4F), -81.30 (6F).

MS (MALDI-TOF): The detection of the building block ($C_{64}H_{56}F_{26}N_2O_2$ $[M]^+$: 1378.392) of **P8** was demonstrated:

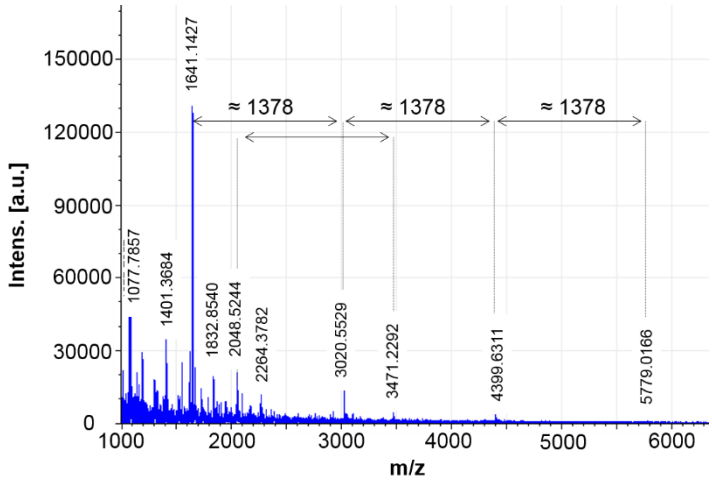

Figure 79. MALDI-TOF spectrum of polymer **P8**.

5.2.3 Electron-Transporting Polymers for PSCs

5.2.3.1 Synthesis of Model Compounds MC1-MC3

Synthesis of model compound MC1[276]

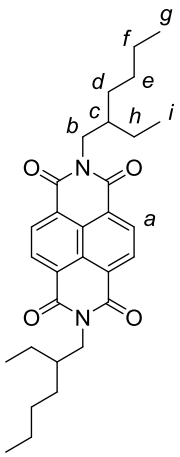

1,4,5,8-Naphthalenetetracarboxylic dianhydride (200 mg, 740 µmmol) and 2-ethylhexylamine (259 µL, 1.58 mmol) were suspended in 4 mL of anhydrous DMF and

the resulting mixture was subjected to microwave at 140 ºC for 10 min. The crude product was poured into 300 mL of water and the precipitate was filtered and dried in vacuum. The resulting solid was purified by flash column chromatography using PE:DCM (1:1) as eluent to yield the product as a white solid (118 mg, 32%).

^{1}H NMR (300 MHz, $CDCl_3$), δ (ppm): 8.76 (s, 4H, H_a), 4.25-4.05 (4H, H_b), 2.02-1.86 (2H, H_c), 1.49-1.19 (16H, $H_{d\text{-}f}$ + H_h), 1.02-0.76 (12H, H_g + H_i).

Synthesis of model compound MC2

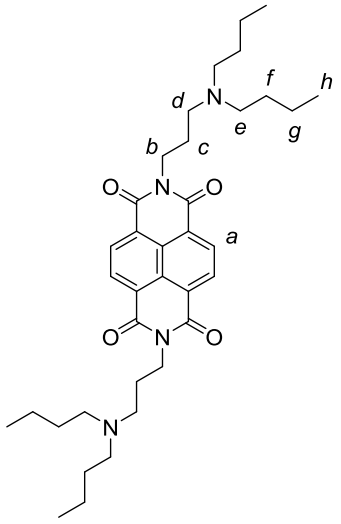

1,4,5,8-Naphthalenetetracarboxylic dianhydride (500 mg, 1.87 mmol) was suspended in 5 mL of DMF together with 3-(dibutylamino)propylamine (834 μL, 3.70 mmol). The mixture was let to react under microwave at 140 ºC for 10 min. The reaction mixture was then poured into 500 mL of water and the precipitate was filtered off, washed 3 times with water and dried under reduced pressure. The product was kept in darkness (900 mg, 80%).

^{1}H NMR (300 MHz, $CDCl_3$), δ (ppm): 8.75 (s, 4H, H_a), 4.22 (t, J = 7.6 Hz, 4H, H_b), 2.58 (t, 4H, J = 7.0 Hz, 4H, H_d), 2.41 (t, J = 7.7 Hz, 8H, H_e), 1.97-1.82 (4H, H_c), 1.47-1.22 (16H, H_f + H_g), 0.89 (t, J = 7.3 Hz, H_h).

^{13}C NMR (75 MHz, $CDCl_3$), δ (ppm): 162.96 (CO), 131.02 (CH), 126.81 (q), 126.78 (q), 53.82 (CH_2), 51.94 (CH_2), 39.86 (CH_2), 29.38 (CH_2), 25.71 (CH_2), 20.86 (CH_2), 14.20 (CH_3).

MS (ESI-TOF): calculated for $C_{36}H_{52}N_4O_4$ $[M+H]^+$: 605.406, found: 605.406.

Synthesis of model compound MC3

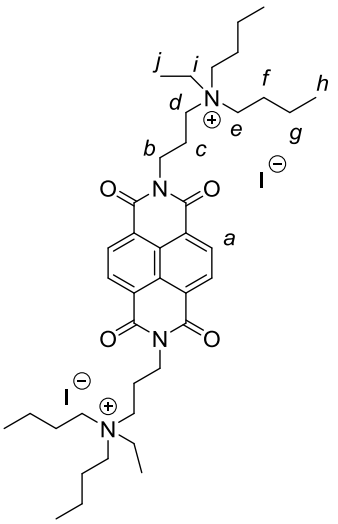

MC2 (400 mg, 661 μmol) was dissolved in 2 mL of CH_3CN and placed in a closed tube under nitrogen atmosphere. After that, iodoethane (3.00 mL. 37.5 mmol) was added to the solution. The mixture was allowed to react at room temperature at dark for 5 d. The product, which precipitates as orange crystals, was collected by filtration, washed several times with Et_2O and dried over vacuum. The solid was recrystallized from DCM to obtain 310 mg of **MC3** (47% yield).

^{1}H NMR (300 MHz, DMSO), δ (ppm): 8.74 (s, 4H, H_a), 4.15 (t, J = 6.5 Hz, 4H, H_b), 3.33-3.22 (8H, H_d + H_i), 3.22-3.10 (8H, H_e), 2.15-2.01 (4H, H_c), 1.64-1.50 (8H, H_f), 1.37-1.22 (8H, H_g), 1.18 (t, J = 7 Hz 6H, H_j), 0.91 (t, J = 7.4 Hz 12H, H_h).

^{13}C NMR (75 MHz, DMSO), δ (ppm): 162.91 (CO), 130.53 (CH), 126.42 (q), 126.25 (q), 57.16 (CH_2), 55.02 (CH_2), 53.42 (CH_2), 37.53 (CH_2), 23.07 (CH_2), 20.31 (CH_2), 19.16 (CH_2), 13.49 (CH_3), 7.38 (CH_3).

MS (ESI-TOF): calculated for $C_{40}H_{62}N_4O_4$ $[M]^+$: 662.477, found: 662.476.

5.2.3.2 Synthesis of Precursors 12-14

Synthesis of 1,4-bis(2-ethylhexyl)benzene (12)[277]

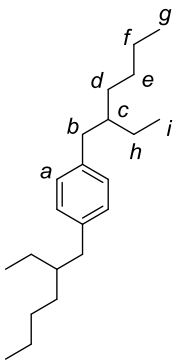

This product was prepared in two steps: (1) preparation of the Grignard reagent (RMgX); (2) the reaction of RMgX with 1,4 dibromobenzene by *Kumada* coupling.

1) Grignard reaction. To a solution of magnesium (1.65 g, 67.8 mmol) in 4 mL of anhydrous Et_2O was added one crystal of iodine and 2-ethylhexyl bromide (9.82 g, 50.9 mmol) together with 4 mL of anhydrous Et_2O slowly (30 min). The mixture was refluxed under argon atmosphere for 1 h.

2) Kumada reaction. To an ice-cooled solution of 1,4-dibromobenzene (4.00 g, 16.9 mmol) and Ni(dppp)Cl_2 (279 mg, 514 μmol) in 5 mL of anhydrous Et_2O was added slowly the solution with the Grignard reagent (previously synthesized) together with 5 mL of Et_2O to transfer that reagent completely. The reaction mixture was stirred at 40 ºC under argon atmosphere during 2 d. After this time, 50 mL of HCl (1 M) was added to the reaction mixture and the aqueous phase was extracted with Et_2O (3 x 50 mL). The combined organic phases were washed with water (2 x 150 mL) and brine (1 x 150 mL), dried over Na_2SO_4 and concentrated under reduced pressure. The resulting yellowish oil was purified by vacuum distillation (43 mbar, 200 ºC) to give a colorless oil (3.82 g, 74%), which was used directly in the next step without further purification. This compound was previously described in literature and showed identical spectroscopic data as those reported therein.[277]

^{1}H NMR (300 MHz, $CDCl_3$), δ (ppm): 7.31 (s, 2H, H_a), 2.58 (d, J = 7.2 Hz, 4H, H_b), 1.73-1.60 (2H, H_c), 1.36-1.21 (16H, $H_{d\text{-}f}$ + H_h), 0.92-0.84 (12H, H_g + H_i).

Synthesis of 1,4-dibromo-2,5-bis(2-ethylhexyl)benzene (13)[278]

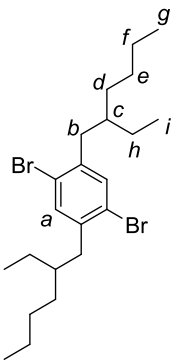

Bromine (1.51 mL, 29.1 mmol) was added dropwise in the dark to a mixture of 1,4-bis(2-ethylhexyl)benzene (**12**, 3.83 g, 12.7 mmol) and iodine (32.8 mg, 129 μmol) at 0 ºC. The mixture was stirred for 48 h at room temperature. After that time, 20 mL of DCM and 20 mL of NaOH (20%) were added and the phases were separated. The aqueous phase was extracted with DCM (2 x 20 mL) and the combined organic phases were washed with 60 mL of NaOH (20%), $Na_2S_2O_3$ (2 x 60 mL) and brine (1 x 60 mL), dried over Na_2SO_4 and concentrated under reduced pressure. The crude product was purified by flash column chromatography using hexane as eluent to afford compound **13** as a colourless oil (3.43 g, 58%)

^{1}H NMR (300 MHz, $CDCl_3$), δ (ppm): 7.31 (s, 2H, H_a), 2.58 (d, J = 7.2 Hz, 4H, H_b), 1.73-1.60 (2H, H_c), 1.36-1.21 (16H, $H_{d\text{-}f}$ + H_h), 0.92-0.84 (12H, H_g + H_i).

Synthesis of 2,6-dibromo-1,4,5,8-naphthalenetetracarboxylic dianhydride (14)[259]

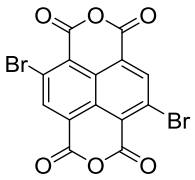

1,4,4,8-Naphthalenetetracarboxylic dianhydride (2.70 g, 9.99 mmol) was suspended in 25 mL of H_2SO_4 (96%) and the mixture was stirred for 5 min. Next, 1,3-dibromo-5,5-dimethylhydantoin (DBDMH, 4.28 g, 15.0 mmol) was added to the mixture in portions over a period of 1 h at room temperature. The reaction mixture was then stirred during 48 h at 50 ºC. After that time, the mixture was poured into crushed ice and the precipitated solid was filtered and washed several times with water. Finally,

the yellow product was dried in vacuum (3.80 g, 89%), which was used directly in the next step without further purification.

^{1}H NMR (300 MHz, DMSO), δ (ppm): 8.79 (s, 2H).

5.2.3.3 Synthesis of Monomers M8-M10

Synthesis of monomer M8

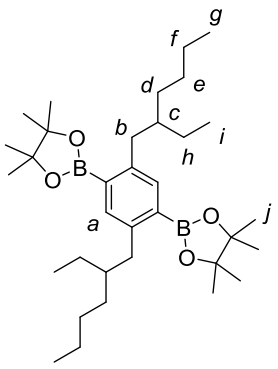

1,4-Dibromo-2,5-bis(2-ethylhexyl)benzene (**13**, 240 mg, 521 µmol), bis(pinacolato)diboron (389 mg, 1.53 mmol) and potassium acetate (400 mg, 4.08 mmol) were dissolved in 8 mL of anhydrous 1,4-dioxane. The resulting suspension was degassed with an argon stream before and after the addition of $PdCl_2$(dppf) (11.0 mg, 15.3 µmol), and the mixture was stirred at 80 ºC for 3 d . After cooling down to room temperature, 40 mL of water were added and the aqueous phase was extracted with DCM (2 x 40 mL). The combined organic phases were washed with water (2 x 150 mL), brine (1 x 50 mL) and then dried over anhydrous Na_2SO_4, concentrated under reduced pressure and purified by flash column chromatography using hexane:AcOEt (20:1) as eluent to give monomer **M8** as a white solid (249 mg, 84%).

^{1}H NMR (300 MHz, $CDCl_3$), δ (ppm): 7.48 (s, 2H, H_a), 2.85-2.70 (4H, H_b), 1.59-1.45 (2H, H_c), 1.38-1.11 (40H, $H_{d\text{-}f}$ + H_h + H_j), 0.91-0.77 (12H, H_g + H_i).

^{13}C NMR (75 MHz, $CDCl_3$), δ: 144.73 (q), 137.61 (CH_{Ar}), 83.41 (q), 42.03 (CH), 39.56 (CH_2), 32.02 (CH_2), 28.63 (CH_2), 25.48 (CH_2), 25.00 (CH_3), 23.35 (CH_2), 14.30 (CH_3), 10.84 (CH_3)

MS (MALDI-TOF): calculated for $C_{34}H_{60}B_2NaO_4$ $[M+Na]^+$: 577.462, found: 577.459.

Synthesis of monomer M9[279]

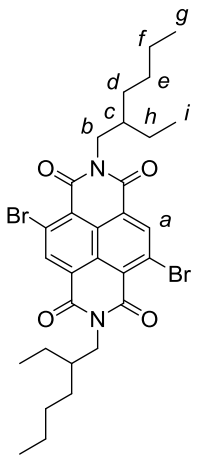

2,6-Dibromo-1,4,5,8-naphthalenetetracarboxylic dianhydride (**14**, 2.00 g, 4.70 mmol) and 2-ethylhexylamine (1.82 g, 14.1 mmol) were dissolved in AcOH (40 mL) and the resulting mixture was stirred at 120 ºC for 4 h. Then, the solvent was removed under reduced pressure and subsequently poured into 100 mL of MeOH. The precipitate was filtered, washed with MeOH and dried in vacuum. The crude product was dissolved in PE:DCM (1:1) and the remaining insoluble yellow solid was filtered off. The filtered solid turned out to be the pure product **M9**. The solvent of the filtrate was removed under reduced pressure and the residue was purified by flash column chromatography using the mixture PE:DCM (1:1→ 2:3) to yield more quantity of monomer **M9** (1.02 g, 34%).

^{1}H NMR (300 MHz, $CDCl_3$), δ (ppm): 9.00 (s, 2H, H_a), 4.22-4.09 (4H, H_b), 2.02-1.87 (2H, H_c), 1.46-1.22 (16H, $H_{d\text{-}f}$ + H_h), 0.99-0.84 (12H, H_g + H_i).

Synthesis of monomer M10

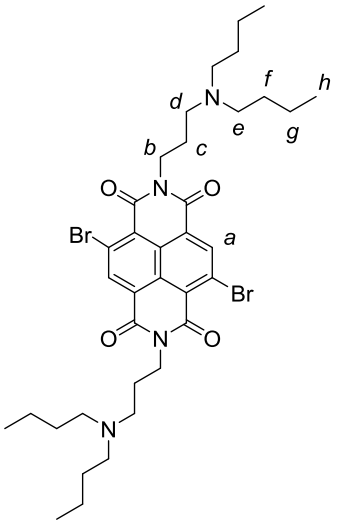

To a solution of 2,6-dibromo-1,4,5,8-naphthalenetetracarboxylic dianhydride (**14**, 500 mg, 1.17 mmol) in 15 mL of AcOH, 3-(dibutylamino)propylamine (660 μL, 2.92 mmol) was added slowly at room temperature and stirred at 130 ºC for 45 min. Upon completion, the reaction mixture was poured into cooled water and the aqueous phase was neutralized with Na_2CO_3 and extracted with chloroform until no color could be seen in the organic phase. The combined organic extracts were washed with brine, dried over Na_2SO_4, filtered and the solvent removed under reduced pressure. The crude product was purified by flash column chromatography using the mixture chloroform:EtOH (95:5) with 0.5% of NEt_3 as eluent to yield the product (200 mg, 23%).

^{1}H NMR (300 MHz, $CDCl_3$), δ (ppm): 8.99 (s, 2H, H_a), 4.28-4.18 (4H, H_b), 2.58 (t, J = 7.0 Hz, 4H, H_d), 2.40 (t, J = 7.6 Hz, 8H, H_e), 1.95-1.81 (4H, H_c), 1.46-1.21 (16H, H_f + H_g), 0.90 (t, J = 7.2 Hz, 12H, H_h).

^{13}C NMR (100 MHz, $CDCl_3$), δ (ppm): 160.87 (CO), 160.85 (CO), 139.14 (CH), 128.41 (q), 127.82 (q), 125.49 (q), 124.23 (q), 53.77 (CH_2), 51.89 (CH_2), 40.45 (CH_2), 29.27 (CH_2), 25.41 (CH_2), 20.85 (CH_2), 14.28 (CH_3).

MS (MALDI-TOF) calculated for $C_{36}H_{51}Br_2N_4O_4$ $[M+H]^+$: 761.228, found: 761.202.

5.2.3.4 Synthesis of Polymers P9-P11

Synthesis of polymer P9

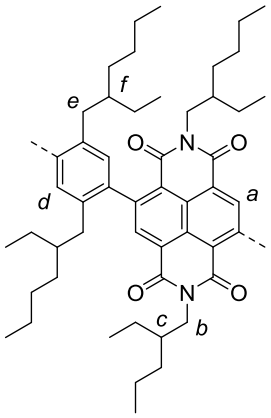

In a Schlenk flask three cycles of argon-vacuum were applied. Next, monomer **M9** (234 mg, 361 μmol), monomer **M8** (200 mg, 361 μmol), $NaHCO_3$ (1.21 g, 14.4 mmol) and $Pd(PPh_3)_4$ (8.34 mg, 7.22 μmol,) were dissolved in 8 mL of a mixture of THF:water (8:3) previously degassed. The reaction mixture was stirred and refluxed for 6 d. After that, 30 mL of chloroform and 30 mL of water were added to the mixture and the phases were separated. The aqueous phase was extracted with chloroform (2 x 30 mL) and the combined organic phases were washed with brine (1 x 100 mL), dried over Na_2SO_4 and the solvent removed under reduced pressure. The crude product was dissolved in 1.5 mL of chloroform and dripped into 200 mL of MeOH. The orange precipitate was filtered off and washed with MeOH (3 d), acetone (3 d), CH_3CN (2 d), and hexane (1 d) using a *Soxhlet* extractor to afford polymer **P9** (64.5 mg, 23%). SEC: M_n = 6405, M_w = 10694, PDI = 1.7.

^{1}H NMR (300 MHz, $CDCl_3$), δ (ppm): 8.92-8.82 (2H, H_a), 7.23-7.02 (2H, H_d), 4.29-4.03 (4H, H_b), 2.66-2.23 (4H, H_e), 2.05-1.91 (2H, H_c), 1.48-1.20 (18H, H_f + $CH_{2benzene}$), 1.17-0.81 (28H, CH_{2NDI} + CH_{3NDI}), 0.75-0.52 (12H, $CH_{3benzene}$)

MS (MALDI-TOF): The detection of the building block ($C_{52}H_{72}N_2O_4$ $[M]^+$: 788.548) of **P9** was demonstrated (Figure 69).

Synthesis of polymer P10

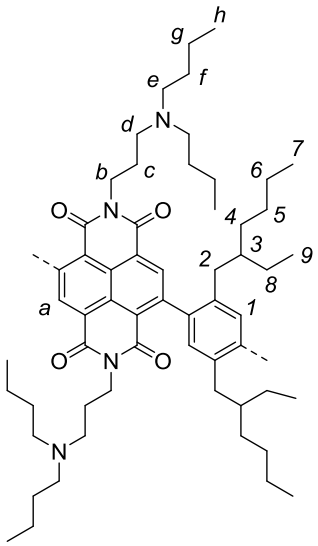

In a Schlenk flask three cycles of argon-vacuum were applied. Next, monomer **M10** (549 mg, 721 μmol), monomer **M8** (400 mg, 721 μmol), $NaHCO_3$ (2.42 g, 28.8 mmol) and $Pd(PPh_3)_4$ (16.7 mg, 14.4 μmol,) were dissolved in 10 mL of a mixture of THF:water (8:3) previously degassed. The reaction mixture was stirred and refluxed for 6 d. After that, 30 mL of chloroform and 30 mL of water were added to the mixture and the phases were separated. The aqueous phase was extracted with chloroform (2 x 30 mL) and the combined organic phases were washed with brine (1 x 100 mL), dried over Na_2SO_4 and the solvent removed under reduced pressure. The crude product was dissolved in 0.7 mL of chloroform and dripped into 200 mL of MeOH. The orange precipitate was filtered off and washed with MeOH (4 d), acetone (3 d) and CH_3CN (3 d) using a *Soxhlet* extractor to afford **P10** (90.7 mg, 14%). SEC: M_n = 4350, M_w = 6953, PDI = 1.6.

^{1}H NMR (300 MHz, CD_2Cl_2), δ (ppm): 8.82 (s, 2H, H_a), 7.18 (s, 2H, H_1), 4.49-3.82 (4H, H_b), 2.68-2.22 (16H, $H_{d\text{-}e}$ + H_2), 2.02-1.71 (4H, H_c), 1.69-1.52 (2H, H_3), 1.52-1.28 (16H, $H_{f\text{-}g}$), 1.18-0.80 (28H, H_h + $H_{4\text{-}6}$ + H_8), 0.77-0.55 (12H, H_7 + H_9).

MS (MALDI-TOF): The detection of the building block ($C_{58}H_{86}N_4O_4$ $[M]^+$: 902.664) of **P10** was demonstrated:

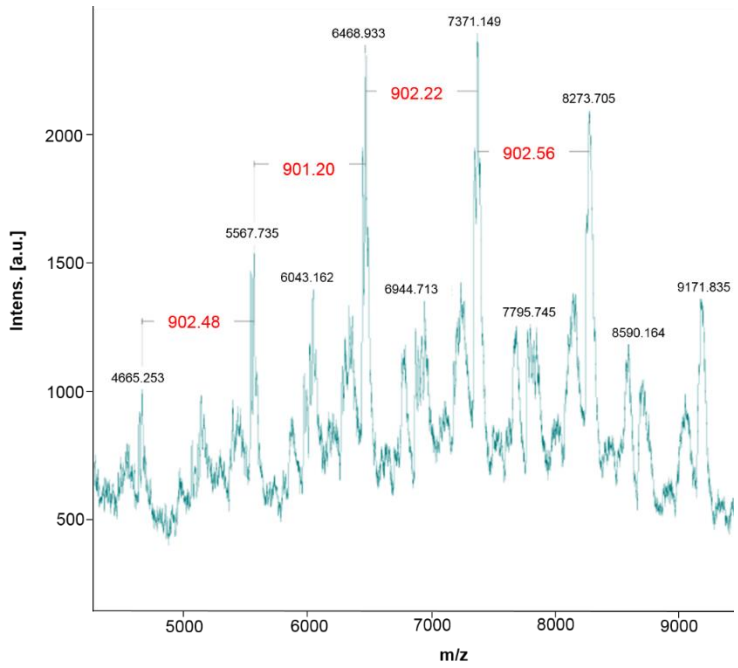

Figure 80. MALDI-TOF spectrum of polymer **P10**.

Synthesis of polymer P11

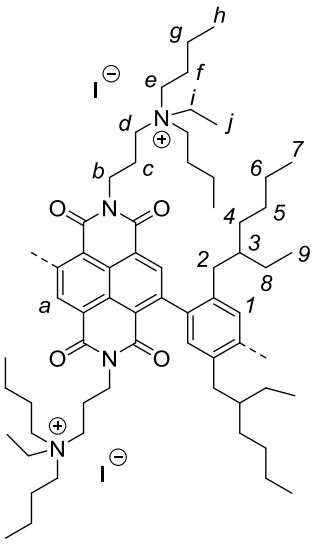

Copolymer **P10** (130 mg, 144 μmol) was dissolved in 2 mL of THF. Next, iodoethane (690 μL, 8.64 mmol) and 1 mL of DMF were added, and the solution was stirred for 5 d at room temperature in darkness. After that, the reaction was put into water and the resulting precipitate was filtered and washed with AcOEt for 1 d using a *Soxhlet* extractor. The solid was dissolved in DCM and the remained solid was filtered

off. The filtrated was evaporated under reduced pressure to give polymer **P11** as an orange solid (100 mg, 57%).

^{1}H NMR (300 MHz, CD_2Cl_2), δ (ppm): 8.97-8.60 (2H, H_a), 7.42-7.10 (2H, H_1), 4.52-4.05 (4H, H_b), 3.74-2.76 (16H, H_{d-e} + H_i), 2.61-2.12 (4H, H_2), 1.91-1.68 (6H, H_c + H_3), 1.56-1.33 (16H, H_{f-g}), 1.18-0.78 (34H, H_h + H_j + H_{4-6} + H_8), 0.78-0.48 (12H, H_7 + H_9).

5.3 Construction and Testing of Perovskite Solar Cells

5.3.1 Perovskite Solar Cells Employing P1-P6 as HTMs

5.3.1.1 Device Fabrication

a) Substrate and electron-transporting layer preparation

Prior to the deposition of the ETM, FTO-glass substrates (10 Ω sq^{-1}) were cleaned by ultrasonication in deionized water with soap (2% Hellmanex water solution) for 15 min. After rinsing with deionized water, the substrates were further ultrasonicated with EtOH and acetone each for 15 min. Finally, the substrates were dried under a nitrogen flow and, in order to eliminate any organic residual placed onto the substrate surface, they were further treated in an UV-ozone cleaner for 15 min. Afterwards, a TiO_2 compact layer was deposited on FTO via spray pyrolysis at 450 °C from a precursor solution of titanium diisopropoxide bis(acetylacetonate) and acetylacetone in EtOH. After the spraying, the substrates were left at 450 °C for 30 min and left to cool down to room temperature. Then, the mesoporous TiO_2 layer was deposited by spin coating for 10 s at 4000 rpm with a ramp of 2000 rpm s^{-1}, using 30 nm particle paste diluted in EtOH to achieve 150-200 nm thick layer. Subsequently, the substrates were sintered following a heating ramp up to 450 °C, at which they were left for 30 min under dry air flow. The mesoporous TiO_2 was doped by spin-coating of a solution of Li-TFSI in CH_3CN (10 mg mL^{-1}) at 3000 rpm for 10 s. Finally, the electrode with Li-doped mesoporous TiO_2 was completed with a second sintering process, the same as before. After cooling down to 150 °C, the substrates were

immediately transferred to a nitrogen atmosphere glove box for the deposition of the perovskite films.

b) Perovskite precursor solution and film preparation

The perovskite films were deposited from a precursor solution containing FAI (1 M), PbI_2 (1.1 M), CsI (0.05 M), MABr (0.2 M) and $PbBr_2$ (0.22 M) in anhydrous DMF:DMSO 4:1 (v:v) solvent, following a previously reported procedure.[280] The perovskite solution was spin coated in a nitrogen-filled glove box through a two-step program at 1000 and 5000 rpm for 10 and 20 s, respectively. During the second step, 150 μL of chlorobenzene were poured on the spinning substrate 5 s before the end of the program. The substrates were then annealed at 100 °C for 45 min in a nitrogen filled glove box.

c) Hole-transporting layer and top electrode preparation

After the perovskite annealing the substrates were cooled down for few minutes and the HTM solution was spun at 4000 rpm for 20 s. The solutions were prepared as follows: PTAA was dissolved in chlorobenzene at a concentration of 10 mg mL^{-1}, while the novel polymers (**P1**-**P6**) were dissolved in chlorobenzene at a concentration of 7 mg mL^{-1}. Finally, an 80 nm-thick gold electrode was thermally evaporated (through an appropriate shadow mask) on top of the HTM to produce a completed PSC device.

5.3.1.2 Device Characterization

The solar cells were measured using a 450 W xenon light source (Oriel). The light intensity was calibrated with a Si photodiode equipped with an IR-cutoff filter (KG3, Schott) and it was recorded during each measurement. Current-voltage characteristics of the cells were obtained by applying an external voltage bias while measuring the current response with a digital source meter (Keithley 2400). The voltage scan rate was 20 mV s^{-1}, and no device preconditioning was applied before starting the measurement, such as light soaking or forward voltage bias applied for a long time. The cells were masked with a black metal mask of 0.16 cm^2 to estimate the active area and reduce the influence of the scattered light.

The thickness of the layers were measured on a profilometre BRUKER DektakXT.

5.3.2 Perovskite Solar Cells Employing S1 and P7 as Additives

5.3.2.1 Device Fabrication

a) Electron-transporting layer preparation

Prior to the ETM deposition, FTO covered glass substrates were cleaned as previously explained. Afterwards, SnO_2 ETL were prepared as reported by Hagfeldt, Correa-Baena and co-workers.[281] Firstly, a 0.05 M solution of $SnCl_4$ x 5 H_2O in isopropanol was spin-coated onto clean FTO at 3000 rmp for 30 s with a ramp of 200 rpm s^{-1}. The layers were then annealed at 180 °C for 1 h. To increase the homogeneity of the films, the substrates were then treated by chemical bath deposition. For the solution of the chemical bath, 500 mg of urea were dissolved in 250 mL of deionized water, followed the addition of 10 μL mercaptoacetic acid and 0.5 mL of HCL (37% wt%). Finally, 0.108 mg of $SnCl_2$ x 2 H_2O were added. The substrates were placed vertically in a glass container filled with the solution and kept in a water bath for 3 h. The temperature was maintained at 70 °C.[280] After the end of the process, the substrates were sonicated in deionized water for 2 min, rinsed with EtOH, dried with compressed air and annealed at 180 °C for 1 h. Prior to the perovskite deposition, the substrates were cleaned by UV-ozone treatment.

b) Perovskite precursor solution and film preparation

The perovskite films were deposited from a precursor solution with the same composition as previously described in section 5.3.1.1. The stabilized devices using additives **S1** and **P7** were prepared using the same precursor solution, in which **S1** and **P7** were dissolved (2 mg mL^{-1}). The perovskite solution was spin-coated onto FTO covered glass substrates in a nitrogen-filled glove box following a two-step procedure at 1000 and 6000 rpm for 10 and 20 s, respectively. During the second step, 200 μL of chlorobenzene were poured on the spinning substrate 5 s before the end of the program. The substrates were then annealed at 100 °C for 40 min in a nitrogen-filled glove box.

c) Hole-transporting layer and top electrode preparation

After perovskite deposition, the substrates were cooled down for few minutes and *spiro*-OMeTAD (0.06 M in chlorobenzene) was spun at 4000 rpm for 20 s. *Spiro*-OMeTAD was doped with Li-TFSI, *t*BP and FK209, with the molar ratio to *spiro*-OMeTAD of 0.5, 3.5 and 0.05, respectively. Finally, an 80 nm-thick gold top electrode was thermally evaporated (through an appropriate shadow mask) on top of the HTM to produce a completed PSC device.

5.3.2.2 Device Characterization

Current–voltage characteristics were recorded by applying an external potential bias to the cells while recording the generated photocurrent with a digital source meter (Keithley Model 2401). The settling time was set to 200 ms. The light source was Solinox A20 solar simulator (Solaronix), calibrated with Si reference diode, the light intensity was 100 mV cm^{-2}. The aperture area was 0.16 cm^2.

For stability measurements, devices were kept at MPP using software Rera. The temperature and humidity tracking during the stability experiments were recorded using TFA digital data logger for measuring temperature, humidity and pressure.

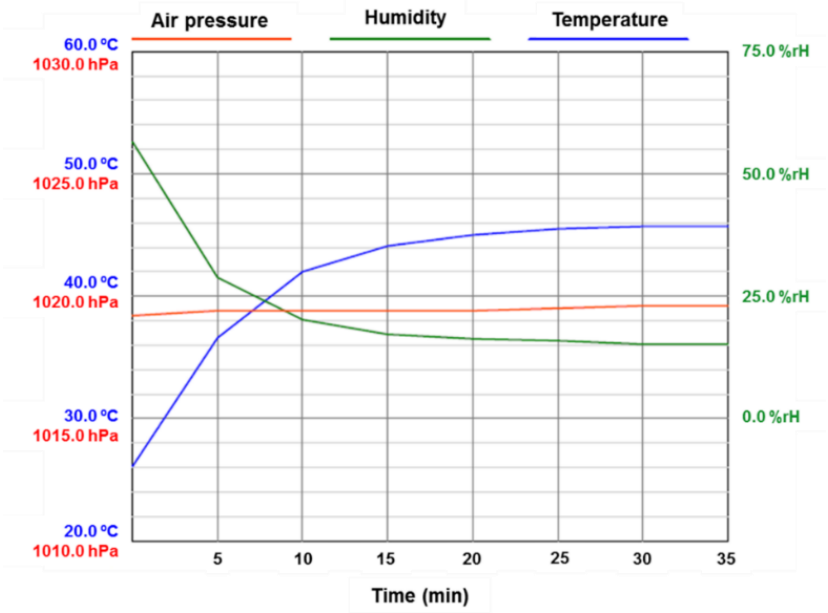

Figure 81. Temperature and humidity tracking in the cavity of the solar simulator where the MPP measurements took place (short-term stability measurement).

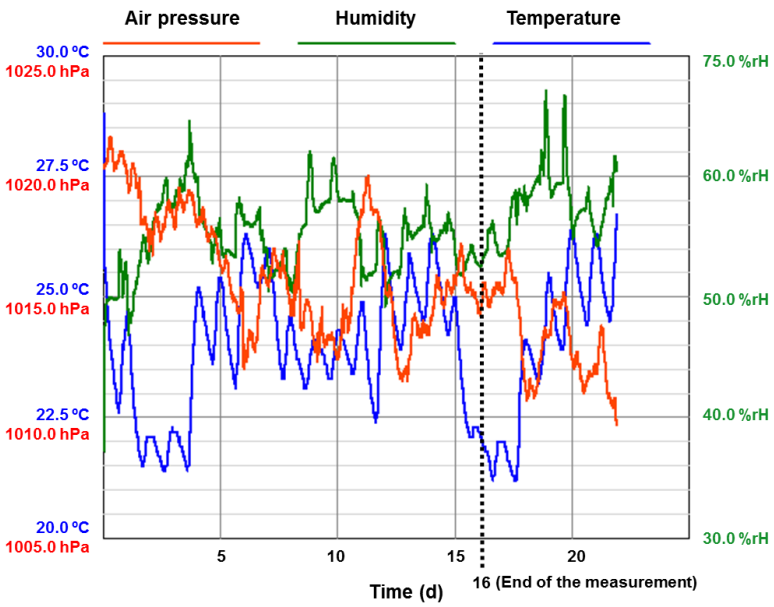

Figure 82. Temperature and humidity tracking in the place where the cells were kept until they were measured (long-term stability measurement)

6. SUMMARY/RESUMEN

6 SUMMARY/RESUMEN

6.1 Summary

Since the discovery of fire by primitive humans, mankind has been searching ways to take advantage of different energy sources. By the 19th century, nearly all of the world´s energy was produced from traditional biomass (essentially burning wood and other organic matter) as is shown in Figure 83. However, since the industrial revolution and especially over the past several decades, the consumption of energy has undergone an unprecedented change and nowadays, fossil fuels (coil, oil and natural gas) are the world´s dominant energy source (Figure 83).

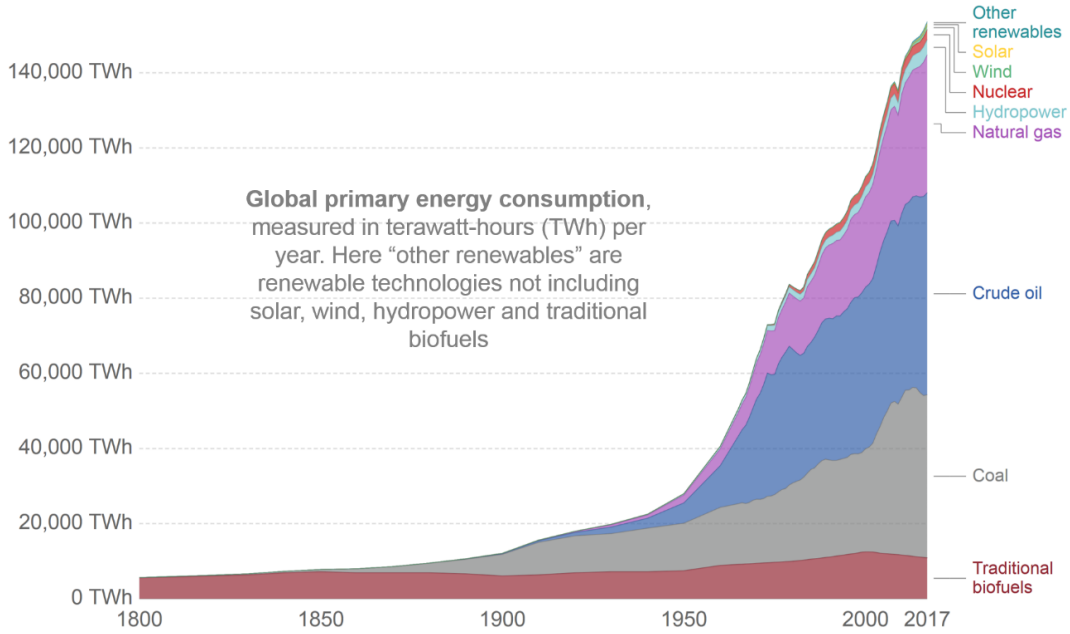

Figure 83. Global energy production from 1800 to 2017.[282]

However, our actual energy system based on fossil fuels has an important environmental impact. In this regard, to produce energy from fossil fuels and convert them into suitable forms for human use, they have to be burned. This process releases a great deal of pollutants (CO, CO_2, SO_2, NO_x, N_2O, etc), which in turn traps heat in our atmosphere, making them the primary contributors to global warming and climate change. In fact, the concentration of CO_2 (around 410 ppm) is the highest in 650,000 years, which has increased the global temperature on Earth by about 0.8 ºC. As a result, there are already evidences, which point that the climate is changing and observable

phenomena are appearing. For instance, the arctic ice is decreasing 12.8% per decade while the sea level is increasing 3.3 mm per year. The scenario is envisaged to be worse. In fact, by 2040 is expected an increase in the world population from 7.4 billion to more than 9.2 billion people. This growth together with technology advancements will result in an increase in the energy demand.

These concerns together with the finite nature of fossil fuels have triggered society to the exploration and development of clean, inexpensive and renewable energy sources. In this sense, of the possible renewable energy approaches, solar energy is probably the best alternative to replace the use of fossil fuels. In fact, within one hour, we receive enough sunlight to provide the world with enough electricity for an entire year. For this reason, scientists all over the world have been focusing on the development of new energy technologies for converting solar energy into electricity. Among them, PSCs have emerged as promising photovoltaic technology due to their high PCE, low cost or easy fabrication processes. In this regard, the performance of PSCs has increased at an unprecedented rate, with efficiencies currently exceeding 24%. However, this exceptional fast growth is not yet enough to guarantee a spot in the market of solar cell considering there are still several issues that have to be resolved to promote PSCs as a feasible photovoltaic technology. These include long-term stability, toxicity, hysteresis or scale up of the cell area. The limited long-term stability of PSCs is one of the biggest challenges to be addressed, since they suffer from low stability due to high sensitivity to environmental factors like moisture, oxygen, UV light or high temperatures.

Briefly, the work carried out in the present thesis aimed to develop new materials for their application in PSCs with enhanced performance and stability, in order to solve the main obstacles currently hindering the further development of this kind of devices. In particular, three different strategies were followed:

In **Chapter 2** we described the development of new polymeric hole-transporting materials for the application in PSCs. In this sense, a series of novel polymers (**P1**-**P6**) derived from the combination of different units including thiophene, triarylamine and sprirobifluorene, were successfully synthesized (Figure 84).

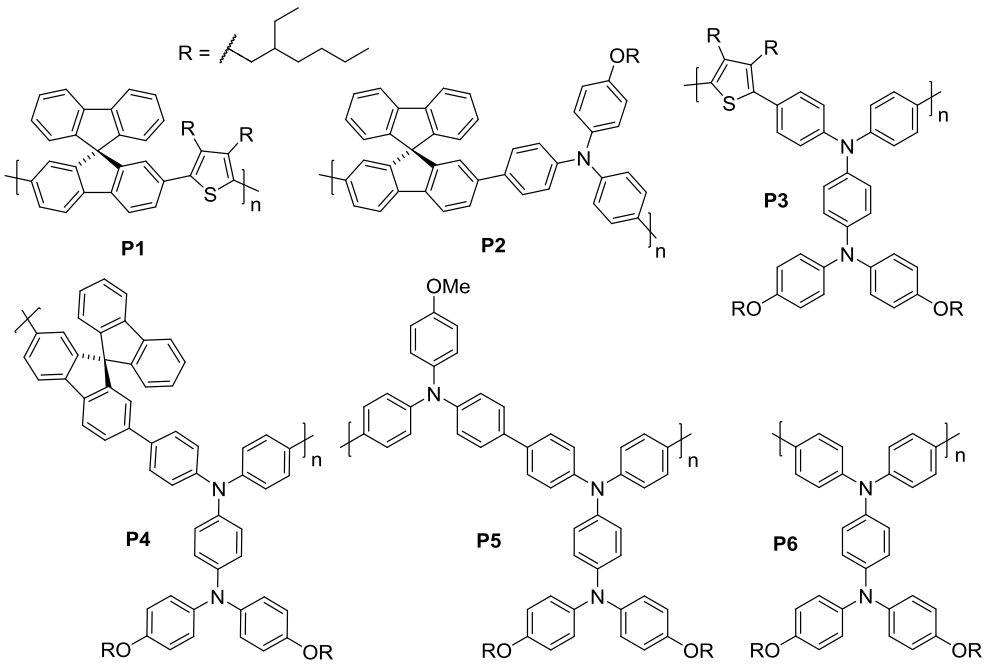

Figure 84. Chemical structures of the target polymers **P1**-**P6**.

These new materials were characterized by thermal, optical and electrochemical techniques in order to evaluate their properties. In a further step, PSCs were fabricated using polymers **P1**-**P6** as dopant-free HTMs in order to determine their performance and develop a structure-property relationship. Interestingly, thiophene-containing polymers (**P1** and **P3**) gave very low efficiencies while the rest of the polymers showed good efficiencies, which in case of **P4** and **P6**, with PCEs of 12.8 and 12.4%, respectively, were highly comparable to those obtained using the reference material PTAA. By studying the series resistance of the different cells, it was possible to conclude that the polymers which gave the lowest efficiencies had the highest series resistance. In general, the novel materials enabled efficient PSCs without the use of chemical doping to enhance charge transport. The presence of dopants or additives has been linked to long-term degradation, so the possibility of working without doping additives is undoubtedly an important step towards improving stability of this kind of solar cells. In addition, we demonstrated that PSCs based on **P4** and **P6** showed higher thermal stability than devices based on PTAA.

In **Chapter 3** we presented a strategy to improve the quality of the perovskite layer, which is of paramount importance for achieving both efficiency and stability of PSCs. In this regard, the incorporation of additives into the perovskite layer has been

demonstrated to be a suitable strategy for enhancing the quality of that layer. In this work, three novel semiconducting compounds containing perfluorinated side chains in their structure (**S1**, **P7** and **P8**) were developed and used as additives in PSCs. The novel materials contain 26 fluorine atoms per unit, which is the largest amount of fluorine atoms reported for additives in PSCs (Figure 85).

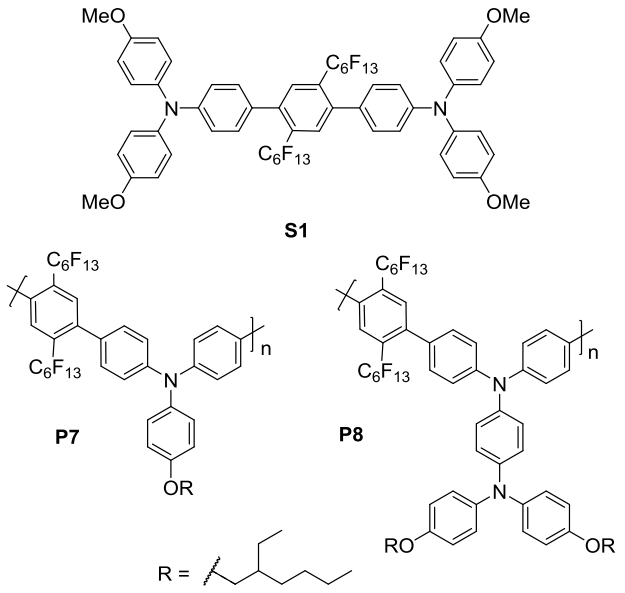

Figure 85. Chemical structures of the target compounds **S1**, **P7** and **P8**.

A novel small molecule (**S1**) and two polymeric compounds (**P7** and **P8**) were successfully synthesized and their chemical, thermal and optoelectronic properties were studied. Moreover, they were incorporated into the perovskite layer as additives and their effect on the film formation, stability and performance of PSCs was studied. In this regard, the doped-perovskite layer showed larger crystals and reduced grain boundaries compared to the undoped one. Moreover, the stability of PSCs based on additives **S1** and **P7** was studied. **S1** and **P7** were chosen for the stability study in order to check how the incorporation of small molecule and polymeric nature compounds, respectively, was affecting the PSC stability. As a result, **S1**- and **P7**-based devices showed increased stability, maintaining 94 and 85% of their initial power, respectively, after 80 minutes, while reference devices broke down completely measured under the same conditions. Importantly, the semiconducting nature of the novel additives might be favoring charge transport, allowing **S1**-containing device to achieve an improved

PCE value of 17%. On account of this, our newly developed perfluorinated materials guarantee both efficiency and stability in PSCs.

In **Chapter 4** we have designed and synthesized a new family of NDI-based polymers (**P9**-**P11**) with the potential to be used as ETMs in PSCs. Furthermore a series of NDI-based small molecules (**MC1**-**MC3**) bearing identical fragments to those of polymers **P9**-**P11** have also been prepared for comparison purposes (Figure 86).

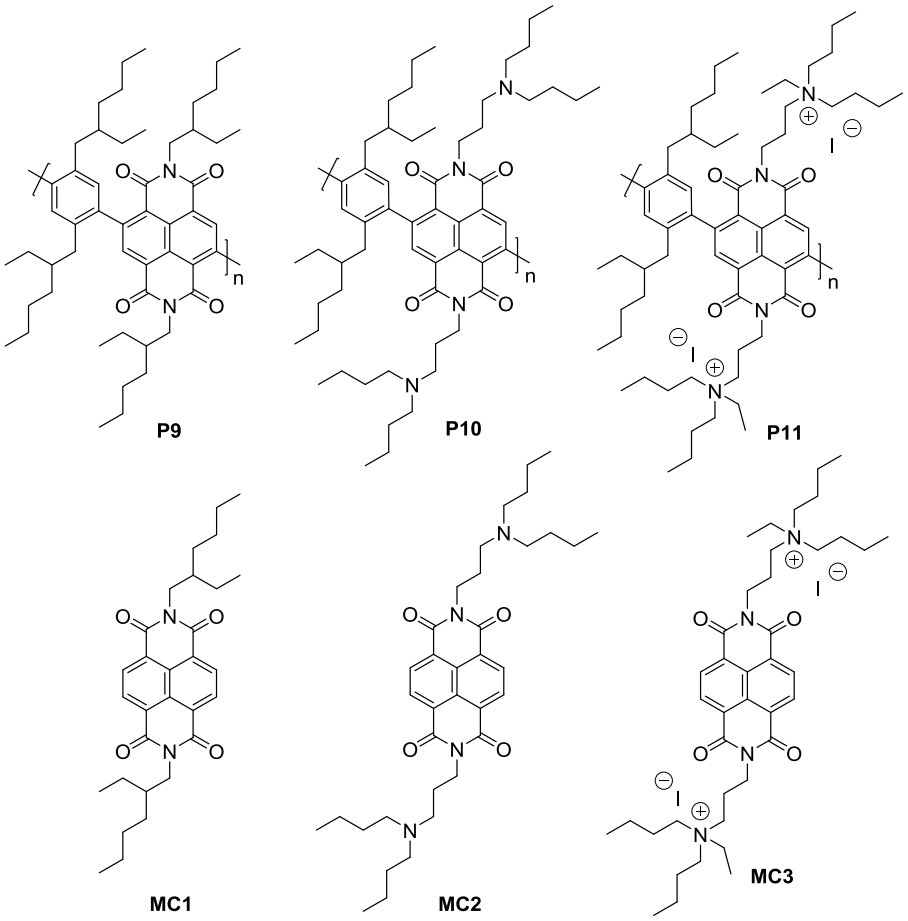

Figure 86. Chemical structures of polymers **P9**-**P11** and molecules **MC1**-**MC3**.

The backbone of the polymers is composed of a benzene unit in combination with different NDI-based moieties, which are well-known to possess high electron-transporting and hole-blocking abilities. Furthermore, they were designed to be processed from solution, so branched alkyl chains were introduced in the benzene unit. The new polymers were characterized by thermal, optical and electrochemical techniques in order to evaluate if they could be used as ETMs in PSCs. In this regard, they showed suitable energy levels, high thermal stability with no phase transitions

under the temperature range of PSCs operation. In view of all this properties, the novel polymers would be attractive candidates for using them as ETMs in PSCs.

Moreover, the charge transporting properties of the model compounds **MC1**-**MC3** were studied. Both, the amino and iodine-quaternized ammonium groups in molecules **MC2** and **MC3**, respectively, exhibited higher pseudo-photoconductivity compared to molecule **MC1**. Polymers **P9**-**P11** display the same structural fragments than model compounds **MC1**-**MC3**. Thus, in principle we could expect the same tendency in the charge transporting properties of these polymers. To confirm this trend, we are currently collaborating with Prof. Seki at Kyoto University (Japan). In any case, to demonstrate the applicability of the proposed polymers, they should be tested in PSCs as ETMs in further experiments.

6.2 Resumen

Desde el descubrimiento del fuego por los primeros homínidos, la humanidad ha estado buscando maneras de aprovechar las diferentes fuentes de energía. En el siglo XIX, casi toda la energía del mundo se producía a partir de biomasa (esencialmente leña y otra materia orgánica) como se muestra en la Figura 87. Sin embargo, desde la revolución industrial y especialmente en las últimas décadas, el consumo de energía ha experimentado un cambio sin precedentes y hoy en día, los combustibles fósiles (carbón, petróleo y gas natural) son la fuente de energía dominante en todo el mundo (Figura 87).

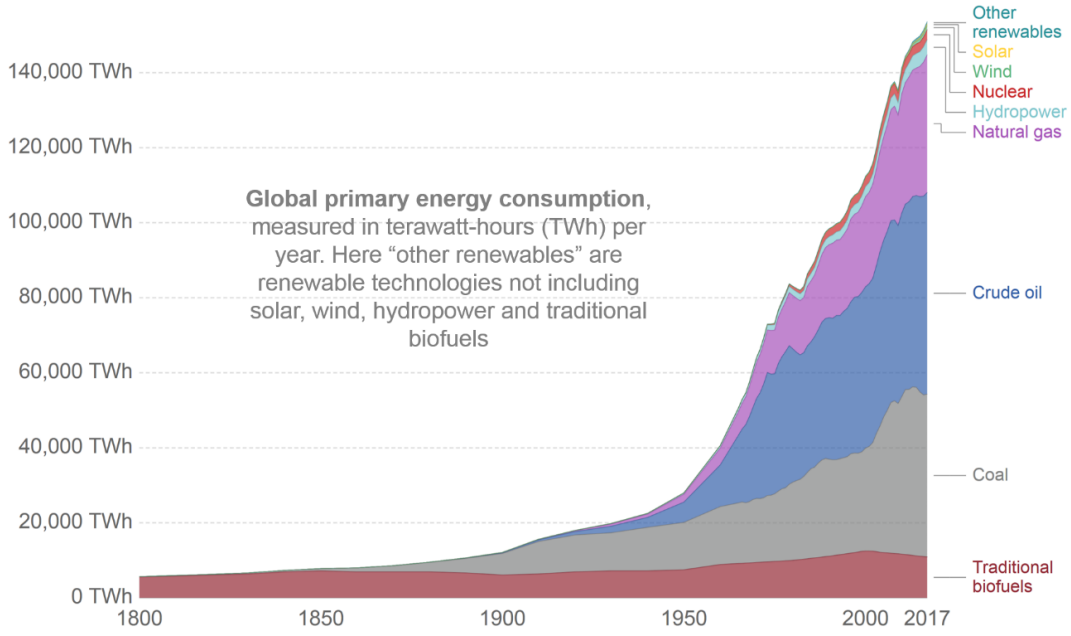

Figura 87. Producción mundial de energía desde 1800 a 2017.[282]

Sin embargo, nuestro actual sistema energético, basado en los combustibles fósiles, tiene un gran impacto medioambiental. A este respecto, para extraer energía de los combustibles fósiles y transformarlos en formas de energía que puedan ser usadas por el ser humano, éstos tienen que ser sometidos a un proceso de combustión. Durante este proceso se libera una gran cantidad de contaminantes (CO, CO_2, SO_2, NO_x, N_2O, etc), que a su vez atrapan el calor en nuestra atmósfera, convirtiéndolos en los principales contribuyentes al calentamiento global y al cambio climático. De hecho, la concentración de CO_2 (410 ppm aproximadamente) en nuestra atmósfera es la más alta en 650,000 años, lo que ha dado lugar a un incremento de la temperatura de la tierra en

aproximadamente 0.8 ºC. Como resultado, ya hay evidencias que apuntan que el clima está cambiando y ya se pueden observar algunos efectos. Por ejemplo, la cantidad de hielo presente en el ártico está sufriendo una disminución del 12.8% por década, lo que a su vez está incrementando el nivel del mar 3.3 mm por año, y se prevé que la situación empeore. De hecho, para 2040 se espera un aumento de la población mundial de 7.4 billones a más de 9.2 billones de personas. Este crecimiento, junto con los avances tecnológicos, dará lugar a un aumento de la demanda de energía.

Teniendo en cuenta estos factores junto con la naturaleza finita de los combustibles fósiles, nuestra sociedad debe buscar y desarrollar nuevas formas de energía que sean limpias, económicas y renovables. En este sentido, de entre las fuentes de energía renovables, la energía solar es probablemente la mejor alternativa al uso de combustibles fósiles, ya que la Tierra recibe en tan solo una hora toda la energía que requiere actualmente toda la humanidad para funcionar durante un año. Por esta razón, científicos de todo el mundo están trabajando en la búsqueda de sistemas capaces de transformar toda esa energía solar en energía eléctrica de una forma eficiente. Entre ellas, las celdas solares de perovskita se han convertido en una de las tecnologías más prometedoras en los últimos tiempos debido a sus altas eficiencias, bajo coste o sus fáciles procesos de fabricación. De hecho, es de destacar que en tan solo unos pocos años, las eficiencias de conversión energéticas de este tipo de celdas solares han aumentado rápidamente, alcanzando actualmente eficiencias de más del 24%. Sin embargo, este rápido crecimiento no es suficiente para hacerse un hueco en el mercado fotovoltaico ya que todavía persisten grandes desafíos para hacer de estas celdas una tecnología viable. Estos desafíos incluyen, la estabilidad a largo plazo, la toxicidad, la histéresis o la fabricación a gran escala. La inestabilidad a largo plazo es unos de los mayores desafíos a ser abordados, ya que las celdas solares de perovskita sufren baja estabilidad frente a factores medioambientales como humedad, oxígeno, luz UV o altas temperaturas.

El trabajo realizado en esta tesis se centró en la búsqueda de nuevos materiales que den lugar a celdas solares de perovskita estables y eficientes, y de esta forma resolver los principales obstáculos que actualmente dificultan el desarrollo de este tipo de dispositivos. En particular, se siguieron tres estrategias distintas:

En el **Capítulo 2** se describe el desarrollo de nuevos polímeros conductores de huecos para su posterior aplicación en celdas solares de perovskita. En este sentido, se prepararon una serie de polímeros (**P1**-**P6**) basados en la combinación de diferentes unidades como tiofenos, triarilaminas o espirobifluorenos (Figura 88).

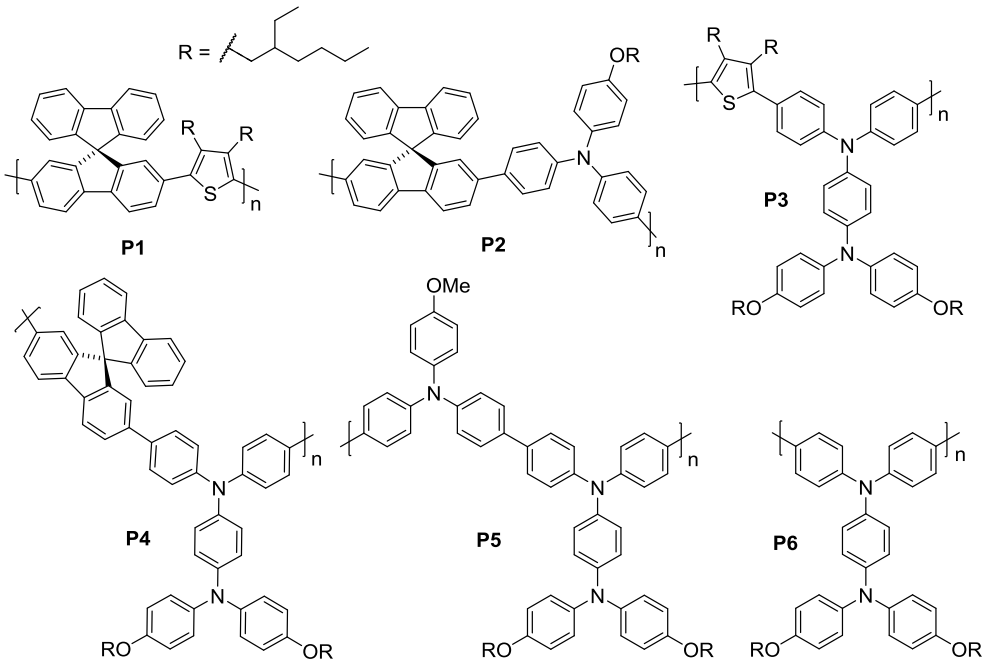

Figura 88. Estructura química de los polímeros sintetizados **P1**-**P6**.

Los nuevos materiales se caracterizaron térmica, óptica y electroquímicamente con el objetivo de estudiar sus propiedades. Posteriormente, estos 6 polímeros se evaluaron como transportadores de huecos en celdas solares de perovskita sin la necesidad de usar ningún aditivo o material dopante, y de este modo establecer algún tipo de relación entre la estructura de los polímeros y la actividad fotovoltaica. Curiosamente, los polímeros que contenían unidades de tiofeno en su estructura (**P1** y **P3**) dieron lugar a las eficiencias más bajas, mientras que el resto de polímeros mostraron eficiencias aceptables. En el caso de **P4** y **P6**, las eficiencias fueron similares a las que se obtuvieron usando el material de referencia PTAA, con valores del 12.8 y 12.4%, respectivamente. Estudiando la resistencia en serie de los diferentes dispositivos, se pudo concluir que los polímeros que originaban las celdas con eficiencias más bajas, presentaban la resistencia en serie más alta. En general, los nuevos polímeros dieron lugar a celdas solares eficientes sin la necesidad de usar ningún dopante o aditivo para mejorar el transporte de carga. De hecho, la presencia

de aditivos o dopantes se ha relacionado con la degradación de las celdas, por lo que la posibilidad de trabajar sin aditivos o dopantes es sin duda un gran paso hacia la mejora de la estabilidad de éste tipo de celdas. Además, se demostró que los dispositivos fabricados usando los polímeros **P4** y **P6** tenían una mayor estabilidad térmica comparada con los dispositivos que usaban el material de referencia PTAA.

En el **Capítulo 3** se presenta una nueva estrategia para mejorar la calidad de la capa de perovskita, lo que es de gran importancia para alcanzar tanto una buena eficiencia como estabilidad en las celdas solares de perovskita. En este sentido, la incorporación de aditivos a la capa de perovskita ha demostrado ser una estrategia adecuada para mejorar la calidad de dicha capa. En este trabajo, se han desarrollado tres nuevos semiconductores orgánicos (**S1**, **P7** y **P8**) con cadenas perfluoradas en su estructura para su uso como aditivos en celdas solares de perovskita. Cada material contiene 26 átomos de flúor por unidad, lo que constituye la mayor cantidad de átomos de flúor que se ha reportado para aditivos en este tipo de celdas (Figura 89).

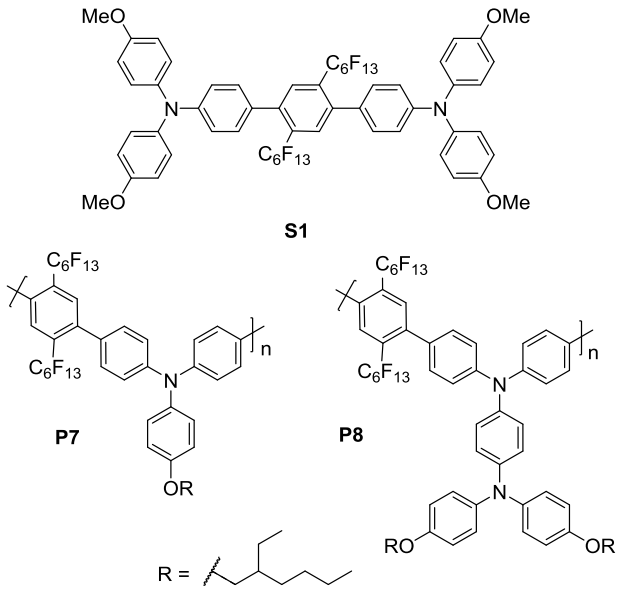

Figura 89. Estructura química de los materiales **S1**, **P7** y **P8**.

Se han sintetizado dos nuevos polímeros (**P7** y **P8**) y una molécula (**S1**) y estudiado sus propiedades químicas, térmicas y optoelectrónicas. Además, los nuevos materiales se incorporaron a la capa de perovskita como aditivos y se estudió el efecto que tenían en la formación de dicha capa, en la estabilidad y en el funcionamiento de las celdas solares. En este contexto, las capas de perovskita que contenían aditivos

mostraban cristales más grandes, lo que implica menos límites de granos, comparado con las capas sin dopar. Además, se estudió la estabilidad de celdas solares, donde la capa de perovskita se había tratado con los aditivos. Para este fin, se eligieron **S1** y **P7** para comprobar de qué manera la incorporación de moléculas y compuestos de naturaleza polimérica, respectivamente, afectaba a la estabilidad de los dispositivos. Como resultado, las celdas basadas en **S1** y **P7** mostraron una mayor estabilidad comparada con la celda de referencia (sin aditivos), manteniendo el 94 y el 85% de su potencia inicial, respectivamente, después de 80 minutos, mientras que los dispositivos de referencia se destruían completamente, medidos bajo las mismas condiciones. Es importante destacar que el carácter semiconductor de los nuevos aditivos podría estar favoreciendo el transporte de carga, permitiendo de este modo, que el dispositivo basado en **S1** alcanzase un valor de eficiencia del 17%. Por tanto, los nuevos materiales perfluorados garantizan tanto una buena eficiencia como estabilidad en celdas solares de perovskita.

En el **Capítulo 4** se ha diseñado y sintetizado una nueva familia de polímeros (**P9**-**P11**) basados en bis(naftaleno diimidas), con el potencial de ser usados como materiales trasportadores de electrones en celdas solares de perovskita. Además, se sintetizaron una serie de moléculas basadas en la unidad de bis(naftaleno diimida) (**MC1**-**MC3**) con fragmentos idénticos a los de los polímeros **P9**-**P11**, con el objetivo de hacer una comparación entre moléculas y polímeros (Figura 90).

Los polímeros están compuestos de una unidad de benceno en combinación con diferentes unidades de bis(naftaleno dimida), que son muy conocidas por poseer una gran habilidad para transportar electrones, así como la capacidad para bloquear huecos. Además, los polímeros fueron diseñados para ser procesados en disolución, para lo que se introdujeron cadenas alquílicas en la unidad de benceno. Los materiales se caracterizaron térmica, óptica y electroquímicamente para evaluar si eran aptos para ser utilizados como transportadores de electrones en celdas solares de perovskita. A este respecto, los polímeros presentaban unos niveles electrónicos adecuados y gran estabilidad térmica, sin cambios de fases en el rango de temperatura en el que suelen funcionar este tipo de celdas. En vista a las propiedades, los polímeros serían

candidatos adecuados para utilizarlos como transportadores de electrones en celdas solares de perovskita.

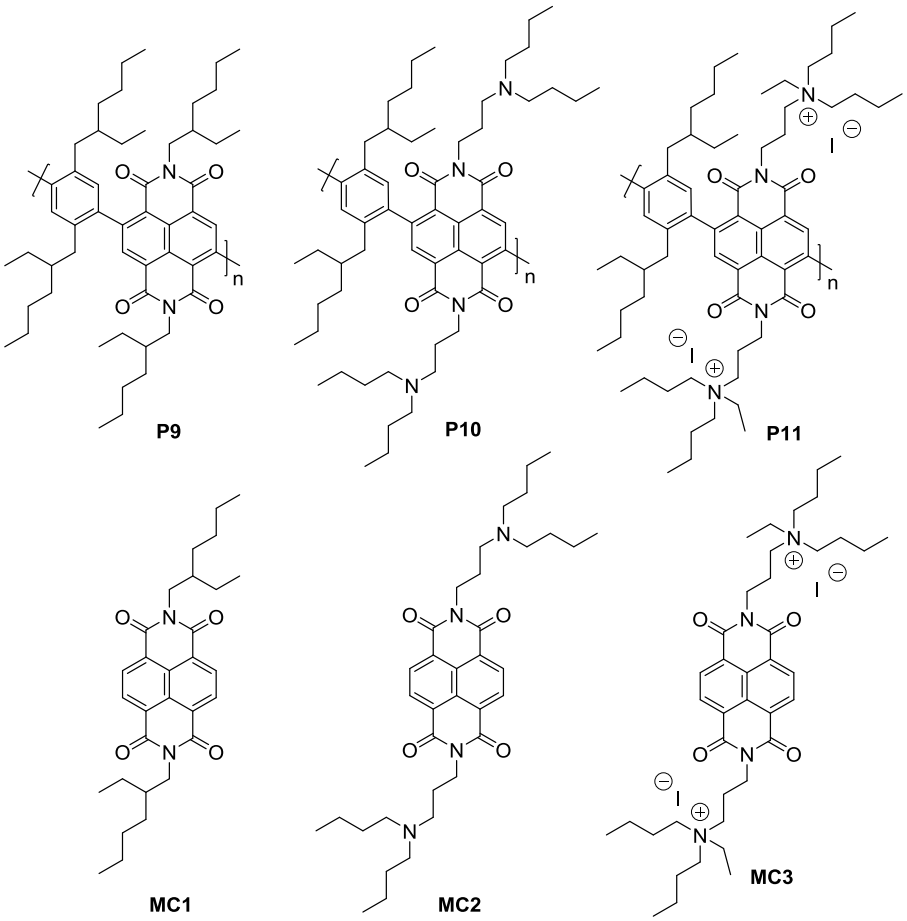

Figura 90. Estructuras químicas de los polímeros **P9**-**P11** y de las moléculas **MC1**-**MC3**.

Además, se estudiaron las propiedades de transporte de cargas de las moléculas **MC1**-**MC3**. Tanto **MC2** como **MC3**, que tienen fragmentos con amina terciaria y cuaternaria, respectivamente, mostraron mayor pseudo-fotoconductividad en comparación con la molécula **MC1**. Los polímeros **P9**-**P11** tienen los mismos fragmentos estructurales que las moléculas **MC1**-**MC3**. Por lo tanto, en principio, se podría esperar la misma tendencia en las propiedades de transporte de carga en estos polímeros. Para confirmar esta hipótesis, actualmente se está colaborando con el Prof. Seki de la Universidad de Kyoto (Japón). En cualquier caso, para demostrar la aplicabilidad de los polímeros propuestos, se deben de probar como materiales trasportadores de electrones en celdas solares de perovskita.

7. REFERENCES

7 REFERENCES

[1] https://www.worldenergy.org/work-programme/strategic-insight/survey-of-energy-resources-and-technologies/.

[2] A. P. Mathews, *Procedia Comput. Sci.*, **2014**, *32*, 731–737.

[3] https://scripps.ucsd.edu/programs/keelingcurve/.

[4] J. A. Church, N. J. White, *Geophys. Res. Lett.*, **2006**, *33*, L01602.

[5] K. E. Kunkel, T. R. Karl, D. R. Easterling, K. Redmond, J. Young, X. Yin, P. Hennon, *Geophys. Res. Lett.*, **2013**, *40*, 1402–1408.

[6] K. E. Kunkel, T. R. Karl, H. Brooks, J. Kossin, J. H. Lawrimore, D. Arndt, L. Bosart, D. Changnon, S. L. Cutter, N. Doesken, K. Emanuel, P. Y. Groisman, R. W. Katz, T. Knutson, J. O'Brien, C. J. Paciorek, T. C. Peterson, K. Redmond, D. Robinson, J. Trapp, R. Vose, S. Weaver, M. Wehner, K. Wolter, D. Wuebbles, *Am. Meteorol. Soc.*, **2013**, *94*, 499–514.

[7] https://climate.nasa.gov/images-of-change?id=623#623-arctic-sea-ice-coverage-hits-record-low.

[8] Outlook for Energy: A View to 2040, **2018**.

[9] International Energy Outlook, **2017**.

[10] UNFCCC. 2015 Adoption of the Paris Agreement. I: Proposal by the President (Draft Decision), United Nations Office, Geneva (Switzerland). 1–105.

[11] D. Reckien, M. Salvia, O. Heidrich, J. M. Church, F. Pietrapertosa, S. De Gregorio-Hurtado, V. D'Alonzo, A. Foley, S. G. Simoes, E. K. Lorencová, H. Orru, K. Orru, A. Wejs, J. Flacke, M. Olazabal, D. Geneletti, E. Feliu, S. Vasilie, C. Nador, A. Krook-Riekkola, M. Matosović, P. A. Fokaides, B. I. Ioannou, A. Flamos, N.-A. Spyridaki, M. V. Balzan, O. Fülöp, I. Paspaldzhiev, S. Grafakos, R. Dawson, *J. Clean. Prod.*, **2018**, *191*, 207–219.

[12] D. W. Cash, *Energy Res. Soc. Sci.*, **2018**, *35*, 224–226.

[13] BP Statistical Review of World Energy, **2018**.

[14] https://www.nytimes.com/2007/06/03/magazine/03wwln-essay-t.html.

[15] T. Wolfgang, *Organic solar cells: Theory, Experiment, and Device Simulation*; Springer.; **2014**.

[16] F. H. Alharbi, S. Kais, *Renew. Sustain. Energy Rev.*, **2015**, *43*, 1073–1089.

[17] https://pveducation.org/.

[18] G. Antonicelli, Thesis, University of the Basque Country (Donostia-San Sebastián), **2017**.

[19] D. J. Friedman, *Curr. Opin. Solid State Mater. Sci.*, **2010**, *14*, 131–138.

[20] S. Rühle, *Sol. Energy*, **2016**, *130*, 139–147.

[21] W. Shockley, H. J. Queisser, *J. Appl. Phys.*, **1961**, *32*, 510–519.

[22] H. K. A. Shah, P. Torres, R. Tscharner, N. Wyrsch, *Science*, **1999**, *285*, 692–699.

[23] A. E. Brooks, in *Future Energy: Improved, Sustainable and Clean Options for our Planet (Ed: Trevor Letcher)*; **2013**; 383–404.

[24] C. Lin, in *The Current Trends of Optics and Photonics (Ed: Chen-Chung Lee)*; **2015**; 237–259.

[25] N. Marinova, S. Valero, J. L. Delgado, *J. Colloid Interface Sci.*, **2017**, *488*, 373–389.

[26] J. Jean, P. R. Brown, R. L. Jaffe, T. Buonassisi, V. Bulović, *Energy Environ. Sci.*, **2015**, *8*, 1200–1219.

[27] T. D. Lee, A. U. Ebong, *Renew. Sustain. Energy Rev.*, **2017**, *70*, 1286–1297.

[28] A. Mohammad Bagher, M. Mahmoud Abadi Vahid, *Am. J. Opt. Photonics*, **2015**, *3*, 94–113.

[29] M. A. Green, Y. Hishikawa, E. D. Dunlop, D. H. Levi, M. A. Green, J. Hohl, E. Masahiro, Y. Anita, W. Y. H. Baillie, *Prog. Photovoltaics Res. Appl.*, **2019**, *27*, 3–12.

[30] T. Ibn-Mohammed, S. C. L. Koh, I. M. Reaney, A. Acquaye, G. Schileo, K. B. Mustapha, R. Greenough, *Renew. Sustain. Energy Rev.*, **2017**, *80*, 1321–1344.

[31] https://energyeducation.ca/encyclopedia/types_of_photovoltaic_cells.

[32] K. L. Chopra, P. D. Paulson, V. Dutta, *Prog. Photovoltaics Res. Appl.*, **2004**, *12*, 69–92.

[33] W. Qarony, M. I. Hossain, M. K. Hossain, U. M. Jalal, A. Haque, A. R. Saad, Y. H. Tsang, *Results Phys.*, **2017**, *7*, 4287–4293.

[34] H. Sai, T. Matsui, T. Koida, K. Matsubara, M. Kondo, S. Sugiyama, H. Katayama, Y. Takeuchi, I. Yoshida, *Appl. Phys. Lett.*, **2015**, *106*, 213902.

[35] G. H. Carey, A. L. Abdelhady, Z. Ning, S. M. Thon, O. M. Bakr, E. H. Sargent,

Chem. Rev., **2015**, *115*, 12732–12763.

[36] NREL Chart of Best Research-Cell Efficiencies (https://www.nrel.gov/pv/cell-efficiency.html), **2019**.

[37] N. Kaur, M. Singh, D. Pathak, T. Wagner, J. M. Nunzi, *Synth. Met.*, **2014**, *190*, 20–26.

[38] G. J. Hedley, A. Ruseckas, I. D. W. Samuel, *Chem. Rev.*, **2017**, *117*, 796–837.

[39] M. Privado, C. R. Seco, R. Singhal, P. D. La Cruz, F. Langa, G. D. Sharma, E. Palomares, *ACS Energy Lett.*, **2018**, *3*, 2418–2424.

[40] G. N. Tiwari, R. K. Mishra, S. C. Solanki, *Appl. Energy*, **2011**, *88*, 2287–2304.

[41] H. Youn, H. J. Park, L. J. Guo, *Small*, **2015**, *11*, 2228–2246.

[42] V. Cuesta, R. Singhal, P. De La Cruz, G. D. Sharma, F. Langa, *ACS Appl. Mater. Interfaces*, **2019**, *11*, 7216–7225.

[43] P. Hudhomme, *EPJ Photovoltaics*, **2013**, *4*, 40401.

[44] B. O'Regan, M. Gratzel, *Nature*, **1991**, *353*, 737–740.

[45] A. Hagfeldt, *Ambio*, **2012**, *41*, 151–155.

[46] M. Pazoki, U. B. Cappel, E. M. J. Johansson, A. Hagfeldt, G. Boschloo, *Energy Environ. Sci.*, **2017**, *10*, 672–709.

[47] S. Shi, Y. Li, X. Li, H. Wang, *Mater. Horizons*, **2015**, *2*, 378–405.

[48] S. Mathew, A. Yella, P. Gao, R. Humphry-Baker, B. F. E. Curchod, N. Ashari-Astani, I. Tavernelli, U. Rothlisberger, M. K. Nazeeruddin, M. Grätzel, *Nat. Chem.*, **2014**, *6*, 242–247.

[49] U. Bach, D. Lupo, P. Comte, J. E. Moser, F. Weissörtel, J. Salbeck, H. Spreitzer, M. Grätzel, *Nature*, **1998**, *395*, 583–585.

[50] A. Andualem, S. Demiss, *Edelweiss Appli Sci Tech.*, **2018**, *2*, 145–150.

[51] A. Kojima, K. Teshima, Y. Shirai, T. Miyasaka, *J. Am. Chem. Soc.*, **2009**, *131*, 6050–6051.

[52] J. Im, C. Lee, J. Lee, S. Park, N. Park, *Nanoscale*, **2011**, *3*, 4088–4093.

[53] H. Kim, C. Lee, J. Im, K. Lee, T. Moehl, A. Marchioro, S. Moon, R. Humphry-baker, J. Yum, J. E. Moser, M. Gra, N.-G. Park, *Sci. Rep.*, **2012**, *2*, 591.

[54] T. M. Brenner, D. A. Egger, L. Kronik, G. Hodes, D. Cahen, *Nat. Rev. Mater.*, **2016**, *1*, 15007.

[55] N. Park, *Mater. Today*, **2015**, *18*, 65–72.

[56] X. Tong, Z. M. Wang, *J. Electron. Sci. Technol.*, **2017**, *15*, 326–332.

[57] A. R. B. M. Yusoff, M. K. Nazeeruddin, *J. Phys. Chem. Lett.*, **2016**, *7*, 851–866.

[58] Y. Zhao, K. Zhu, *Chem. Soc. Rev.*, **2016**, *45*, 655–689.

[59] Q. Lin, A. Armin, P. L. Burn, P. Meredith, *Acc. Chem. Res.*, **2016**, *49*, 545–553.

[60] S. Gholipour, M. Saliba, *Small*, **2018**, *14*, 1802385.

[61] C. R. Kalaiselvi, N. Muthukumarasamy, D. Velauthapillai, M. Kang, T. S. Senthil, *Mater. Lett.*, **2018**, *219*, 198–200.

[62] A. K. Jena, A. Kulkarni, T. Miyasaka, *Chem. Rev.*, **2019**, *119*, 3036–3103.

[63] S. De Wolf, J. Holovsky, S. J. Moon, P. Löper, B. Niesen, M. Ledinsky, F. J. Haug, J. H. Yum, C. Ballif, *J. Phys. Chem. Lett.*, **2014**, *5*, 1035–1039.

[64] M. A. Green, A. Ho-Baillie, *ACS Energy Lett.*, **2017**, *2*, 822–830.

[65] H. S. Jung, N. G. Park, *Small*, **2015**, *11*, 10–25.

[66] W. J. Yin, T. Shi, Y. Yan, *Adv. Mater.*, **2014**, *26*, 4653–4658.

[67] B. Wang, X. Xiao, T. Chen, *Nanoscale*, **2014**, *6*, 12287–12297.

[68] G. Xing, N. Mathews, S. Sun, S. S. Lim, Y. M. Lam, M. Graẗzel, S. Mhaisalkar, T. C. Sum, *Science*, **2013**, *342*, 344–347.

[69] C. Motta, F. El-Mellouhi, S. Sanvito, *Sci. Rep.*, **2015**, *5*, 12746.

[70] T. C. Sum, N. Mathews, *Energy Environ. Sci.*, **2014**, *7*, 2518–2534.

[71] A. Jha, H. G. Duan, V. Tiwari, P. K. Nayak, H. J. Snaith, M. Thorwart, R. J. Dwayne Miller, *ACS Photonics*, **2018**, *5*, 852–860.

[72] W. Wang, Y. Li, X. Wang, Y. Lv, S. Wang, K. Wang, Y. Shi, L. Xiao, Z. Chen, Q. Gong, *Phys. Rev. B*, **2016**, *94*, 140302.

[73] V. D'Innocenzo, G. Grancini, M. J. P. Alcocer, A. R. S. Kandada, S. D. Stranks, M. M. Lee, G. Lanzani, H. J. Snaith, A. Petrozza, *Nat. Commun.*, **2014**, *5*, 3586.

[74] C. Sheng, C. Zhang, Y. Zhai, K. Mielczarek, W. Wang, W. Ma, A. Zakhidov, Z. V. Vardeny, *Phys. Rev. Lett.*, **2015**, *114*, 116601.

[75] Z. Zhao, W. Sun, Y. Li, S. Ye, H. Rao, F. Gu, Z. Liu, Z. Bian, C. Huang, *J. Mater. Chem. A*, **2017**, *5*, 4756–4773.

[76] T. Salim, S. Sun, Y. Abe, A. Krishna, A. C. Grimsdale, Y. M. Lam, *J. Mater.*

Chem. A, **2015**, *3*, 8943–8969.

[77] S. F. Völker, S. Collavini, J. L. Delgado, *ChemSusChem*, **2015**, *8*, 3012–3028.

[78] B. J. Kim, S. Lee, H. S. Jung, *J. Mater. Chem. A*, **2018**, *6*, 12215–12236.

[79] C. H. Ng, H. N. Lim, S. Hayase, Z. Zainal, N. M. Huang, *Renew. Sustain. Energy Rev.*, **2018**, *90*, 248–274.

[80] F. Li, M. Liu, *J. Mater. Chem. A*, **2017**, *5*, 15447–15459.

[81] I. Hwang, I. Jeong, J. Lee, M. J. Ko, K. Yong, *ACS Appl. Mater. Interfaces*, **2015**, *7*, 17330–17336.

[82] J. You, L. Meng, T. Bin Song, T. F. Guo, W. H. Chang, Z. Hong, H. Chen, H. Zhou, Q. Chen, Y. Liu, N. De Marco, Y. Yang, *Nat. Nanotechnol.*, **2016**, *11*, 75–81.

[83] J. Yang, B. D. Siempelkamp, D. Liu, T. L. Kelly, *ACS Nano*, **2015**, *9*, 1955–1963.

[84] A. M. A. Leguy, Y. Hu, M. Campoy-Quiles, M. I. Alonso, O. J. Weber, P. Azarhoosh, M. Van Schilfgaarde, M. T. Weller, T. Bein, J. Nelson, P. Docampo, P. R. F. Barnes, *Chem. Mater.*, **2015**, *27*, 3397–3407.

[85] D. Wang, M. Wright, N. K. Elumalai, A. Uddin, *Sol. Energy Mater. Sol. Cells*, **2016**, *147*, 255–275.

[86] G. W. Kim, G. Kang, M. Malekshahi Byranvand, G. Y. Lee, T. Park, *ACS Appl. Mater. Interfaces*, **2017**, *9*, 27720–27726.

[87] Q. Fu, X. Tang, B. Huang, T. Hu, L. Tan, L. Chen, Y. Chen, *Adv. Sci.*, **2018**, *5*, 1700387.

[88] T. Leijtens, G. E. Eperon, S. Pathak, A. Abate, M. M. Lee, H. J. Snaith, *Nat. Commun.*, **2013**, *4*, 2885.

[89] S. Ito, S. Tanaka, K. Manabe, H. Nishino, *J. Phys. Chem. C*, **2014**, *118*, 16995–17000.

[90] D. Liu, Y. Liu, *J. Semicond.*, **2017**, *38*, 011005.

[91] I. Mesquita, L. Andrade, A. Mendes, *Renew. Sustain. Energy Rev.*, **2018**, *82*, 2471–2489.

[92] B. Salhi, Y. S. Wudil, M. K. Hossain, A. Al-Ahmed, F. A. Al-Sulaiman, *Renew. Sustain. Energy Rev.*, **2018**, *90*, 210–222.

[93] E. Raza, F. Aziz, Z. Ahmad, *RSC Adv.*, **2018**, *8*, 20952–20967.

[94] B. Philippe, B. W. Park, R. Lindblad, J. Oscarsson, S. Ahmadi, E. M. J. Johansson, H. Rensmo, *Chem. Mater.*, **2015**, *27*, 1720–1731.

[95] P. S. Whitfield, N. Herron, W. E. Guise, K. Page, Y. Q. Cheng, I. Milas, M. K. Crawford, *Sci. Rep.*, **2016**, *6*, 35685.

[96] M. R. Leyden, Y. Jiang, Y. Qi, *J. Mater. Chem. A*, **2016**, *4*, 13125–13132.

[97] L. Cojocaru, S. Uchida, Y. Sanehira, V. Gonzalez-Pedro, J. Bisquert, J. Nakazaki, T. Kubo, H. Segawa, *Chem. Lett.*, **2015**, *44*, 1557–1559.

[98] M. Yavari, M. Mazloum-Ardakani, S. Gholipour, N. Marinova, J. L. Delgado, S. H. Turren-Cruz, K. Domanski, N. Taghavinia, M. Saliba, M. Grätzel, A. Hagfeldt, W. Tress, *Adv. Energy Mater.*, **2018**, *8*, 1702719.

[99] Z. Shi, J. Guo, Y. Chen, Q. Li, Y. Pan, H. Zhang, Y. Xia, W. Huang, *Adv. Mater.*, **2017**, *29*, 1605005.

[100] A. Abate, *Joule*, **2017**, *1*, 659–664.

[101] M. Lyu, J. H. Yun, P. Chen, M. Hao, L. Wang, *Adv. Energy Mater.*, **2017**, *7*, 1602512.

[102] I. Kopacic, B. Friesenbichler, S. F. Hoefler, B. Kunert, H. Plank, T. Rath, G. Trimmel, *ACS Appl. Energy Mater.*, **2018**, *1*, 343–347.

[103] F. Hao, C. C. Stoumpos, D. H. Cao, R. P. H. Chang, M. G. Kanatzidis, *Nat. Photonics*, **2014**, *8*, 489–494.

[104] N. Ito, M. A. Kamarudin, D. Hirotani, Y. Zhang, Q. Shen, Y. Ogomi, S. Iikubo, T. Minemoto, K. Yoshino, S. Hayase, *J. Phys. Chem. Lett.*, **2018**, *9*, 1682–1688.

[105] N. Kumari, S. R. Patel, J. V Gohel, *J. Mater. Sci. Mater. Electron.*, **2018**, *29*, 18144–18150.

[106] P. Liu, W. Wang, S. Liu, H. Yang, Z. Shao, *Adv. Energy Mater.*, **2019**, *9*, 1803017.

[107] N. K. Elumalai, A. Uddin, *Sol. Energy Mater. Sol. Cells*, **2016**, *157*, 476–509.

[108] M. Yang, Y. Zhou, Y. Zeng, C. S. Jiang, N. P. Padture, K. Zhu, *Adv. Mater.*, **2015**, *27*, 6363–6370.

[109] L. Cai, L. Liang, J. Wu, B. Ding, L. Gao, B. Fan, *J. Semicond.*, **2017**, *38*, 014006.

[110] Y. Hu, S. Si, A. Mei, Y. Rong, H. Liu, X. Li, H. Han, *Sol. RRL*, **2017**, *1*, 1600019.

[111] L. Calió, S. Kazim, M. Grätzel, S. Ahmad, *Angew. Chem. Int. Ed.*, **2016**, *55*, 14522–14545.

[112] X. Yang, H. Wang, B. Cai, Z. Yu, L. Sun, *J. Energy Chem.*, **2018**, *27*, 650–672.

[113] Z. Yu, L. Sun, *Small Methods*, **2018**, *2*, 1700280.

[114] Z. H. Bakr, Q. Wali, A. Fakharuddin, L. Schmidt-Mende, T. M. Brown, R. Jose, *Nano Energy*, **2017**, *34*, 271–305.

[115] Y. Shao, Y. Yuan, J. Huang, *Nat. Energy*, **2016**, *1*, 15001.

[116] J. Urieta-Mora, I. García-Benito, A. Molina-Ontoria, N. Martín, *Chem. Soc. Rev.*, **2018**, *47*, 8541–8571.

[117] Z. Yu, L. Sun, *Adv. Energy Mater.*, **2015**, *5*, 1500213.

[118] X. Zhao, M. Wang, *Mater. Today Energy*, **2018**, *7*, 208–220.

[119] P. Vivo, J. K. Salunke, A. Priimagi, *Materials*, **2017**, *10*, 1087.

[120] R. Misra, G. SivaKumar, *J. Mater. Chem. A*, **2018**, *6*, 18750–18765.

[121] J. Salbeck, J. Bauer, F. Weissgrtel, H. Bestgen, *Synth. Met.*, **1997**, *91*, 209–215.

[122] Z. Hawash, L. K. Ono, Y. Qi, *Adv. Mater. Interfaces*, **2018**, *5*, 1700623.

[123] N. J. Jeon, J. Lee, J. H. Noh, M. K. Nazeeruddin, S. Il Seok, *J. Am. Chem. Soc.*, **2013**, *135*, 19087–19090.

[124] B. Xu, J. Zhang, Y. Hua, P. Liu, L. Wang, C. Ruan, Y. Li, G. Boschloo, E. M. J. Johansson, L. Kloo, A. Hagfeldt, A. K. Y. Jen, L. Sun, *Chem*, **2017**, *2*, 676–687.

[125] T. Malinauskas, D. Tomkute-Luksiene, R. Sens, M. Daskeviciene, R. Send, H. Wonneberger, V. Jankauskas, I. Bruder, V. Getautis, *ACS Appl. Mater. Interfaces.*, **2015**, *7*, 11107–11116.

[126] G. Divitini, S. Cacovich, F. Matteocci, L. Cinà, A. Di Carlo, C. Ducati, *Nat. Energy*, **2016**, *1*, 15012.

[127] J. Burschka, Thesis, École polytechnique fédérale de Lausanne (Laussane), **2013**.

[128] G. Niu, X. Guo, L. Wang, *J. Mater. Chem. A*, **2015**, *3*, 8970–8980.

[129] C. D. Bailie, E. L. Unger, S. M. Zakeeruddin, M. Grätzel, M. D. McGehee, *Phys. Chem. Chem. Phys.*, **2014**, *16*, 4864–4870.

[130] A. Krishna, A. C. Grimsdale, *J. Mater. Chem. A*, **2017**, *5*, 16446–16466.

[131] M. Ulfa, T. Zhu, F. Goubard, T. Pauporté, *J. Mater. Chem. A*, **2018**, *6*, 13350–13358.

[132] B. Roose, Q. Wang, A. Abate, *Adv. Energy Mater.*, **2018**, *9*, 1803140.

[133] W. S. Yang, B.-W. Park, E. H. Jung, N. J. Jeon, Y. C. Kim, D. U. Lee, S. S. Shin, J. Seo, E. K. Kim, J. H. Noh, S. Il Seok, *Science*, **2017**, *356*, 1376–1379.

[134] P. Qin, N. Tetreault, M. I. Dar, P. Gao, K. L. McCall, S. R. Rutter, S. D. Ogier, N. D. Forrest, J. S. Bissett, M. J. Simms, A. J. Page, R. Fisher, M. Grätzel, M. K. Nazeeruddin, *Adv. Energy Mater.*, **2015**, *5*, 1400980.

[135] K. Sun, S. Zhang, P. Li, Y. Xia, X. Zhang, D. Du, F. H. Isikgor, J. Ouyang, *J. Mater. Sci. Mater. Electron.*, **2015**, *26*, 4438–4462.

[136] J. H. Heo, H. J. Han, D. Kim, T. K. Ahn, S. H. Im, *Energy Environ. Sci.*, **2015**, *8*, 1602–1608.

[137] H. A. Abbas, R. Kottokkaran, B. Ganapathy, M. Samiee, L. Zhang, A. Kitahara, M. Noack, V. L. Dalal, *APL Mater.*, **2015**, *3*, 016105.

[138] J. Xiao, J. Shi, H. Liu, Y. Xu, S. Lv, Y. Luo, D. Li, Q. Meng, Y. Li, *Adv. Energy Mater.*, **2015**, *5*, 1401943.

[139] S. N. Habisreutinger, T. Leijtens, G. E. Eperon, S. D. Stranks, R. J. Nicholas, H. J. Snaith, *Nano Lett.*, **2014**, *14*, 5561–5568.

[140] P. Zhou, T. Bu, S. Shi, L. Li, Y. Zhang, Z. Ku, Y. Peng, J. Zhong, Y. B. Cheng, F. Huang, *J. Mater. Chem. C*, **2018**, *6*, 5733–5737.

[141] M. Wong-Stringer, J. E. Bishop, J. A. Smith, D. K. Mohamad, A. J. Parnell, V. Kumar, C. Rodenburg, D. G. Lidzey, *J. Mater. Chem. A*, **2017**, *5*, 15714–15723.

[142] Z. Yu, Y. Zhang, X. Jiang, X. Li, J. Lai, M. Hu, M. Elawad, G. G. Gurzadyan, X. Yang, L. Sun, *RSC Adv.*, **2017**, *7*, 27189–27197.

[143] B. Cai, Y. Xing, Z. Yang, W. H. Zhang, J. Qiu, *Energy Environ. Sci.*, **2013**, *6*, 1480–1485.

[144] Y. S. Kwon, J. Lim, H. J. Yun, Y. H. Kim, T. Park, *Energy Environ. Sci.*, **2014**, *7*, 1454–1460.

[145] J. M. Marin-Beloqui, J. Pérez Hernández, E. Palomares, *Chem. Commun.*, **2014**, *50*, 14566–14569.

[146] Z. Zhu, Y. Bai, H. Ka, H. Lee, C. Mu, T. Zhang, L. Zhang, *Adv. Funct. Mater.*, **2014**, *24*, 7357–7365.

[147] G.-W. Kim, G. Kang, J. Kim, G.-Y. Lee, H. Il Kim, L. Pyeon, J. Lee, T. Park, *Energy Environ. Sci.*, **2016**, *9*, 2326–2333.

[148] C. Huang, W. Fu, C.-Z. Li, Z. Zhang, W. Qiu, M. Shi, P. Heremans, A. K.-Y. Jen, H. Chen, *J. Am. Chem. Soc.*, **2016**, *138*, 2528–2531.

[149] S. Paek, P. Qin, Y. Lee, K. T. Cho, P. Gao, G. Grancini, E. Oveisi, P. Gratia, K.

Rakstys, S. A. Al-Muhtaseb, C. Ludwig, J. Ko, M. K. Nazeeruddin, *Adv. Mater.*, **2017**, *29*, 1606555.

[150] F. Zhang, X. Zhao, C. Yi, D. Bi, X. Bi, P. Wei, X. Liu, S. Wang, X. Li, S. M. Zakeeruddin, M. Grätzel, *Dyes Pigm.*, **2017**, *136*, 273–277.

[151] K. Rakstys, S. Paek, P. Gao, P. Gratia, T. Marszalek, G. Grancini, K. T. Cho, K. Genevicius, V. Jankauskas, W. Pisula, M. K. Nazeeruddin, *J. Mater. Chem. A*, **2017**, *5*, 7811–7815.

[152] M. Sun, X. Liu, F. Zhang, H. Liu, X. Liu, S. Wang, Y. Xiao, D. Li, Q. Meng, X. Li, *Appl. Surf. Sci.*, **2017**, *416*, 124–132.

[153] X. Liu, F. Zhang, Z. Liu, Y. Xiao, S. Wang, X. Li, *J. Mater. Chem. C*, **2017**, *5*, 11429–11435.

[154] S. F. Völker, M. Vallés-Pelarda, J. Pascual, S. Collavini, F. Ruipérez, E. Zuccatti, L. E. Hueso, R. Tena-Zaera, I. Mora-Seró, J. L. Delgado, *Chem. A Eur. J.*, **2018**, *24*, 8524–8529.

[155] H. D. Pham, T. T. Do, J. Kim, C. Charbonneau, S. Manzhos, K. Feron, W. C. Tsoi, J. R. Durrant, S. M. Jain, P. Sonar, *Adv. Energy Mater.*, **2018**, *8*, 1703007.

[156] G. W. Kim, J. Lee, G. Kang, T. Kim, T. Park, *Adv. Energy Mater.*, **2017**, 1701935.

[157] T. Matsui, I. Petrikyte, T. Malinauskas, K. Domanski, M. Daskeviciene, M. Steponaitis, P. Gratia, W. Tress, J. P. Correa-Baena, A. Abate, A. Hagfeldt, M. Grätzel, M. K. Nazeeruddin, V. Getautis, M. Saliba, *ChemSusChem*, **2016**, *9*, 2567–2571.

[158] A. Dubey, N. Adhikari, S. Venkatesan, S. Gu, D. Khatiwada, Q. Wang, L. Mohammad, M. Kumar, Q. Qiao, *Sol. Energy Mater. Sol. Cells*, **2016**, *145*, 193–199.

[159] X. Jiang, Z. Yu, Y. Zhang, J. Lai, J. Li, G. G. Gurzadyan, X. Yang, L. Sun, *Sci. Rep.*, **2017**, *7*, 42564.

[160] P. Agarwala, D. Kabra, *J. Mater. Chem. A*, **2017**, *5*, 1348–1373.

[161] I. R. Perera, A. Gupta, W. Xiang, T. Daeneke, U. Bach, R. A. Evans, C. A. Ohlin, L. Spiccia, *Phys. Chem. Chem. Phys.*, **2014**, *16*, 12021–12028.

[162] S. M. Park, K. S. Yook, W. H. Lee, Y. Hong, J. Y. Lee, I. N. Kang, *J. Polym. Sci. Part A. Polym. Chem.*, **2013**, *51*, 5111–5117.

[163] K. Neumann, C. Schwarz, A. Köhler, M. Thelakkat, *J. Phys. Chem. C*, **2014**, *118*, 27–36.

[164] X. Zhang, S. Cao, L. Huang, L. Chen, X. Ouyang, *Dyes Pigm.*, **2017**, *145*, 110–

115.

[165] M. R. Talipov, M. M. Hossain, A. Boddeda, K. Thakur, R. Rathore, *Org. Biomol. Chem.*, **2016**, *14*, 2961–2968.

[166] S. F. Völker, T. Dellermann, H. Ceymann, M. Holzapfel, C. Lambert, *J. Polym. Sci. Part A. Polym. Chem.*, **2014**, *52*, 890–911.

[167] T. Leijtens, I. K. Ding, T. Giovenzana, J. T. Bloking, M. D. McGehee, A. Sellinger, *ACS Nano*, **2012**, *6*, 1455–1462.

[168] M. Deepa, M. Salado, L. Calio, S. Kazim, S. M. Shivaprasad, S. Ahmad, *Phys. Chem. Chem. Phys.*, **2017**, *19*, 4069–4077.

[169] A. K. Baranwal, S. Kanaya, T. A. N. Peiris, G. Mizuta, T. Nishina, H. Kanda, T. Miyasaka, H. Segawa, S. Ito, *ChemSusChem*, **2016**, *9*, 2604–2608.

[170] T. Leijtens, G. E. Eperon, N. K. Noel, S. N. Habisreutinger, A. Petrozza, H. J. Snaith, *Adv. Energy Mater.*, **2015**, *5*, 1500963.

[171] K. Poorkazem, T. L. Kelly, *Sustain. Energy Fuels*, **2018**, *2*, 1332–1341.

[172] N. J. Jeon, J. H. Noh, W. S. Yang, Y. C. Kim, S. Ryu, J. Seo, S. Il Seok, *Nature*, **2014**, *517*, 476–480.

[173] M. Saliba, T. Matsui, J. Y. Seo, K. Domanski, J. P. Correa-Baena, M. K. Nazeeruddin, S. M. Zakeeruddin, W. Tress, A. Abate, A. Hagfeldt, M. Grätzel, *Energy Environ. Sci.*, **2016**, *9*, 1989–1997.

[174] F. Bella, G. Griffini, J. P. Correa-Baena, G. Saracco, M. Grätzel, A. Hagfeldt, S. Turri, C. Gerbaldi, *Science*, **2016**, *354*, 203–206.

[175] Z. Yang, A. Rajagopal, C. Chueh, S. B. Jo, B. Liu, T. Zhao, A. K. Jen, *Adv. Mater.*, **2016**, *28*, 8990–8997.

[176] S. Paek, P. Schouwink, E. N. Athanasopoulou, K. T. Cho, G. Grancini, Y. Lee, Y. Zhang, F. Stellacci, M. K. Nazeeruddin, P. Gao, *Chem. Mater.*, **2017**, *29*, 3490–3498.

[177] F. Huang, Y. Dkhissi, W. Huang, M. Xiao, I. Benesperi, S. Rubanov, Y. Zhu, X. Lin, L. Jiang, Y. Zhou, A. Gray-weale, J. Etheridge, C. R. Mcneill, R. A. Caruso, U. Bach, L. Spiccia, Y. Cheng, *Nano Energy*, **2014**, *10*, 10–18.

[178] N. J. Jeon, J. H. Noh, Y. C. Kim, W. S. Yang, S. Ryu, S. Il Seok, *Nat. Mater.*, **2014**, *13*, 897–903.

[179] M. Xiao, L. Zhao, M. Geng, Y. Li, B. Dong, Z. Xu, L. Wan, W. Li, S. Wang, *Nanoscale*, **2018**, *10*, 12141–12148.

[180] T. Li, Y. Pan, Z. Wang, Y. Xia, Y. Chen, W. Huang, *J. Mater. Chem. A*, **2017**,

5, 12602–12652.

[181] D. Bi, X. Li, J. V Milic, D. J. Kubicki, N. Pellet, J. Luo, T. Lagrange, P. Mettraux, L. Emsley, S. M. Zakeeruddin, M. Grätzel, *Nat. Commun.*, **2018**, *9*, 4482.

[182] C. Zhang, M. Li, Z. Wang, Y. Jiang, H. Liu, Y. Yang, X. Gao, H. Ma, *J. Mater. Chem. A*, **2017**, *5*, 2572–2579.

[183] B. Yang, O. Dyck, J. Poplawsky, J. Keum, A. Puretzky, S. Das, I. Ivanov, C. Rouleau, G. Duscher, D. Geohegan, K. Xiao, *J. Am. Chem. Soc.*, **2015**, *137*, 9210–9213.

[184] Y. Zhao, J. Wei, H. Li, Y. Yan, W. Zhou, D. Yu, Q. Zhao, *Nat. Commun.*, **2016**, *7*, 10228.

[185] Y. Guo, K. Shoyama, W. Sato, E. Nakamura, *Adv. Energy Mater.*, **2016**, *6*, 1502317.

[186] C. Zuo, L. Ding, *Nanoscale*, **2014**, *6*, 9935–9938.

[187] Y. Jeon, S. Lee, R. Kang, J. Kim, J. Yeo, S. Lee, S. Kim, J. Yun, D. Kim, *Sci. Rep.*, **2014**, *4*, 6953.

[188] P. Liang, C. Liao, C. Chueh, F. Zuo, S. T. Williams, X. Xin, J. Lin, A. K. Jen, *Adv. Mater.*, **2014**, *26*, 3748–3754.

[189] C. Gao, H. Dong, X. Bao, Y. Zhang, A. Saparbaev, L. Yu, S. Wen, R. Yang, L. Dong, *J. Mater. Chem. C*, **2018**, *6*, 8234–8241.

[190] M. Sun, F. Zhang, H. Liu, X. Li, Y. Xiao, S. Wang, *J. Mater. Chem. A*, **2017**, *5*, 13448–13456.

[191] S. Collavini, M. Saliba, W. R. Tress, P. J. Holzhey, S. F. Völker, K. Domanski, S. H. Turren-Cruz, A. Ummadisingu, S. M. Zakeeruddin, A. Hagfeldt, M. Grätzel, J. L. Delgado, *ChemSusChem*, **2018**, *11*, 1032–1039.

[192] C. Chang, C. Chu, Y. Huang, C. Huang, S. Chang, C. Chen, C. Chao, W. Su, *ACS Appl. Mater. Interfaces*, **2015**, *7*, 4955–4961.

[193] Q. Xue, Z. Hu, C. Sun, Z. Chen, F. Huang, H. Yip, Y. Cao, *RSC Adv.*, **2015**, *5*, 775–783.

[194] Q. Dong, Z. Wang, K. Zhang, H. Yu, P. Huang, X. Liu, Y. Zhou, N. Chen, B. Song, *Nanoscale*, **2016**, *8*, 5552–5558.

[195] B. Li, Y. Zhang, L. Fu, T. Yu, S. Zhou, L. Zhang, L. Yin, *Nat. Commun.*, **2018**, *9*, 1076.

[196] F. Li, J. Yuan, X. Ling, Y. Zhang, Y. Yang, S. H. Cheung, *Adv. Funct. Mater.*, **2018**, *28*, 1706377.

[197] J. C. Yu, S. Badgujar, E. D. Jung, V. K. Singh, D. W. Kim, J. Gierschner, E. Lee, Y. S. Kim, S. Cho, M. S. Kwon, M. H. Song, *Adv. Mater.*, **2019**, *31*, 1805554.

[198] J. Jiang, Q. Wang, Z. Jin, X. Zhang, J. Lei, H. Bin, Z. Zhang, *Adv. Energy Mater.*, **2018**, *8*, 1701757.

[199] J. Pascual, I. Kosta, T. T. Ngo, A. Chuvilin, G. Cabanero, H. J. Grande, E. M. Barea, I. Mora-Seró, J. L. Delgado, R. Tena-Zaera, *ChemSusChem*, **2016**, *9*, 2679–2685.

[200] R. Sandoval-Torrientes, J. Pascual, I. García-Benito, S. Collavini, I. Kosta, R. Tena-Zaera, N. Martín, J. L. Delgado, *ChemSusChem*, **2017**, *10*, 2023–2029.

[201] Y. Takeda, T. L. Andrew, J. M. Lobez, A. J. Mork, T. M. Swager, *Angew. Commun.*, **2012**, *51*, 9042–9046.

[202] D. Wei, F. Ma, R. Wang, S. Dou, P. Cui, H. Huang, J. Ji, E. Jia, X. Jia, S. Sajid, A. M. Elseman, L. Chu, Y. Li, B. Jiang, J. Qiao, Y. Yuan, M. Li, M. Li, *Adv. Mater.*, **2018**, *30*, 1707583.

[203] D. Bi, P. Gao, R. Scopelliti, E. Oveisi, J. Luo, M. Grätzel, A. Hagfeldt, K. Nazeeruddin, *Adv. Mater.*, **2016**, *28*, 2910–2915.

[204] M. Salado, F. J. Ramos, V. M. Manzanares, P. Gao, K. Nazeeruddin, P. J. Dyson, S. Ahmad, *ChemSusChem*, **2016**, *9*, 2708–2714.

[205] M. Salado, M. Asunci, J. P. Holgado, S. Kazim, M. K. Nazeeruddin, P. J. Dyson, S. Ahmad, *ChemSusChem*, **2017**, *10*, 3846–3853.

[206] K. M. M. Salim, T. M. Koh, D. Bahulayan, P. C. Harikesh, N. F. Jamaludin, B. Febriansyah, A. Bruno, S. Mhaisalkar, N. Mathews, *ACS Energy Lett.*, **2018**, *3*, 1068–1076.

[207] J. Yang, C. Liu, C. Cai, X. Hu, Z. Huang, X. Duan, X. Meng, Z. Yuan, L. Tan, Y. Chen, *Adv. Energy Mater.*, **2019**, *9*, 1900198.

[208] J. Lim, T. M. Swager, *Angew. Chem. Int. Ed.*, **2010**, *49*, 7486–7488.

[209] T. Li, C. Su, S. B. Akula, W. Sun, H. Chien, W. Li, *Org. Lett.*, **2016**, *18*, 3386–3389.

[210] A. Facchetti, M. Yoon, C. L. Stern, G. R. Hutchison, M. A. Ratner, T. J. Marks, *J. Am. Chem. Soc.*, **2004**, *126*, 13480–13501.

[211] A. B. López, J. C. de la Cal, J. M. Asua, *Langmuir*, **2016**, *32*, 7459–7466.

[212] H. J. Son, W. Wang, T. Xu, Y. Liang, Y. Wu, G. Li, L. Yu, *J. Am. Chem. Soc.*, **2011**, *133*, 1885–1894.

[213] P. Calado, A. M. Telford, D. Bryant, X. Li, J. Nelson, B. C. O´Regan, P. R. F.

Barnes, *Nat. Commun.*, **2016**, *7*, 13831.

[214] A. Dualeh, N. Tétreault, T. Moehl, P. Gao, *Adv. Funct. Mater.*, **2014**, *24*, 3250–3258.

[215] H. Yang, J. Zhang, C. Z, J. Chang, Z. Lin, D. Chen, H. Xi, Y. Hao, *Materials*, **2017**, *10*, 837.

[216] S. Masi, A. Rizzo, R. Munir, A. Listorti, A. Giuri, C. E. Corcione, N. D. Treat, G. Gigli, A. Amassian, N. Stingelin, S. Colella, *Adv. Funct. Mater*, **2017**, *7*, 1602600.

[217] D. Bryant, N. Aristidou, S. Pont, I. Sanchez-molina, T. Chotchunangatchaval, S. Wheeler, R. Durrant, S. A. Haque, *Energy Environ. Sci.*, **2016**, *9*, 1655–1660.

[218] N. Marinova, F. M., I. Matulaitiene, A. Devizis, G. Niaura, V. Gulbinas, J. L. Delgado, *ChemSusChem*, **2017**, *10*, 3760–3764.

[219] R. Schlaf, H. Murata, Z. H. Kafafi, *J. Electron Spectrosc.*, **2001**, *120*, 149–154.

[220] E. J. Juarez-Perez, Z. Hawash, S. R. Raga, L. K. Ono, Y. Qi, *Energy Environ. Sci.*, **2016**, *9*, 3406–3410.

[221] F. Babudri, G. M. Farinola, F. Naso, R. Ragni, *Chem. Commun.*, **2007**, 1003–1022.

[222] A. Marchioro, J. Teuscher, D. Friedrich, M. Kunst, R. Van De Krol, T. Moehl, M. Grätzel, J. E. Moser, *Nat. Photonics*, **2014**, *8*, 250–255.

[223] G. Yang, H. Tao, P. Qin, W. Ke, G. Fang, *J. Mater. Chem. A*, **2016**, *4*, 3970–3990.

[224] A. Isakova, P. D. Topham, *J. Polym. Sci. Part B Polym. Phys.*, **2017**, *55*, 549–568.

[225] W. Ke, G. Fang, J. Wan, H. Tao, Q. Liu, L. Xiong, P. Qin, J. Wang, H. Lei, G. Yang, M. Qin, X. Zhao, Y. Yan, *Nat. Commun.*, **2015**, *6*, 6700.

[226] S. Gharibzadeh, F. Valduga de Almeida Camargo, C. Roldán-Carmona, G. C. Gschwend, J. Pascual, R. Tena-Zaera, G. Cerullo, G. Grancini, M. K. Nazeeruddin, *Adv. Mater.*, **2018**, *30*, 1801496.

[227] H. D. Pham, L. Xianqiang, W. Li, S. Manzhos, A. K. K. Kyaw, P. Sonar, *Energy Environ. Sci.*, **2019**, *12*, 1177–1209.

[228] S. K. Jung, D. S. Lee, M. H. Ann, S. H. Im, J. H. Kim, O. P. Kwon, *ChemSusChem*, **2018**, *11*, 3835.

[229] J. Lian, B. Lu, F. Niu, P. Zeng, X. Zhan, *Small Methods*, **2018**, *2*, 1800082.

[230] H. Liu, Z. Huang, S. Wei, L. Zheng, L. Xiao, Q. Gong, *Nanoscale*, **2016**, *8*, 6209–6221.

[231] M. F. Mohamad Noh, C. H. Teh, R. Daik, E. L. Lim, C. C. Yap, M. A. Ibrahim, N. Ahmad Ludin, A. R. Bin Mohd Yusoff, J. Jang, M. A. Mat Teridi, *J. Mater. Chem. C*, **2018**, *6*, 682–712.

[232] S. Sun, T. Buonassisi, J. P. Correa-Baena, *Adv. Mater. Interfaces*, **2018**, *5*, 1800408.

[233] E. Castro, J. Murillo, O. Fernandez-Delgado, L. Echegoyen, *J. Mater. Chem. C*, **2018**, *6*, 2635–2651.

[234] J. Y. Jeng, Y. F. Chiang, M. H. Lee, S. R. Peng, T. F. Guo, P. Chen, T. C. Wen, *Adv. Mater.*, **2013**, *25*, 3727–3732.

[235] T. Gatti, E. Menna, M. Meneghetti, M. Maggini, A. Petrozza, F. Lamberti, *Nano Energy*, **2017**, *41*, 84–100.

[236] D. Luo, W. Yang, Z. Wang, A. Sadhanala, Q. Hu, R. Su, R. Shivanna, G. F. Trindade, J. F. Watts, Z. Xu, T. Liu, K. Chen, F. Ye, P. Wu, L. Zhao, J. Wu, Y. Tu, Y. Zhang, X. Yang, W. Zhang, R. H. Friend, Q. Gong, H. J. Snaith, R. Zhu, *Science*, **2018**, *360*, 1442–1446.

[237] Y. C. Wang, X. Li, L. Zhu, X. Liu, W. Zhang, J. Fang, *Adv. Energy Mater.*, **2017**, *7*, 1701144.

[238] E. Castro, G. Zavala, S. Seetharaman, F. D'Souza, L. Echegoyen, *J. Mater. Chem. A*, **2017**, *5*, 19485–19490.

[239] Y. Bai, Q. Dong, Y. Shao, Y. Deng, Q. Wang, L. Shen, D. Wang, W. Wei, J. Huang, *Nat. Commun.*, **2016**, *7*, 12806.

[240] M. Zhang, X. Zhan, *Adv. Energy Mater.*, **2019**, 1900860.

[241] M. Al Kobaisi, S. V. Bhosale, K. Latham, A. M. Raynor, S. V. Bhosale, *Chem. Rev.*, **2016**, *116*, 11685–11796.

[242] J. H. Heo, S. C. Lee, S. K. Jung, O. P. Kwon, S. H. Im, *J. Mater. Chem. A*, **2017**, *5*, 20615–20622.

[243] S. K. Jung, J. H. Heo, D. W. Lee, S. C. Lee, S. H. Lee, W. Yoon, H. Yun, S. H. Im, J. H. Kim, O. P. Kwon, *Adv. Funct. Mater.*, **2018**, *28*, 1800346.

[244] S. K. Jung, J. H. Heo, D. W. Lee, S. H. Lee, S. C. Lee, W. Yoon, H. Yun, D. Kim, J. H. Kim, S. H. Im, O. P. Kwon, *ChemSusChem*, **2019**, *12*, 224–230.

[245] C. Ge, W. Wu, L. Hu, Y. Hu, Y. Zhou, W. S. Li, X. Gao, *Org. Electron.*, **2018**, *61*, 113–118.

[246] W. Wang, J. Yuan, G. Shi, X. Zhu, S. Shi, Z. Liu, L. Han, H. Q. Wang, W. Ma, *ACS Appl. Mater. Interfaces*, **2015**, *7*, 3994–3999.

[247] S. Shao, Z. Chen, H. H. Fang, G. H. Ten Brink, D. Bartesaghi, S. Adjokatse, L. J. A. Koster, B. J. Kooi, A. Facchetti, M. A. Loi, *J. Mater. Chem. A*, **2016**, *4*, 2419–2426.

[248] C. Sun, Z. Wu, H. L. Yip, H. Zhang, X. F. Jiang, Q. Xue, Z. Hu, Z. Hu, Y. Shen, M. Wang, F. Huang, Y. Cao, *Adv. Energy Mater.*, **2016**, *6*, 1501534.

[249] X. Zhan, A. Facchetti, S. Barlow, T. J. Marks, M. A. Ratner, M. R. Wasielewski, S. R. Marder, *Adv. Mater.*, **2011**, *23*, 268–284.

[250] X. Zheng, B. Chen, J. Dai, Y. Fang, Y. Bai, Y. Lin, H. Wei, X. C. Zeng, J. Huang, *Nat. Energy*, **2017**, *2*, 17102.

[251] Z. Wu, C. Sun, S. Dong, X. Jiang, S. Wu, H. Wu, H. Yip, F. Huang, Y. Cao, *J. Am. Chem. Soc.*, **2016**, *138*, 2004–2013.

[252] A. Luzio, D. Fazzi, D. Natali, E. Giussani, K. Baeg, Z. Chen, Y. Noh, A. Facchetti, M. Caironi, *Adv. Funct. Mater.*, **2014**, *24*, 1151–1162.

[253] P. M. Alvey, B. L. Iverson, *Org. Lett.*, **2012**, *15*, 2706–2709.

[254] B. L. Schottel, H. T. Chifotides, K. R. Dunbar, *Chem. Soc. Rev.*, **2008**, *37*, 68–83.

[255] Q. Song, F. Li, Z. Wang, X. Zhang, *Chem. Sci.*, **2015**, *6*, 3342–3346.

[256] D. Duan, W. Cai, B. B. Y.Hsu, C. Zhong, K. Zhang, C. Liu, Z. Hu, F. Huang, G. C. Bazan, A. J. Heeger, Y. Cao, *Energy Environ. Sci.*, **2013**, *6*, 3022–3034.

[257] A. Saeki, Y. Koizumi, T. Aida, S. Seki, *Acc. Chem. Res.*, **2012**, *45*, 1193–1202.

[258] C. Colbeau-Justin, M. A. Valenzuela, *Rev. Mex. Fis.*, **2013**, *59*, 191–200.

[259] M. Sasikumar, Y. V. Suseela, T. Govindaraju, *Asian J. Org. Chem.*, **2013**, *2*, 779–785.

[260] L. Li, in *MALDI MS: A Practical Guide to Instrumentation, Methods and Applications (Ed: Franz Hillenkamp and Jasna Peter-Katalinić)*; **2007**; 245–297.

[261] H. Huang, N. Zhou, R. P. Ortiz, Z. Chen, S. Loser, S. Zhang, X. Guo, J. Casado, J. T. L. Navarrete, X. Yu, A. Facchetti, T. J. Marks, *Adv. Funct. Mater.*, **2014**, *24*, 2782–2793.

[262] P. M. Alvey, R. J. Ono, C. W. Bielawski, B. L. Iverson, *Macromolecules*, **2013**, *46*, 718–726.

[263] N. B. Kolhe, A. Z. Ashar, K. S. Narayan, S. K. Asha, *Macromolecules*, **2014**, *47*, 2296–2305.

[264] S. Vasimalla, S. P. Senanayak, M. Sharma, K. S. Narayan, K. P. Iyer, *Chem. Mater.*, **2014**, *26*, 4030–4037.

[265] F. Huang, L. Hou, H. Wu, X. Wang, H. Shen, W. Cao, *J. Am. Chem. Soc.*, **2004**, *126*, 9845–9853.

[266] P. B. Balanda, M. B. Ramey, J. R. Reynolds, *Macromolecules*, **1999**, *32*, 3970–3978.

[267] Y. Kim, J. Hong, J. H. Oh, C. Yang, *Chem. Mater.*, **2013**, *25*, 3251–3259.

[268] F. Doria, I. Manet, V. Grande, S. Monti, M. Freccero, *J. Org. Chem.*, **2013**, *78*, 8065–8073.

[269] H. Chen, Y. Guo, Z. Mao, G. Yu, J. Huang, Y. Zhao, Y. Liu, *Chem. Mater.*, **2013**, *25*, 3589–3596.

[270] T. Jia, C. Sun, R. Xu, Z. Chen, Q. Yin, Y. Jin, H. Yip, F. Huang, Y. Cao, *ACS Appl. Mater. Interfaces*, **2017**, *9*, 36070–36081.

[271] C. M. Cardona, W. Li, A. E. Kaifer, D. Stockdale, G. C. Bazan, *Adv. Mater.*, **2011**, *23*, 2367–2371.

[272] K.-H. Lee, H.-J. Lee, K. Kuramoto, Y. Tanaka, K. Morino, A. Sudo, T. Okauchi, A. Tsuge, T. Endo, *J. Polym. Sci. Part A Polym. Chem.*, **2011**, *49*, 3543–3549.

[273] D. H. Lee, M. J. Lee, H. M. Song, B. J. Song, K. D. Seo, M. Pastore, C. Anselmi, S. Fantacci, F. De Angelis, M. K. Nazeeruddin, M. Gräetzel, H. K. Kim, *Dyes Pigm.*, **2011**, *91*, 192–198.

[274] X. Xu, Y. Zhu, L. Zhang, J. Sun, J. Huang, J. Chen, Y. Cao, *J. Mater. Chem.*, **2012**, *22*, 4329–4336.

[275] S. Amthor, C. Lambert, *J. Phys. Chem. A*, **2006**, *110*, 1177–1189.

[276] S. Guo, W. Wu, H. Guo, J. Zhao, *J. Org. Chem.*, **2012**, *77*, 3933–3943.

[277] T. Schwalm, M. Rehahn, *Macromolecules*, **2007**, *40*, 3921–3928.

[278] P. Wessig, M. Gerngroß, D. Freyse, P. Bruhns, M. Przezdziak, U. Schilde, A. Kelling, *J. Org. Chem.*, **2016**, *81*, 1125–1136.

[279] S. F. Völker, A. Schmiedel, M. Holzapfel, C. Böhm, C. Lambert, *Phys. Chem. Chem. Phys.*, **2013**, *15*, 19831–19844.

[280] M. Saliba, J.-P. Correa-Baena, C. M. Wolff, M. Stolterfoht, N. Phung, S. Albrecht, D. Neher, A. Abate, *Chem. Mater.*, **2018**, *30*, 4193–4201.

[281] E. H. Anaraki, A. Kermanpur, L. Steier, K. Domanski, T. Matsui, W. Tress, M. Saliba, A. Abate, M. Grätzel, A. Hagfeldt, J.-P. Correa-Baena, *Energy Environ. Sci.*, **2016**, *9*, 3128–3134.

[282] https://ourworldindata.org/energy-production-and-changing-energy-sources#empirical-view.

ACKNOWLEDGEMENTS

Este trabajo de investigación para optar al Grado de Doctor por la Universidad del País Vasco (UPV/EHU) se ha realizado en Polymat, bajo la dirección del Dr. Juan Luis Delgado Cruz y el Dr. Aurelio Mateo-Alonso.

En primer lugar, me gustaría agradecer a mi director de tesis, Dr. Juan Luis Delgado Cruz, sin el que no hubiera sido posible la realización de esta tesis. Me gustaría agradecerle su siempre buena disposición y dedicación, por su apoyo, por la libertad para desarrollar cualquier idea que pudiera tener, pero sobre todo por confiar en mí y darme la oportunidad de realizar este trabajo. Muchas gracias.

También quería agradecer al Dr. Aurelio Mateo-Alonso, por proporcionarme los medios necesarios para llevar a cabo muchas de las medidas necesarias para la caracterización de los materiales presentados en esta tesis.

Agradezco sinceramente a Polymat por el apoyo financiero recibido para la realización de esta Tesis Doctoral. En especial, me gustaría agradecer al Prof. José María Asua y al Prof. David Mecerreyes porque sus consejos en las reuniones de proyecto han sido de gran ayuda para el desarrollo de este trabajo.

También me gustaría agradecer a todo el personal administrativo (Idoia Azaldegui, Izaskum Balza, Dr. Mónica Moreno, Liudmila Zhyhmiantovich, Álvaro Moreno y Dr. Maike Lukowiak) que forma parte de Polymat, que son imprescindibles para el funcionamiento de este centro, destacando la labor de Izaskun Balza por su ayuda desde el principio.

En este trabajo han participado otros grupos de investigación a los que agradezco enormemente su colaboración y contribución: Al grupo de investigación del Prof. Shu Seki de la Universidad de Kyoto (Japón) por los estudios de conductividad que se recogen en este trabajo. Al grupo de investigación del Prof. Michael Grätzel de la Escuela Politécnica Federal de Lausane (Suiza) por las medidas fotovoltaicas de las células solares de perovskita. En especial a Silvia Collavini, quien fue quien llevó a cabo dichas medidas.

A todo el personal técnico (SGIker, Polymat, Biomagune), por el apoyo durante estos cuatro años en la caracterización de los materiales. En especial, me gustaría agradecer a la Dra. Sofía Guezala, por su gran ayuda y siempre buena disposición para cualquier dificultad en la caracterización.

Agradecer a todos los que han formado parte del grupo Hybrid materials for photovoltaics y con los que he tenido la suerte de compartir laboratorio en algún momento durante estos años. En especial: A la ahora ya Dra. Silvia Collavini, la primera persona que conocí y con la que he compartido muchísimos momentos, y los que nos quedan… Eres muy especial para mi, y ha sido un placer compartir toda esta etapa contigo. Te voy a echar muchísimo de menos. También a Sebastian; la persona de la que más aprendí en este doctorado y a la que echo de menos desde que se marchó. Gracias por enseñarme, por ayudarme, por estar siempre dispuesto, aun cuando no seguía tus consejos. ¡De verdad, gracias! A Jorge; me alegro haber coincidido contigo en la última etapa. Sin duda fue la mejor noticia saber que bajarías a la facultad a escribir tu tesis. Gracias por estar, por la ayuda, por las risas, por el ping pong (¡has mejorado mucho!). A Ottavia, que llegó para revolucionarlo todo. Son infinitos los momentos que se me vienen a la mente a pesar de que estuviste poco tiempo. Gracias por todo, especialmente por hacerme llorar de la risa. A Nevena, gracias por los consejos, por los cafés con un toque inglés, por los buenos momentos (que han sido muchos). No tengo palabras para agradecerte tu ayuda en este último año, sobre todo en la escritura.... sin esperar nada a cambio. Te deseo lo mejor. A Miki, que aunque oficialmente formaba parte de otro grupo para mi era uno más del nuestro. Muchas gracias por todo, por siempre estar dispuesto a echarme una mano, por los buenos ratos que hemos pasado, por los conciertos, pero sobre todo por la paciencia que tuviste. ¡Te deberían poner una estatua por aguantarnos! Por último, pero no menos importante, a Melissa, la última en incorporarse, y que nos ha hecho esta etapa final más agradable, contagiándonos su siempre estado de optimismo y felicidad. Te deseo lo mejor, no tengo duda de que tu tesis va a ser excelente.

También quiero dar las gracias de forma especial al que para mí es mi segundo grupo (lo pone claramente en la web), a todos los que forman parte del grupo de Koke, tanto a los que ya terminaron (Belén, Valentina, Diego, Helena, Jose, Marco, Mauro, Gabri, Cristian, Alessandro…) como a los que continúan (Felix, Bet, Elena, Rajeev, Fengkun, Marta, Javi, Alberto, Juanpi…). Han sido muchas risas, tanto cuando me acogíais en vuestro laboratorio para hacer medidas como fuera del laboratorio. A todos, gracias, pues sin vosotros estos 4 años no hubieran sido lo mismo. Mención especial me gustaría hacer: A Alberto; al que fue toda una suerte haber conocido. Gracias por todos los buenos momentos, por el surf, por las cervezas de después (sobre todo), por tantas risas ¡Te voy a echar de menos amigo! También, me gustaría agradecer a Juanpi; de esas personas que quieres tener cerca. Animo para el

final, ¡ahora te toca a ti! De los que ya terminaron aquí, no me olvido de Cristian y Gabri, con los que pasé grandes momentos, y de los que guardo un recuerdo muy bonito.

Muy especialmente me gustaría agradecer a Marta: gracias por todo; por ayudarme (personal y científicamente), escucharme, y por apoyarme siempre, especialmente este último año. No puedo imaginar cómo hubieran sido estos años sin ti cada día. Gracias por ser la mejor amiga, compañera de piso y un largo etcétera, que alguien puede tener. Seguiría, pero ya escribí una tesis y necesitaría escribir otra solo para agradecerte. Dicen que no es el lugar, si no la compañía. ¡Ahí lo dejo! Te voy a echar mucho de menos Marta.

Durante estos 4 años he tenido la oportunidad de conocer a muchas personas tanto dentro como fuera de Polymat que, aunque no coincidíamos en el "día a día", han sido muchos pintxopotes, fines de semana… y me llevo grandes amistades. ¡Gracias a todos! En especial me gustaría agradecer a Shagha y Ali, a los que he cogido mucho cariño. A Ali, que se sabía más dichos en castellano que yo, y a Shagha por enseñarme su habilidad para encontrar sillas libres. ¡Os voy a echar de menos chicos! También agradecer a Ander, por los buenos ratos fuera del laboratorio. ¡Me alegro haberte conocido!

A mis amigas "de toda la vida" por permitirme desconectar de la rutina, por estar en todos los momentos importantes, desde siempre.

A mis amigos de la carrera, en especial a Ana, Mónica, Rocio, Belén y Julián. Cada uno en una punta, pero sé que estáis. ¡Me acuerdo mucho de vosotros!

También, me hace especial ilusión agradecer a Mire, Kris y Leti por estar ahí desde el momento en que formamos nuestro gran cuadrado, hace ya más de 10 años. Gracias chicas.

No puedo dejar de agradecer a Javi, por ser un pilar fundamental en esta etapa. Son muchas las cosas que podría decirte en agradecimiento de esta memoria. Aunque ya sabes lo poco expresiva que soy, esta es una buena oportunidad para darte las gracias por comprenderme, por tu saber escuchar, por tu paciencia infinita, por apoyarme y creer mí. Me siento muy afortunada de haberme cruzado contigo.

Por último, me gustaría agradecer a mi familia, por apoyarme desde siempre en todo lo que hago. En especial a mis padres, porque gracias a ellos soy lo que soy. A mis hermanas, Lauri, Ester y Reyes, gracias por comprenderme siempre, que aún en la distancia, sé que os alegráis mucho por mí.

A todas aquellas personas que de un modo u otro han contribuido a la elaboración de esta memoria.